Understanding and Controlling the Reactivity of Metal Oxide Nanoparticles

Toby William Bird

Doctor of Philosophy

University of York

Physics

September 2022

Abstract

This thesis describes the development and application of a gas aggregation cluster source for the production of metallic nanoparticles (NPs). This high vacuum technique can produce a beam of crystalline particles through magnetron sputtering which may then be manipulated in-flight to further modify the properties of the particles. The particles were then subject to a detailed study of their reactivity as oxidation, in particular, proceeds very differently at the nanoscale compared to the bulk. Creating an understanding of oxidation at the nanoscale is critical to a more widespread application of these particles in industry.

After an introduction, the theory of solid state diffusion and oxidation is discussed. Particular attention is paid to the shortfalls of the bulk theories of oxidation at the nanoscale as well as highlighting the work to bridge the gap between the two length scales. Chapter 3 focuses on the experimental techniques used throughout this project to investigate the oxidation of the metal NPs. Chapter 4 describes in detail the gas aggreggation cluster source, starting with the theory of particle growth and beam production, then providing a comparison to other popular methods of growing NPs, before finally describing the work that took place to develop the cluster source at York. Chapters 5, 6, and 7 then present the results of targeted studies into the oxidation of Fe NPs. Fe is particularly relevant due its magnetic properties and high reactivity. Chapter 5 shows the work of *in-situ* environmental transmission electron microscopy experiments that allowed the determination of the diffusion coefficient of Fe in Fe oxide for the first time. Chapter 6 shows the results of *in-situ* spectroscopic measurements investigating the different types of oxide that form, with Chapter 7 showing the work that was undertaken to attempt to control/inhibit the oxidation process through coating with a secondary material.

Contents

List of Tables

List of Figures

Acknowledgements

Completing a project like this is never just a solo undertaking with a number of people giving their time, expertise, and patience to help guide me through and I'd like to take this opportunity to acknowledge them. My thanks go to Shuayl Alotaibi, Dr Sitki Aktas, and Dr Phillip Bentley. The research support staff in the department in Research Services, Mechanical Workshop, and Electronic Workshop. As well as Maha Alotaibi for their time and effort on the SEM. My thanks also go to Dr Demie Kepaptsoglou for the images acquired at SuperSTEM and also Dr Leonardo Lari for the extensive experimental work that he undertook on our behalf. I'd also like to thank Dr Ben Coulson for their time on the SEM as well as being a great support to me personally as we battled lockdowns to continue working in the lab.

I'd like to acknowledge the work of Dr Steve Baker, Stuart Thornton, and Dr Katie Dexter for the legacy samples produced in Leicester that were used in part of this project.

My thanks go to my supervisors Dr Andrew Pratt and Prof Roland Kröger for giving me the opportunity to work on this project. Furthermore, in particular, my thanks go to Andy for his daily advice and encouragement.

I would like to extend my gratitude to my family whose love and support have given me the freedom to complete this work. In particular a special thank you goes to my mum, Dr Julie Bird, who's been a great influence on me as well as having the unenviable job of translating my early drafts of this thesis into readable English.

Finally, to Lauren without whom I'd never have completed this. You have constantly inspired and motivated me to keep going. You have always been there at every turn and I'm so thankful for everything you have done for me.

Declaration

I declare that this thesis is a presentation of original work and I am the sole author. This work has not previously been presented for an award at this, or any other, University. All sources are acknowledged as References.

The following publications, either in print or soon to be submitted, have arisen from this work:

[1] *Dynamic Observation of the Nano-Kirkendall Effect using e-TEM* T. W. Bird, et al., (in preparation)

[2] *Investigation of the Stability of Ag-Coated Metal Core-Shell Nanoparticles* T. W. Bird, et al., (in preparation)

[3] *Formation of quasi-free-standing graphene on SiC(0001) through intercalation of erbium* P. D. Bentley, T. W. Bird, A. P. J. Graham, O. Fossberg, S. P. Tear, and A. Pratt, AIP Adv. 11:025314,2021

Chapter 1

Introduction

1.1 Time to Think Small

Nanoparticles (NPs), small collections of atoms below 100 nm in diameter, have been studied extensively due to their incredible properties that have the possibility of affecting many walks of life, from biomedical research in drug delivery [1], cancer treatment [2], and contrast improvement in MRI machines [3], to improving the environment in water remediation [4] and catalysis [5]. NPs can act as the basic building blocks on which complex systems can be built with their properties intrinsically linked to size; they exhibit interesting phenomena including optical, electronic, and magnetic [6, 7]. For example, super-paramagnetism becomes prevalent as the particle size is decreased. Super-paramagnetism is the phenomenon where the magnetisation direction can change along the easy axis due to thermal fluctuations [8] with the time between each change being the Néel relaxation time. Below a certain temperature, termed the "blocking temperature", there is not enough thermal energy for the magnetisation direction to change and so the particles exhibit ferromagnetic behaviour. Above this temperature, the particles exhibit super-paramagnetic behaviour when no external field is applied as the overall magnetisation, if measured at lower frequencies than the Néel relaxation time, is shown to be zero.

Through well-established chemical [9] or biological [10] methods, amorphous or polycrystalline metal NPs can be synthesised with relative ease and scaled up to produce industrial quantities. Multi-element and functionalised NPs can also be produced

allowing the ability to craft and tailor the particles to suit the desired outcome. Functionalisation can occur through the attachment of surfactants and ligands to improve physical stability, increase hydrophilicity as well as allow further functionalization and conjugation with bioactive molecules or by targeting ligands to obtain multi-functional NPs [4]. Active medicinal agents can be attached to magnetic particles and, through the application of a magnetic field, delivered to the targeted areas and released [11]. Another example is the use of a functionalised lipid NP in the mRNA COVID-19 vaccine. This allowed the mRNA to pass through the cell membrane where the mRNA was then replicated in the cells making the vaccine effective [12].

For many of the listed applications above the use of an external magnetic field to influence the particles is key. A well known example is the case of magnetic hyperthermia where the application of an alternating magnetic field causes the particles to heat up so that if the particles are then injected into cancerous tissue this can lead to very localised cell death allowing for targeted treatment [13]. The magnetic properties can also be applied in water remediation where functionalised magnetic particles can be used to remove heavy metal contaminants and microbes from water. The targeted contaminant binds to the functionalised section and then the particle is drawn out of the water through the use of a magnetic field [14].

Though lots of magnetic NP systems exist, iron and its various oxides have naturally become a core focus [15]. Unfortunately, Fe oxidises very readily and can form many different types of oxide [16] which all have different structures and therefore differing magnetic properties. For example, magnetite (Fe_3O_4) has an inverse spinel crystal structure with Fe^{2+} and Fe^{3+} ions coordinated in a 50:50 mix in octahedral sites as well as Fe^{3+} in tetrahedral sites. This is in contrast to wüstite ($Fe_{1-x}O$) that has a cubic crystal structure which only has Fe^{2+} ions in octrahedral sites. Many other Fe oxide structures exist such as α- and γ-Fe_2O_3. These differing crystal structures mean that, for example, magnetite is a ferrimagnet and wüstite is an antiferromagnet [16]. Understanding how Fe oxidises and which oxide structure is formed is therefore of critical importance so as to control which properties are expressed for the desired application.

How metals oxidise has been studied since the 1930s with various theories developed, e.g. by Cabrera-Mott [17] and Wagner [18] to explain bulk metal oxidation. However, as will be shown later (in Chapter 2), these theories have shortcomings when it comes to describing nanoscale oxidation. Various phenomena such as strain [19], space charge [20], and vacancy formation [21] are not adequately accounted for in the bulk theories and significant work has gone in to modifying the theories of Carbrera-Mott and Wagner to fit subsequent experimental data. The Cabrera-Mott theory of oxidation explains the initial oxidation of a metal surface across a thickness of 0 - 4 nm but above 4 nm the explanation of continued oxide growth does not match experimental data. Wagner's theory is only applicable to oxides growing past a thickness of 20 nm due to underlying assumptions made in the theory. This means there is a large intermediary size range where neither theory adequately describes the oxidation kinetics observed [22].

Production of pure single crystalline metal NPs through common chemical synthesis routes is not trivial and typically the particles produced are fully oxidised [9]. Pure Fe has a higher saturation magnetisation of 217.6 emu/g [23] compared to 72.5 emu/g for hematite (α-Fe_2O_3) [24]. So finding a viable route to producing pure Fe particles is of key importance. One way this could be achieved is through the use of high vacuum techniques such as a gas aggregation cluster source where production of pure crystalline metal particles is possible. Due to the condensation of a metal vapour under vacuum, the surface is typically free of oxides and unwanted surface contaminants allowing the study of the particle's native properties. Manipulation of the particle beam also allows for functionalised particles to be produced which could be an avenue to a pure Fe metal core with a protective shell surrounding it which prevents any oxidation. The downside of this technique is that the particles cannot be produced in large quantities as easily as the chemical route.

In this project, a gas aggregation cluster source was developed which allowed the production of clean metal NPs. These were then studied through *in-situ* measurements on an electron microscope as well as a spectroscopy system to explore the oxidation of Fe NPs. This led to the study of core-shell particles where an attempt at protecting the metal core with a secondary shell material was investigated.

1.2 Thesis Overview

Following this Introduction, Chapter 2 describes the theory of solid state diffusion as well as the two most popular theories of bulk metal oxidation. The limitations of these theories with regards to NP oxidation is then explored with a particular focus on the role of space charges, grain boundaries, and strain on the oxidation process.

Chapter 3 describes the various experimental techniques used during this project to investigate the reactivity and oxidation of metal NPs, namely photoelectron spectroscopy and transmission electron microscopy.

Chapter 4 begins with an explanation of the cluster source, how it operates, particle nucleation, and beam formation. A few popular methods of particle manipulation are also explored followed by a description of other particle formation techniques with a comparison to the cluster source. The chapter closes with a description of the newly acquired cluster source at York and how it was developed to improve and enhance its capability. Characteristic data is also reported showing the capabilities of the source during its operation. Finally, a second cluster source is described which was used by collaborators to provide samples which were investigated during this project.

Chapter 5 shows the results from *in-situ* environmental transmission electron microscopy of Fe NPs where the effects of temperature and beam dosage on the oxidation of the NPs are explored. The nano-Kirkendall effect, the production of hollow particles due to an imbalance of diffusion rates, is observed. The complete oxidation of the particles allows for the determination of the diffusion coeffecient of Fe in Fe_xO_y, as reported here and believed to be for the first time.

Chapter 6 shows the results of *in-situ* photoelectron spectroscopy studies where the initial oxidation states of Fe NPs are explored. The gas aggregation cluster source was connected to the analysis chamber of the spectroscopy vacuum system in the laboratory and particles were deposited directly onto clean Si surfaces. After initial characterisation, the particles were exposed to low partial pressures of oxygen while being heated at different temperatures to see how this would affect the form of oxide that was grown. The initial oxide was shown to be $Fe_{1-x}O$ with this then

transforming into Fe_3O_4.

Chapter 7 explores the way in which coating the particles with a secondary material can affect their reactivity and oxidation. Fe and Cu NPs were coated in Ag and found to produce Janus-like particles instead of coating the particle in a secondary layer. After taking the initial readings following growth the stability of the particles was investigated through two methods. Firstly, one of the samples was placed in a ceramic tube furnace and heated in atmosphere to 150 °C for a few hours and the others were left in a desiccator at atmosphere for one month. The Ag was found to catalyse the oxidation reaction in both cases with nanowires found to grow out of the particles where the Ag had been present, similar to that of the growth processes of vapour-solid-solid growth. The Ag-coated Cu (Cu@Ag) particles were found to be stable after a month with no nanowire growth shown.

The final chapter, Chapter 8, will conclude the findings in this thesis as well as lay out the next steps that could be taken in the development of the cluster source as well as further experiments to investigate nanoscale oxidation.

Chapter 2

Oxidation and Diffusion Theory

How atoms move in solids is important to understand for a wide variety of fundamental processes and also for many industrial applications. How atoms and molecules diffuse is largely understood in gasses but less so in solids. For example, in manufacturing, the unwanted diffusion of dopants in an alloy could lead to unforeseen structural weaknesses developing inside the substance being created. So gaining an understanding of solid state diffusion is critical to limit or control these effects. How atoms diffuse during oxidation is also important as unwanted oxides could develop and change the properties of the material that is being used or created. The movement of atoms during oxidation does not have an accepted mechanism and understanding has not progressed much beyond two popular theories that date back to the mid 1900s, those of Cabrera-Mott (CM) [17] and Wagner [18]. These bulk theories of metal oxidation do not apply in the same way on the nanoscale and as such, struggle to explain the various phenomena that occur during nanoscale oxidation. In this chapter, atomic diffusion and movement through solids will be described as well as the theories of Cabrera-Mott and Wagner. The chapter will then explore how these theories fall short at the nanoscale.

2.1 How Atoms Move

2.1.1 Fick's Law and Movement of Atoms in a Lattice

The flux of particles across a concentration gradient can be described by Fick's law which states that the flux of the particles is proportional to the concentration gradient through the equation

$$J = -D\frac{\partial C}{\partial x} \tag{2.1}$$

where J is the flux of particles across the concentration gradient $\frac{\partial C}{\partial x}$, C is the concentration, and x is the length scale of the movement, i.e. the thickness of an oxide shell, and D is the diffusion coefficient. The movement of particles can in fact be due to two factors, the concentration gradient as mentioned and an external force or driving force. The influence of this force causes the particles to move with an average velocity $\langle\nu\rangle$ which leads to a flux of $\langle\nu\rangle C$. This modifies Equation 2.1 to

$$J = -D\frac{\partial C}{\partial x} + \langle\nu\rangle C \tag{2.2}$$

The second term on the right hand side of Equation 2.2 can be seen as the drift term due to the external force. The external force can be an external electric field, a temperature gradient, or a stress gradient such as the Gorski effect where there is migration of atoms in an elastically deformed sample [25]. These all modify Equation 2.2 such that the flux can be enhanced due to the applied force. If the force is in the opposite direction to the concentration gradient, then a steady state situation can occur where the two effects cancel each other out. This leads to the Nernst-Einstein relationship which describes the relationship between drift versus diffusion:

$$\frac{\langle\nu\rangle}{D} = \frac{F}{kT} \tag{2.3}$$

where F is the applied force, k is Boltzmann's constant, and T is the temperature. Diffusion in gasses and liquids is taught at school (osmosis for example) but there remains a lack of understanding of diffusional processes in solids. How do atoms

move such that chemical reactions like oxidation can occur? After all, atoms have to move somehow for these reactions to take place. Movement of atoms is known to occur during the processing of alloys where impurities diffuse in the solid structure as well as thermo-migration at elevated temperatures. Figure 2.1 shows the mechanisms that allow these processes to happen.

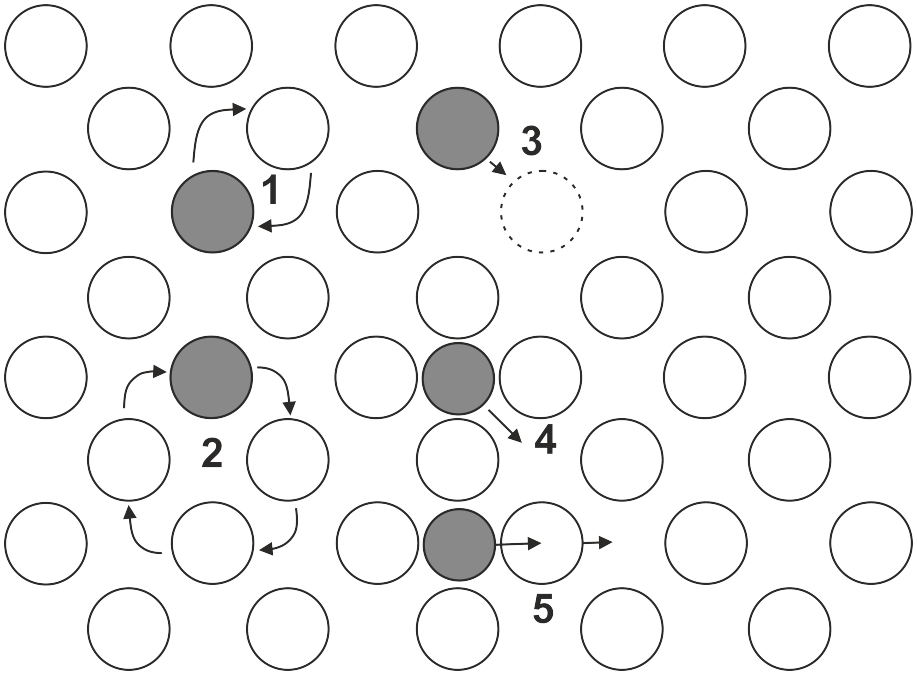

Figure 2.1: Atomic movement mechanisms that could occur in a solid with details explained inside the text. The grey atoms are the tagged atoms, which are performing the possible movements such as 1: direct exchange, 2: ring movement, 3: vacancy exchange, 4: interstitial mechanism, 5: interstitialcy mechanism [26].

From Figure 2.1, mechanism 1 shows a direct exchange where the tagged atom swaps places on the crystal lattice with a neighbouring atom. Mechanism 2 is a similar process where a circular movement or "ring" movement occurs. These processes are unrealistic/improbable since, in mechanism 1, the atomic repulsion between the two atoms would stop this from happening, as at the nominal halfway point in the exchange, the two atoms would be on top of each other which would repel them. With mechanism 2, this repulsive force can be used as an advantage as the tagged atoms can be pushed and therefore push the next atom around to form the ring mechanism. This is unrealistic however as it requires the co-ordination of many atomic jumps.

Mechanism 3, from Figure 2.1, shows the vacancy exchange mechanism where an atom can move into a vacant site in the lattice. This causes the vacancy to then be in the position the atom was just in and this can be seen as the movement of the atoms or the vacancies with the vacancies being conserved. In general, this is one of the few ways that an atom can move within a crystal lattice. Shown in Figure 2.2, the tagged atom originated at lattice site A when a vacancy arrived at B and so the tagged atom exchanges with it and is now situated at B. The vacancy, now at site A can then exchange with any of the atoms that are now its nearest neighbours, otherwise known as its coordination number ζ. The tagged atom that exchanged with the vacancy can then swap back with said vacancy with each jump between the same atom and the same vacancy not being independent of each other. The probability that the vacancy will exchange back with the original tagged atom is $\frac{1}{\zeta}$.

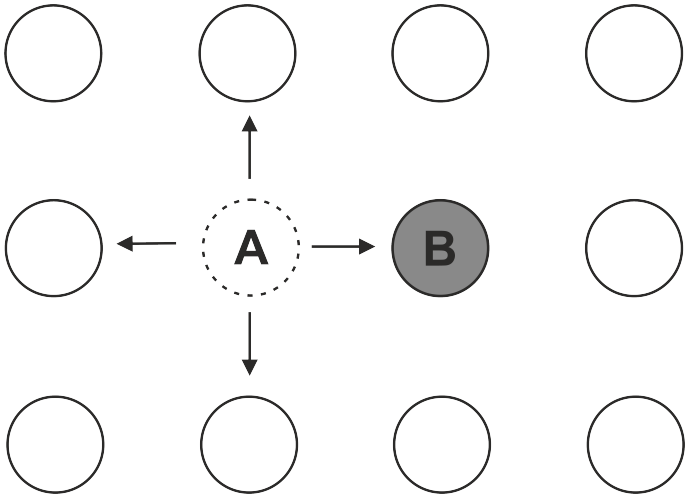

Figure 2.2: Tagged atom exchanges with a vacancy that arrived on lattice site B so the movement A to B is complete. The vacancy can then exchange with any of its nearest neighbours with a probability of $\frac{1}{\zeta}$ where ζ is the coordination number (number of nearest neighbours).

The vacancy does not necessarily have to immediately exchange back with the tagged atom and after a purely random walk through the lattice, the vacancy can end up once again as a nearest neighbour of the tagged atom. If they then exchange for a second time this is then not independent of the first jump as the two moving species are the same. Though this does not necessarily mean that the second jump cancels the first jump as the vacancy could be on a different nearest neighbour position.

Therefore, for n jumps there are $n(\frac{1}{\zeta})$ pairs of jumps and $2n(\frac{1}{\zeta})$ lost jumps or $n(1-\frac{2}{\zeta})$ effective jumps. This parameter is known as the correlation factor which shows how successive jumps are correlated. The factor modifies the diffusion equation from a purely random walk approach to a process that is determined by the interaction of a vacancy with the same atom.

Mechanism 4, in Figure 2.1, shows the movement of an atom from interstitial site to interstitial site. Mechanism 5 is the indirect version of this known as the interstitialcy mechanism. In this mechanism, an atom is pushed to an interstitial site by the arrival of an interstitial atom on one of its nearest neighbour positions. This pushed atom can then push another atom out in the same fashion. Both of the mechanisms (4 and 5) are possible and present alternative pathways, along with the vacancy exchange mechanism, for atoms to move through a solid crystal lattice. Mechanism 5 can also occur between planes to form what is known as a dumbbell interstitial where in a BCC structure the movement of the interstitial atom can push the central atom out so that the two atoms then inhabit the centre point at half distances.

The diffusion coefficient can be derived for a cubic lattice if only nearest neighbour jumps are considered. The full derivation of this is available in Ref. [26] (pages 39-41).

$$D = \frac{1}{2}\Gamma_s \sum_{s=1}^{\zeta} \lambda^2 \tag{2.4}$$

where Γ_s is the jump frequency of an atom towards a given site s and λ is the jump distance. This equation still applies if the atom is moving towards an interstitial or substitutional lattice site in BCC and FCC crystal structures.

When the atoms move via these mechanisms there is an associated energy barrier that they must overcome. In Figure 2.3(a), an atom is situated in a potential well at the lattice site at point M and is going to move to point M* which is another potential well site a distance λ away. The barrier to this movement can be seen to be defined by the four nearest neighbour atoms to point M* which act as a sort of gate which the tagged atom has to pass through, shown in Figure 2.3(b). As the tagged atom moves between the points it has to pass through the "gate" which is defined by the nearest neighbour atoms and is shown in the figure as the shaded

area. The saddle point of the potential barrier can then be seen as the limiting factor to the diffusion of the atoms through the lattice as they have to surpass this energy barrier.

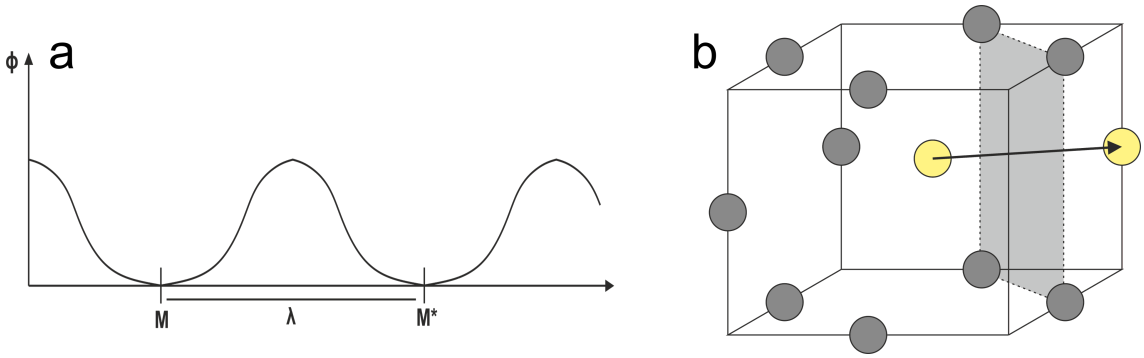

Figure 2.3: (a) Periodic potential barrier to the atom's movement through the crystal lattice from point M to point M*. (b) The movement of an atom through the crystal lattice can be seen as the atom passing through a "gate" (shown by the shaded area) which is defined by the potential from the four nearest neighbours.

The lowest potential barrier to this movement then defines the most likely diffusion mechanism that occurs. The potential barrier can be reduced by the effect of a driving force such as the application of an electric field. The effect of this driving force is shown in Figure 2.4. Here, the applied force lowers the potential barrier in the direction of the applied force and heightens it in the opposite direction. This means that the atoms can move more easily in the direction of the force which can cause mass diffusion in that direction, as shown above in Equation 2.2.

2.1.2 Short Circuit Diffusion

Short circuit diffusion is the term used for the diffusion of atoms through imperfect crystal lattice sites, e.g. grain boundaries between oxide domains, over the surface on interstitial sites, or through long range defects in the crystal [26]. Diffusion across these sites is generally considered to be faster than that of lattice diffusion [27]. The diffusion across the surface is considered the fastest process compared to through the lattice which is the slowest, shown in the relation below,

$$D_s > D_{GB} > D_l \tag{2.5}$$

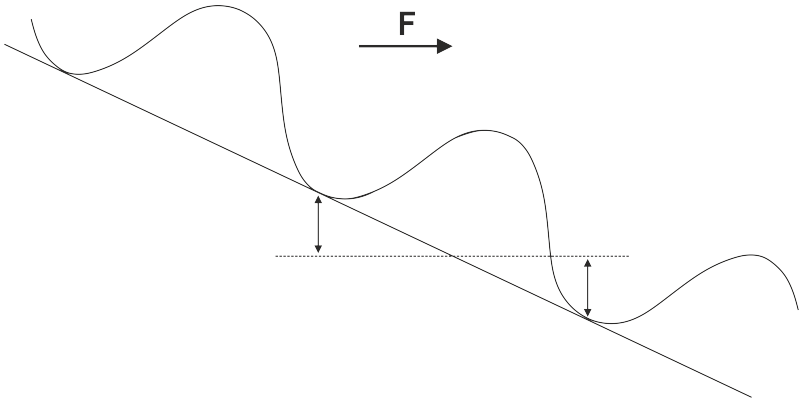

Figure 2.4: An applied force, F, shown by the arrow, lowers the potential barrier in the direction of the force and heightens it in the opposing direction. This force then helps drive the drift of the atoms in the direction of the force.

where D_s, D_{GB}, and D_l are the diffusion coefficients for the surface, grain boundary (GB), and the lattice respectively. Diffusion through these short circuits is quicker compared to bulk diffusion as the energy barrier to the movement of the atom is much lower [26]. This is due to the generally lower co-ordination number of the atoms in and around a GB or at the surface as compared to the bulk. When comparing this to the idea of a potential gate in Figure 2.3(b), the number of atoms forming this gate is reduced and so the barrier will be lower. This allows the atoms to move more freely in these environments; multiple atomic length jumps are possible on the surface for example [28].

These regions are also known as short circuits as they can "short" the diffusion circuit and also trap moving atoms. In the case of a GB, an atom could be trapped inside the defect and a "short" circuit could occur. Figure 2.5 shows a schematic of a GB and the various jump frequencies of atoms from the defect to the bulk and vice versa ($\Gamma_\circ$ and Γ_i respectively) as well as the jump frequencies inside the defect (Γ^*) and inside the bulk (Γ).

If $\Gamma_\circ \ll \Gamma_i$ then this is referred to as a deep trap as the jump frequency out of the defect is much lower than the jump frequency from the bulk to the defect. This means that the atoms entering the defect are unlikely to leave as the time scales of the movement through the defect are too long. A short circuit can occur if $\Gamma_\circ < \Gamma_i < \Gamma^*$ as the dominant jump frequency is the movement of the atoms through the defect which is much larger compared to the movement of the atoms out of

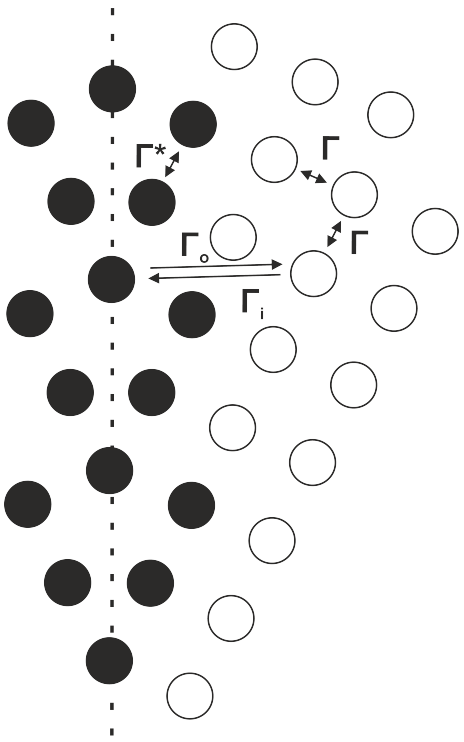

Figure 2.5: A GB shown by the black dots and mirrored through the dashed line with the regular lattice around it shown by the white dots. Jump frequencies of the bulk to the defect and vice versa as well as inside the bulk and the defect are labelled Γ_i, $\Gamma_\circ$, Γ, Γ^* respectively. How these jump frequencies determine whether the defect is a short-circuit or trap is described in the text.

the defect. In essence this shows how defects, and especially GBs, can act as fast diffusion channels as the energy barrier to the movement of atoms is lower due to the region being generally less ordered or less dense compared to the bulk. At low temperatures, these short circuit paths could constitute the only path for transport of material and the defects generally then appear to an observer to attract atoms due to the faster movement. Ingle et al. [29] modelled the energy barrier for a vacancy moving through an α-Fe BCC crystal structure and then through a coherent twin GB and showed the barrier was significantly lower for the movement in a GB. They calculated the barrier in the bulk to be 0.68 eV whereas moving into the GB was between 0.42 and 0.51 eV.

In the case of GB diffusion, when a solute is diffusing from the surface into a medium with GBs three types can occur A-, B-, or C-type diffusion. A-type and C-type are the two extremes of the more general B-type which describes the amount of

penetration and mixing the solute will have with the medium as it diffuses through the GB. Figure 2.6 shows these different types of diffusion where (a), (b), and (c) show A-, B-, and C-type diffusion of a solute on a surface respectively.

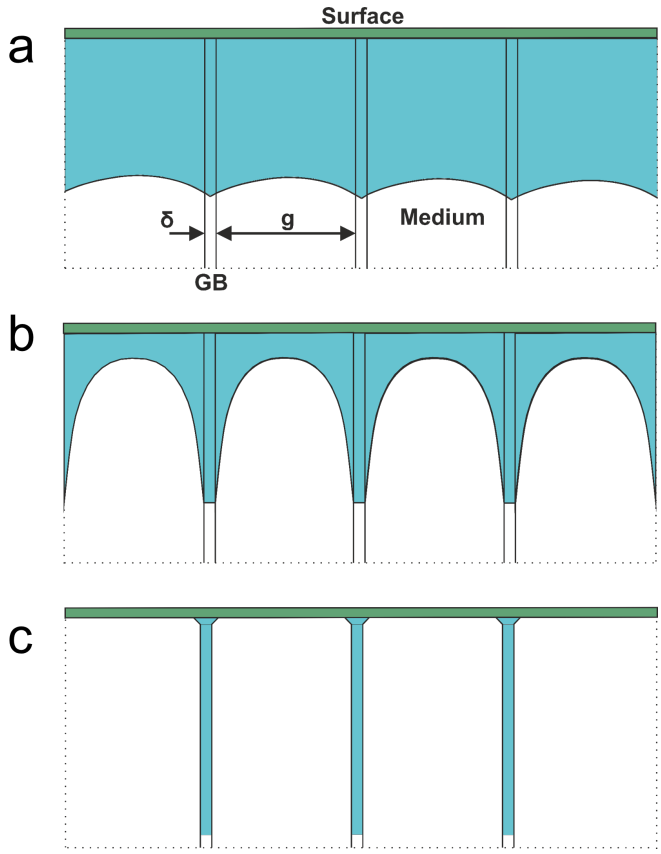

Figure 2.6: Three distinct modes of diffusion can occur when a solute is diffusing from the surface into a medium that contains grain boundaries. (a) and (c) are the two extremes of this where the solute either completely mixes with the medium and thus is not contained to the GB in (a) or where there is no mixing and so the solute is confined to the GB in (c). The more general case is shown in (b).

A-type is where the penetration depth of the solute is significant and there is long range intermixing of the solute and the medium. This means that diffusion is occurring through the medium and is not just confined to the GBs as the mean free path of the diffusing species is much larger than that of the GB width [30]. C-type diffusion is the exact opposite of this case where the diffusion is entirely confined to the GBs which can then be said to be acting as fast diffusion channels. In general, B-type diffusion is more common as there is simultaneous diffusion within the medium which starts from the surface and moves along the GBs which leads to some

leakage. This intermixing of GB and lattice diffusion leads to Hart's law [31] which gives an effective diffusion coefficient, D_{eff}, as

$$D_{eff} = D_l(1 - f) + D_{GB}f \tag{2.6}$$

where f equals

$$f = \frac{2\delta}{g} \tag{2.7}$$

where the values are defined as above in Equation 2.5 and Figure 2.6. The structure factor, f, takes into account the GBs in the determination of diffusion rate. The information contained above is a brief summary of atomic movements and diffusion theory. More in depth information is provided by Philibert [26].

2.2 The Competing Theories of Oxidation

2.2.1 Initial Oxide Formation

The oxidation theory of Cabrera-Mott (CM) was first mooted in the 1950s in an encompassing review article [17]. This theory explains the initial oxidation of a metal surface for oxide thicknesses ranging from 0.5 - 10 nm. The theory posits that drift dominated ionic diffusion is entailed where the slow movement of ionic species across the growing oxide characterises the overall reaction. In this theory, oxygen atoms adsorb on the surface and an electron from the metal tunnels out to ionise the oxygen ion which establishes an electric field. This electric field then forms a potential difference, known as the Mott potential [32], between the metal and the adsorbing oxygen atoms which then draws out the metal cations.

The assumptions made in CM theory are as follows:

1. Electrons can freely pass from the metal to ionize adsorbed oxygen atoms or molecules at the oxide/gas interface.

2. There is a uniform electric field in the film (zero space charge) created by a

positive surface charge on the metal and a negative one from excess oxygen ions (assumed to be O^{2-} ions) at the oxide/gas interface.

3. The electric field created by the electron transfer drives the slow ionic transport across the film and causes it to thicken.

The adsorption of the oxygen molecules at the oxide surface is accompanied by the formation of surface states on the oxide, as shown in Figure 2.7. These surface states are located below the metal Fermi level but above the oxide valence band. The electrons that tunnel from the metal to the vacant surface states raise the energy level to be equal with the metal Fermi level. This results in a charge developing in the adsorbed layer resulting in the uniform electric field. The electrons therefore continue to cross the film readily to maintain zero electrical current. This electric field acts to lower the potential for jumps made by the metal ions, as described above, to either an interstitial site or through vacancy exchange.

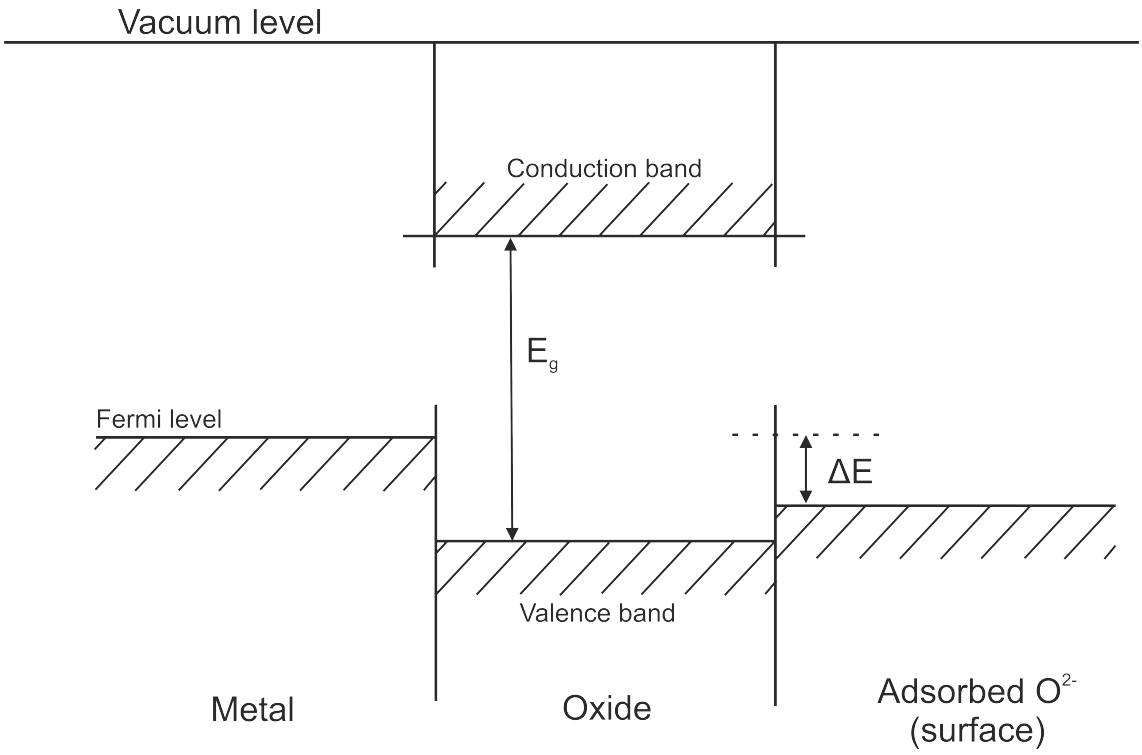

Figure 2.7: Energy (E) level diagram showing how the adsorbed O^{2-} energy level is above the valence band of the oxide but below the Fermi level of the metal. This allows for the electrons from the metal to tunnel to the vacant surface states of the adsorbed O^{2-} layer.

To calculate the rate of the reaction, Cabrera and Mott assumed that the rate controlling process is the injection of a defect into the oxide at one of the film interfaces. Oxide defects can be injected at the metal/oxide interface or at the oxide/gas interface. Shown in Figure 2.8, it can be seen that for the case at the metal/oxide interface (Figure 2.8(a)), this defect can either be an oxygen vacancy or an interstitial metal ion with the reverse being true at the other interface (Figure 2.8(b)).

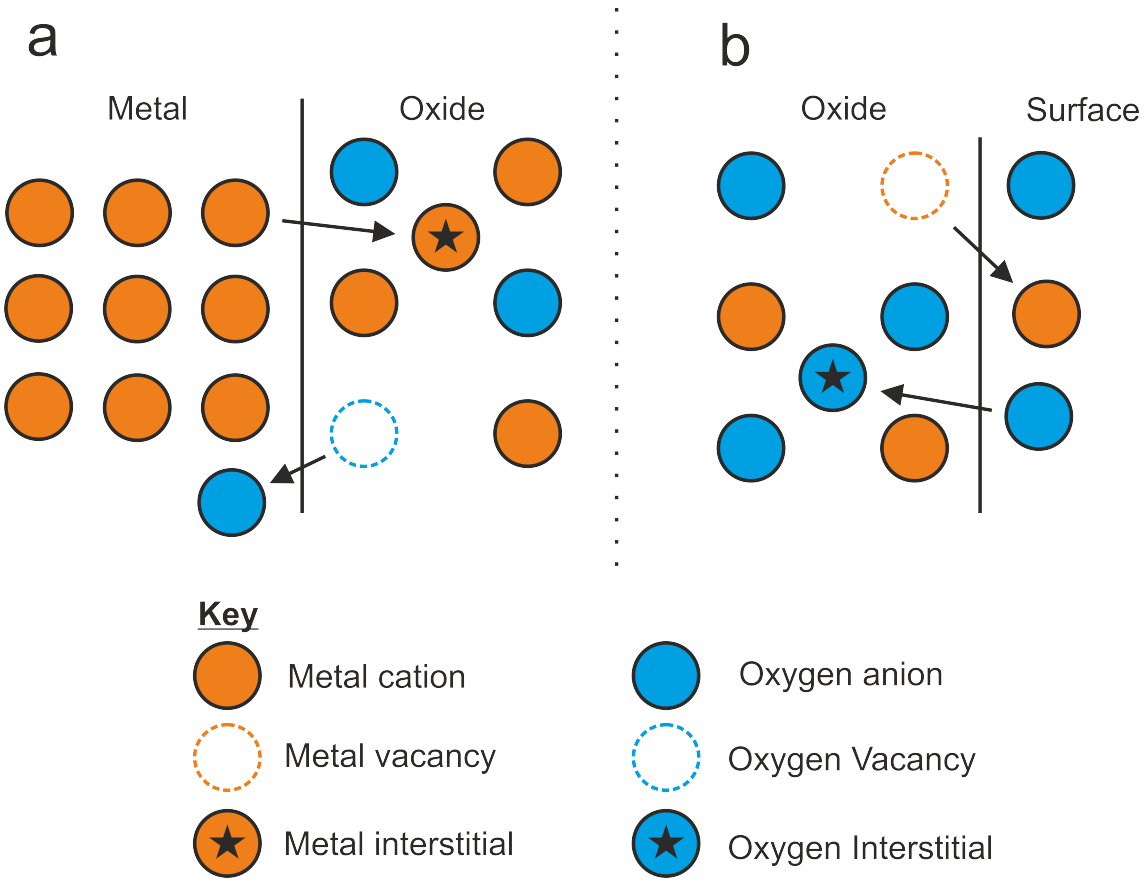

Figure 2.8: Diagram showing the two mechanisms of defect injection considered in CM theory as the rate limiting processes. (a) is at the metal/oxide interface where a metal interstitial or an oxygen vacancy is created compared to (b) where the inverse is true at the oxide/surface interface.

Considering just Figure 2.8(a), the barrier to the injection of the vacancy or interstitial metal ion from the metal into the oxide film is greater than the activation energy for its subsequent movement through the oxide film. Under the influence of the electric field the barriers for the interface and oxide jumps are reduced with the field increasing the number of metal ions entering the oxide. The jump over

the interface has the highest activation energy which therefore determines the rate of film growth. This results in an energy landscape such as that shown in Figure 2.3 in the metal core up to the interface which is then reduced due to the electric field in the oxide as in Figure 2.4. The calculated growth rate follows an inverse log relationship, as defined by:

$$\frac{X_1}{X} = -\ln \frac{D_i X_1 t}{a X_L^2} \tag{2.8}$$

where X_1 is the oxide thickness after the ion jump, X is the oxide thickness before the ion jump, D_i is the diffusion coefficient, t is the time for the jump, and a is the atomic jump distance. X_L is the limiting thickness to which the oxide growth rate becomes negligible which is dependent on the temperature. A more rigorous derivation is given in Atkinson [33].

The kinetics described by CM have been modified to apply to spherical NPs as the shape of the particles will affect the electric field that develops in the oxide. The work of Ermoline et al. [34] showed how the oxidation rate equation can be adjusted to fit a spherical geometry in Cartesian co-ordinates in two schemes. Firstly, where the core is metal surrounded by an oxide and then oxidiser and secondly, where the core is the oxidiser and is surrounded by an oxide and then metal. This second case is important where oxide inclusions are sought after in thin films. Zhdanov et al. [35] showed how the electric field developed in the oxide of a NP will be larger than that expected in a bulk arrangement which leads to faster initial oxidation. The authors note that they only considered the effect of the electric field and that the faster initial oxidation rate could be down to multiple factors, which will be discussed in Section 2.2.3.

Due to the various assumptions outlined above, the theory has an upper limit on the thickness of the growing film of around 10 nm after which the growth rate is assumed to be negligible. The work of Fromhold and Cook (FC) [20, 36–40] showed that the upper limit of the growth of the predicted oxide was in fact around 3 nm. This is due to the fact that the potential barrier for the tunnelling current becomes too large and so the flux of electrons becomes so small that it is rate limiting. This then limits the electric field which means the metal cations are not drawn out as easily

from the metal surface. The authors also considered the role of direct thermionic emission of the electrons via the oxide conduction band or holes through the valence band for films thinner than 30 nm. The temperature effect becomes important as with temperatures below 420 K the tunnelling is dominant up to around 2 nm of oxide growth; after that the thermionic emission increases rapidly. Above this temperature, thermionic emission is the main mechanism for electron movement through the oxide layer which is considered to be Schottky emission.

This dependence on the electron current places a temperature dependence on the critical thickness of the oxide that forms. At a low temperature, there is little to no thermionic emission so oxidation stops when it reaches this critical thickness. As the temperature increases thermionic emission becomes possible and this raises the critical thickness. At higher temperatures, the drop off in the thermionic emitted current as the oxide gets thicker is much less compared to the decrease in the tunnelling current. This means that the oxide growth can continue at a good rate even when the oxide gets rather thick. This oxidation rate is given by

$$\frac{dL(t)}{dt} = R_i J_i L \tag{2.9}$$

where L is the oxide thickness, R_i is the increase in volume of the oxide per cation arriving at the surface, and J_i is the current density of the metal cations. FC theory introduced the concept of coupled currents where the net current across the oxide is zero. The theory also stated that the reaction must take place at the growing oxide/oxygen interface, compared to CM where it can happen at either interface. This requires both metal ions and electrons to move through the oxide layer to the surface and FC theory applies if the following conditions are met:

1. The oxide layer thickens homogeneously.
2. Cations are the moving species across the growing oxide layer.
3. Only one type of oxide is involved.

Due to assumption 2, at high oxygen pressures the movement of electrons or metal cations across the oxide interface becomes the rate limiting step. At lower oxygen

pressures, the supply of oxygen from the gas phase becomes the rate limiting step [41]. Several experimental papers have been published which support the theoretical rates that can be calculated using FC and CM theory such as Leibbrandt et al. [41], Roosendaal et al. [42], and Graat et al. [43].

Leibbrandt et al. [41] exposed clean Fe(100) films in ultra-high vacuum conditions to ^{18}O followed by ^{16}O for a sample and then performed the reverse for a second sample. The authors tracked the amount of each oxygen isotope on their sample as they used Ar^+ ion sputtering to remove layers. It was shown for the sample that was exposed to ^{18}O second that after 100 min of Ar^+ ion sputtering 80 % of it had been removed as compared to the other sample where this was not observed. This shows that the ^{18}O had to be in the top few layers of the sample which leads to the result that the Fe cations had to be the predominant (if only) moving species in the layer. Comparing this to the assumptions of the FC theory above it can be seen that this experimental result satisfies these conditions. The cations are the only moving species and the oxide layer thickens homogeneously as the authors would not be able to distinguish between the two oxygen isotopes if this was not the case. Using high energy ion scattering, Leibbrandt et al. showed how the stoichiometry of the grown oxide layer fits that of FeO and so satisfies the final condition that only one type of oxide is involved.

Roosendaal et al. [42] expanded the work of Leibbrandt to look at the continued oxidation of Fe(100) and how, at different temperatures, self limiting oxidation could occur. The authors showed how the formation of Fe^{3+} states in the growing oxide leads to the oxidation rate decreasing up to a critical thickness. This thickness was shown to increase on annealing the surface, which changes the Fe^{3+} states to Fe^{2+} states. At high enough temperatures (above 120 °C), Fe^{3+} states do not form and so do not block the pathway to continued oxidation. This fits the theory of FC as the current of electrons is more blocked when the Fe^{3+} state is present as the work function of the metal/oxide interface is increased. The authors also calculated the oxidation rates using the FC framework, which they compared to their experimental data, which was found to fit remarkably well. These results show how the initial oxide formation on Fe(100) can follow the growth as explained using FC theory.

Graat et al. [43] also investigated the application of FC theory to the initial oxidation of clean Fe surfaces. However, they investigated a polycrystalline surface as compared to Roosendaal and Leibbrandt's work, which only looked at Fe(100). Graat et al. also exposed the surface to much higher temperatures, investigating from RT up to around 500 K. Having produced a clean polycrystalline Fe surface, Graat et al. exposed it to oxygen under vacuum while heating at various temperatures. Unsurprisingly, they showed that at the higher temperatures, more oxide formed and at a much faster rate. The oxide thickness was determined using ellipsometry measurements with a He-Ne laser. From these oxide growth curves the expected growth was fitted using FC theory and it showed how there was good agreement for the lower temperatures (from 300 - 400 K) but above this there were discrepancies. This is due to the electron current changing from being tunnelling dominated, to thermionic emission dominated which the fitting model did not take in to account. The authors also showed how the initial oxide formation could be theoretically predicted by allowing for a change in the oxide work function, which has been shown to change with thickness.

2.2.2 High Temperature and Thick Oxide Scales

As shown above, the CM theory of oxidation only describes oxide scales up to around 4 nm and FC theory was only considered up to 30 nm. In practice, oxide scales of much greater thicknesses have been observed. Wagner's theory was described in the 1930s [18] and shows a parabolic rate dependence for continual oxide growth of very thick films past 1 μm. The rate of oxide growth is shown in Equation 2.10 below:

$$\frac{dX}{dt} = \frac{k_p}{2X} \tag{2.10}$$

where X is the film thickness and k_p is the parabolic rate constant, which can be seen as the self-diffusion coefficient of the moving species [44]. The assumption of Wagner's theory is that there is no net flow across the film, i.e. that an equal number of oxygen anions are passing across the oxide interface as the metal cations are travelling the other way. Wagner considered the self-diffusion of the ions across the oxide film to be the rate limiting step. This means that there is a small electric

field depending on which species is moving faster, the electrons or the ionic species, along with the assumption that only one type of oxide is formed.

The theory is valid while the Nernst-Einstein relation, shown below in Equation 2.11, still holds.

$$qEa << kT \tag{2.11}$$

where q is the charge of the ions, a is the elementary jump distance (i.e. the distance the ions jump to move through the lattice which is the same order as the lattice parameter), k is Boltzmann's constant, and T is the temperature. As the oxide shells gets thinner, the electric field E gets stronger which then invalidates the Nernst-Einstein relation meaning that Wagner's theory no longer applies. If the temperature was raised to a high enough degree then the Nernst-Einstein relation in Equation 2.11 would then be valid again.

A review article by Chen et al. [45] explores over 100 references in the literature of experiments that prove the parabolic rate for high temperature and continued oxidation of thick oxide scales. Monceau et al. [46] is one such example where the authors show how the parabolic rate constant, k_p, can be obtained from mass gain graphs from thermogravimetric measurements. Analysis showed how some experiments have discrepancies in the fit when plotting Equation 2.10 and in fact changes are needed to fully explain the reaction taking place. They establish four equations that can be used interchangeably depending on whether the surface is a pure metal or an alloy all of which can lead to a parabolic rate constant to be fitted. Essentially, the constants in a standard parabolic equation change depending on the surface and the authors show how by applying these various methods the oxidation rate of these different surfaces can be described with a parabolic rate law. Mrowec et al. [44] also showed how the oxidation of a pure copper sample at temperatures exceeding 900 °C follows a parabolic rate constant. The use of thermogravimetric measurements was also employed in this study and the pure copper sample was exposed under vacuum.

2.2.3 Applications and Modifications of the Theories at the Nanoscale

As can be expected from theories based on bulk length scales, their application at the nanoscale is limited with a few flaws. As mentioned in the introduction, the influence of space charge, strain, and void growth are effects which can not be adequately explained by the theories presented in the preceding sections. Moreover, there is a large gap in oxide shell growth between the predictions of FC theory (up to 30 nm) and where Wagner's theory becomes viable (≈ 1 μm). However, oxides have regularly been shown to grow between these limits and so this needs exploring further. The concept of void growth, termed the Kirkendall effect, is explored more thoroughly in the next section (Section 2.3).

The theories of CM and FC both assume that there is a uniform electric field in the developing oxide layer, which for bulk surfaces, can be assumed to be true. At the nanoscale with the oxidation of NPs, the size effect of the particles comes into play. There are large space charge effects present in the growing oxide layer that must be addressed as this will then cause an inhomogeneous electric field to develop. This is the case for Sutter et al. [47] who see enhanced oxidation of smaller particles when compared to larger ones. The authors investigated the oxidation of Sn for different sized particles: below 12 nm, between 12 and 20 nm, and above 20 nm. They show how the particles below 12 nm were completely oxidised whereas particles above this size had a core shell structure after the initial exposure of 10 days to atmosphere. After a further exposure the particles below 20 nm were completely oxidised whereas the larger particles still had a core-shell structure but with an even thicker oxide shell. The authors put this size dependent oxidation down to the fact that the spherical geometry of the particles leads to an inhomogeneous field which is enhanced at the metal/oxide interface. This larger field then allows for the oxidation reaction to occur at a much faster rate as compared to the assumptions for a planar geometry leading to a homogeneous field.

This enhancement was also explained by Fromhold and Cook [20, 48] who showed that if the moving ionic species encountered an inhomogeneous field (or space charge field) of the opposite sign inside the oxide layer then the diffusion rate would be

enhanced. The reverse is also true where if the space charge is the same sign as the moving species than the diffusion rate can be slowed. This effect is based on the fact that if the rate limiting species in the diffusion is the ionic species then the electron current can be assumed to be at a virtual equilibrium. The space charge is then predominantly ionic and thus causes the retardation of the diffusion. The reverse is true for the case of enhancement of the diffusion reaction when the electron current is the rate limiting step. This analysis by Fromhold and Cook only truly applies to the case of planar diffusion and as such does not take into account the role shape and size effects would have on the diffusion process at the nanoscale.

Oxidation at the nanoscale can be heavily influenced by strain, similar to the problem with space charge where the size and shape of the NPs can have an influence on the strain profile across the particle and oxide shell. Pratt et al. [19] showed how Fe nanocubes, $\approx$ 12 nm in size, displayed enhanced oxidation due to the strain in the oxide shell. This strain was shown to increase away from the metal/oxide interface which is contrary to that seen in bulk properties with it arising due to the grain boundaries between oxide domains. Significant rotation and strain is placed on the oxide domains so that they form a coherent grain boundary which leads to a large strain profile across the domain. This results in an expansive strain in the oxide layer which lowers the energy barrier for the movement of the ions through the lattice. Numerical modelling performed by the authors showed how when strain is taken into account enhanced oxidation is predicted when compared to just diffusion of ions through CM theory. This enhanced oxidation due to strain led to a completely oxidised particle within 24 months instead of a core-shell arrangement as predicted by CM theory.

In contrast, Chen et al. [49] showed that a compressive strain in the oxide shell in Cu NPs limited the oxidation process. Here it was shown that the oxide shell growth rate nearly completely stopped around 2 nm at 298 K with an effective growth rate of 1 monolayer of oxide every year. At an increased temperature of 323 K this limit on the oxide was surpassed with the oxidation rate occurring at a much higher rate. This increase in temperature is not enough to influence the reaction to the degree the authors see which leads them to the conclusion that at this elevated temperature the oxide can be relaxed which releases the strain. This relaxation then allows for

the continued transport of the ions across the growing oxide as the energy barrier to their movement has lowered.

Both of these experiments were performed at (or around) room temperature meaning that the continued electron current due to thermionic emission (as predicted by FC theory) will not be taking effect. Therefore, the strain in the oxide shell is the dominant effect causing these observed kinetics to occur. This strain can have large scale implications on the growth rate of the initial oxide which is not adequately explained in the theory from CM. At higher temperatures, the influence on the energy barrier due to strain can be easily overcome due to thermal energy so it will have a lesser effect.

The oxidation rate can be described by an inverse log relationship for the initial growth and then a parabolic dependence for high temperature or very thick oxides with various experimental results (as shown previously) supporting this. As stated previously, the theories only apply between 0.5-30 nm and then from 1 μm onward which leaves a large gap. Xu et al. [22] showed how the gap between the two regions can be described by a direct log dependence of oxide thickness. Assuming the movement of ions is due to the electric field and diffusion under a concentration gradient, Xu et al. accounted for this as an inverse log relationship under a strong electric field and a parabolic relationship for a negligible electric field. The authors attribute both of these as being akin to CM's and Wagner's theories. At in-between values of electric field, the authors arrive at the direct log dependence as the oxide blocks the surface charge of the metal in the oxide and lessens the effect of the electric field.

This direct-log relationship was also shown by Fromhold and Cook [36] where transition from CM inverse log to direct log occurred around 20 to 30 Å which coincides with a change in sign of the electric potential in the oxide. This was shown to be entirely dependent on the work function of the metal/oxide interface which would in turn affect the tunnelling/thermionic emission current of the electrons.

A direct log relationship was shown to occur during the initial stages of the oxidation of Cu [50] and Fe [51] by theoretical modelling using molecular dynamic simulations. These two papers showed how the different crystal surfaces of each of these metals

had a different reactivity with the activation energies for the (100), (110), (111) surfaces being different. The study into the oxidation of Fe showed how a mixed phase of oxide is predicted due to the fast initial inward oxidation of the oxygen anions through interstitial sites which then slows as the oxide grows in size. This effect was consistent across different temperatures. The encompassing review article by Atkinson [33] described how the initial oxidation rate may not follow an inverse-log relationship as the theory hinges on the injection of one type of defect at either interface, as described in Section 2.2.1 and shown in Figure 2.8, whereas in reality the process will not be as clear cut and can be much more complex. Atkinson makes the point that while the relationship may not follow an inverse-log relationship in practice this does not invalidate the fact that the overall assumptions of the theory are correct.

2.3 The Kirkendall Effect

The Kirkendall effect can occur when the diffusion rates in a diffusion couple are imbalanced. This can lead to a net flux of vacancies back in the direction of the faster diffusing species. These vacancies can then coalesce to form voids at the interface of the product and the source of the faster diffusing species. This is shown schematically in Figure 2.9. Here, A is diffusing faster into B than B is into A leading to a flux of vacancies back towards A which can saturate to form voids at the interface between A and the product AB.

This effect has large scale implications in industry and was first shown by Kirkendall and Smigelskas in 1947 [21] when they looked at the interdiffusion of copper and brass at elevated temperatures. The initial interface was observed to move due to the faster diffusion rate of zinc into the copper than copper into the brass structure. The experiment established that the diffusion of atoms in a lattice occurred through vacancy exchange. The presence of the voids in a material (especially alloys) can make them weaker and so the Kirkendall effect was investigated for many years in order to try and limit the effect so that industry could produce alloys that were stronger [53].

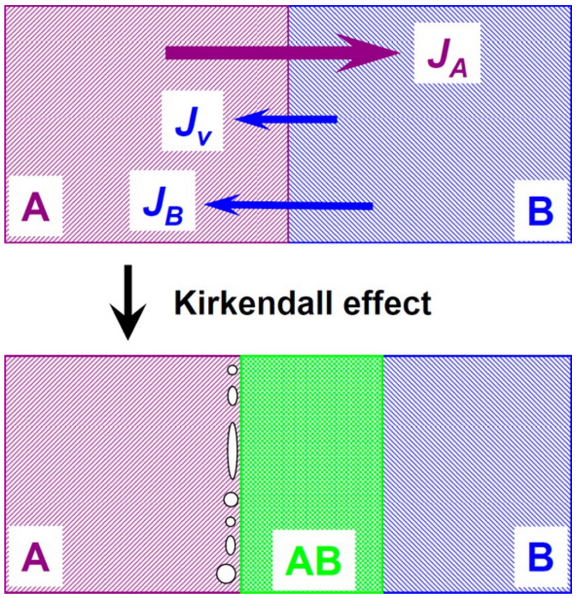

Figure 2.9: Diagram showing the Kirkendall effect in a diffusion couple. A has a higher net diffusion rate into B than B has into A so there is a net flux of vacancies back into A labelled J_V. These vacancies can saturate and form voids at the interface between A and the product AB. Reproduced with permission from Ref. [52].

Investigation of the effect at the nanoscale started with NPs when researchers noticed the imbalance of diffusion rates could lead to the production of hollow NPs. This was a result of the diffusion rate of the core out of the particle being faster compared to that of the inward diffusion of the shell material. The work of Yin et al. [54], cited well over 3000 times, showed that hollow Co NPs could be produced during sulfidation or oxidation at temperatures of 373 K and above.

A few theories have been put forward to explain the hollowing process when it comes to the nano-Kirkendall effect (NKE). Yin et al. in a separate work put forward an idealised case based on simple steady state diffusion governed by Fick's first law [55]. A few assumptions were made:

1. The electric field in the initial oxide can be neglected.
2. The oxide shell is of uniform thickness.
3. The core material can access the shell at all times.
4. The reaction happens at such a rate that the inward growth of the shell is not impeded by stress at the interface.

This means that the diffusion of mass is induced by the difference in the atom concentrations. Figure 2.10 shows the definition of the values used in the derived equations below whilst a more in depth derivation is provided in Ref. [55].

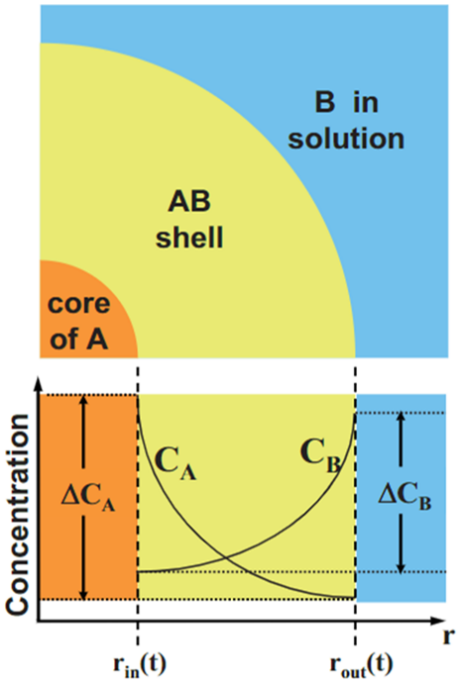

Figure 2.10: Core A reacts with product B to form the shell A_mB_n. The radii r_{in}(t) and r_{out}(t) are also shown here and define the outer edge of the core and shell respectively. The concentration gradients of both reactants are also shown across the shell. The variables shown are used in the equations provided in the text. Reproduced with permission from Ref. [55].

Core A reacts with product B to produce a shell of A_mB_n. The position of the inner and outer boundaries as they grow with time are defined as $r_{in}(t)$ and $r_{out}(t)$. The outward growth is then defined as

$$\frac{dr_{out}}{dt} = \frac{n_A D_A \Delta C_A r_{in}(t)}{r_{out}(t)[\Delta r(t)]} \tag{2.12}$$

where D_A is the diffusivity of A in the product layer, ΔC_A is the concentration gradient of A across the product layer (as shown in Figure 2.10), n_A is the volume density of A in the product layer, and $\Delta r(t)$ is the change in radius of $r_{out}(t)$ and $r_{in}(t)$. The authors then derive a minimum condition for the production of hollow structures to be

$$\frac{n \cdot D_A |\Delta C_A|}{m \cdot D_B |\Delta C_B|} + 1 > r_{out}(t)^3 - r_{in}(t)^3 \tag{2.13}$$

If this minimum condition is violated then the outward growth rate becomes the rate limiting step and therefore the structures obtained are solid shells with a core/shell structure obtained in between.

Tu et al. [56] considered the case of the thermodynamic effects on the hollowing process by applying the Gibbs-Thomson effect. This means that the diffusion is driven by the difference of the chemical potential of the atoms. The authors applied this work to a bi-layer flat surface as well as a spherical particle with both systems comprising Ni and Si. They found that the outward growth rate for the system could be defined as

$$\frac{dr_{out}}{dt} \approx \frac{D_A}{kT}(-\frac{\Delta\mu}{\Delta r}) \tag{2.14}$$

where

$$\Delta\mu = \Delta G + 2\Omega(\frac{\gamma_{out}}{r_{out}} + \frac{\gamma_{in}}{r_{in}}) \tag{2.15}$$

ΔG is the formation energy of the product phase per atom, Ω is the atomic volume of A in the product phase, and γ is the surface energy at the labelled interfaces. The variables in the equations have been altered, in line with [53], so they are consistent with those in Equation 2.13. Equation 2.14 implies that the direction of the reaction can be controlled by thermodynamics and geometry. As in the extreme case of very high values of γ and very small values of r_{out} and r_{in} (as can be expected at the nanoscale) the out-diffusion of the core could be completely stopped.

Tu et al. [56] then considered the stability of a hollow NP that formed. They showed that the concentration gradient of the vacancies from the hollow core to the outside of the shell causes a net flux of vacancies back across the interface. This causes the sphere to shrink and reform as a solid particle. This is particularly relevant for single element hollow spheres as the atoms flow inwards to compensate for the net flux of vacancies outwards [57]. Tu et al. formulated the time it would take for the shrinking to occur to be

$$t_{shrink} \approx \frac{kTr_{in}^3}{10\gamma D\Omega} \tag{2.16}$$

They showed that for a Au particle with initial values of $r_{in} = 30$ nm and $r_{out} = 60$ nm that at 400 °C it would take about 5 $\times 10^3$ s to transform from a hollow to a solid particle. This is compared to a value of only a few seconds if the initial values were $r_{in} = 3$ nm and $r_{out} = 6$ nm.

Yin et al. posited that for the hollow particles to be stable at a given temperature then $t_{shrink} \gg t_{synth}$ where t_{synth} is defined from their model as:

$$t_{synth} = \frac{r_{in}^2(r_{out}^3 - r_{in}^3)^{2/3}}{6D_A\Delta C_A} \tag{2.17}$$

Equating the two together gives

$$\frac{t_{shrink}}{t_{synth}} = \frac{3}{5} \times \frac{\Delta C_A}{(r_{out}^3 - r_{in}^3)^{2/3}} \times \frac{kT_{synth}r_{in}}{\gamma\Omega} \times \frac{D_A}{D_B} \tag{2.18}$$

This means that Equations 2.13 and 2.18 give the minimum requirements for the synthesis of stable hollow particles which Yin et al. [55] summarised in Figure 2.11. The straight line that ends at r_{out}^3 - $r_{in}^3 = 1$ is the condition set by Equation 2.13 and the sloped curve is attained by plotting Equation 2.18. The shaded area above the lines corresponds to the combination of material parameters that allows for the synthesis of hollow particles.

Klinger et al. [58] considered the case of a spherical nanowire to investigate the roles of diffusion through three distinct interfaces, shown below in Figure 2.12 where the view is down the nanowire. Interface 1 denotes the self-diffusion of the metal cations along the "exposed" metal surface. Interface 2 is the core/shell interface where the continued self-diffusion of the metal cations progresses towards a grain boundary. Here the cations cross the oxide shell to complete the oxidation reaction at the shell/gas interface. Finally, interface 3 is the inner surface of the shell where the voids have coalesced.

Klinger et al. [58] considered the interplay of the diffusion coefficients along each of these labelled interfaces, surface D_s, interface D_i, and grain boundary D_{GB}. This group then simulated how changing the values for each of these coefficients changed

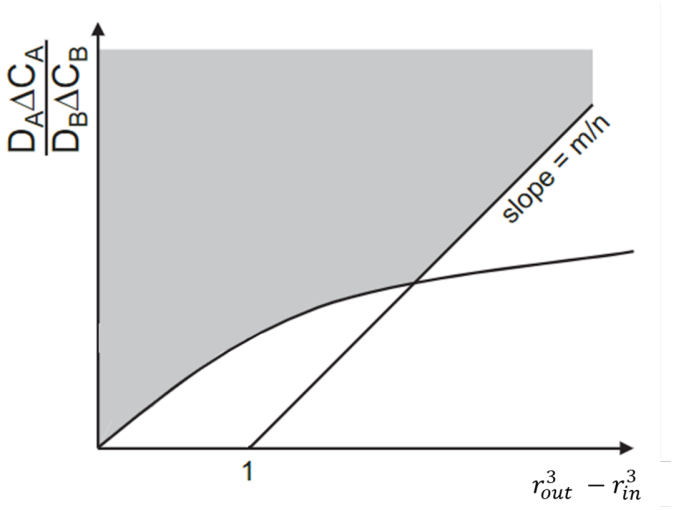

Figure 2.11: Phase like diagram showing the material parameters required to have stable production of hollow particles shown in the shaded region above the lines. The straight line is the result of plotting Equation 2.13 whereas the curve is the result of plotting Equation 2.18. Reproduced with permisson from Ref. [55].

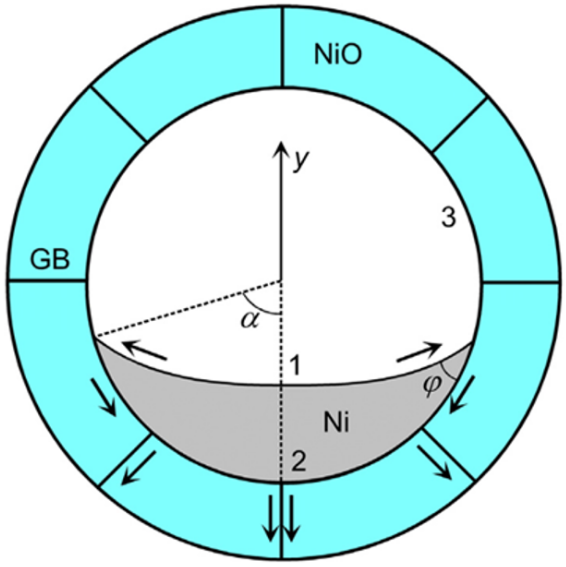

Figure 2.12: Diagram of a circular nanowire used by Klinger et al. [58] to model the hollowing process specifically to investigate the interplay between diffusion rates along the three interfaces that are labelled 1, 2, and 3. Reproduced with permission from Ref. [58].

how the core hollows. In these simulations it was shown that the main driver for the hollowing process was D_{GB} as the total hollowing time was altered the most by changing this value. Changing D_s and D_i was found to have little effect on the total

hollowing time, though the core was shown to change morphology as it depleted and secondary voids were formed as these values changed.

The work of Ibanez et al. [59] shows how different core/void/shell structures can be obtained through chemical synthesis of particles by altering the secondary material. While initially this could be thought to be due to differing diffusion rates, and thus just being the Kirkendall effect, the authors showed that this can be achieved by applying different concentrations of the same product and through different reaction temperatures. The work shows how the structures can be altered and selected for by the careful selection of reacting materials.

Overall, the review paper from Fan et al. [53] summarises that as a general conclusion the formation of perfect hollow NPs is not a necessary result just because the diffusion rates of the core and shell material are imbalanced. Several factors such as the geometry, concentration, or diffusivity do not satisfy the above equations. The product phase could be rich in defects which absorb the vacancies and so the core does not deplete. Alternatively, the particle is too small to start with so it is thermodynamically unstable if it were to form a hollow particle. All these factors can stop the growth of hollow particles.

2.4 Summary

This chapter outlined the basic theory of atomic diffusion in the solid state as well as discussing several theories of metal oxidation and how they fall short at the nanoscale. This is due to the limitations of the theories to properly explain the effect of strain, space charge in the oxide shell, and void formation. Theories on how the Kirkendall effect applies at the nanoscale were also presented showing how the effect is not just the case of competing diffusion rates and careful selection of core and shell materials is needed as well to produce stable hollow nanoparticles.

Proper investigation of oxidation at the nanoscale is required due to the variance from the theory to experimental measurement. Understanding the various effects that can change the oxidation process at the nanoscale allows for a broader picture to be created when studying nanoscale oxidation. This is relevant for the work

undertaken in this research where the oxidation of these NPs was studied so as to gain knowledge of how to potentially tailor the particles so that the oxidation is either enhanced or diminished.

Chapter 3

Experimental Techniques

This chapter will detail the main experimental techniques used throughout this project (aside from the gas aggregation cluster source (GACS) which is the focus of Chapter 4) to characterise the NPs produced. Starting with an overview of the ultra-high vacuum (UHV) system used at York, a description of the various photoelectron spectroscopy techniques available on this system is then given. Finally, the transmission electron microscope (TEM) which was used to image the NPs to gain structural insights is described.

3.1 Ultrahigh Vacuum

It is beneficial to characterise the NPs in as clean an environment as possible, where contamination is kept to a minimum such that the materials are not modified. As will be explained later, a key advantage of using the GACS is that the NPs are produced under vacuum conditions and so will be cleaner than other common production methods. Depositing the particles in vacuum onto a clean substrate is then important if the native properties of the particles are to be analysed. The use of ultra-high vacuum (UHV) is therefore critical as the typical pressures involved are between 8 $\times 10^{-9}$ and 10^{-10} mbar [60]. Pressures above 8 $\times 10^{-9}$ mbar are classed as high vacuum until above around 1 $\times 10^{-5}$ mbar which is referred to as low vacuum. If the GACS is attached to the electron spectroscopy system then the particles can be deposited from a high vacuum into a UHV environment. The benefit is that

under such low pressures the samples can, theoretically, remain clean for a few days as well as allowing spectroscopy techniques to be performed which can not run at higher pressures [61].

3.1.1 Electron Spectroscopy System

The electron spectroscopy system used during this project is shown in Figure 3.1. This consists of three chambers: a fast entry lock (FEL), a preparation chamber where surfaces can be prepared, and the analysis chamber where the samples are analysed with the various spectroscopy techniques.

The FEL has an Omicron-style sample plate rack installed that allows up to four samples to be placed in the system at once. Gate valves are placed between the FEL, the preparation chamber, and analysis chamber allowing each chamber to be isolated and pumped/vented separately as necessary. A long transfer arm allows the effective movement of samples from the FEL through to the analysis chamber.

When a new sample has been loaded into the FEL and a pressure of $\approx 5 \times 10^{-7}$ mbar or lower is reached, the gate valve can then be opened and the new sample can be transferred through the system. Nitrogen is used to vent the FEL (and the rest of the system if needed) to atmospheric pressure to allow for sample exchange. Nitrogen is used to maintain clean conditions inside the vacuum system and allow for more effective pumping.

The preparation chamber houses an Omicron sample stage, equipped with a Th/W filament for e-beam heating and a Cu comb for DC heating. There is also a quartz crystal microbalance (QCM) on the manipulator arm allowing for monitoring of the deposition rate of the various metallic and organic sources attached to the preparation chamber. The QCM is a common tool for measuring deposition rates where the resonant frequency of a quartz crystal decreases as mass is added on top of it. This drop in frequency can then be related to the deposition rate through the Sauerbrey equations where the deposited mass is treated as an extension of the quartz crystal [62].

The analysis chamber houses the electron spectroscopy analysis techniques as well as

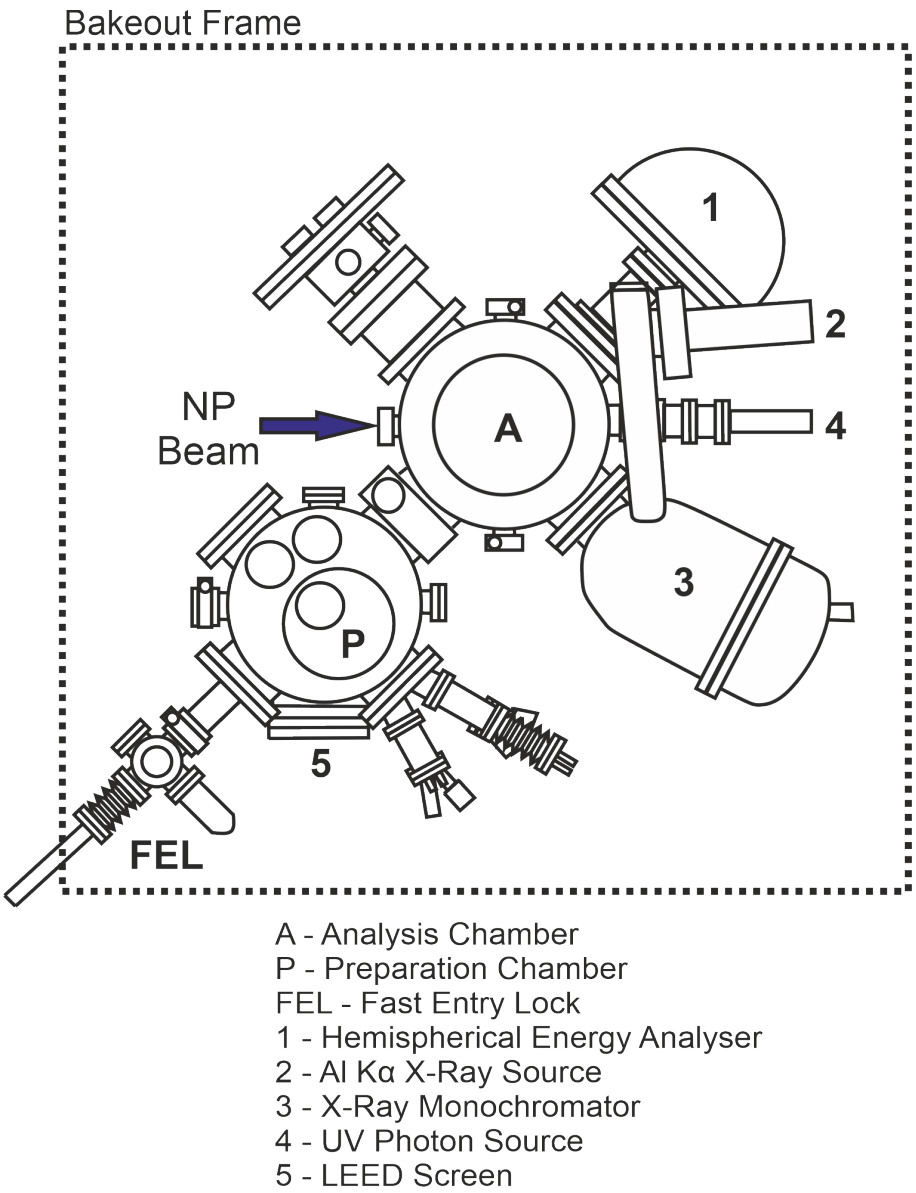

Figure 3.1: Plan view schematic figure showing the electron spectroscopy system used throughout this project. See text for details.

the hemispherical energy analyser for collecting the electrons emitted from a sample due to the interaction of various different excitation sources. The ultraviolet photoemission spectroscopy (UPS) source, an Omicron VUV HIS 13, is situated at a 45° angle to the analyser and monochromator. He I α photons ($hf = 21.22$ eV) are produced when helium is introduced through a needle valve which is connected to a 99.999 % purity He cylinder. He is let into the chamber through a thin glass capillary which requires additional pumping to control the increase in pressure during operation. The source is also cooled when the discharge is struck by flowing cold water through a shroud that surrounds the source.

The monochromated X-ray source (Oxford Instruments XM1000 MKII Mono X-ray) is connected to a bespoke flange adaptor with a 5° offset to ensure correct alignment to the sample, and mounted at 90° to the electron analyser. X-ray Al Kα photons (1486.7±0.1 eV) are produced from one of two filaments, which enables control of the emission current and therefore the intensity of the X-rays being generated. The power used in the standard operating conditions ranges from 300-450 W depending on the filament. A constant temperature is maintained by an ATC KT1 chiller pump that flows deionised water around a closed loop at 18 °C. The emitted X-rays are aligned via a port aligner to the quartz crystal in the monochromator which focuses and monochromates the X-rays onto the sample stage. The analyser that collects the electrons produced by the various spectroscopy techniques is an Omicron EA 125 hemispherical energy analyser. The analyser consists of seven channel electron multipliers that have a reported energy resolution of 10 meV up to 2000 eV and maximum counts of 10^7 s^{-1}. A more detailed explanation on how this works will be given in the following section.

The analysis chamber also has the potential to clean and prepare samples through a pyrolytic boron nitride (PBN) radiative heater that heats samples by passing a current through a wire surrounded by the boron nitride elements. The samples can also be cooled through liquid nitrogen cooling via a heat exchanger submerged in liquid nitrogen that cools the nitrogen gas flowing through it. The cooled gas is then passed through a copper labyrinth that is situated behind the sample allowing sample temperatures $\leq$120 K to be reached.

All three sections of the system, the FEL, preparation chamber, and analysis chamber, are pumped by a separate turbo molecular pump (TMP) backed by a rotary vane pump. The preparation and analysis chambers also contain a titanium sublimation pump (TSP) which helps maintain UHV conditions.

To achieve ultra-high vacuum conditions, it is standard practice to perform what is known as a 'bake'. This is a process where the system is heated to above 100 °C such that any water vapour that has absorbed on the chamber walls while the system was at atmosphere is removed. UHV conditions could be reached without a bake but it would take a considerably longer time due to the slow desorption of

gases such as water vapour under vacuum. The bake means UHV conditions can be achieved in a few days [63].

First, the system is pumped down until a pressure in the 10^{-7} mbar range is reached. This allows time for leaks to be detected and any problems to be resolved before baking. All non-essential wires and connectors are removed from the system and sensitive areas (such as windows and electronic feed-throughs) are insulated with foil to protect them from thermal shock. The system is then boxed up using large insulated panels that sit on the frame labelled in Figure 3.1. Radiators are placed inside the system and turned on as well as two fan heaters located in the bakeout panels. The system temperature is then slowly raised to around 120 ^{o}C and left for approximately two days or until the pressure is stable in the low 10^{-7} mbar range. After this period the heaters are switched off and the system allowed to slowly cool. Once the cooling has started, the TSPs are fired regularly (every 5-10 minutes for $\approx$ 1 hour) to help pump away any excess material and lower the ultimate pressure. The system takes around a day to cool, after which the equipment can be wired up and various components out-gassed (slowly turned on to remove contamination from filaments). With this all finished, the system should have achieved UHV conditions and be ready to use. Typical base pressures for the experiments reported in this thesis that use this system are $\leq 1 \times 10^{-9}$ mbar for both the preparation and analysis chambers.

3.2 Photoemission Spectroscopy

Photoemission spectroscopy utilises the photoelectric effect which was described by Einstein in 1905 [64]. This explains how an electron (or photoelectron) is emitted from an illuminated surface if the photon energy of the incident light is greater than or equal to the work function of the surface. The kinetic energy of the emitted photoelectron is given by:

$$E_k = hf - \phi_s - E_B \tag{3.1}$$

where E_k is the kinetic energy, hf is the energy of the incident photon, ϕ_s is the

work function of the surface, and E_B is the binding energy of the emitted electron. By measuring the intensity of the emitted electrons as a function of their kinetic energy, a spectrum can be produced.

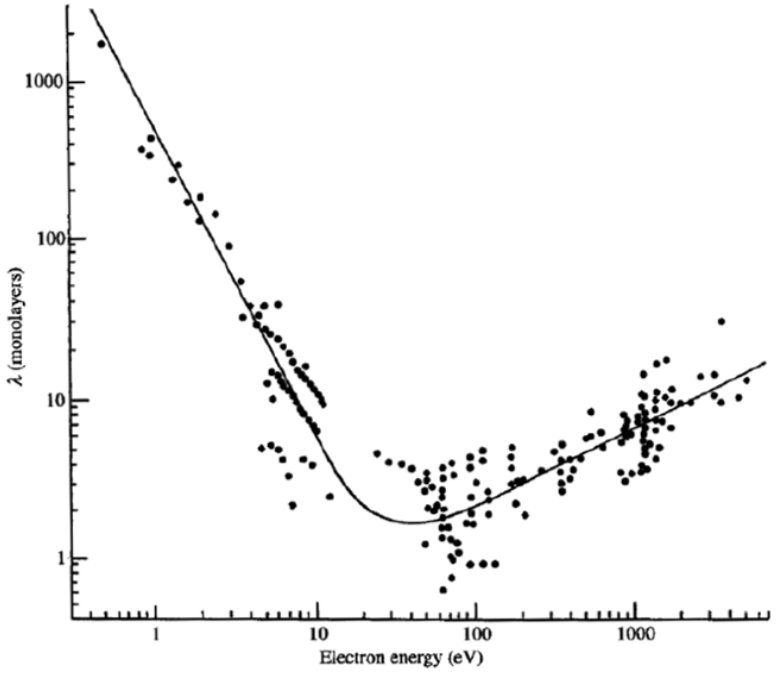

Figure 3.2: Plot known as the universal curve which shows the relationship between attenuation length (λ in atomic monolayers) and kinetic energy of the emerging electron for a wide range of materials. The minimum in information depth, i.e. the shortest attenuation length, corresponds to an energy of ≈40 eV. Graph taken from Briggs et al. [65].

The surface sensitivity of the photoemission technique does not depend on the penetration depth but in fact on the attenuation length of the photoelectron. Inelastic collisions and processes may occur which cause the escaping electron to lose energy and therefore information regarding its origin, e.g electronic structure. This means the true surface sensitivity is measured in the depth of electron emission without energy loss as shown in the well known universal curve of Figure 3.2. In principle, the most surface sensitive emitted electron is around 40 eV as the emerging electrons at this energy have the smallest attenuation length, i.e. information depth, meaning that the electrons do not travel far through the solid before inelastic processes take place.

3.2.1 X-ray Photoemission Spectroscopy

X-ray photoemission spectroscopy (XPS) is a standard laboratory technique that allows for chemical analysis of samples. Soft X-rays with an energy of around 1500 eV are utilised such that the photoelectrons originate from more strongly bound core states as compared to UV photons which probe the valence band electronic structure. Compared to other photoelectron spectroscopy techniques, XPS is not particularly surface sensitive due to the relatively high energy of the X-ray radiation. The production of photoelectrons from a surface when exposed to the X-ray radiation is shown in Figure 3.3. These core states have unique energies which correspond to a particular element meaning that the spectra produced can be used to chemically fingerprint the sample. For oxide samples, the different chemical environments present can also be evaluated through XPS. The bonding environments shift to higher or lower energies depending on their oxidation state such that the peaks seen in the spectra are convoluted and shifted. These can then be deconvoluted into a series of Lorentzian/Gaussian peaks with each representing a unique binding environment of the element. This is shown later in the results sections with data obtained using XPS.

To perform this deconvolution accurately, a monochromated source of X-rays should be used. For example, Al contains both the $K\alpha$ and $K\beta$ spectral lines so photoemission will occur from both which will broaden the obtained spectra. A monochromated source will only produce photoelectrons from the selected spectral line allowing a more accurate assignment of Lorentzian/Gaussian peaks to the observed spectra. To produce monochromated X-rays, an aluminium anode is used to first generate a beam of X-ray radiation which is directed towards a quartz crystal. The X-rays are then diffracted through the crystal back-plane if their wavelength constructively interferes according to Bragg's law:

$$n\lambda = 2d\sin(\theta) \tag{3.2}$$

where λ is the wavelength of the X-ray, d is the lattice spacing, and θ is the Bragg angle. The lattice spacing of the quartz crystal planes matches the wavelength of the Al $K\alpha_1$ spectral line such that it constructively interferes through the quartz crystal.

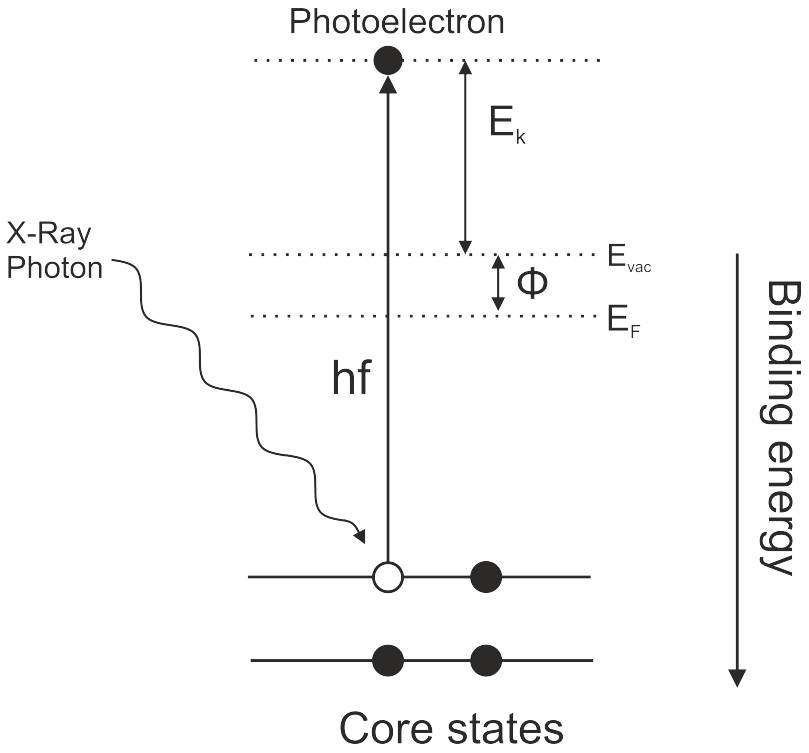

Figure 3.3: Diagram of the electron emission process in XPS process showing the different energy levels and their relationship to Einstein's photoelectric equation (Equation 3.1). The high energy X-ray photon can cause emission from more tightly bound core states which have unique energy levels allowing for chemical analysis of the sample.

Radiation from the other spectral lines present in Al is blocked from diffracting through the crystal due to destructive interference. The quartz crystal is curved so that the monochromated X-rays are focused to a $\approx 2{\times}5$ mm^2 spot.

The Oxford Instruments XM1000 MKII Mono X-ray source used during this project consists of two different filaments (long and short) which are controlled via software on a PC. The typical operating conditions are an emission current of 18 mA and an anode voltage of 12 kV to give a power of 216 W.

The relative amounts of each element can also be determined using quantitative XPS. Wagner showed an empirical method that has become the accepted standard for determining atomic concentrations [66]. The relative concentration of each element can be calculated from the peak area divided by the sensitivity factor of the element, given by:

$$n_i = \frac{I_i}{S_i} \tag{3.3}$$

where n_i is the relative atomic concentration of element i, I_i the area or intensity of the peak in the relevant spectrum, and S_i the sensitivity factor. The sensitivity factor is a scaling factor which allows for a more meaningful understanding of relative concentrations such that each elemental transition can be scaled to the same degree and compared.

3.2.2 Ultraviolet Photoemission Spectroscopy

In ultraviolet photoemission spectroscopy (UPS), lower energy UV photons are used meaning that photoelectrons produced from a surface originate from the valence band. In this project, He I α photons with an energy of 21.22 eV were used allowing an electron emission spectrum to be collected that relates to the density of states of the valence band of the surface and the first few sublayers. The relevant photoemission process is shown in Figure 3.4.

While the penetration depth into the sample of the UV photons used in UPS is less than the X-rays used in XPS, and so UPS is considered more surface sensitive, the information depth is still described by the universal curve shown in Figure 3.2. This shows that photoelectrons that escape the surface will have originated from around one to three atomic monolayers of the material meaning that UPS using He I α photons is considered to be surface sensitive. The generated photoelectron emission spectrum will contain a mixture of subsurface and surface states due to this information depth.

To generate He I α photons, a cold cathode discharge source is used. Helium gas of 99.999 % purity is passed through a glass capillary which is surrounded by a water cooled shroud. A positive 1 kV bias is applied to the anode at the end of the capillary which results in a breakdown of the gas and the creation of a helium discharge. The typical operating conditions of the source are a 100 mA emission current, a sustaining discharge voltage of 480 V, and a He inlet pressure of approximately 1×10^{-8} mbar. The sample normal is oriented at 45° to both the source and the analyser.

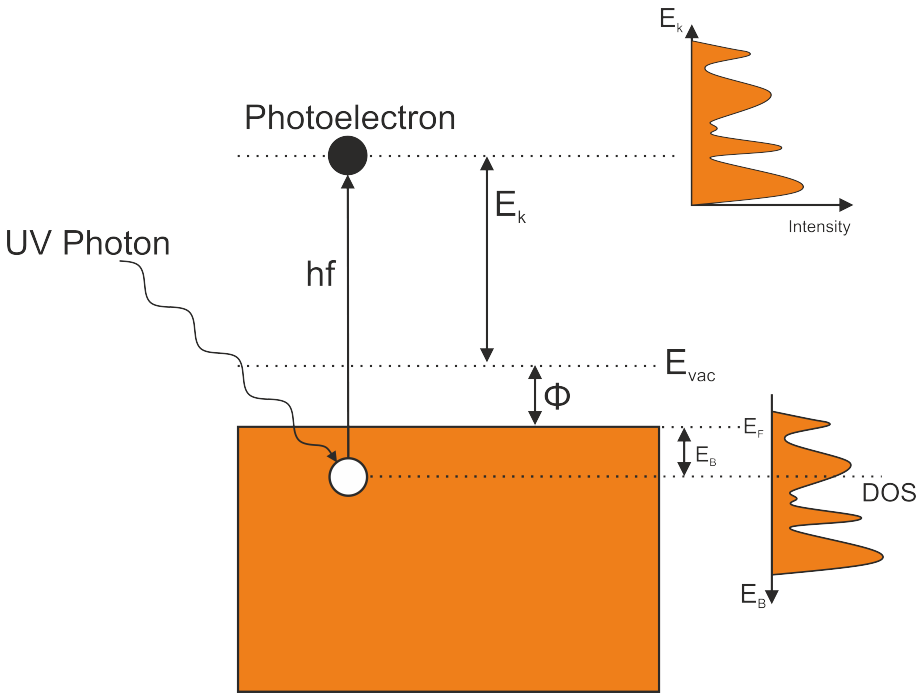

Figure 3.4: Diagram of the electron emission process in UPS showing the different energy levels and their relationship to Einstein's photoelectric equation (Equation 3.1). The measured electron emission spectrum reflects the surface density of states (DOS) of the sample.

3.2.3 Hemispherical Energy Analyser

All the emitted electrons generated from the techniques described above are collected by a hemispherical energy analyser (Omicron EA125), schematically shown in Figure 3.5.

Electrostatic lenses are used at the entrance to focus electrons emitted from a sample into the analyser where they are deflected by the two concentric hemispherical shells. The shells have a potential applied between them which causes only electrons of a particular pass energy to be deflected between the hemispheres along a semi-circular path with a radius R_0. Electrons with a kinetic energy less than the pass energy are attracted to the inner hemisphere and neutralised. While electrons with a higher kinetic energy than the pass energy impinge on the outer hemisphere and are also lost. The electrons that match the pass energy then impinge on a detector mounted after the exit aperture. A retarding potential, not shown in Figure 3.5, is applied before the entrance aperture which slows the electrons down to then match the

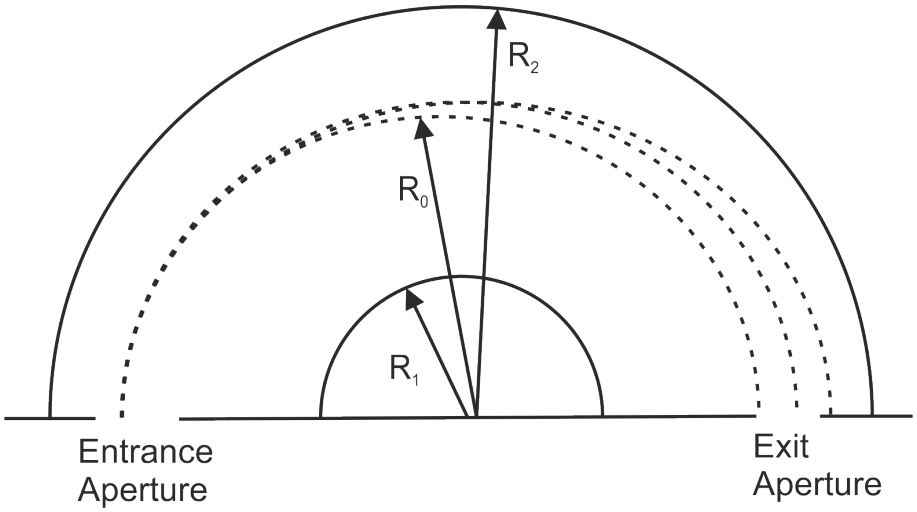

Figure 3.5: Schematic of the hemispherical energy analyser with the inner, outer, and mean radii shown. Incoming electrons are deflected and focused by electrostatic lenses before entering the analyser through the entrance aperture. They are then deflected by two concentric hemispherical shells and only a certain pass energy of electrons is allowed to pass through the exit aperture. Here they impinge on an array of seven channel electron multipliers which produces a signal.

pass energy of the analyser. By varying this potential, the kinetic energies of the incoming electrons can be scanned [67].

The error in the pass energy of the electrons is proportional to the ratio between the detector size and the radius of the path of the passing electrons. Therefore, the energy resolution of the instrument is improved with a larger radius which can be described as follows:

$$\Delta E = E_p \frac{d}{2R_0} \tag{3.4}$$

where E_p is the pass energy, d is the diameter of the exit aperture, and R_0 is the mean radius of the two hemispherical shells. The analyser used here has an R_0 value of 125 mm, and a value of d equal to 2 mm. For UPS the pass energy is set to 10 eV which yields a resolution of 0.08 eV. XPS has a pass energy of 50 eV which yields a resolution of 0.4 eV. The spectra are taken in constant analyser energy (CAE) mode which varies the electrostatic lenses to scan through different electron kinetic energies keeping the pass energy constant. This means the energy resolution of the

analyser is constant as ΔE has no dependence on the electrostatic lenses and E_p is constant. The analyser can also operate in constant retard ratio (CRR) where the electrons entering the analyser from the sample are retarded by the electrostatic lenses by a constant proportion of their kinetic energy. The pass energy of the analyser is then varied to maintain the constant retard ratio and so produce the spectra. This mode was not used because ΔE increases with kinetic energy of the incoming electrons meaning that at high kinetic energies the resolution is poor.

The detector at the exit aperture is fitted with seven channel electron multipliers (channeltrons) which are used to collect electrons and are placed in different positions in the exit plane to increase the detected count rate. When an electron is incident on the channeltron, secondary electrons are produced and are accelerated through the detector due to a high voltage bias (> 2 kV). These secondary electrons produce more secondary electrons in a cascade effect until they reach the collector where they have generated a high enough signal to be measured.

The entrance aperture to the analyser can be controlled and is varied between a slit, a 1 mm circle, a 2 mm circle, a 6 mm circle, and a 13 mm^2 rectangle. These are chosen depending on the technique being used - XPS uses the 6 mm circle aperture whereas UPS uses the 1 mm circle aperture. UPS uses a smaller aperture due to a much higher count rate. The counts are lower with the XPS so a 6 mm aperture is used in order to increase the signal entering the hemispherical energy analyser. The apertures can also mask the analyser from photoelectrons that have not been produced by the sample.

3.3 LEED

Low energy electron diffraction (LEED) is a surface sensitive technique that uses low-enery electrons (typically in the range of 50-200 eV) to produce a diffraction pattern of the crystal surface. The electron's wavelength, as explained later in section 3.4, is comparable to that of the atomic spacing of the crystal surface. This means that the electrons can diffract like light through a grating. The diffraction pattern observed will show the reciprocal lattice of the sample surface which can

then be related to the 2D crystal structure through Wood's notation. The way the reciprocal lattice is formed is through the incoming electron wave satisfying the Laue equations.

$$a \bullet \Delta k = 2\pi h \tag{3.5}$$

$$b \bullet \Delta k = 2\pi k \tag{3.6}$$

where Δk is the scattering vector, *(a,b)* are the atomic coordinates, and *(h,k)* are the Miller indices. These equations must be integer numbers with each choice of Miller index determining a scattering vector. This results in many solutions which can then be formed into the reciprocal lattice from a single incident beam [68].

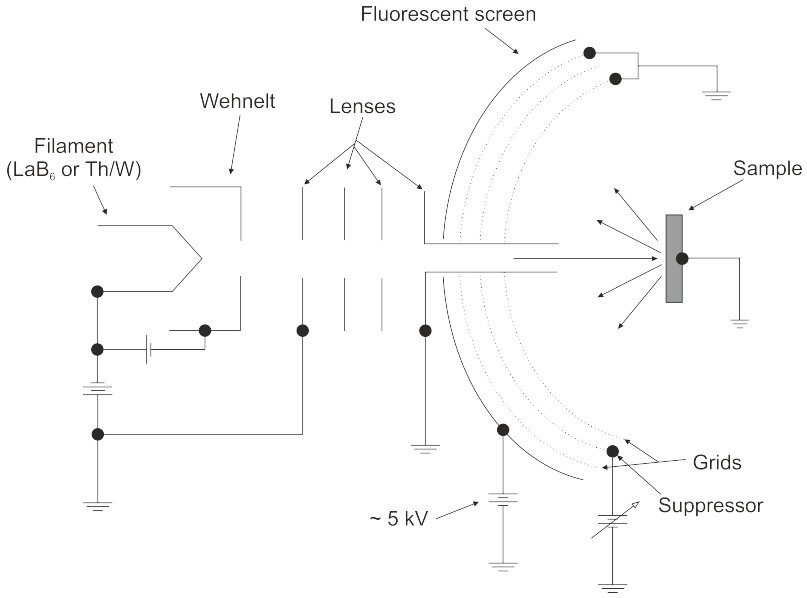

Figure 3.6: Diagram showing the LEED screen with the various components outlined. The electron gun emits electrons thermionically which then impinge on the sample after being accelerated by the electrostatic grids. These also act to screen out the inelastically scattered electrons from the surface as these diminish the resolution of the final diffraction pattern. A phosphor screen or microchannel plate is used to visualise the diffraction pattern. Reproduced with permission from Ref. [69].

Figure 3.6 shows a schematic diagram of the LEED system. The electron gun emits electrons through thermionic emission and electrostatic lenses are used to focus and accelerate the beam of electrons onto the sample. Grids are placed between the sample and the screen to zone out the inelastically produced electrons from the

sample as they reduce the resolution of the image. The first screen is used to block the retarding field from the sample which is supplied by the second grid. This is at a potential to block low energy electrons and is called the suppressor or the gate. To make the retarding field homogeneous and mechanically more stable this grid often consists of two grids [69]. The elastically backscattered electrons produced then impede on the phosphor screen causing it to fluoresce. A LEED pattern is observed if the surface has a periodic reconstruction across the surface, if the surface is rough or disordered then the LEED pattern will be diffuse.

3.4 Transmission Electron Microscopy

Transmission electron microscopy (TEM) allows for the structural properties of NPs to be investigated at the atomic level. Compared to spectroscopic techniques that give information on the oxidation state and electronic properties, electron microscopy allows for quantification of such things as shape, size, and grain boundary formation. This is achieved due to the small wavelength of the electron, which can scatter through crystal lattices and be collected on a screen or CCD camera to form an image. The wavelength of the electrons is given by the de Broglie equation:

$$\lambda = \frac{h}{p} \tag{3.7}$$

with λ the wavelength, h Plank's constant, and p momentum. In a typical TEM, electrons are accelerated towards the sample by a 200 kV potential (it can range between 100-300 kV). The electrons are accelerated to $\approx$ 0.6c (c being the speed of light) so that relativistic effects have to be considered to obtain a more accurate wavelength. This modifies Equation 3.8 to:

$$\lambda = \frac{h}{(2m_0E(1+\frac{E}{2E_0}))^{\frac{1}{2}}} \tag{3.8}$$

where m_0 is the rest mass of the electron, E is the kinetic energy of the electron, and E_0 is the rest energy of the electron which is equal to m_0c^2. This gives the wavelength of the electron to be $\approx$ 2.5 pm for 200 kV acceleration. Electrons are

generated either through thermionic emission or field emission. Thermionic emission involves heating a filament to generate electrons so that they have enough energy to overcome the work function of the material. Field emission was developed to improve the brightness and reduce the energy distribution of the emitted electrons. Schottky field emission involves heating the filament as well as applying an electric field to the tip. Generally W is used for this source where the electric potential, heating, and fine tip shape of the filament allow the electrons to overcome the work function sufficiently. Cold field emission guns were developed to generate a more monochromatic electron beam such that chromatic aberrations are limited with a similar brightness. W filaments can be replaced with a single crystal of LaB_6 as the filament as this can achieve a higher brightness at a lower temperature. A Wehnelt cylinder is also placed after the electron source to provide energy filtering and lensing of the emitted electrons. The electrons are then further lensed by electromagnetic lenses as required. The paths of the electrons through a conventional TEM column are shown Figure 3.7.

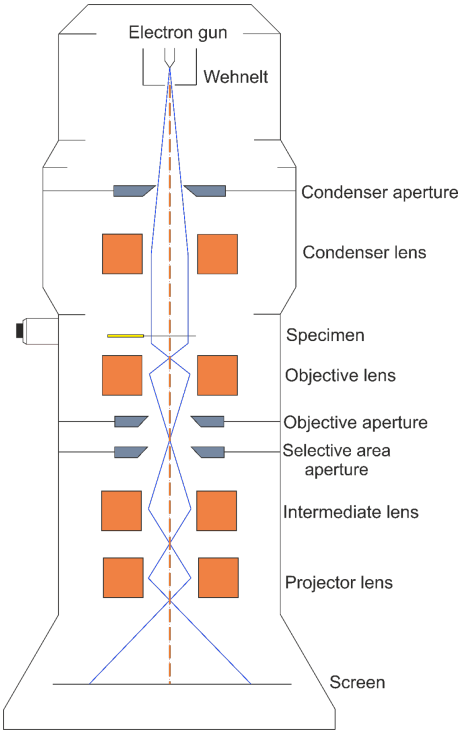

Figure 3.7: TEM column in a typical arrangement showing the various apertures and lenses that form the image. The blue line shows the electron's path through the column with the orange dotted line showing the optical axis.

The lenses are not perfect and aberrations can occur such as chromatic and spherical aberrations, which are schematically shown in Figure 3.8(a) and (b). Chromatic aberration occurs due to the energy spread in the electron beam meaning the electrons are brought to a different focus depending on their energy.

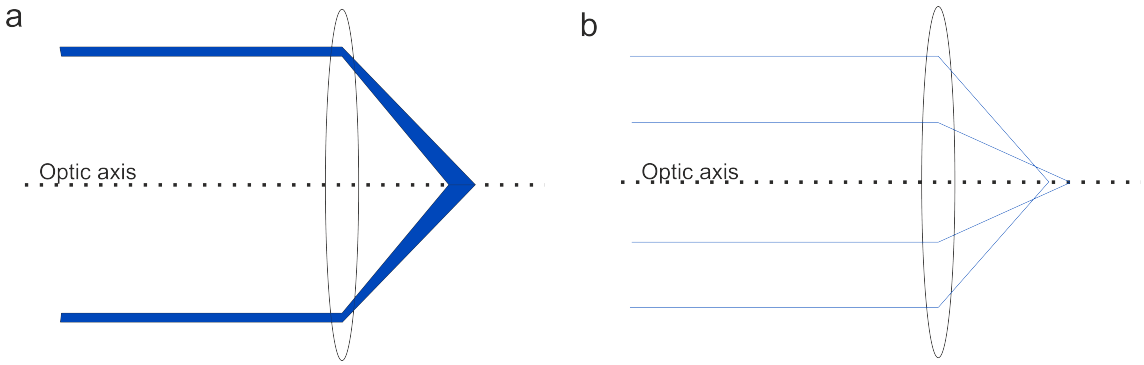

Figure 3.8: Diagram showing the different aberrations present in a lens. (a) shows chromatic aberration where, due to the variance in energy of a beam, the incoming electrons are focused by different amounts. Spherical aberration is shown in (b) where the degree that the beam is focused depends on distance from the optical axis.

Spherical aberrations occur when electrons that are farther from the optic axis are focused more than electrons that were closer to the optic axis before passing through the lens. Astigmatisms can also arise due to the shape of the lens. The field inside the lenses should be spherical such that all the electrons are focused equally but this can be altered as the lens strength is increased to amplify the magnification due to hysteresis. Corrections to the astigmatism can be achieved through stigmators which are weak electromagnetic quadrupole fields. Overall, These aberrations and astigmatisms then cause limitations on the true resolution of the microscope as they cause smearing in the images. So while the theoretical wavelength of the electrons is in the pm range, the resolution of the microscope is sub-nm.

Apertures are used throughout the column to reduce the beam spot size as well as changing the imaging mode and thus the information attainable from the microscope. This is shown in Figure 3.9 where the objective aperture is placed in various points in a diffraction image. Placing the objective aperture over the direct beam and blocking the scattered electrons produces what is known as a bright field (BF)

image. This helps reduce the background as the aperture stops electrons that have been scattered by high angles, i.e from the sample itself. This also means that, in general, high-resolution transmission electron microscopy (HR-TEM) can also not be performed as electrons that have been elastically scattered by the sample are blocked. These electrons carry the information which allows for imaging of lattice planes and atomic columns. In this mode the background appears bright and the specimen dark as electrons impacting these regions have been blocked from forming the image. Regions that have scattered electrons the most then appear the darkest in these images.

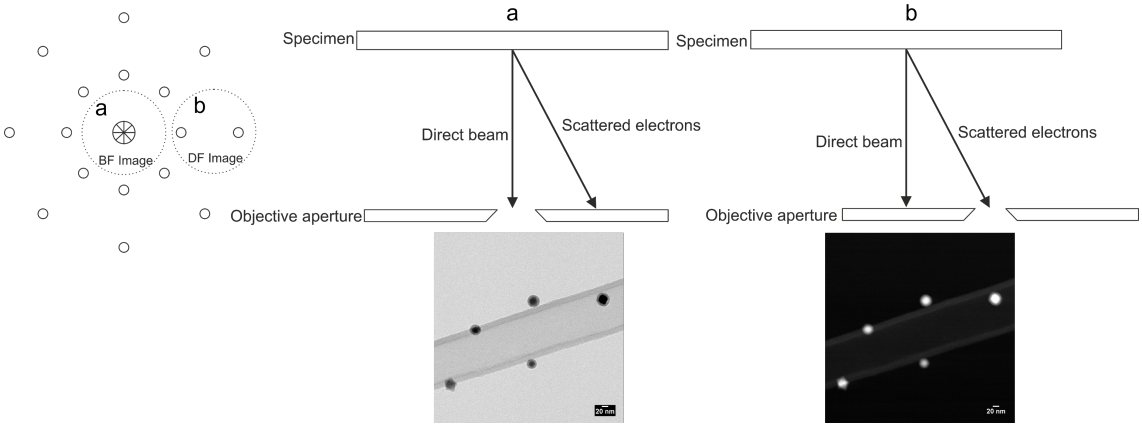

Figure 3.9: By careful placement of the objective aperture, two different images can be obtained. Aligning it to different places in the diffraction image (represented on the left) produces (a) a bright field (BF) image by only transmitting the direct beam (shown by the circle with a star) of electrons which have not elastically scattered through the specimen, or (b) a dark field (DF) image by placing it over certain diffraction spots which have arisen due to elastic interference from the specimen. This then changes the image formation with details given in the text.

The objective aperture can be placed in the beam over a chosen diffraction spot which yields an image of the specimen containing only the information that generates that spot. This imaging mode is known as dark field (DF) imaging. The background is now dark and the structure seen in the specimen is bright with the highest scattering components being the brightest. This allows for improved contrast to the background.

The TEM can be modified to operate in scanning mode to work as a scanning

transmission electron microscopy (STEM). Here, the electrons form a very small probe on the specimen which is scanned across the surface with an image formed by collecting the information at each scanned point. In STEM, an annular detector is used instead of a CCD camera meaning that the central beam is completely blocked and only electrons that have been elastically scattered by the specimen are detected. This is similar to dark field imaging in the TEM except that all of the scattered electrons are detected compared to a select few. This method can be expanded to a high-angle annular dark field (HAADF) detector which only detects electrons that have been scattered to a high degree from changes in the atomic composition of the sample. The scattering of the electrons is highly dependent on the atomic number, Z, of the sample (i.e. elemental composition) and HAADF-STEM is also called Z-contrast imaging. The information contained above is a brief summary of TEM operation and theory and the reader is encouraged to seek out more formative texts such as Reimer and Kohl [70] and the series by Williams and Carter [71].

During the research presented in this thesis, several electron microscopes were utilised, a JEOL 2100+ and the aberration corrected JEOL 2200. The 2100+ allows for easy characterisation of NPs through HR-TEM and STEM imaging. Due to the use of a thermal emission source the STEM imaging mode does not have atomic resolution and HAADF imaging is not available. The 2200 has these capabilities due to having a field emission electron source as well as the HAADF detector. The 2200 is aberration corrected meaning that the resolution is sub angstrom allowing for accurate imaging of the atomic columns in the samples. This is achieved by the use of two pole pieces which have a negative value for spherical aberration. During microscope alignment, this value is set to counteract the inherent aberration in the microscope, allowing sub-angstrom resolution to be achieved. It can also be operated under "environmental" conditions such as heating the samples and exposing them to gasses at high pressures, known as environmental transmission electron microscopy e-TEM.

Gasses can be let into the microscope through the use of an innovative radial objective pole piece developed by P. L. Gai and E. D. Boyes [72]. Shown in Figure 3.10, the placement of apertures between the column and the sample cell chamber allows for the sample to be exposed to high gas pressures. Differential pumping then

maintains the necessary high vacuum in the rest of the column. This method was first designed by Gai and Boyes before they modified it further on the JEOL 2200 in York to demonstrate for the first time the use of environmental imaging during STEM mode with angstrom resolution [73].

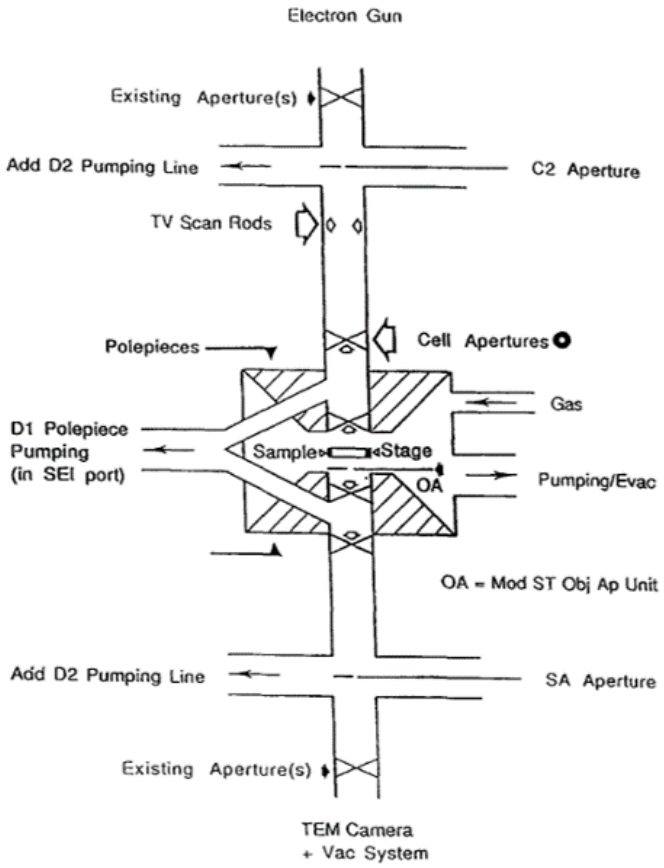

Figure 3.10: Schematic of the gas cell design used in e-TEM where the objective lens becomes part of the gas cell arrangement with bore holes for differential pumping. Pairs of apertures are placed between the sample chamber and the rest of the TEM column to allow for high vacuum conditions to be maintained outside of the gas cell. Reproduced with permission from Ref. [72].

The sample stage can also be heated through a furnace arrangement where a small furnace is in direct contact with the specimen. The sample holder also contains a water cooling line which leads from the specimen to the base of the sample holder to help maintain the temperature. The maximum temperature these can achieve is 1000 °C but Boyes and Gai have developed a sample holder that can go much hotter [74]. The ability to image and characterise in-situ reactions and solid state interactions at elevated temperatures has applications in many fields and as such

the design and implementation of these environmental capabilities has now become an industry standard.

3.5 Scanning Electron Microscopy

Another type of electron microscope that is useful in the characterisation of grown samples is a scanning electron microscope (SEM). In this project, an SEM was used to quantify deposition rates as well as to obtain deposited size distributions of samples that would allow for comparison to the mass spectra produced from the source, described in Section 4.1.4. The SEM utilises a focussed electron beam which is then scanned across the surface with the secondary electrons that are given off detected to produce an image. The contrast in the image is provided by the variances in secondary electron yield of different elements and topography. This is different to the TEM as the samples used in this technique do not have to be electronically transparent and rarely need special preparation apart from possibly coating with Ag DAG to help with charging effects.

The electron beam is typically operated between 1 - 5 keV with a probe diameter in the range of 2 - 10 nm. This means that crystallographic features like lattice planes noticeable in the TEM are not imaged in the SEM. Though due to the limited sample preparation needed as well as the fast imaging times, the SEM is still a useful technique. During the research presented in this thesis, the SEM data was collected for the author at the JEOL York Nanocentre on the JEOL 7800 SEM by Dr Ben Coulson and Ms Maha Alotaibi. The author would like to extend his gratitude to these colleagues.

Chapter 4

The Gas Aggregation Cluster Source and Nanoparticle Growth

A gas aggregation cluster source (GACS) is a high vacuum instrument used to produce nanoparticles (NPs) that allows for high level of control of particle size and shape [75, 76]. Due to the high vacuum conditions, the source can quickly and easily produce clean particles when compared to other popular methods, such as chemical synthesis, that require a more involved process [9]. By sputtering a solid target with an inert gas inside an aggregation chamber, a NP beam can be produced. The particles can be manipulated in flight to produce more complex structures (for example core-shell structures) whilst real time feedback on the properties of the particles can be obtained using time-of-flight measurements or a quadrupole mass filter (QMF). This high degree of control allows the study of the native properties of the particles as well as providing the possibility to tailor them to fulfil specific needs. This chapter will explain the technique and how a recently acquired cluster source at the University of York (known as Merlin) has been developed and characterised. This source is then also compared to other NP production techniques.

4.1 The Gas Aggregation Cluster Source

The design of a GACS with a magnetron sputter head to produce NPs was first described in 1991 by Haberland and co-workers [77] and was further developed by

Hihara et al. [78] who improved the technique to the point at which it is recognisable today where gas condensation meets plasma sputtering with narrow NP size width control. The basic principle of the source is that a solid target is sputtered to produce a cloud of atoms which condense to form particles. These particles are then carried on gas streams through the system as they move down a pressure gradient established by differential pumping.

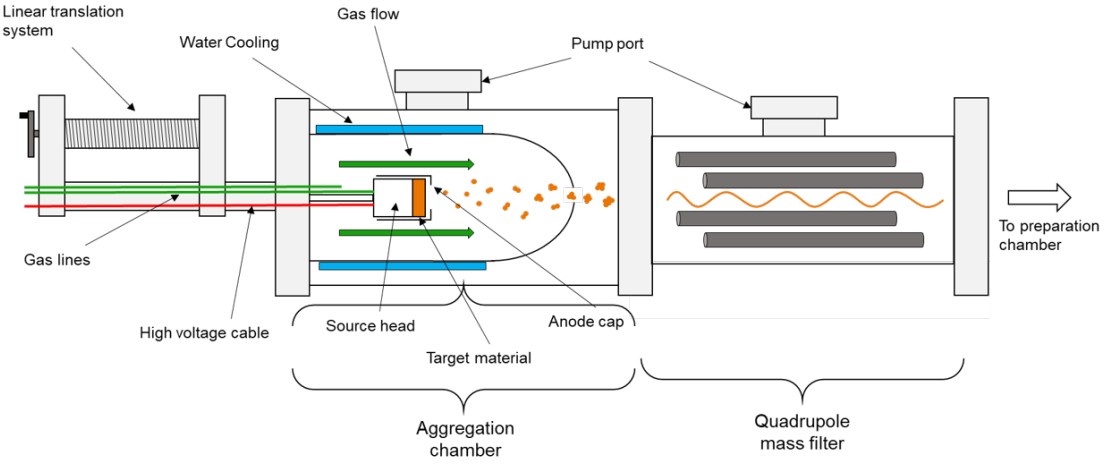

Figure 4.1: A schematic view of the gas aggregation cluster source showing the magnetron head, aggregation chamber, and quadrupole mass filter. Particles are formed from sputtering the target material in the aggregation chamber where the sputtered vapour aggregates into particles. The particle beam then passes through the mass filter which produces mass spectra in real time. The particles can then be deposited onto the desired sample held in the preparation chamber.

The aggregation chamber is where the particles are produced from the sputtering of a solid target. This chamber is usually bullet shaped with a small aperture at the curved end as can be seen in Figure 4.1. Inside the aggregation chamber sits the magnetron head, shown schematically in Figure 4.2

Inert gas, usually argon, flows into the aggregation chamber through mass flow controllers (MFCs) which allows the gas flow rate, measured in standard cubic centimeter per minute (sccm), to be directly controlled. The Ar gas flows directly between the anode cap and the target as shown in Figure 4.2. A large potential, typically between 600 V and 1 kV, is held between the anode cap and the target (the cathode) which causes latent Ar ions to accelerate into the target. This ejects target

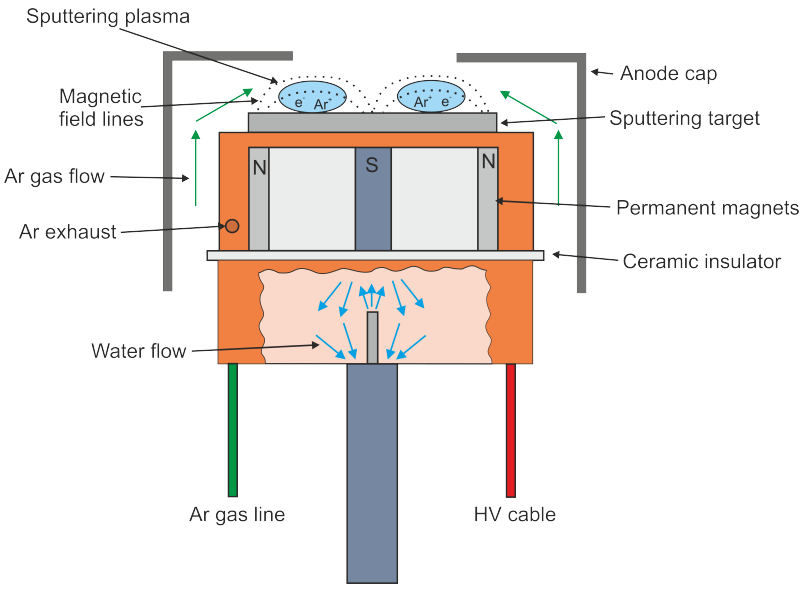

Figure 4.2: A cross section of the magnetron head with the plasma sputtering the target material. The Ar gas exhausts out through the hole underneath the anode cap which completely surrounds the magnetron head and fills it with Ar. The ceramic insulator isolates the top half of the head from the anode cap which is screwed to the bottom half. The water cooling fills the bottom copper block which cools the target by conduction through the ceramic and top copper block. The HV line passes through the bottom block (which it is insulated from) and connects with the top block through a grub screw. This ensures that the target is established as the cathode and the cap is the anode such that a plasma is formed allowing current to flow. A permanent magnet in the top half of the head constrains the plasma to impinge on the target.

atoms as well as electrons with the electrons going on to ionise more Ar atoms which replenishes the process. The plasma is sustained by this continuous recycling and is contained by the magnets in the magnetron head [79] which are placed directly behind the target. The magnetic field forces the plasma onto the target and etches out what is called the “racetrack”, an example of which is shown in Figure 4.3. This confinement does mean there is a lot of wastage from the target as only a small percentage is actually sputtered from the “racetrack”.

Figure 4.3: A used iron target with the racetrack labelled. The racetrack is formed from the sputtering of the material during NP production. A large amount of the target is not sputtered, i.e. wasted, during this process.

4.1.1 Aggregation Kinetics Of Particle Formation

The particles form from the material being sputtered from the target which creates a supersaturated vapour in the aggregation chamber. Supersaturation is the process where the solute exceeds the concentration of the solubility of the solution [80], typically applying to solids in liquids. The sputtered atoms are cooled by collisions and interactions with the surrounding gas to such a point that nucleation can occur. The high plasma temperature means that nucleation near the head is not possible [81]. Interactions in the gas that can lead to particle formation happen through a three-body collision of sputtered atoms and the gas [82]. This is where a gas molecule collides with a newly formed pair of atoms (known as "embryos") taking energy and momentum away from the pair inducing a bond to form as they are cooled due to the collision. The embryos can assemble through homogeneous or heterogeneous nucleation. Homogeneous nucleation is the process described above where embryos are created through spontaneous collisions in the vapour phase such that the embryos form at the size dictated by the Kelvin limit. This is the critical size that the embryos must reach to then remain stable as below this they will

evaporate back into the vapour phase. Above this limit the particles can continue to grow.

Heterogeneous nucleation is the formation of embryos and clusters from sites known as seeds [81]. These are sites which the atoms in the vapour phase can collide with and condense on such that the particle then grows. This is different to homogeneous nucleation where all of the atoms condense together to form a single particle whereas heterogeneous nucleation can involve many collisions and grow slowly. In the case of magnetron sputtering, these seeds can be dimers or trimers of atoms which are produced during the sputtering process. Hihara et al. [78] also seem to suggest that the seeds could be metal atoms ionized through the Penning process, where electrically excited gas molecules can ionize other molecules through a collision [83]. The electrons in the glow discharge have enough energy to excite the Ar atoms into a metastable state of 11.6 eV which can then interact with the metal atoms [84]. This means the fraction of ionized metal atoms increases which Hihara suggested may promote embryo formation [78].

The work of Winkler et al. [85] showed that the assumption that the particles must reach the Kelvin limit might not be the case. They show that particles can exist stably far below the Kelvin limit and that a large pitfall of studies on nanomaterials is that the studies assume growth starts at the Kelvin limit. They reported that if heterogeneous nucleation is taken into account then the critical size for stable particles is actually smaller; stating that the work of formation of an embryo on a seed particle is always less than the work of formation of a Kelvin size embryo in homogeneous nucleation. Essentially, the metal vapour will preferentially condense on the smallest pre-exisiting seed particles than form new particles due to having a smaller energy barrier [85].

Particles can then grow through further embryo-embryo collisions or through condensation of metal atoms on the surface of the forming particle. Knauer et al. [86] showed that collisions alone, assuming this to be the main growth method [87], does not produce large enough particles when compared to the experimental data. This confirmed that condensation of atoms also needs to be considered which Knauer et al. states happens through a three step process of individual atoms condensing,

moving across the surface, and finally forming bonds when in the lowest energy state [86].

4.1.2 Dynamic Control Of Particle Size

The GACS has great control over the size and morphology of the particles it is producing by varying several source parameters. The magnetron head in most source designs sits on a linear drive, allowing the distance between the target and the exit aperture of the aggregation chamber to be varied. This distance is known as the insertion length and changing it affects the particle size. Gas flow and plasma power can also play a role in altering the particle size as discussed below.

Merlin has two input gas lines, one discussed already above that feeds directly into the magnetron head between the anode cap and the target. The gas produced by this line will be known as the plasma gas from now on. The other gas line exhausts into the aggregation chamber behind the magnetron head producing what is known as the carrier gas. The carrier gas influences particle size because it more effectively traps the particles [88] in its flow resulting in quicker passage through the aggregation chamber. Less time in the aggregation chamber results in smaller particles. This can also be affected by varying the insertion length of the head. A larger insertion length means the head is closer to the exit aperture of the chamber so the aggregation time is diminished again resulting in smaller particles. The same is true for the reverse where a shorter insertion length leads to a longer aggregation time and so larger particles.

Khojasteh et al. [88] investigated the effect on the size distribution of the particles when they varied the parameters outlined above. The authors found that the best way to make significant changes to the mean diameter was through the introduction of the carrier gas and by changing the insertion length. They found that changing the plasma power did not influence the mean size nor did increasing the plasma gas flow rate. Gracia-Pinilla et al. [89] published similar findings showing the particle size was only really affected by changing the aggregation time (insertion length or carrier gas). That is not to say that the other two variables did not have an effect with both studies [88, 89] showing that the NP flux increased with higher plasma

power. Theoretically, a higher power would sputter more of the target in a shorter amount of time so there will be more atoms to nucleate and condense which would form larger particles. This was not seen by Khojasteh et al. nor Gracia-Pinilla et al. In fact another paper reported that increasing the plasma power actually decreased the particle size [90].

The thermal environment the clusters find themselves in has an important affect on the morphology of the particles, especially on the growth of Fe NPs for example. Vernieres et al. [91] and Zhao et al. [92] showed that with a lower plasma temperature, Fe forms cubic NPs instead of spherical ones. The thermal environment can be changed by the magnetron power as a higher power leads to higher plasma temperature [81]. Cubic formation is remarkable in itself as the cubic shape is energetically unfavourable compared to a more spherical shape at thermodynamic equilibrium. The actual equilibrium shape will not be spherical and will be dictated by Wulff's rules with the equilibrium shape of Fe NPs being a truncated dodecahedron for example [93], as shown in Figure 4.4(a). Cubic shapes form due to competing growth and diffusion rates of the island growth on the {110} face compared to the layer-by-layer growth on the {100} face.

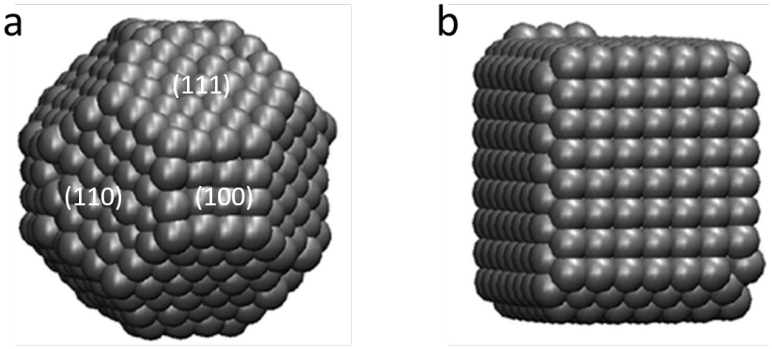

Figure 4.4: Diagram showing the difference in structure between the Wulff reconstruction of an iron NP (a) and a cubic core (b). Reproduced with permission from Ref. [94].

Atoms landing on a (110) surface diffuse rapidly and form single-layer nano-islands with any new atoms deposited only diffusing within the island due to the Schwoebel-Ehrlich barrier [92]. This barrier is an additional energy barrier for an adatom to diffuse down a surface step which dictates the growth modes of thin films [95]. This

fact explains why these islands are stable and grow in all dimensions until they finally take over the entire (110) surface. On the other hand, growth on a (100) surface follows a layer-by-layer growth and is rather flat. However, after about three layers have been grown the fast diffusion specific to the (110) surface comes into play and is preferential compared to the layer-by-layer growth of the (100) surface. This then prevents further upward growth of the (100) surface and the growth in the (110) direction is preferred which leads to the formation of nanocubes [92], shown in Figure 4.4 (b).

The thickness of the target is important; if the material is magnetic, then a thicker target has been shown to screen the magnetic field from the head and thus make sputtering less efficient [91]. It was also shown by Vernieres et al. [91] that the distribution of particle sizes will also be different for targets of different thicknesses as a thicker target of 1 mm leads to a bimodal distribution instead of a sole log-normal peak. They compared 1 mm thickness to 0.3 mm and 0.5 mm cases and showed an overall change from a well defined log-normal peak in the 0.3 mm case to the bimodal distribution for the 1 mm case. The authors put this down to the change in the confinement of the plasma on top of the target due to magnetic screening. This then changed the formation of the racetrack and thermal environment of the plasma which, as discussed above, has a large impact on the growth conditions of the particles.

4.1.3 Aerodynamic Control Of The Particle Beam

Particles that form in the aggregation chamber are moved through the system by establishing a particle beam. The particle beam is formed by the creation of a large pressure difference between the aggregation region and the rest of the source with the application of aerodynamic lenses. The lenses are typically small apertures that can either be shaped as a flat plate or a nozzle. The gas flow has to contract and re-expand through the lenses in order to continue moving down the pressure gradient [96] as shown in Figure 4.5. Typically the flow of the gas down the pressure gradient is subsonic (Mach numbers below 1) in order to limit turbulent effects that can form and disrupt the forming beam [97]. The particles get trapped in the flowing

gas and are dragged along with it as it flows downstream due to the pressure gradient.

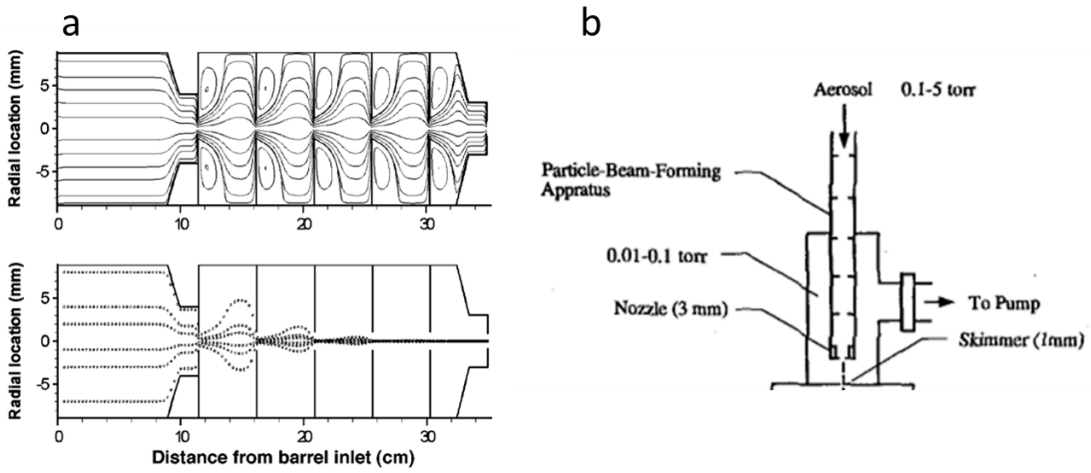

Figure 4.5: (a) shows the simulated gas (top) and particle flow (bottom) through an aerodynamic lens assembly. It can be seen how the particles are progressively lensed as they travel down the gas flow before forming an intense beam. Reproduced with permission from Ref. [98]. (b) shows a diagram from a vertically mounted aerodynamic lens assembly though the operation is the same. Reproduced with permission from Ref. [99].

Smaller particles endure smaller radial drag forces and as such are typically closer to the central axis beam line. Inversely, larger particles experience greater radial drag forces and are pushed towards the beamline edges [87]. Particles on the edges of the gas flow are more likely to impact on the walls of the vacuum chambers or the apertures that are placed in the system [98]. Therefore, it is important to limit the beam spread as much as possible by designing a lensing system that lenses a wide range of particle sizes onto the central axis. Particles that are closer to the central axis experience less radial drag regardless of size [96]. After passing through an aperture; particle inertia results in particle movement closer to the central axis as shown in Figure 4.6.

In Figure 4.6, upstream of the axis-symmetric lens, the particle follows the gas streamline towards the lens. As the gas approaches the lens, it is accelerated radially inward as it contracts pulling the particles inwards toward the central axis. The gas then re-expands after passing through the aperture but due to the particles' inertia they do not rejoin the original fluid streamline as they slow down [97]. In Figure 4.6,

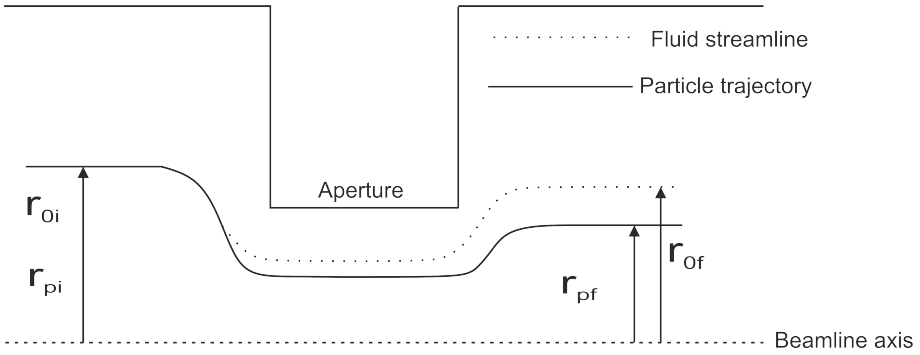

Figure 4.6: Figure showing a particle trajectory as it passes through a flat plate orifice. The final radial position of the particle at r_{pf} is smaller compared to the radial position of the fluid streamline r_{0f} due to contraction through the aperture. The figure is axis symmetric through the dotted line at the bottom of the figure. Adapted with permission from Liu et al. [96].

showing the motion of a single particle, the particle ends up closer to the central axis but it can cross the central axis and end up with a larger final radial position [99]. Through the careful application of this process, particles of varying sizes can be collimated to the central axis.

How effective this lensing is can be determined by the "contraction factor" (first coined by Liu et al. [96]) which is a measure of the percentage difference between the final radial position of a particle and the radial position of the fluid streamline after passing through a constriction.

The contraction factor, η, is calculated to be:

$$\eta = \frac{r_{pf}}{r_{0f}} \tag{4.1}$$

where r_{pf} is the radial position of the particle after the contraction, and r_{0f} is the radial position of the fluid streamline after the contraction. If the contraction factor is equal to 0, it means that the particle has been moved perfectly on axis with a negative value meaning that the particle has crossed the axis.

How a particle behaves before and after moving through an aperture can be described by the particle Stokes number (S) and particle Knudsen number (Kn_{p0}) or particle Reynolds number (Re_{p0}). These are defined as:

$$S = \frac{\tau_0 U_0}{d_f} \tag{4.2}$$

$$Kn_{p0} = \frac{\lambda_0}{D_p} \tag{4.3}$$

$$Re_{p0} = \frac{\rho_0 U_0 D_p}{\mu_0} \tag{4.4}$$

where τ_0 is the particle relaxation time which is a measure of the particle's response time to the fluid flow around it. τ_0 is based on the upstream conditions of the fluid flow and aperture dimensions and is equal to

$$\tau_0 = \frac{\rho_p D_p^2 C_s}{18 \mu f_d} \tag{4.5}$$

where ρ_p is the material density of the particles, C_s is a correction factor for particle slip effects at the walls of the lens and is equal to

$$C_s = 1 + Kn_{p0}[A + Qexp(\frac{-B}{Kn_{p0}})] \tag{4.6}$$

where A, Q, and B are all constants [96] and Kn_{p0} is the Knudsen particle number as defined before. f_d is another correction factor to account for the particle Reynolds number, as defined previously, and equals

$$f_d = 1 + 0.15 Re_{p0}^{0.687} \tag{4.7}$$

The other terms in the above equations are defined as follows, U_0 is the average flow velocity at the entrance to the aperture, d_f is the inner diameter of the cylindrical constriction, λ_0 is the fluid molecular mean free path, D_p is the particle diameter, ρ_0 is the fluid density, and μ_0 is the fluid viscosity. τ_0, λ_0, ρ_0, and μ_0 are all based on upstream conditions, i.e. before the aperture/constriction. These equations are not independent of each other with particle motion intrinsically linked to the flow of the gas containing the particles. The gas flow can be described by the lens Reynolds number (Re_0) and the lens Mach number (M_0).

$$Re_0 = \frac{\rho_0 U_0 d_f}{\mu_0} \tag{4.8}$$

$$M_0 = \frac{U_0}{C_0} \tag{4.9}$$

where the terms in these equations are as defined previously apart from C_0, the speed of sound. These sets of equations can be used to fully describe the motion of the particles and the fluid. So, for example, a particle with a Stokes number of $\ll$1 will follow the fluid flow, a value of $\sim$1 will result in the particle being pushed out by vortices in the flow and remaining at the flow periphery, and particles with S$\gg$1 will not follow the fluid flow at all [100].

P. Liu et al. [96] investigated the effects of lens geometric dimensions, off-axis particle initial locations, and lens Reynolds numbers on particle contraction factors for increasing particle Stokes numbers. In these calculations they showed that there exists an optimum Stokes number, S_0, where the contraction factor equals 0, and S_{-1} where it equals -1. Particles with a larger Stokes number than S_{-1} will have a contraction factor that is lower than -1 meaning that particle trajectories cross the axis and move to greater radial distances than they started at. This means that the lens will only effectively lens particles that have Stokes numbers less than S_{-1} thus creating a critical size that the particles must be below. This critical size means the lenses act as a low-pass filter for the population of particles. Liu et al. make the important point that S_0 and S_{-1} are greatly dependent on the lens geometries [96].

The research reported by Liu et al. [96] has formed the basis for many follow-on studies into the effect of aerodynamic lensing of particles. The authors also discussed the influence of Brownian motion on the beam broadening but the effect of this on particle sizes was not taken into account in their calculations of contraction factors. Wang et al. [101] showed that diffusional broadening of the beam through Brownian motion has an adverse effect on very small particles but had a limited effect as the particle size increases. These researchers showed that particles of 3 nm and above were still effectively lensed when Brownian motion was considered such that the process could be ignored for particles of larger sizes.

Inertial drag forces and broadening affects particles of different shapes as well; Wang

et al. [101] only investigated the Brownian broadening on spherical particles even though it is established that other shaped particles, e.g. cubes, will experience a larger amount of broadening due to their higher drag coefficient [96, 102]. One way of reducing the broadening is through increasing the axial velocity of the particles once they leave the aerodynamic lens setup [102]. Increasing the speed can either be done by employing a so-called accelerating nozzle which has a constriction that has a very small opening after a long throat [102], or by employing carrier gasses that are less dense as they will accelerate to faster speeds compared to a denser gas [101]. Zhang et al. [97] found that regardless of nozzle geometry the gas behaviour was the same and that a sonic expansion after the nozzle was identical. The authors explored this further in a separate paper [102] where they showed the application of a nozzle after a series of apertures had the greatest chance of lensing a wide range of particle sizes. The nozzle was effective for very small or very large particles which were typically not lensed by the aerodynamic lenses.

The application of aerodynamic lenses allows for a well collimated beam to be produced. Certain allowed particle sizes, as discussed above, can be specially selected for allowing the beam to be tuned in a specific way, as shown by Di Fonzo et al. [98]. They used a highly collimated beam to deposit nanowires as well as print samples after rastering the sample in front of the intense beam, a schematic of which is shown in the second part of Figure 4.5(a).

4.1.4 Particle Manipulation and Deposition

Once the particle beam has formed, various techniques can be used to manipulate and monitor it in real time such as core-shell coating and using a quadrupole mass filter (QMF) to produce in-situ mass spectra.

Core-shell coating involves the formed particle beam passing through a vapour cloud that coats the particles in a secondary material. This then produces so called core-shell particles such that the core is composed of the sputtered NPs and the shell is the secondary material, as shown diagrammatically in Figure 4.7.

Coating the particles in a secondary material is beneficial because it can potentially be used as a protective layer against oxidation. The core would remain intact as

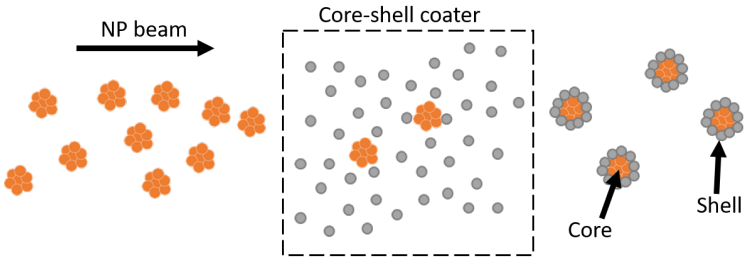

Figure 4.7: Diagram showing the incoming NP beam from the left passing through a core-shell coater and then producing core-shell particles. The original NPs (orange) are coated in the secondary material (grey) before the beam carries on through the system.

the shell oxidises meaning the desired properties from the original core particle can be studied and utilised. This has been shown chemically with Cu NPs coated in formate to make a copper formate shell [103]. Coating the NPs in a secondary material may also increase the functionality of the particles such as modifying the magnetic properties by coupling ferromagnetic materials with anti-ferromagnetic materials [104, 105]. This can be achieved with the cylindrical crucible arrangement, as described later in Section 4.3.1, or with a tubular magnetron where sputtering a secondary target produces a vapour which can then coat the particles in the secondary material [106, 107].

A schematic diagram of a QMF is shown in Figure 4.8. Four electrodes, radially arrayed and connected in pairs, create a quadrupole field due to applied DC and AC voltages. This acts as a bandpass filter due to the mass-to-charge ratio of the particles as they move through the instrument [108]. The filter works by the planes operating independently of each other. Considering the XZ plane first, shown in Figure 4.8(a), the time-dependent AC voltage will spend half of its cycle positive and the other half negative meaning that positively charged particles will be focused to the central axis half of the time. Essentially, the particles are repulsed from the rods when they are positive and attracted when they are negative. The particle will only collide with the rods if the negative potential is applied for long enough so normally it more strongly depends on their mass-to-charge ratio [108].

For the XZ plane, the applied DC voltage is positive, meaning that positive ions will be focused due to this potential. The overall effect is that heavier particles

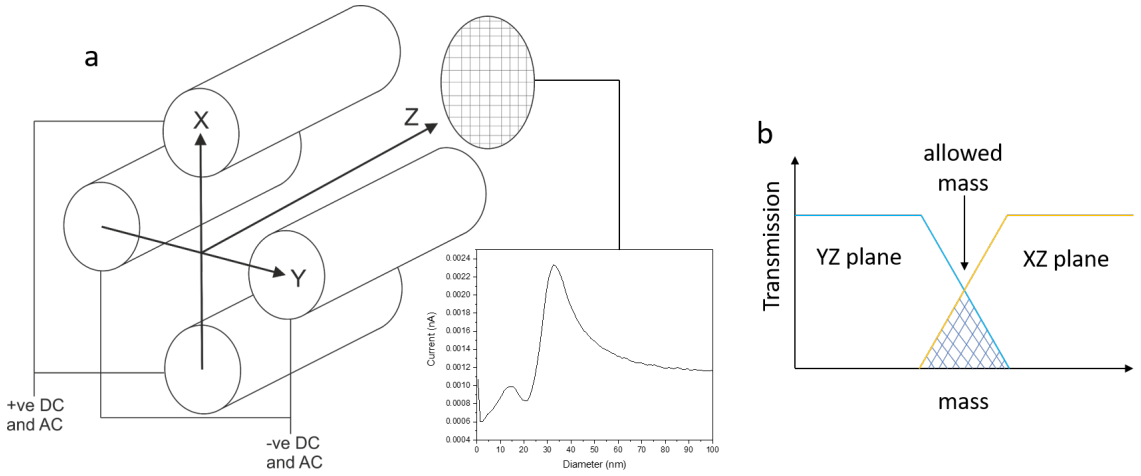

Figure 4.8: (a) Schematic diagram of the quadrupole mass filter with four rods placed around the axis of the beam. A DC and AC voltage is applied to the two pairs of rods which then act as a band pass filter for the mass of the particles travelling through. Only a very specific allowed mass will stably make it through the filter before inducing a current signal in the collection grid at the end. This induced signal can then be related back to the allowed mass to create a mass spectrum. (b) Transmission overlap from the combination of the YZ and XZ planes that allows a small selection of mass to transmit through the filter. This can be changed by applying different AC and DC voltages. Adapted from Ref. [108].

will only be focused due to the DC voltage as the oscillating AC voltage will not be strong enough to overcome the DC potential. Lighter particles, conversely, may have their paths severely altered by the negative potential from the AC voltage and thus they may collide with the negative rods. This makes the XZ plane act as a high-band pass filter. The YZ plane is the opposite, with the applied DC potential being negative meaning that heavier particles are strongly defocussed and lighter particles more strongly influenced by the positive AC potential. This establishes a low-band pass filter in this plane [109].

Overall, the combination of both planes means there exists an allowed mass that is light enough to stably pass the YZ plane but not so light that it does not pass the XZ plane. Figure 4.8(b) shows the overlap of the two planes and thus the transmitted mass range. By scanning the applied DC and AC voltages, this allowed region can then be changed. Once the particles have made it through the rods, they then pass

through a grid and as the particles are charged they induce a current in the grid. The induced current signal can then be related back to the allowed mass of the particles with mass spectra produced as the transmitted mass is scanned. An example mass spectrum is shown in Figure 4.8(a). The mass spectra produced should follow a log-normal distribution as expected.

The filter also allows for the selection of a certain particle size by setting the voltages applied to the rod to be constant therefore only allowing the selected particle size through the filter.

Once the particles have gone through the filter they are typically then deposited onto some type of sample. Various samples have been used by different research groups such as an ice-matrix to prepare liquid samples [110] and co-depositing clusters into metal matrices to study their interaction [111]. Having NPs in a liquid is useful as it then allows for heating tests to be performed for magnetic hyperthermia applications [110]. Preparing these samples is theoretically very straightforward. Water vapour is directed onto a cold sample plate (typically liquid nitrogen cooled) where it condenses and freezes to form ice. While this process is taking place, the nanoparticle beam is also impinging the sample plate thus embedding the NPs into the forming ice. The sample can be retrieved and as the ice melts into a liquid the NPs are retained in the solution. Aktas et al. [112] discovered that the particles aggregated much more than expected in water and were therefore unfit for the purposes of magnetic hyperthermia studies. These workers found that Sorbitol was a much better solvent to deposit the particles in as it limited aggregation and made the particles far more suited for hyperthermia treatments.

Baker et al. [111] found that when cobalt (Co) clusters were deposited into a formed iron (Fe) matrix they adopted a bcc crystal structure over the normal hcp structure of bulk Co. Co clusters by themselves also showed an hcp crystal structure demonstrating that the Fe matrix was affecting the Co film. This is important as bcc Co is predicted to be strongly magnetic [113] with magnetic moments comparable to or stronger than hcp Co. This is difficult to test as bcc Co reverts back to hcp Co as the film gets thicker but Baker et al. [111] found it was stable up to high coverages. Skumryev et al. [114] showed that the superparamagnetic limit of Co

NPs 4 nm in size could be increased from 10 K to 290 K when the Co particles were embedded in an anti ferromagnetic matrix. Increasing the superparamagnetic limit has implications for high density recording media applications [115].

4.2 Other Growth Methods

A more common growth method for making NPs is through a chemical synthesis route. This is popular as the methodology is thoroughly documented and repeatable plus it is easy to expand production to an industrial scale [9]. However, the reactions can be complex multi-staged processes [116] that often involve harmful reactants.

There are two popular methods for creating metal NPs, either through thermal decomposition of a metal-pentacarbonyl or the chemical reduction of a metal salt in solution [117]. Thermal decomposition involves dissolving the metal-pentacarbonyl in an organic solvent and then heating to near 200 °C which produces uniform metal NPs [117]. An organic surfactant is then used to prevent the particles from aggregating by coating them to stop agglomeration through steric repulsion [9]. This method produces uniform particles with a high purity [117].

A slightly different approach to the decomposition of iron pentacarbonyl was developed where the solution is sonicated producing localised heating which removes the need to heat the solution to 200 ^{o}C. Suslick et al. [116] were the first researchers to report this method producing iron powders which were shown to be amorphous in TEM. Crystalline samples could be recovered through e-beam heating in the microscope to form bcc iron which then readily oxidised when exposed to atmosphere.

However, the thermal decomposition of the metal pentacarbonyl is problematic in that the decomposition reaction can be rather complex as it does not always follow a simple pathway. A range of intermediate carbonyls and clusters can form which can catalyze the decomposition reaction meaning the reaction rate can change over the course of the reaction [118]. This process also requires the careful handling of harmful chemicals as pentacarbonyl is highly toxic [119]. Harmful byproducts such as carbon monoxide are also released during the reaction.

In the chemical reduction process, a metal salt such as metal-chloride is reduced in

aqueous solution to form metal nanoparticles [117]. Hydrazine hydrate and sodium borohydride are the most frequently used reducing agents [120–122]. Hydrazine hydrate is added to alkaline solutions, and sodium borohydride is suitable for neutral or acid solutions. NPs can be obtained without the use of surfactants but as for thermal decomposition they can be added to prevent NP aggregation via steric repulsion [9].

The overall particle size can be increased by Ostwald ripening, a process where smaller particles dissolve in the solution and redeposit onto the larger particles [123]. This process can be slowed by rapidly decreasing the reaction temperature [9]. Particle size selection can also occur using techniques such as magnetic separation [124], size-exclusion chromatography [125], centrifugation [126], and electrophoresis [127].

Magnetic separation is the ability to remove particles from a solution with an applied magnetic field. Size selection takes place due to the fact that if the particles are too small then Brownian motion and viscous drag overcome the magnetic tractive force applied to them so they remain in the solution [124]. The disadvantage of this approach is that it only works for magnetic samples and the equipment needed could be rather expensive as large magnetic fields are required [128].

Size-exclusion chromatography is based on the fact that different sized particles elute through a medium at different rates. This can be applied to a wider range of particles in comparison to the magnetic separation technique though it takes place over a slower timescale. Siswoyo et al. [125] showed that gold NPs of varying sizes could be separated out in around 10 minutes compared to the instantaneous size selection of the QMF.

Centrifugation utilises differences in hydrodynamic behaviour to separate different sized and shaped NPs in solution [126]. Selective pipetting can then be used to produce size-selected NP solutions. Once again this process takes extra time and does not allow for the real time feedback available from the QMF. Electrophoresis, much like magnetic separation, uses an electric field to pull the NPs out of the solution. Size selection occurs through a similar process as well with larger particles more easily passing through the liquid and experiencing less drag. Functional groups can

be added to the NP surface that then increase their charge and thus the attractive force felt by the electric field [127].

While these chemical processes are more readily scaled for industry compared to the cluster source, the inability to easily make crystalline samples is a downside compared to the GACS. With the source also under vacuum, the particles stay clean and thus pure metal NPs can be studied with relative ease. Size selection through the QMF is also trivial compared to the process undertaken in the chemical methods as the population can be monitored in real time and adjustments made to ensure the desired particles are produced. More importantly, no seriously toxic chemicals or materials are used when making NPs using the GACS. Duan et al. [129] described other 'greener' methods to produce particles through more sustainable and less toxic methods but the arguments above in favour of the GACS apply the same.

4.3 The Cluster Source at York

The cluster source used in this project was a Mantis Nanogen 50 equipped with a MesoQ (Mantis' QMF). The source is affectionately known as Merlin and a large part of this project has been the development of the source to a) get it producing particles reliably and b) developing equipment that then meets the research needs of the group and my PhD project. The initial setup suggested by Mantis did not work, as detailed below and a lot of effort was placed in getting it to function properly. Once this was achieved, the source was modified to include new sections that enhanced the production capabilities and broadened the possible research that could be performed. This section will outline the development process and the various steps that were taken throughout the project. Moreover, it will describe the general operation of the source as well as characterising its use to produce particles of different sizes.

4.3.1 Development of the Source

The initial setup of the source from Mantis came as shown in Figure 4.9. Merlin had two sections, an aggregation chamber, and a QMF section. These were pumped

out with the two turbo molecular pumps (TMPs) shown in Figure 4.9 with pumping speeds of 300 ls^{-1} and 85 ls^{-1} for the aggregation chamber and QMF sections respectively. A deposition chamber was not included to begin with as the idea was for the source to attach to various other vacuum systems present in the laboratory and to deposit onto samples produced in them. The first task was to get the source working and observe NP production through the mass spectra. This was initially undertaken with a 6 mm thick Cu target as it has a higher sputter yield compared to Fe [130].

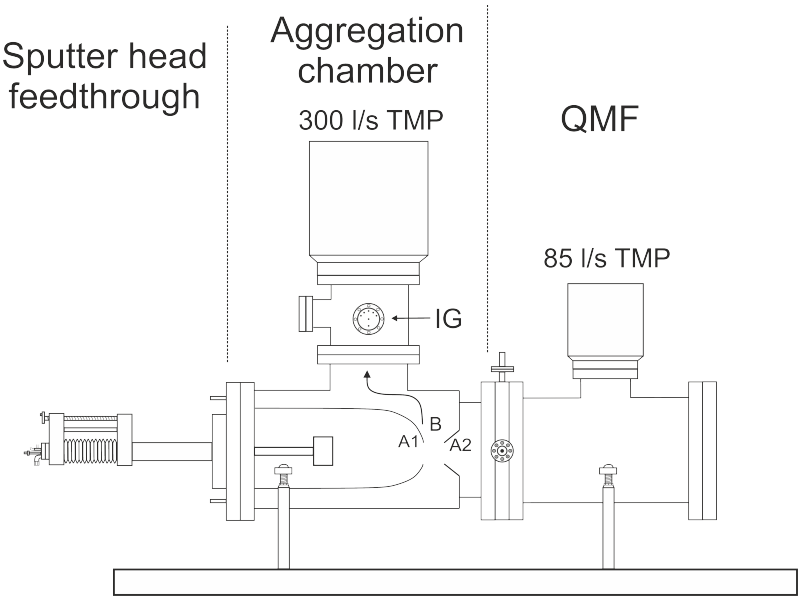

Figure 4.9: The initial setup of Merlin comprising of two sections, the aggregation chamber, and the QMF where IG denotes an ion gauge. The labels A1 and A2 show the aerodynamic apertures with the expansion zone, B, between them. A2 is a skimmer as shown instead of a flat plate aperture. The pumping speeds of the turbos are also labelled.

It was discovered that the source worked better once it had been cleaned. The reason the system is cleaned is because it has been shown by Kousal et al. [131] that many NPs are trapped within the first few millimetres of the target. This work demonstrated that the NPs preferentially accumulate in the central region of the plasma torus and the most abundant cloud of NPs is trapped in a region 3-10 mm away from the head. From there, the average diameter and number of particles travelling through the system drops dramatically, with the trapped particles deposited onto the magnetron head or the chamber walls instead of travelling through the system.

This creates a large buildup of material on and around the head which needs to be cleaned off regularly to maintain the source. The cleaning procedure for Merlin is outlined in the next section.

Changes to the Source Arrangement

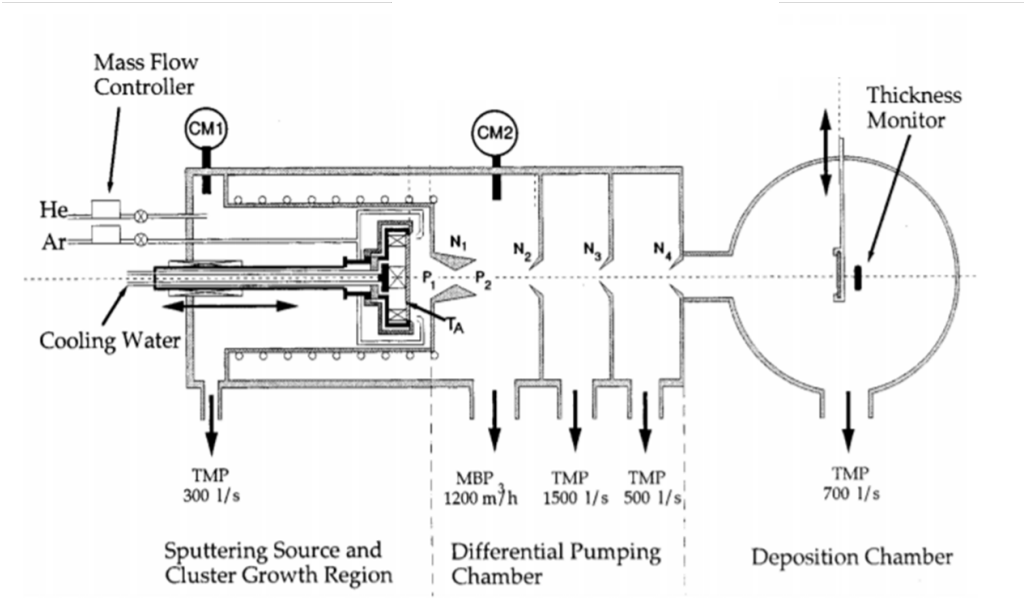

Figure 4.10: Figure showing the cluster source used by Hihara et al. [78]. The cluster source shows multiple apertures and a variety of different sized pumps to achieve a particle beam. Reproduced with permission from Ref. [78].

Comparing the system in Figure 4.9 to that of Hihara et al. [78] in Figure 4.10 shows that the pumping arrangement is drastically different. The main pumping is performed after the expansion zone and the aerodynamic lenses that establish the necessary pressure gradient discussed earlier. Through direct comparison it can be seen that this is not the case for the setup shown in Figure 4.9 so more downstream pumping is required to help shift the high gas load used during operation.

A dedicated sample deposition chamber was therefore developed in order to increase the downstream pumping. A 1000 ls^{-1} turbo pump was installed onto this chamber as well as a QCM and a rotating sample carousel on a linear drive. The QCM, as outlined in Chapter 3, allows for monitoring of the deposition rate which allows for more accurate deposition of either TEM samples where the coverage needs to be low to image individual particles or thicker NP assembled thin films for use in the

spectroscopy system. The hexagonal sample carousel sits on a linear drive so that the samples can be placed in front of the beam or removed to stop the coverage. Omicron style plates can be placed in any one of the six slots available on the carousel meaning multiple samples can be created during source operation. TEM grids can be placed on specially made plates that can hold up to four grids. Having this functionality is important as there is no fast entry load lock nor some form of isolation on the system meaning that to get samples in and out the whole system needs to be vented to atmosphere. So being able to make multiple samples limits downtime.

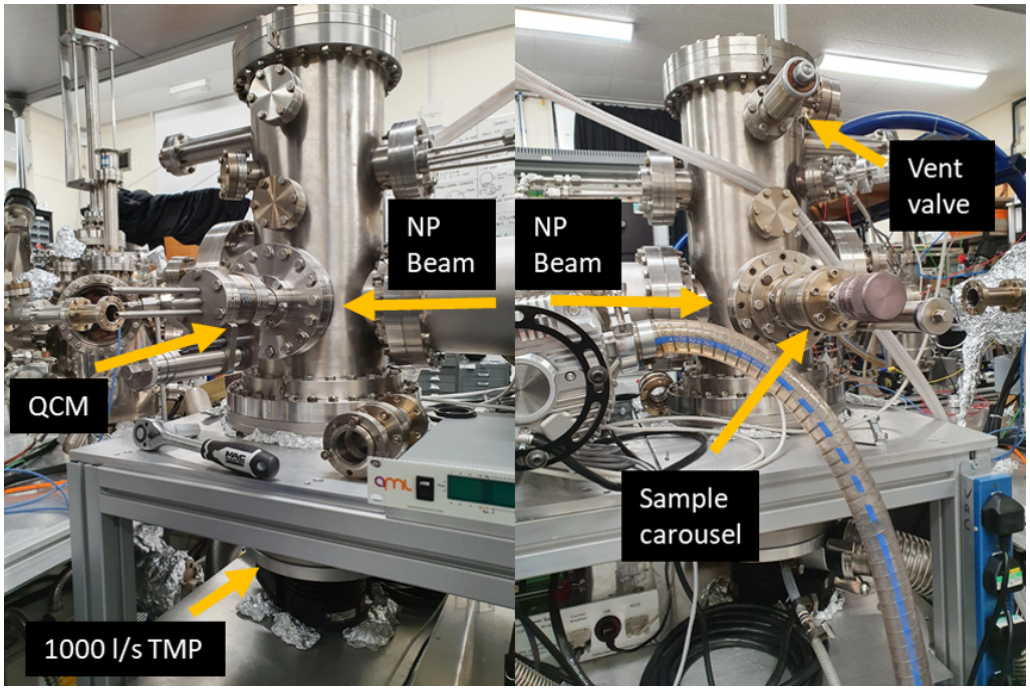

Figure 4.11: Labelled pictures of opposite sides of the deposition chamber that was developed to allow for increased downstream pumping as well as production of multiple samples through the incorporation of the sample carousel. The deposition rate could also be monitored with a QCM and a dedicated vent valve was incorporated.

The deposition chamber was attached to the end of the QMF and the 85 ls^{-1} TMP was removed meaning that the main pumping of the system downstream was achieved by the new larger pump, as shown in Figure 4.11. The new pumping arrangement was shown to work when Merlin produced Cu particles stably for over two hours. It was also discovered that thinner Fe targets were needed when working with this material. If the targets were too thick the magnetic field of the magnetron

head was blocked and thus did not sputter the target properly as the plasma was not confined on top of the target. Thinner targets were made in the mechanical workshop at York which were cut from a large Fe sheet into 2 inch diameter, 0.5 mm thick targets of 99.5 % purity. Once the Fe targets were inserted in the system, a cleaning procedure which is described in the next section was undertaken.

Increasing Functionality

Once stable production of NPs was achieved, the next step was to develop Merlin to increase the production capabilities of the system. A core-shell coater was developed and an extra section was added to the source as a whole. The core-shell coater is a cylindrical crucible that creates a vapour through thermal evaporation which the particles pass through. This vapour then coats the particles creating a shell of secondary material. The system setup is shown in Figure 4.12.

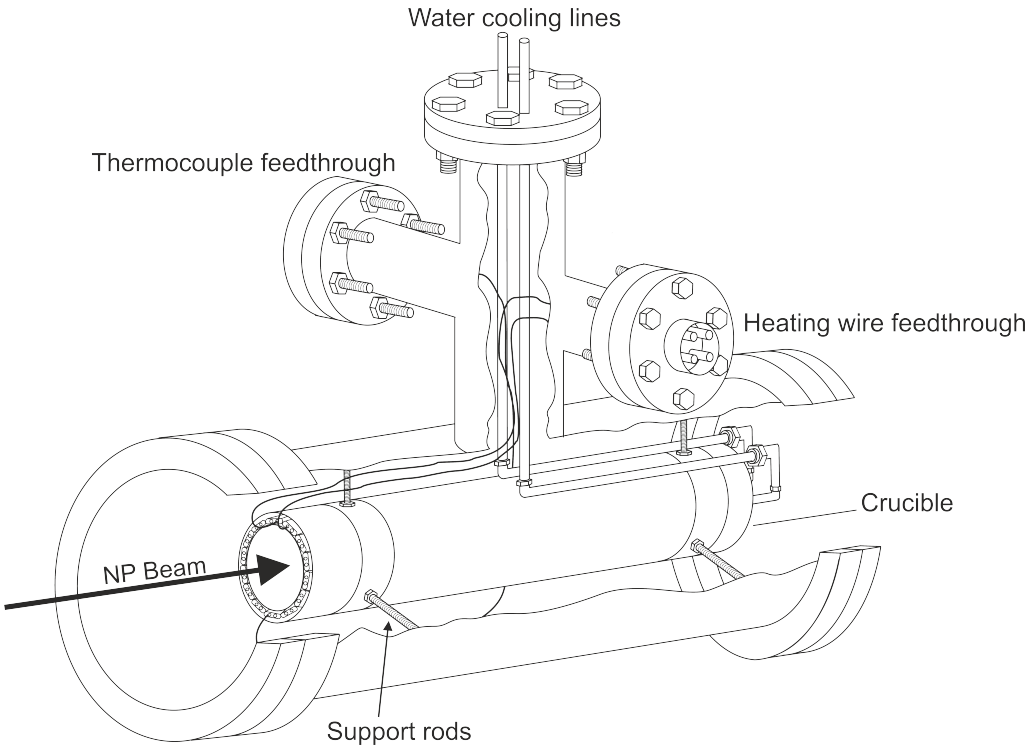

Figure 4.12: A cross-section of the core-shell coater showing the water cooled jacket that surrounds the Ta cylinder which forms the crucible with the evaporation material placed inside. Ta wire connects the feedthrough to the crucible heating wires. A K-type thermocouple is also placed on the outside of the crucible to monitor the temperature.

The design of the crucible was based on the work of the nanoparticle group at the University of Leicester [104] with whom we have previously worked closely. A large current is passed through the wires which are wrapped around a Ta cylinder which forms the inside of the crucible. This current resistively heats the wires which in turn heats the crucible. The crucible, measuring 22 mm (OD) by 106 mm, is housed inside a water cooled jacket, measuring 26 mm (OD) and 200 mm, which is located inside the chamber by six studs that extend to the chamber walls. The temperature of the crucible is monitored by a K-type thermocouple that is placed on the outside of the crucible structure. The ultimate temperature of the crucible for a series of applied currents was calibrated when it was first built with the resulting graphs shown in Figure 4.13.

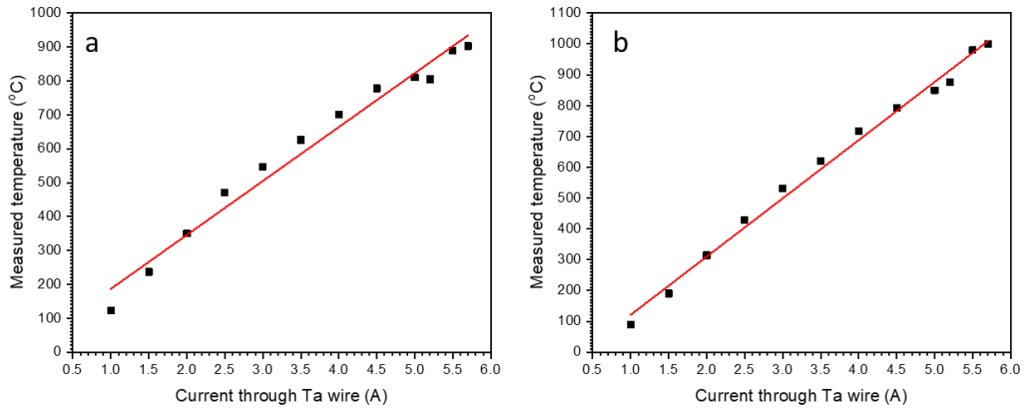

Figure 4.13: Temperature data taken from the crucible for (a) the position where the thermocouple sits permanently and (b) where a thermocouple was placed in the direct centre of the crucible. These are used as calibration curves to then set the growth temperature correctly during deposition.

Figure 4.13(a) shows the temperature readings from the permanent thermocouple position, i.e. where the thermocouple will normally be during operation. Figure 4.13(b) is from a temporary thermocouple that was placed in the direct centre of the crucible. This allows for a comparison of the measured temperatures to the actual temperature in the centre of the crucible where the material will be evaporated. A linear fit has been placed on the graphs as a rough guide to allow for extrapolation at different applied currents through the wire.

Improvements to Particle Flux

The final modification to the system concerned the aerodynamic lens assembly and pumping arrangement. The original Mantis design had a 5 mm aperture at the end of the aggregation zone followed by a small 'expansion zone' that then led to a skimmer (shown in Figure 4.9). The 'expansion zone' was pumped by a large turbo pump which was believed to be disrupting the formation of the particle beam. This was proven when NPs were only produced when a gate valve (temporarily placed between the system and the TMP on the aggregation chamber) was closed. The skimmer, originally supplied by the manufacturer and seen in Figure 4.9, was believed to be blocking a large portion of the particles that would have otherwise been on axis. Downstream pumping, post apertures, also had to be improved as well to create the particle beam. This lead to the development of an aperture assembly to create a more collimated and intense beam shown in Figure 4.14. Figures 4.14(a),(b), and (c) reflect the progressive development in the aperture assembly that then eventually produced a more intense NP beam. The final lens assembly is shown in Figure 4.14(c) where two flat plate apertures are placed after the exit of the aggregation chamber.

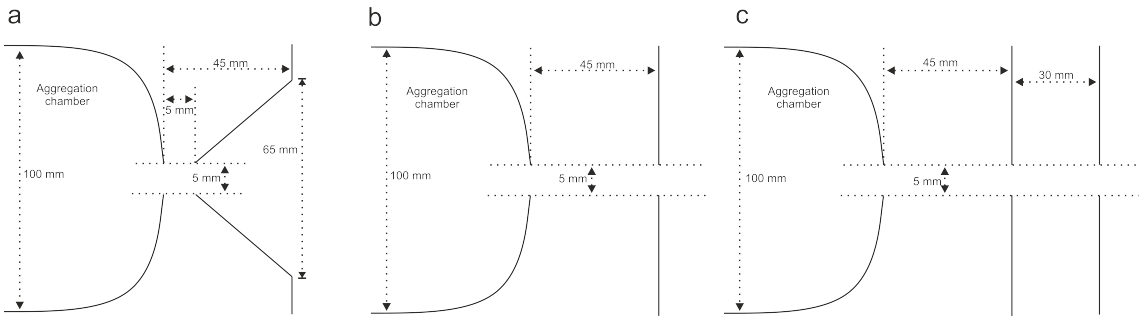

Figure 4.14: (a) Original aperture setup with a skimmer placed very close to the exit aperture of the aggregation chamber, Both apertures have a 5 mm orifice. (b) Second assembly where the skimmer was replaced with a flat plate aperture of the same exit diameter. (c) Final assembly with a third flat plate aperture placed on axis with all the apertures having the same diameter of 5 mm.

The SEM images in Figure 4.15 show the increase in deposition rate as the aerodynamic lenses were modified. The bright spots in the images are Cu NPs which were deposited onto Si crystal wafers. After 90 minutes, the original lens setup, Figure

4.14(a), produced the coverage shown in Figure 4.15(a) which reflects a very low deposition rate. Figure 4.15(b) is after the skimmer was replaced with a flat plate aperture with the same opening diameter of 5 mm, Figure 4.14(b). The deposition rate was much improved with more particles obviously present after only 30 minutes deposition time.

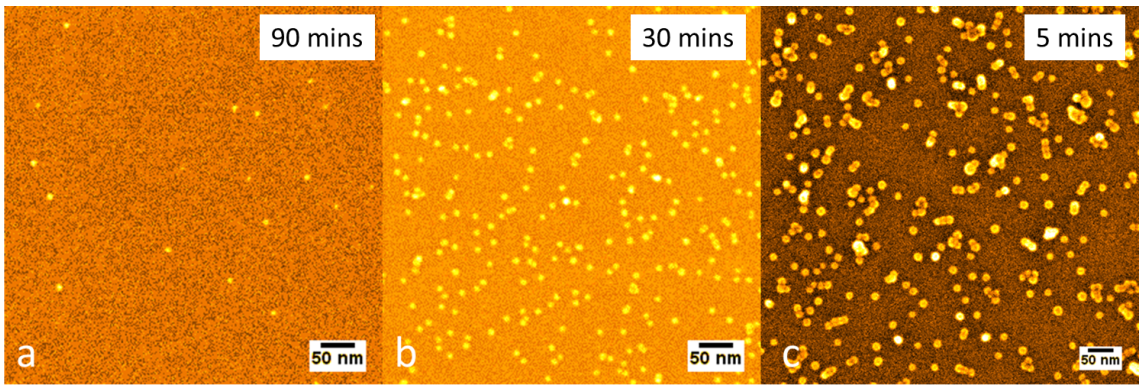

Figure 4.15: SEM images of Cu NPs (bright spots on false-colour orange background) on uncleaned Si substrates showing an increased deposition rate as the aperture assembly was modified. (a) was produced using the original aperture setup consisting of a 5 mm skimmer after the end of the aggregation chamber. The Si wafer in (a) was exposed for 90 minutes to the particle beam. (b) is the result after 30 minutes of exposure following the replacement of the skimmer with a flat plate orifice with the same internal diameter opening (5 mm). (c) shows the deposition rate after a third 5 mm flat plate orifice was installed with the Si sample being exposed for just 5 minutes. It can be seen that the particle size has increased as these larger particles are being placed on axis by the lens assembly.

Though this was an improvement, the source flux with the core-shell coater in place on axis was still low, so a third aperture was placed in the system, as shown in Figure 4.14(c). The result of this is shown in Figure 4.15(c) where deposition on a Si wafer for just 5 minutes showed an increased coverage of NPs. Multiple lenses place more of the particle beam on axis which in turn increases the deposition rate, as discussed in Section 4.1. A benefit of having a highly collimated beam of particles is that more of them will pass through the core-shell coater.

In order to investigate why the change in aperture setup led to a drastic improvement in beam flux, the effect of the various apertures and source arrangements was

investigated using COMSOL. COMSOL is a multiphysics programming package that allows for complex physical problems to be resolved for a variety of geometries. Models can be produced inside the programme using the built-in interface which can then have materials and physics problems applied. Time-independent or -dependent studies based on the initial conditions can be resolved. Results and data are outputted which can then be manipulated to produce the results needed to match any experimental or theoretical observations. Version 5.6 was used on the research1 computer cluster at the University of York.

Models of the original aperture system (exit of the aggregation chamber and skimmer) and the final aperture setup (three orifices) were created using the software's geometry package. A fine mesh was applied to allow for good resolution at the walls and apertures. The κ-ω turbulence model was used to simulate the gas flow as it allows for a more accurate wall treatment as compared to a laminar model [132]. Due to the large pressure gradient, the flow is most likely either transitional or turbulent. The κ-ω model was chosen due to its greater accuracy at determining jets which will form through the apertures [132].

Two 2D models were built using the geometry builder inside COMSOL 5.6, one with the skimmer in place and another with the two replacement apertures. The models were built with the same dimensions of Merlin so that the results could be as accurate as possible. The exterior walls and inside apertures were set to "No Slip" meaning that flow with respect to the wall is equal to zero. This allows for boundary effects to be modelled giving a more accurate description of the interaction of the fluid with the apertures. The left hand wall was defined as the inlet and the right hand wall the outlet. These were set to the average pressure condition with values of 100000 Pa for the inlet (roughly an atm) and the oulet to 50 Pa. These pressures were chosen based on pirani gauge measurements of the source during operation. The gas flow was modelled using Ar with an initial pressure set in the model to 1×10^{-6} Pa with an initial velocity vector of (1,1) ms^{-1} in the (x,y) direction. A variety of initial velocity vectors were trialled to investigate the effect on the final gas flow field but it was found to have no effect on the final outlet speeds of the jet once the simulation was run.

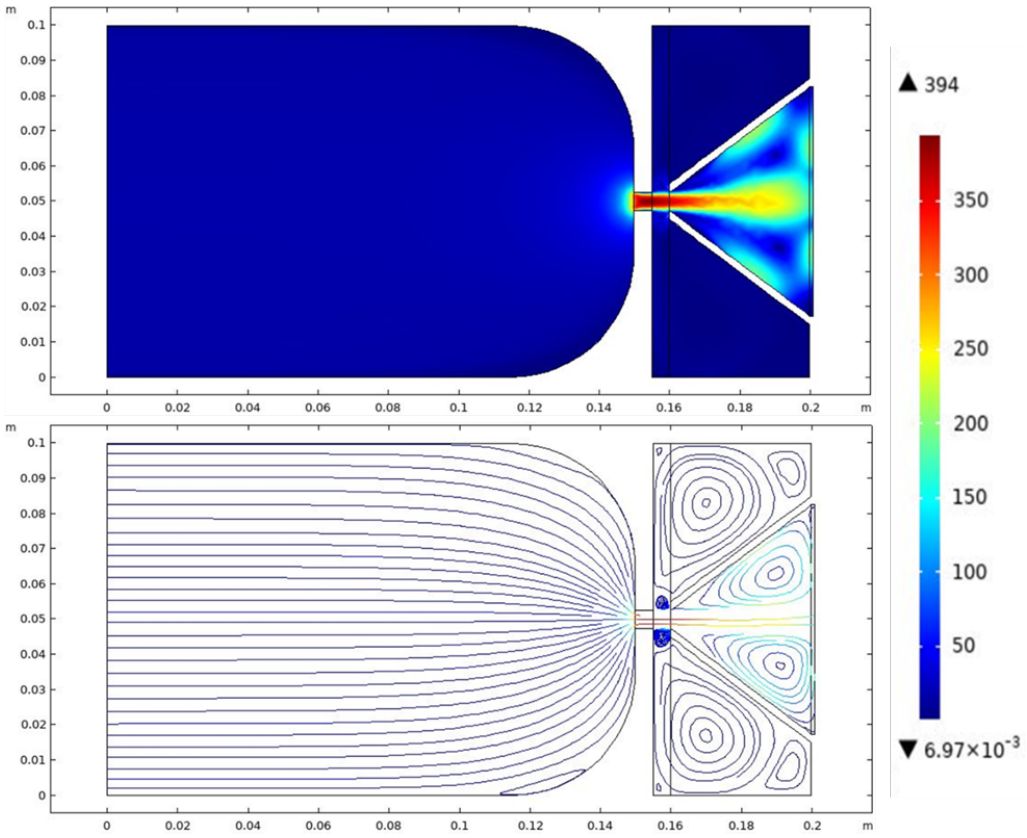

Figure 4.16: Gas velocity fields as modelled in COMSOL 5.6 for the skimmer setup. The velocity surface colour map (top) and streamlines (bottom) are shown with the scale bar showing the speed of the gas flow in m/s. Modelling conditions are described in the text.

Figures 4.16 and 4.17 show the velocity field of the gas flow through the two lensing systems. The maximum velocity is higher through the skimmer setup due to the smaller gap between the exit of the aggregation zone and the start of the skimmer. Large zones of silence are also established in the gas flow which are evidenced in the closed loops in the velocity streamlines. These are due to the high pressure gradient leading to turbulent effects.

Cut point lines were taken after the apertures to assess the beam width, as shown in Figure 4.18. The skimmer arrangement, Figure 4.18(a), has a central beam FWHM equal to 16.6±0.2 mm whereas the second aperture arrangement, Figure 4.18 (b), has a FWHM of 21.7±0.2 mm. While the FWHM of the second arrangement is larger than the skimmer setup, this is due to the fact that only the central peak in the beam profile for the skimmer was taken into consideration. The FWHM was

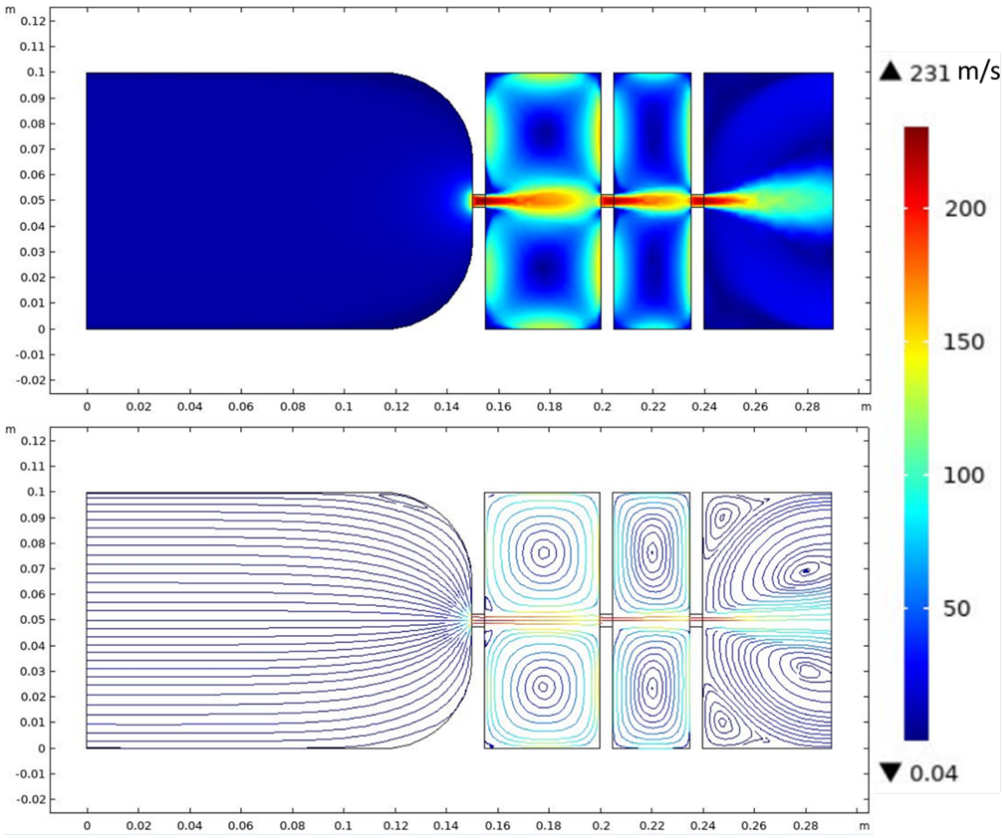

Figure 4.17: Gas velocity fields as modelled in COMSOL 5.6 for the adapted setup with the two extra flat-plate apertures in place. The velocity surface colour map (top) and streamlines (bottom) are shown with the scale bar showing the speed of the gas flow in m/s. Modelling conditions are described in the text.

determined by using the peak analyser function in Origin (the graphing software) which allows the user to determine the baseline and the range of the peaks to investigate by establishing turning points in the graphs such that the ranges are set by changes in gradient. The software then integrates the peak and provides a value for the FWHM as well as associated error. Due to modelling constraints, the fluid flow further downstream of the apertures has not been simulated but it is likely that the beam becomes more defuse as it moves further downstream of the skimmer. While the beam profile of the apertures is technically broader, the beam is more collimated with the majority of the gas velocity concentrated on the central axis.

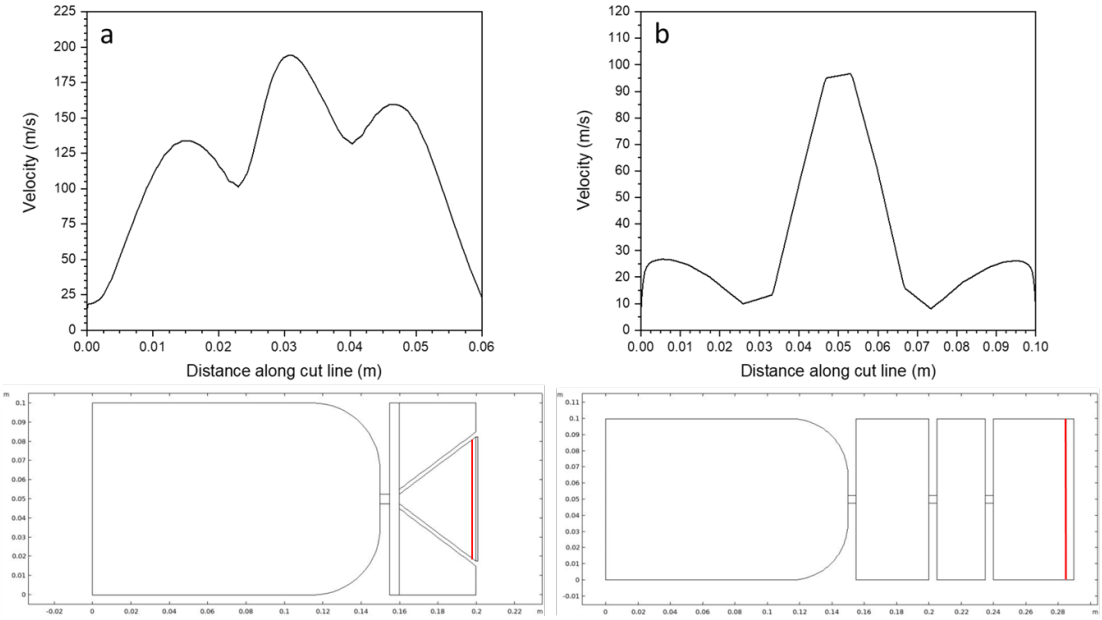

Figure 4.18: Simulated beam profiles of the two setups modelled in COMSOL 5.6 with the red line showing where the profile was taken in the model for (a) the skimmer arrangement, and (b) the final aperture arrangement.

The Final Design of Merlin

The final design of the source is shown in Figure 4.19. An additional turbo pump was added to help evacuate the aggregation region as the source is pumped down to low pressures. The gate valve to this TMP is closed during operation. The length of the entire system is 1630 mm.

4.3.2 Operation and Characterisation of the Cluster Source

As outlined in the previous section, the cluster source can exercise great control of the particle size and shape. Understanding the delicate interplay of all the source parameters and how they affect the size of the particles was a key objective in the development of the source. The first parameter considered was the plasma gas. Figure 4.20 shows how the size distribution measured by the QMF changes with gas flow. Note, the stepped nature of the plots is due to the step size of the scan defined in the MesoQ software with a larger step size resulting in a lower resolution and therefore a stepped graph.

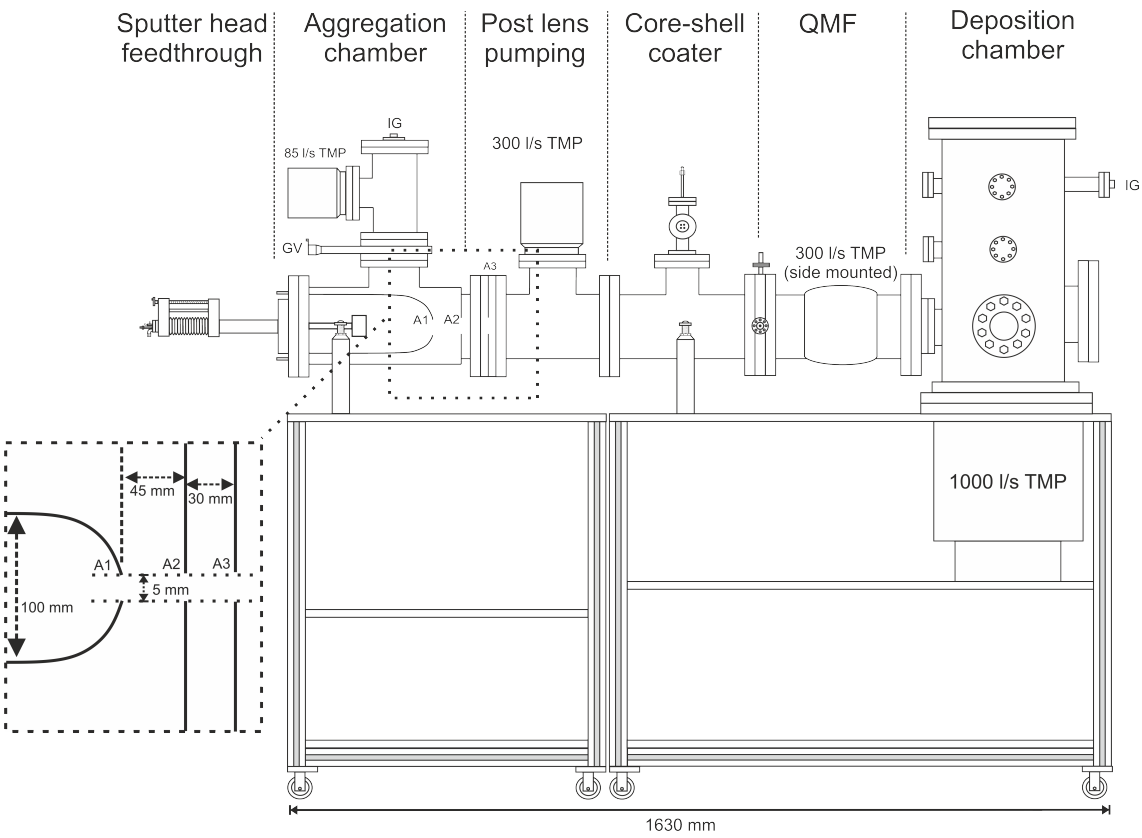

Figure 4.19: Schematic of the final design of Merlin where A1, A2, and A3 are the flat plate orifices, IG is an ion gauge, GV is the gate valve that is closed during operation to protect the smaller TMP, and the other sections such as the core shell coater are covered in more detail in the preceding figures. The pumping speeds of the various TMPs are also labelled.

It can be seen from Figure 4.20 that increasing the plasma gas flow does not impact the mean size in the distribution of the NPs. The current signal of the QMF increases with gas flow and this could be due to creating a higher upstream pressure that more effectively traps the particles in its flow. There is also the possibility that the plasma is contained on top of the target more effectively with a higher gas flow thus sputtering more of the target.

It was found that the source did not produce NPs without the use of the carrier gas. This could be due to the fact that without it an adequate upstream pressure could not be produced so the correct conditions through the apertures to establish a beam were not realised. Helium is routinely used as the carrier gas in other sources but it was found that for Merlin, He was detrimental to the plasma as shown in

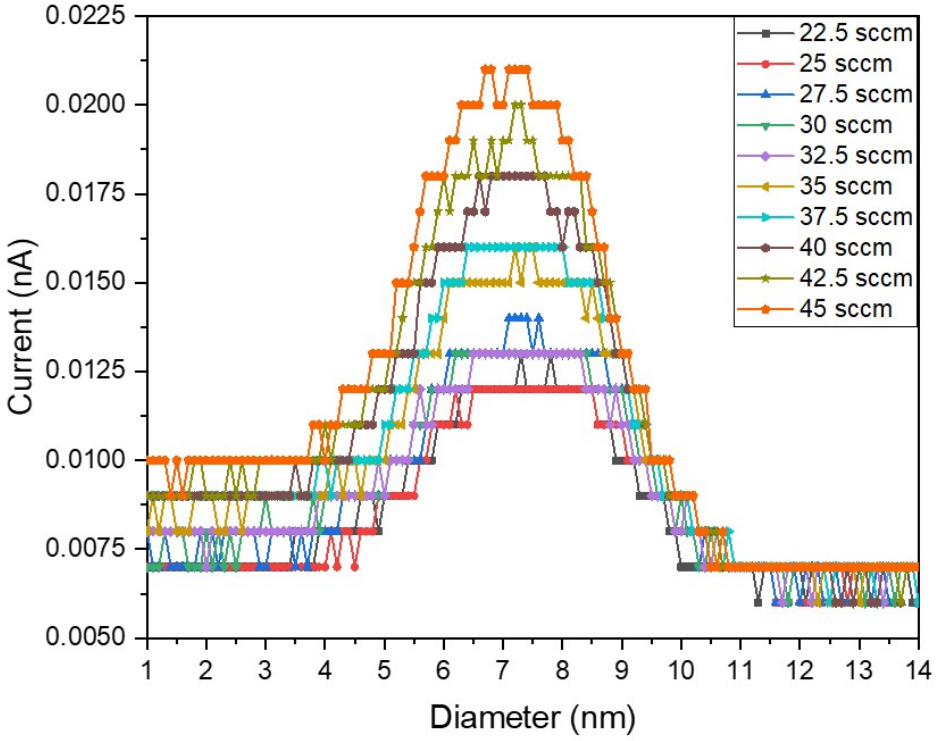

Figure 4.20: The dependence of the plasma gas on the size distribution of Fe NPs produced using a carrier gas inlet flow rate of 5 sccm, the minimum insertion length (140 mm), and a plasma current of 104 mA.

Figure 4.21 where the current signal from the QMF is shown to have significantly reduced, by just under 50 %, after the introduction of He to the system. It could be that the He is interfering with the growth process of the particles or more likely changing the sputtering plasma. The effect of the injection of He into a GACS was investigated by Bray et al. [133] where they showed that increasing the flow rate of He as a carrier gas can cause the particle beam intensity to decrease. They state this is due to the fact that the amount of metal vapour in the aggregation zone decreases due to the He adversely affecting the sputtering conditions on the target. The He also decreases the time the particles spend in the aggregation zone as the He flows faster due to being lighter than Ar. Interestingly, Bray et al. [133] also show that at higher He flow rates and low plasma currents the intensity of the particle beam can be increased. This was explained as being due to a faster gas flow and thus an improvement in the collection efficiency of the source. This effect was not

investigated with Merlin although it would be interesting to see if it is present as the decrease Bray et al. [133] see in intensity is less than for Merlin. The effect was also not seen in Merlin when the carrier gas was changed to Ar which suggests the phenomena is related specifically to the injection of He.

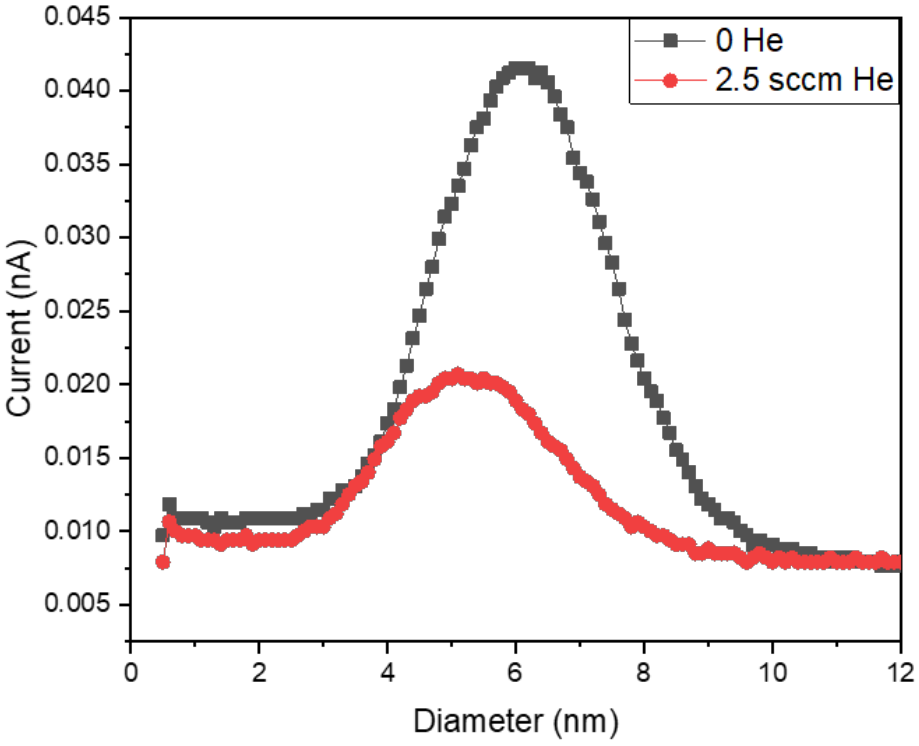

Figure 4.21: The effect of the injection of He on the distribution of Cu NPs (47.5 sccm plasma gas flow rate, 182 mA plasma current, minimum insertion).

What is interesting from Figure 4.21 is that the distribution has shifted towards smaller NP diameters which follows what was expected from the use of the carrier gas as discussed above. As the carrier gas has been shown to be a necessary factor in the operation of Merlin, it means that the particles produced are generally smaller than they otherwise could be. If this dependence was somehow removed, then the particles produced by Merlin would be larger.

The effect of plasma power on the size distribution was found to be the same as that observed in Refs. [88] and [89]. Increasing the power only served to increase the amount of particles produced and did not affect the size. This was tested in Merlin with Cu NPs with the results shown in Figure 4.22. Higher plasma powers

can be applied for Cu NPs than shown in Figure 4.22 and are regularly used to get a larger deposition rate but the effect on the size distribution remains the same. The plasma power for different material targets also varies due to their sputter yield as stated previously. It was found with Merlin that typically the copper targets can produce NPs for plasma powers as low as 15 W whereas the iron targets require a much higher minimum power of 70 W.

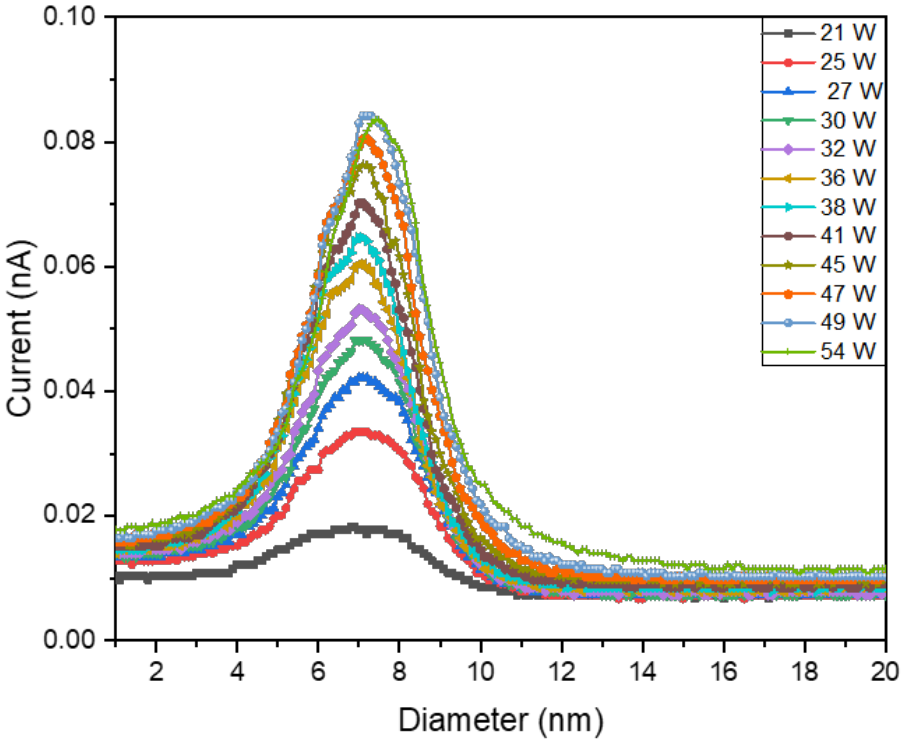

Figure 4.22: The effect of plasma power on the size distribution of Cu NPs in Merlin. Other source parameters were kept the same at 45 sccm plasma gas flow rate, 25 sccm carrier gas flow rate, and minimum insertion length.

Finally, the effect of changing the insertion length on the size distribution was investigated. This is shown in Figure 4.23 where the insertion length was varied from its minimum value of 140 mm, furthest away from the exit aperture of the aggregation chamber, to midway in the chamber. The maximum insertion length, i.e. the shortest distance between the exit aperture and the target, is 30 mm.

Changing the insertion length, as shown in Figure 4.23, drastically affects the particle size. The mean particle diameter changes from 6-7 nm to 3-4 nm proving that by

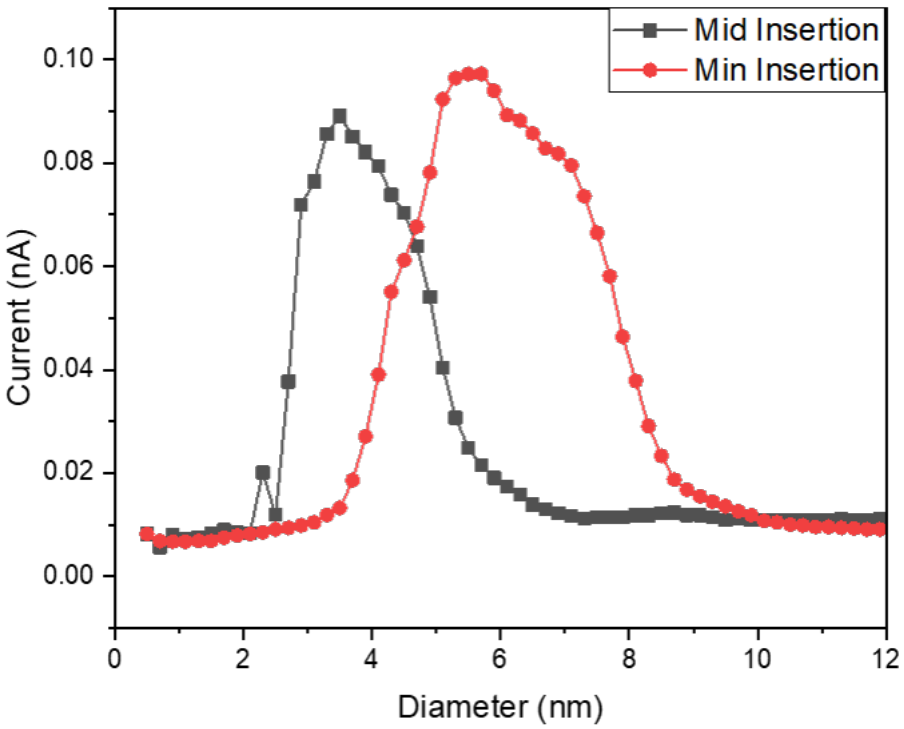

Figure 4.23: The effect of changing the insertion length from the minimum where the magnetron head is furthest away from the exit aperture of the aggregation chamber, to midway in the aggregation chamber (Cu NPs, 15 sccm plasma gas flow rate, 5 sccm carrier gas flow rate, 64 mA plasma current).

varying the aggregation time the mean particle size can be altered. It also follows what has been shown in the literature, i.e., that the source insertion length has the largest effect on the particle size.

The variation of these parameters and their effect on the size distribution was investigated before the aperture system on Merlin was developed. The particle distribution through the QMF was vastly different afterwards, as shown in Figure 4.24, where a much broader distribution is observed covering particles sizes not seen before. This increase in the size is due to these particles getting lensed on the central axis as discussed previously. It was found that the operational parameters that produced a particle distribution post aperture instalment could not be varied as any change would adversely affect the distribution and no particles would be seen.

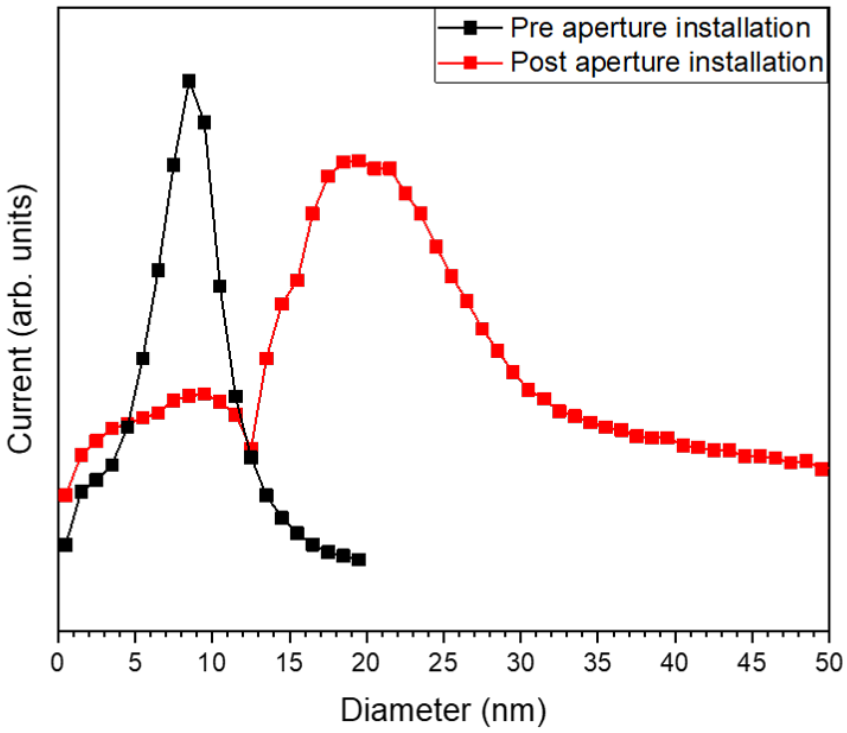

Figure 4.24: The effect on particle size distribution after the apertures were modified to improve the deposition rate. The black line shows a typical scan for the original arrangement (one aperture and the skimmer) and the red line shows the particle size distribution after the two 5 mm flat plate apertures were placed in the system.

It has already been established previously in this chapter that apertures lens different sized particles with varying degrees of success. So the particle distribution can be influenced by varying the aperture sizes that are present in the system. This could either be done by physically changing them each time the system is opened or by some adaptive aperture design. Particles of all sizes are being produced in the aggregation chamber and it is more a question of if they make it through the system which is dictated by the aperture arrangement and aerodynamic lensing. Passig et al. [134] showed that the mean size of the particles changes with the application of apertures compared to none. The authors deduce that the aggregation process of the particles is changing due to the fact that the aggregation occurs in their lensing system, so the particle size will change with the application of apertures. While not directly comparable to Merlin, it shows that clever aperture design can allow greater

control over the particle distribution.

The performance of the QMF was also tested so that once a distribution was established, samples were deposited with the filter off, on and scanning the entire region, and size selected for specific points. The deposited particles were then imaged using electron microscopy and size distributions taken. This allowed the performance of the mass filter to be estimated and the effect it might have on the deposited samples to be determined. This investigation is shown in Figure 4.25 and 4.26 which were obtained after Fe NPs were deposited on three separate TEM grids with the same source parameters and for the same amount of time. For each TEM grid, the QMF was either off (Figure 4.25(a)), on and scanning across the peak from 0.5-20 nm in 0.1 nm steps (Figure 4.25(b)), or on and size selected for the peak at 8.7±0.2 nm (Figure 4.26(a)).

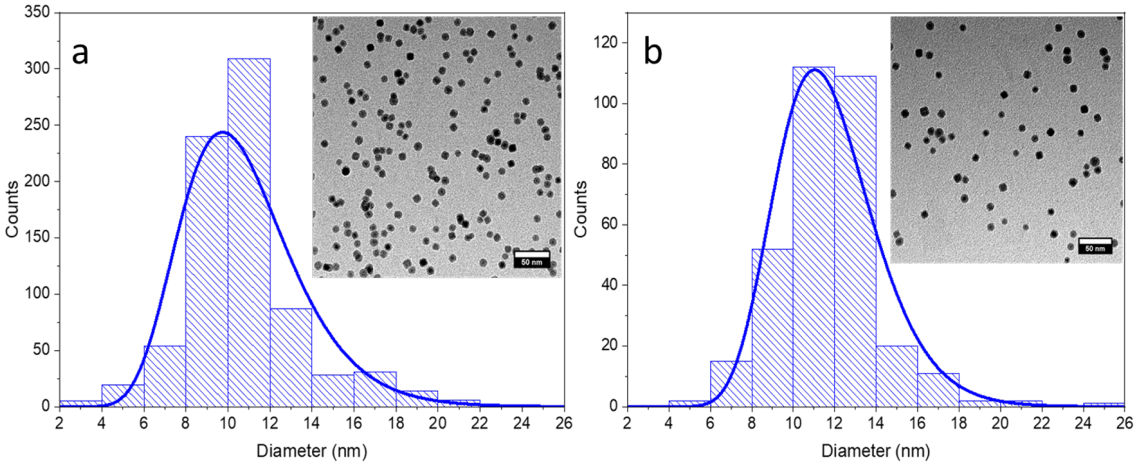

Figure 4.25: Effect of the QMF on the deposition of the particles. Fe NPs were deposited under the same conditions on separate grids for 2 minutes each. Each subfigure shows the measured particle histogram from TEM images using ImageJ software as well as a representative bright field image of the particles with scale bars equal to 50 nm. (a) is with the QMF off, (b) is with the QMF on and scanning a range of 0.5-20 nm in 0.1 nm steps. Source settings: 50 sccm plasma gas flow rate; 55 sccm carrier gas flow rate; 157 mA plasma current; 105 mm insertion length.

The peak position shifts from 9.7±0.3 to 11.0±0.2 nm when the QMF was turned on. This is probably due to less particles of the lower size making it through the filter when it is turned on. As can be seen by comparing Figure 4.25(a) and (b), there are

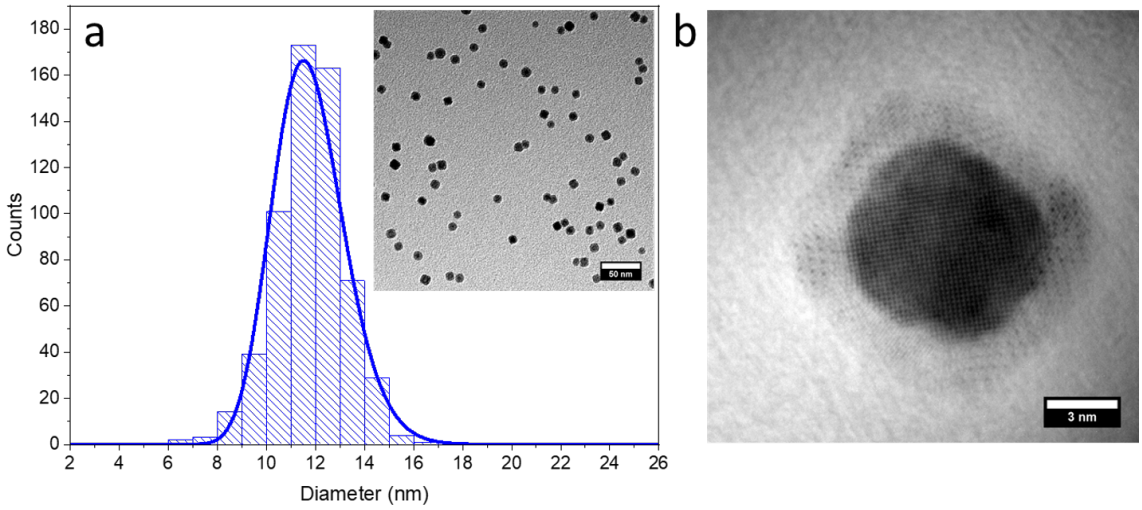

Figure 4.26: Effect of the QMF on the size distribution of Cu particles, deposited on TEM grids for 2 minutes. (a) Measured histogram from TEM images using ImageJ software and a representative bright field image of the particles with a scale bar equal to 50 nm. The QMF is size selected for a peak at 8.7±0.2 nm. (b) a HRTEM image of a particle from the grid shown in (a) revealing an oxide layer of around 1.5 nm. This explains the discrepancy between the size selected for and the particle size measured in (a). Source settings were the same as in Figure 4.25.

no particles of 2-4 nm in size and a significantly reduced population of 4-6 nm in size. This is also true of the larger particle sizes and in fact the FWHM of the log-normal peak in Figure 4.25(b) is 5.5±0.2 nm compared to that of Figure 4.25(a) at 6.0±0.3 nm. This shows that, as discussed previously, the filter acts as a combination of a low- and high-bandpass filter. The performance of the size selection is also shown in Figure 4.26(a) where the QMF was set to only allow a size of 8.7±0.2 nm to transit through. What can be seen is that the FWHM has been reduced from 5.5±0.2 nm to 3.4±0.1 nm showing that the application of size selection does limit the allowed range of sizes through the filter. The particle size that was selected for was 8.7±0.2 nm but the peak position in Figure 4.26(a) is 11.5±0.1 nm. This discrepancy can be explained by the fact that the particles were imaged and measured after an initial oxide layer had formed, as shown in Figure 4.26(b). An oxide layer of around 1.5 nm would then add 3 nm to the size of the particle which explains the discrepancy between the selected size and the observed size. Hence, this analysis shows that the QMF filters the particles to the correct size.

4.3.3 Maintaining and Cleaning the Cluster Source

After the source has completely sputtered a target, a new one needs to be installed to allow for growth of new samples. To do this, the pumps are switched off and the source slowly vented to atmosphere through the venting port shown in Figure 4.11. Once this is complete, the water cooling lines are shut off and detached from the back of the magnetron head as well as the gas input lines from the mass flow controllers. The flange on which the magnetron head is mounted is then fully removed from the chamber and the head is cleaned to remove the build up of material as now described.

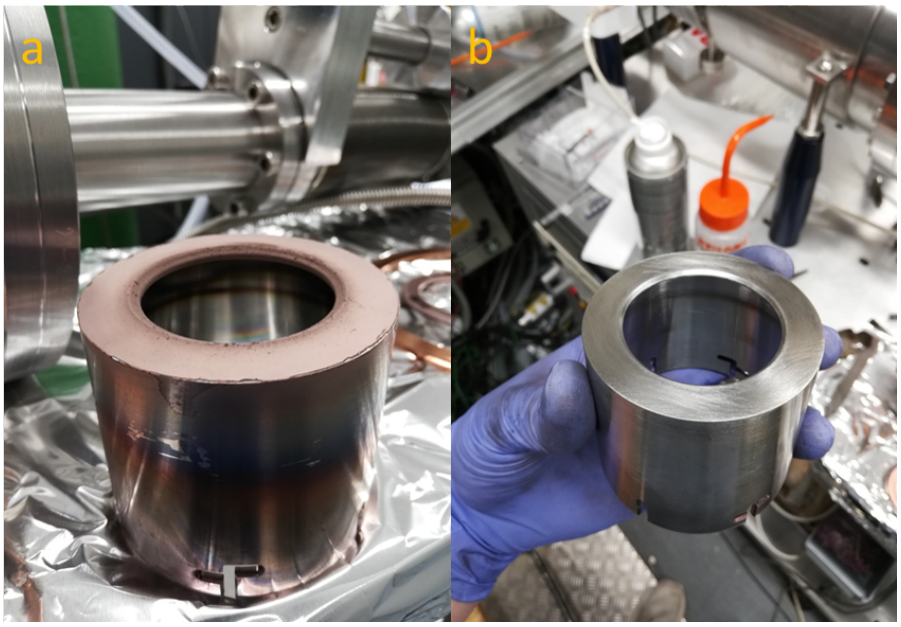

Figure 4.27: Before (a) and after (b) cleaning the anode cap where (a) shows a large amount of Cu deposit due to many particles being trapped in the first few millimetres from the head [131].

The anode cap, target holder ring, and screws are the main components that require cleaning and are first scrubbed with fine sandpaper to remove the sputtered layer. After this step, the components are washed in hot soapy water to remove any fine debris from the abrasive procedure. The components are then dried with a heat gun and placed in a glass beaker to undergo two separate sonicated bath treatments, the first in acetone and the second in ethanol both for 5 minutes. Between each stage, the components are dried with the heat gun. Once this process is complete,

the head components are ready to be re-assembled with a new target in place. The inside of the aggregation chamber is also cleaned with an ethanol wipe to remove any dust and debris that may have accumulated during the sputtering process and the removal of the head which can shake loose large fragments into the chamber. Figure 4.27 shows the anode cap just after it has been removed from the system (Figure 4.27(a)) and after it has been cleaned (Figure 4.27(b)).

If the new target is made of iron, then this is also exposed to the sonicator baths of acetone and ethanol along with the other components. This is because the iron targets were made in the mechanical workshop from a large iron sheet of 99.5 % purity and 0.5 mm thickness which was cut into 2" disks. These targets need to go through the same cleaning process as the other components to reduce contamination during the sputtering process.

The iron target is mounted on the magnetron head with a conductive carbon sheet placed behind it to improve thermal contact and help cool the target. The carbon sheet is cut using a scalpel to the same size and shape of the target. Once these are mounted, the target holder ring is put in place and screwed down. This is mainly to stop the target buckling when it gets too hot during the sputtering process. If it buckled and then made contact with the anode cap then the source would electrically short and it would not sustain a plasma. The anode cap is placed over the target and holder ring; a feeler gauge is used to ensure the gap between the bottom of the anode cap and the target is 0.5 mm. The distance between the two can also change the expected particle size distribution [91] with 0.5 mm being found to work best for the source at York. The magnetron head is then ready to be loaded back into the system and new samples grown.

While the source is at atmosphere, new samples can be loaded onto the sample carousel which sits in the deposition chamber, shown in Figure 4.11. The sample carousel can hold six samples on Omicron style sample plates. Typically, the samples are Si crystal wafers or TEM grids. Si is used in this deposition chamber as an easy way of producing samples to check with X-ray photoemission spectroscopy (XPS) or scanning electron microscopy (SEM). The deposition chamber on Merlin does not yet have the ability to clean the Si through DC heating, such as will be described

later, so these Si samples are not appropriate for a full analysis but were very useful for characterising the source while it was under development. Two types of TEM grids have been used during this project, copper grids with a holey carbon film and gold grids with an ultra-thin graphene layer. These grids, as with the Si, are differentiated in quality due to the nature of their use. The copper grids were used for the characterisation of Merlin as the source was developed and the higher quality gold grids used for more targeted studies on more capable microscopes such as the JEOL 2200 at the JEOL York Nanocentre and the microscope at SuperSTEM in Daresbury.

The design of the source, as shown in Figure 4.19, is such that it can be separated to gain easy access to the core-shell coater. Figure 4.12 does not show all the details as the electrical feedthroughs are actually in two stages with barrel connectors connecting the feedthrough to the crucible itself. A similar idea is used for the thermocouple with vacuum-friendly ceramic couples used such that the thermocouple wire can also be removed from the crucible with little effort. This allows for the crucible to be removed from the chamber with relative ease. The crucible must be replaced with each new shell material to stop cross contamination.

Once the head is mounted again and the source back under vacuum to an acceptable pressure (typically 3×10^{-7} mbar), the iron target then needs to go through a period of plasma cleaning. This is believed to be because the iron targets have slowly oxidised over time so have an insulating layer on them that needs to be removed. This oxide layer stops the plasma from striking properly on the target and sputtering does not take place until it has been removed. The plasma cleaning process is complete when the voltage reading on the power supply is below 300 V and remains constant with an increase in current or change in gas flow. To get to this point, the source is struck at a very low current (around 10 mA) with a gas flow rate of 30-50 sccm of Ar from the plasma gas channel. The voltage will slowly drop (if the source is working) from around 450-500 V down to around 300 V. The gas flow is then increased going up to around 60 sccm on the plasma gas channel and 30 sccm on the carrier gas channel. Once the source voltage has dropped low enough, the current is increased by around 10 - 15 mA typically leading to an increase in the voltage which needs to reduce before increasing the current again. This continues

until the current can be set at high values such as 200 mA and the gas flow set to around 30 sccm on the plasma gas channel without a large change in voltage with a reading below 300 V.

The plasma clean is necessary for two reasons. Firstly, it is supposed that sputtering does not occur without a stable voltage below 300 V. Secondly, without cleaning it is impossible to apply the higher currents necessary to achieve NP production. This is because if the source is operating normally, the power supply operates in current limiting mode and has a maximum voltage limit of 630 V. Before cleaning the iron target, the current cannot be increased above 10 - 15 mA without the supposed voltage between the anode cap and the target exceeding 630 V. This means that the plasma is not struck properly so the slow decrease of the voltage through the plasma clean allows for the source to be operated normally. Overall, the plasma clean usually takes around 20 hours over 2-3 days.

Before sputtering begins, the water cooling flow rate is also checked. The minimum required flow, as recommended by Mantis, to adequately cool the head is 2 l/min. It is important to have an adequate cooling rate so that the magnet does not get damaged during operation and thus demagnetise. The magnet is cooled by water flowing inside the bottom copper reservoir, shown in Figure 4.2, meaning that the water does not directly cool the magnet so it is still susceptible to overheating if the plasma power is too high. Indeed, on several occasions, the magnet was found to have demagnetised due to the poor cooling of the head which vastly affected its efficacy and lifetime. To understand this, the magnet strength profile was checked using an XY-translation stage and a Hall probe mounted on a stand, as shown in Figure 4.28. The Hall probe's height was changed to measure how the magnetic field varies with distance, Z, away from the magnet.

The setup shown in Figure 4.28 allowed for a map to be taken of the magnetic field against different distances from the head. The XY-translation stage was rastered in steps of 5 mm in each direction with the magnetic field strength measured at each point. 3D colour maps were then produced with the magnetic field strength plotted on the Z-axis. Figure 4.29 shows how the magnetic field strength has decreased after the magnet overheated due to poor cooling of the head. Figure 4.29(a) shows the

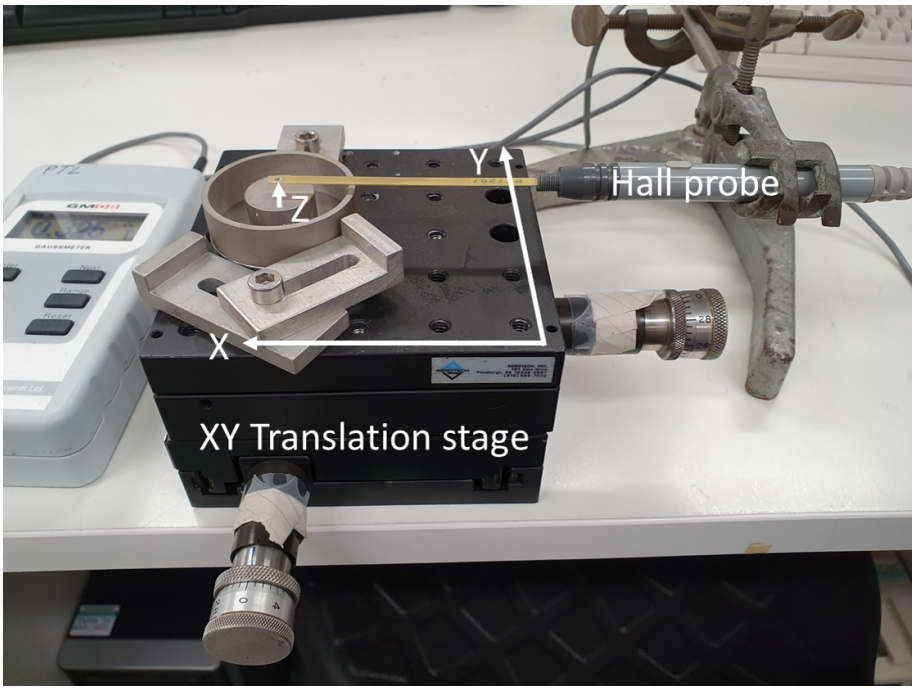

Figure 4.28: Setup to profile the magnets with the Hall probe set at a Z-height with the magnet rastered in the X and Y-axis underneath on the stage. This allows a method to check the magnet strength and any deterioration that may have occurred due to overheating.

profile of a magnet that had not been used and Figure 4.29(b) shows the profile of a magnet after overheating in the source. The central field strength has decreased from ∼350 mT to ∼230 mT. After this decrease in magnetisation, the source stopped stably producing NPs showing the importance of a strong central magnet.

The original central magnet was changed for a stronger alternative, shown in Figure 4.30(a) and (b) along with the measured magnetic field profiles, which made the growth of magnetic NPs easier as the targets blocked less of the field from the head. This then reduced the plasma clean time for Fe targets from 20 hours over 2-3 days to 3-4 hours in a morning with no obvious detriment to the sputtering or cluster production.

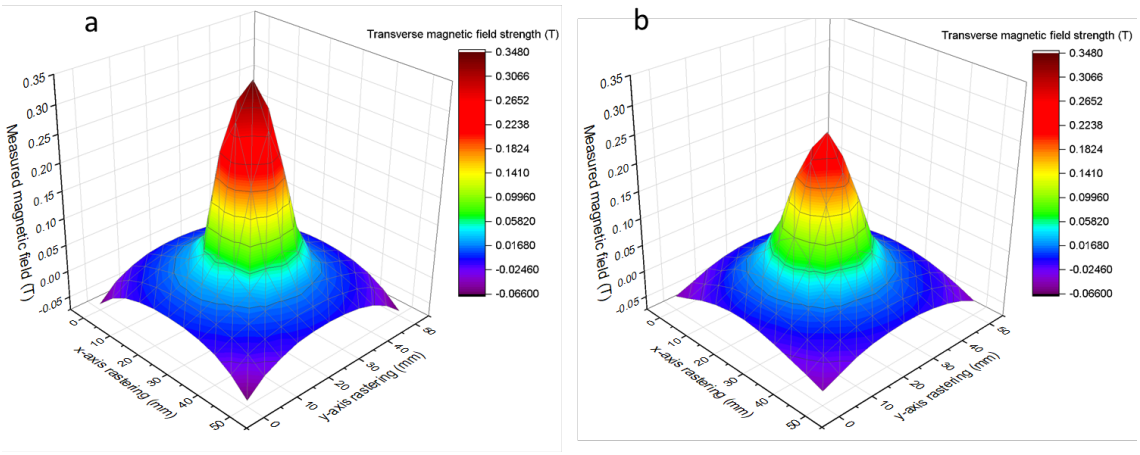

Figure 4.29: Measured magnet field strengths at a Z-height value of 0.25 cm. (a) is the profile of a new magnet that had not been used before with (b) a magnet that had overheated and partially demagnetised affecting the source's capability to produce NPs.

4.4 SLUMPS

The Small Leicester University Mesoscopic Particle System (SLUMPS) is another gas aggregation cluster source (GACS) that was utilised for the production of some samples during this project, as highlighted in the results sections where relevant. The operation of SLUMPS is similar to that of Merlin used here at York. A schematic diagram of the source is shown in Figure 4.31.

The design of SLUMPS is different to Merlin in a few key ways. As well as the aggregation chamber not being bullet shaped, there are only two flat plate apertures between the sputter head and the rest of the source. The expansion zone between the apertures is also actively pumped during operation which is similar to a Haberland [77] type source compared to Merlin which is more of a Liu [99] type source. The deposition chamber on SLUMPS also has capabilities for particles to be deposited into liquids which is currently not available with Merlin. A more complete description of SLUMPS can be found in the following references [135] [110].

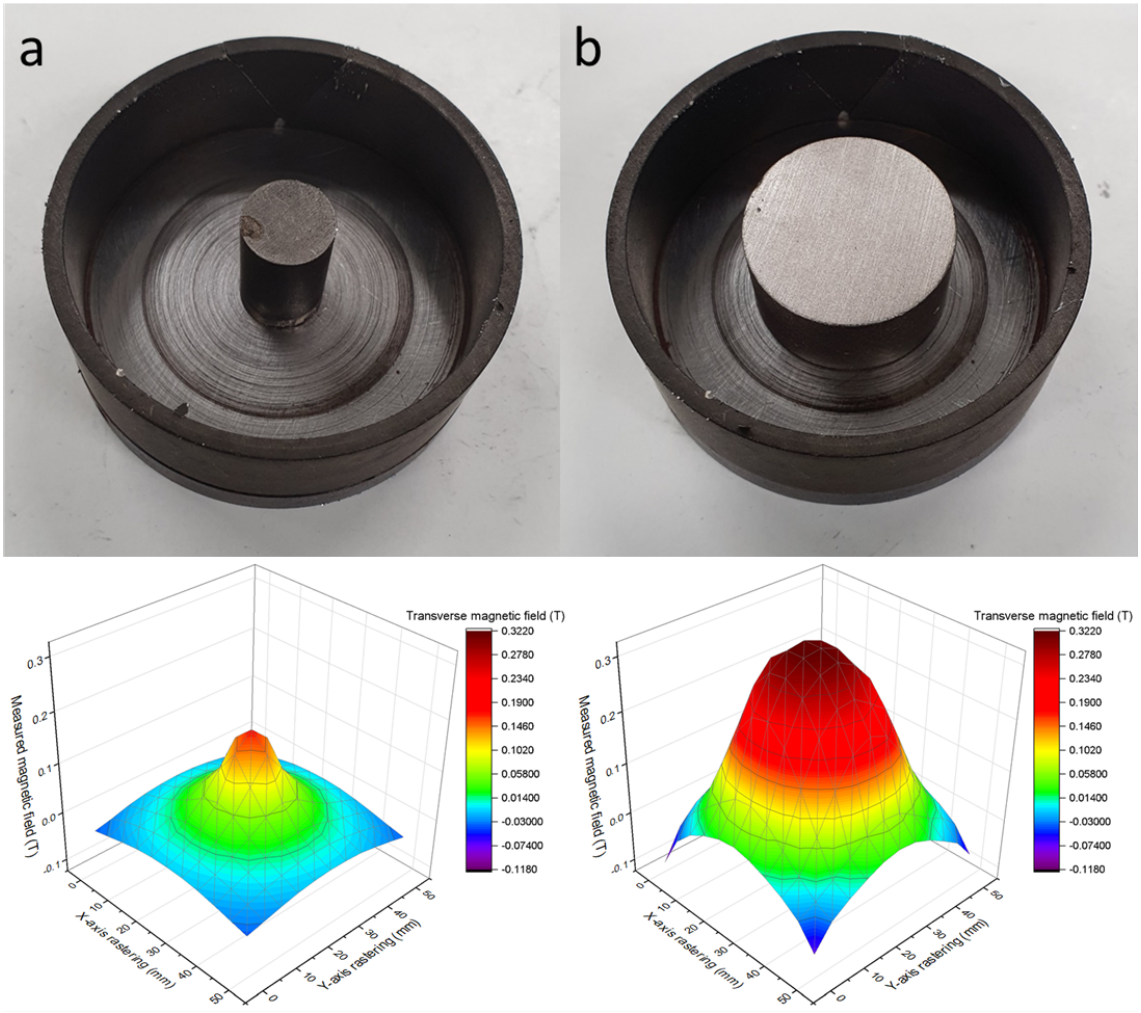

Figure 4.30: (a) Original magnet setup with a smaller, weaker central magnet that was replaced with (b) a stronger central magnet. The associated measured magnet field profiles taken at a Z-height of 0.5 cm are also shown. The change to a stronger magnet reduced the Fe target plasma clean time from 20 hours over 2-3 days to around 3-4 hours.

4.5 Summary

This chapter has described in detail the development and characterisation of a gas aggregation cluster source here at York. An outline has also been given of the various physics involved in source operation, from cluster growth and aggregation to the aerodynamic lensing to form a beam. These theories were put into practice to extend and enhance the capabilities of the commercially acquired source. With the stable production of particles then achieved, the reactivity and oxidation of metal nanoparticles could be investigated as outlined in the following chapters.

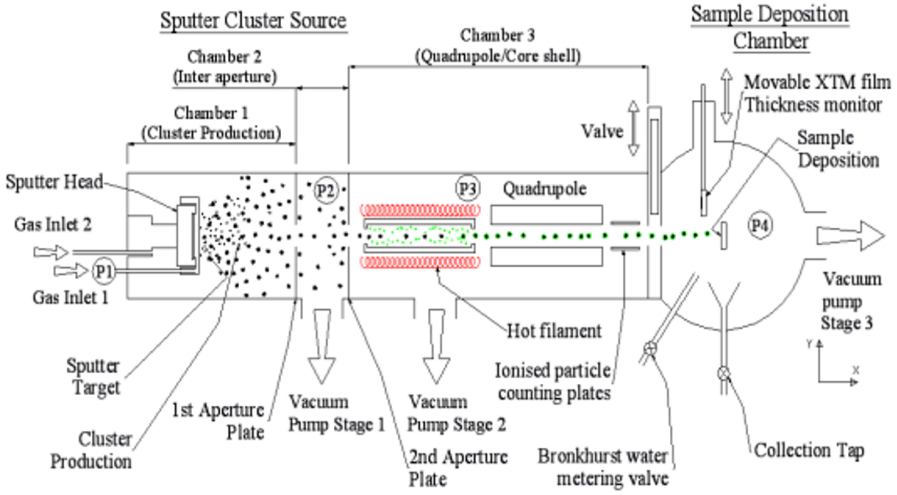

Figure 4.31: Diagram of SLUMPS, the Leicester university particle source, which is based on the Haberland design [77] with more details in the text. Reproduced from [135].

Chapter 5

Dynamic Observation of the Nano-Kirkendall Effect using e-TEM

The long-term stability of metal NPs in environmental conditions is of import to a wide range of applications. As discussed in Chapter 2, oxidation at the nanoscale is far different to that of the bulk and so this study aims to understand the various phenomena at play as a particle oxidises to give a more complete description of the oxidation process. For example, the growth and development of voids at an interface between a diffusion couple, i.e. the Kirkendall effect, was already discussed in Chapter 2.3. This process can occur in NPs where the out-diffusion of the core is faster compared to the inward diffusion of the other product (typically oxygen to form oxide but this process has also been shown to occur with selenium [54]). This leads to the vacancies coalescing in the core to form hollow NPs in a process known as the nano-Kirkendall effect (NKE).

The NKE has received much attention in recent years due to the variety of applications of hollow NPs such as acting as nano reaction chambers, in catalysis, and drug delivery [136, 137]. However, the exact void growth mechanism is not known with various models described in Chapter 2.3 [52, 58, 138]. This, in part, is due to a lack of continuous real time observation methods. Using the capabilities of the environmental transmission electron microscope (e-TEM) at the JEOL York Nanocentre,

real time imaging of the NKE process for Fe NPs was possible for the first time. A range of temperatures and beam dosages were explored to investigate their effects on the oxidation process. The diffusion coefficient of iron in iron oxide was also determined following these results.

5.1 Experimental Details

Cubic and spherical Fe NPs were grown several years ago using SLUMPS and so the exact production details are unknown but it is likely that they are similar to the values quoted in Ref. [139]. The NPs produced in Ref. [139] are believed to be the same particles used in this study when SLUMPS was temporarily transported to York. The values quoted are an Ar pressure of 0.1 mbar in the aggregation zone and a plasma power of 35 W with the grids most likely amorphous holey carbon films on Cu grids. These samples had been left in a dessicator for some years but initial analysis on the JEOL York 2200 showed limited oxidation or degradation and so they were considered good candidates for study while the development of Merlin was ongoing.

After being loaded in the JEOL 2200, several samples were exposed at varying temperatures and electron beam dosages so that the effects of both on the oxidation reaction could be explored. The temperatures used were room temperature (RT), 382 K, and 480 K and either at a "low beam dosage" (LBD) of 23 pA/cm^2 or a "high beam dosage" (HBD) of 45 pA/cm^2. All the particles were under a constant pressure of 0.1 mbar of oxygen during imaging. During the experiment, the particles were either imaged under the "fast" condition so that stop motion films were acquired with an average of 0.7 seconds per frame or the "slow" condition where higher resolution images were taken which is more akin to conventional TEM imaging. Switching between the two imaging conditions results in gaps in the graphs between each image set shown below as the imaging software is reset for each new image set. The HBD roughly equates to 3.15 $\times 10^4$ e/nm^2 per frame and with each movie, on average, containing 1600 frames, this gives a total beam dosage of 5 $\times 10^7$ e/nm^2 for the HBD condition. LBD is about half of the HBD at around 2.5 $\times 10^7$ e/nm^2.

A summary of the particles studied under the different conditions is shown below in Table 5.1.

Sample	Temperature (K)	Beam dose
A7c	RT	HBD
A7a	382	HBD
A7b	382	LBD
A8	480	HBD
A10	480	HBD
A6	480	LBD

Table 5.1: Table showing a summary of samples and their imaging conditions where LBD and HBD refer to low and high beam dosage respectively.

Particles A8 and A10 were imaged with the same conditions to allow a comparison of size to be made. A8 had an average starting diameter of ∼24 nm whereas A10 had an average starting diameter of ∼30 nm. The particles were imaged on an e-TEM operating at 200 kV (JEOL 2200FS double aberration-corrected) with an in-house modified environmental gas open cell [73]. Samples were loaded on a single tilt heating holder (Gatan, model 628.IN) and sample temperature was monitored using a thermocouple (Digitron Instrumentation Ltd, Model 2029T). The temperature was controlled using a Keithley 2614B source meter which was manually changed to give the desired sample temperature. The oxygen gas inlet pressure was set at 0.1 mbar. Individual particles were imaged for different times, from 1100 s for A7a to 2000 s for A6. This time-frame was dependent on the integrity of the carbon supporting film which slowly degraded under the electron beam exposure. This is why A8 was imaged for a shorter period of time as the carbon film collapsed and the particle was no longer stationary.

The images were processed using the ImageJ software. Oxide shell thickness measurements were obtained by taking an average of each side of the square (observed in projection) to get an overall oxide shell thickness. The various projected areas (such as total particle, core, and void projected area) were measured by creating a selection of the relevant structure and applying a spline to smooth out the selection. A mask was then created of the selection such that a binary image was produced of

the selected particle area. Finally, the "Analyze Particle" function in ImageJ was run to obtain the masked area in nm^2. The reason it results in a projected area is because it is a three dimensional object that is projected onto a two dimensional image.

5.2 Results

5.2.1 Structure and Details of Cubic Fe Nanoparticles

The particles that were selected to be imaged were cubic in shape and roughly 20-30 nm in size. The cubic shape was chosen so that the effect of the grain boundaries (GBs), as described in Chapter 2.1, on the oxidation process was clear. This is because the cubic Fe NPs have clearly defined GBs at the corners between the oxide domains, shown in Figure 5.1. The oxide domains form on each face of the cube with a 90° bend to the next face, shown in Figure 5.1(b). This then creates a high-angle GB between each oxide domain which can be easily seen in the images. In comparison, spherical particles will contain many oxide domains across the surface and so quantifying the effect of the GBs on the oxidation will be more difficult.

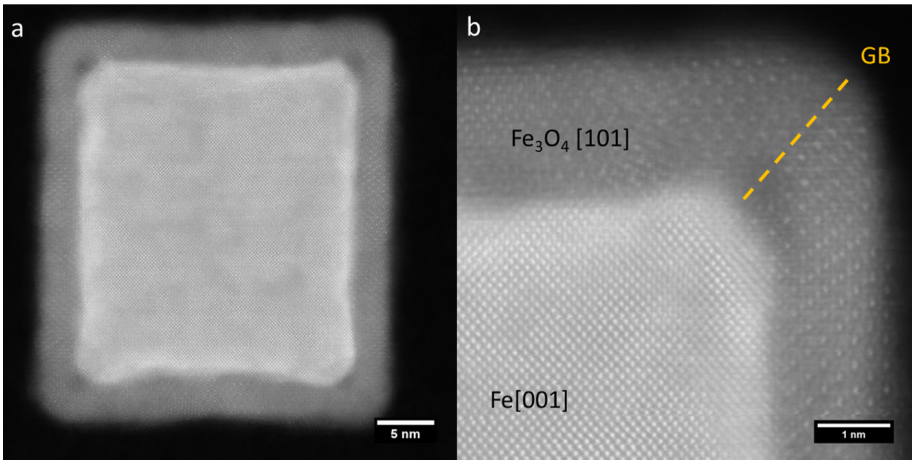

Figure 5.1: Cubic Fe NP imaged at SuperSTEM (by Dr. Demie Kepaptsoglou) where the central Fe core is surrounded by the oxide shell. (a) shows an overview image of the particle with (b) a magnified image at the corner showing the GB between the two oxide domains.

The size of the particles was chosen so that the oxidation reaction would not happen

so quickly that it would not be able to be imaged. Very small particles oxidise very quickly and can form fully oxidised particles in a matter of minutes. As these particles had been produced some time ago, the larger particles were the only ones with a defined core-shell arrangement, thus allowing for a thorough study of the continued oxidation as the particles were exposed to the electron beam. The initial oxide (0-3 nm) forms very quickly and so it is was not possible to study this with the current setup.

5.2.2 The Effect of Temperature

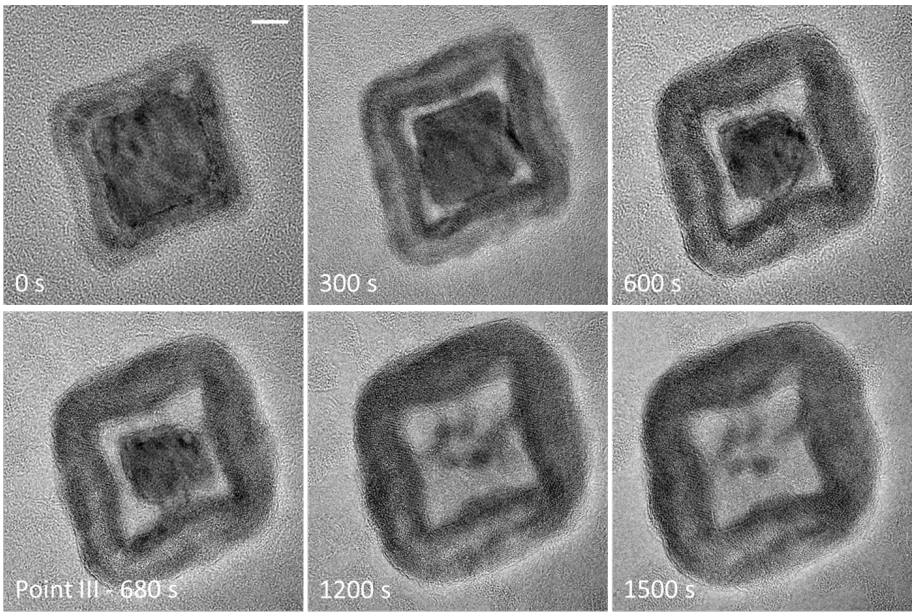

Figure 5.2: TEM images showing the oxidation of A8 under high temperature (480 K) and high beam dose conditions (45 pA/cm^2). The core can be seen to completely deplete after 1118 s with the particle also growing considerably. The scale bar is set to 5 nm and is applicable for each image. Point III is explained in the text and describes a change in the oxidation kinetics.

Figures 5.2-5.6 show selected images of each of the particles at different stages after the onset of oxidation highlighting some of the differences between them. It can be seen when comparing the higher temperatures of A8 and A6 (Figures 5.2 and 5.4) to the lower temperatures in A7 (Figures 5.5 and 5.6) that temperature is the dominant effect. This is due to the fact that A8 and A6 clearly show a much more developed oxidation as compared to the A7 series. It is even clearer when comparing A8 to RT

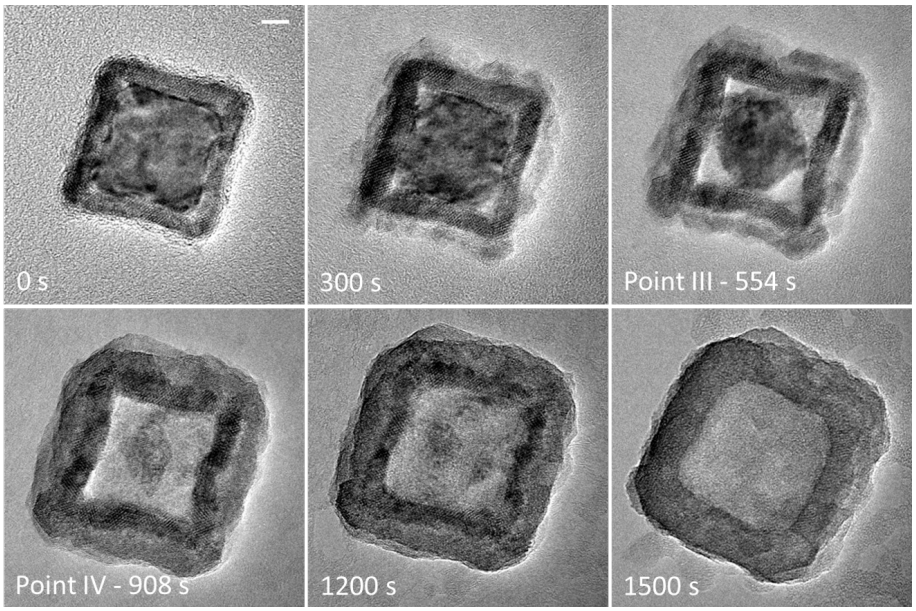

Figure 5.3: TEM images showing the oxidation of A10 under high temperature (480 K) and high beam dose conditions (45 pA/cm^2). The core can be seen to completely deplete after 900 s with the particle then continuing to grow due to beam dose effects which are explained in the text. Points III and IV are explained in the text and describe a change in the oxidation kinetics. The scale bar in the 0 s image is 5 nm and applies to all the images.

as the particle at RT does not oxidise at all whereas A8 shows significant depletion of the Fe core. This is evidenced further in the lack of total particle growth shown in the particle projected area graph in Figure 5.6. This is the measure of the total particle area against the imaging time (i.e. exposure/reaction time). The time $t = 0$ is defined as from when the particles were exposed to the beam and imaging for the movies had begun.

This temperature effect is also shown in the projected area graphs for A8, A6, and A7a and b, shown in Figures 5.7 and 5.8. Here it can be seen that A8 increases from 600±16 to 950±25 nm^2 (58±2 % increase) compared to A7a and b which increase from 600±19 to 740±24 nm^2 and 640±13 to 740±15 nm^2 respectively (A7a increases by 24±1 %).

The temperature effect on the oxidation is non-trivial with a few processes all contributing. First of all, as mentioned in Chapter 2.1 (Figure 2.3), for an atom to diffuse through the lattice it must overcome a potential barrier which can be defined

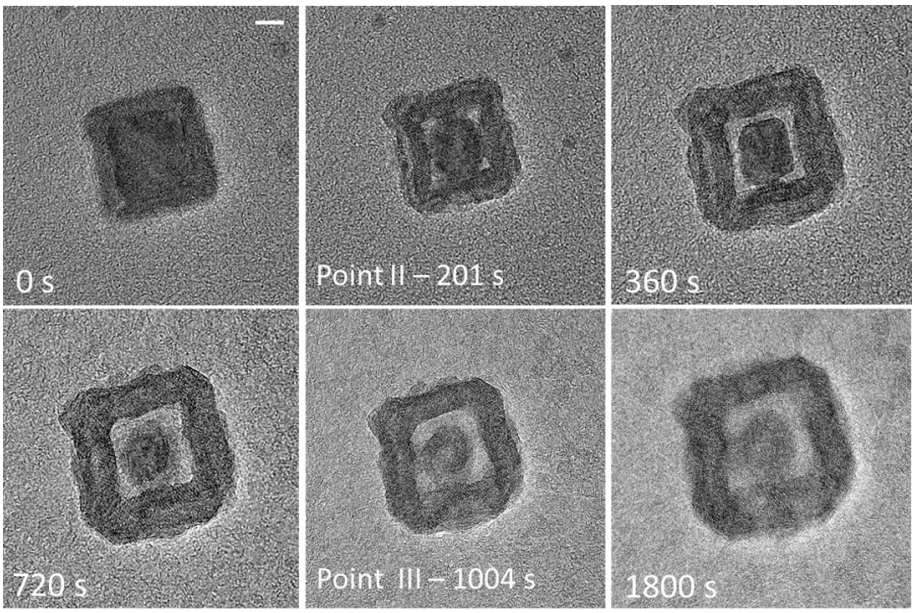

Figure 5.4: TEM images showing the oxidation of A6 under high temperature (480 K) and low beam dose conditions (23 pA/cm^2). The core can be seen to completely deplete after 1800 s with the particle also growing considerably. The scale bar is set to 5 nm and is applicable for each image. Points II and III are explained in the text and describe a change in the oxidation kinetics.

like a "gate" subject to the nearest neighbours of the moving atom. The probability of this movement can be defined by

$$P = A\exp(\frac{-Q}{k_B T}) \tag{5.1}$$

where P is the probability, A is a normalisation factor, Q is the energy barrier, k_B is Boltzmann's constant, and T is the temperature. The increase in temperature will give the atoms more thermal energy and they will thus be able to overcome the potential barrier to the movement more easily. This explains why the diffusivity, D, has an exponential dependence on temperature expressed as

$$D \propto \exp(-\frac{1}{T}) \tag{5.2}$$

For the particles studied here, this means that the Fe cations in the core will diffuse more quickly at the elevated temperature as they have more thermal energy and thus can more easily overcome the potential barrier to their movement.

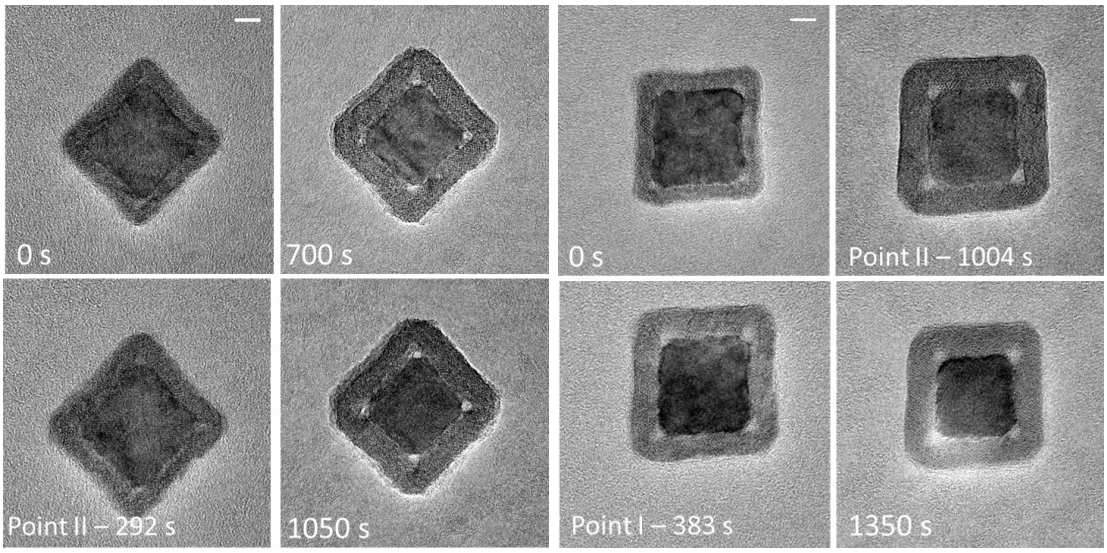

(a) A7a TEM images (b) A7b TEM images

Figure 5.5: TEM images showing the oxidation of A7a and A7b (low temperature (382 K) and high (45 pA/cm^2) and low (23 pA/cm^2) beam dose respectively) where the core is much more intact and less void growth is observed in comparison to A8 and A6 (Figures 5.2 and 5.4). The scale bar is set to 5 nm and is applicable for each image. Points I and II are explained in the text.

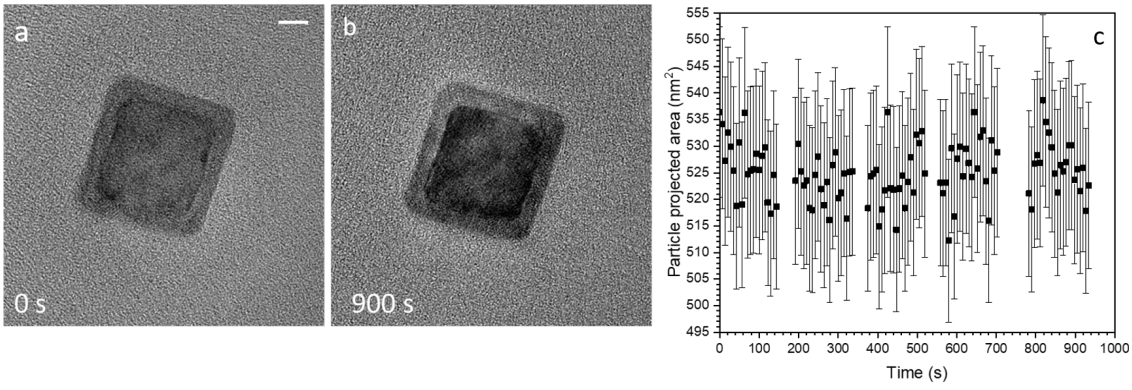

Figure 5.6: TEM images showing the oxidation of A7c (room temperature (296 K), high beam dose (45 pA/cm^2) (a) at the beginning of oxygen exposure and (b) after 900 s of exposure. Little to no oxidation can be seen which results in no real growth in the total particle projected area shown in (c). The scale bar is set to 5 nm and is applicable for both (a) and (b).

The increased temperature will also help provide an electron current to aid in the continuing oxidation reaction. As stated in Chapter 2.2.1, the work of Fromhold and Cook [36–40] showed how the continued growth of oxide films past 3 nm in thickness

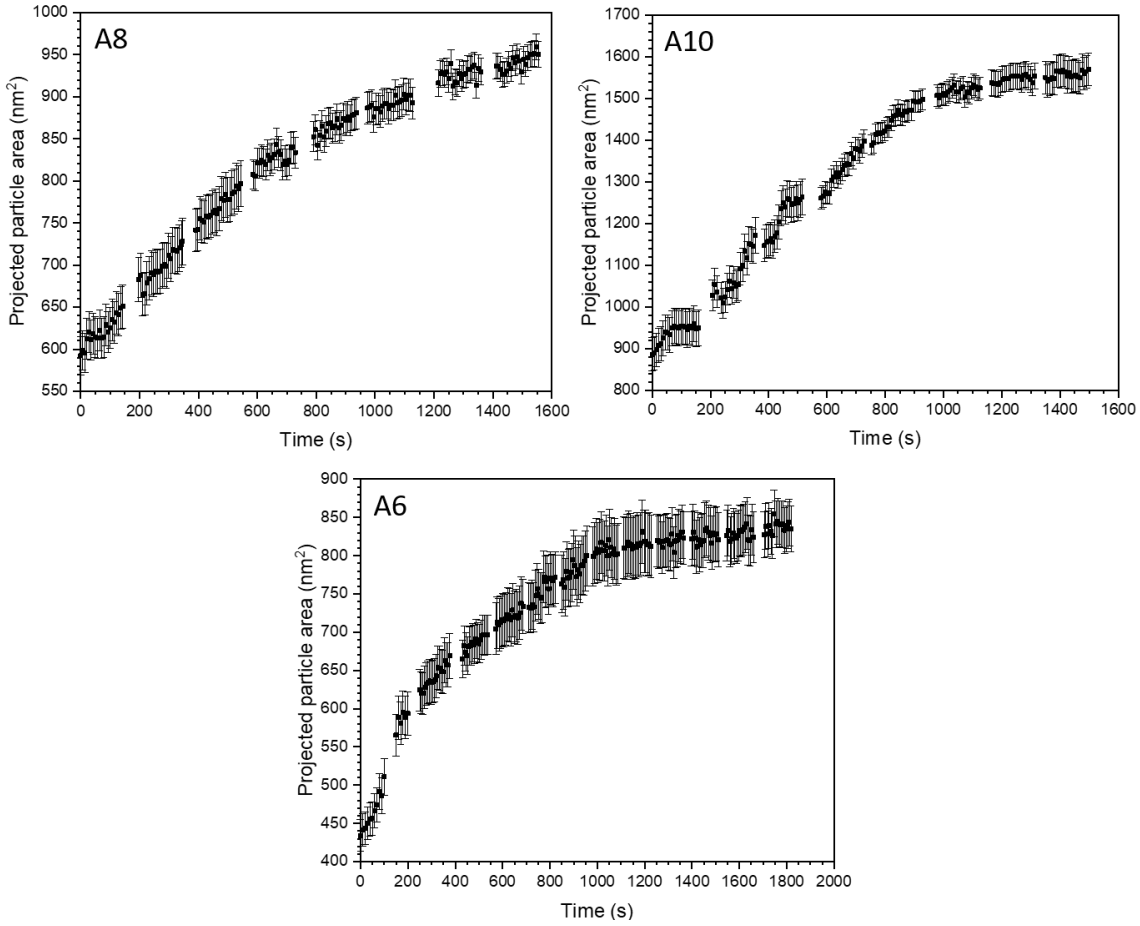

Figure 5.7: Total particle projected area versus time for A8, A10, and A6. These graphs show substantial growth of the particles over time.

depended on a sustained electron current arising from thermionic emission. Electron tunnelling is dominant up to 3 nm where the potential barrier then becomes too great and the thermionic emission current becomes dominant. This electron current maintains the electric field in the oxide that helps draw the metal cations out to react with the adsorbed oxygen anions. The increased temperature will allow for a higher thermionic emission current to be achieved. This can then be seen as a potential rate limit to the oxidation rate between the two temperatures. These two processes, more thermal energy resulting in faster cations and thermionic emission, can explain why the higher temperature particles have oxidised more compared to the lower temperature particles.

Not only is this temperature dependence visibly evident in the differences between A8 and A6 compared to the A7 series, it is also quantifiable. By measuring the mean growth rate of the oxide shell, the differences in oxidation rates can be determined.

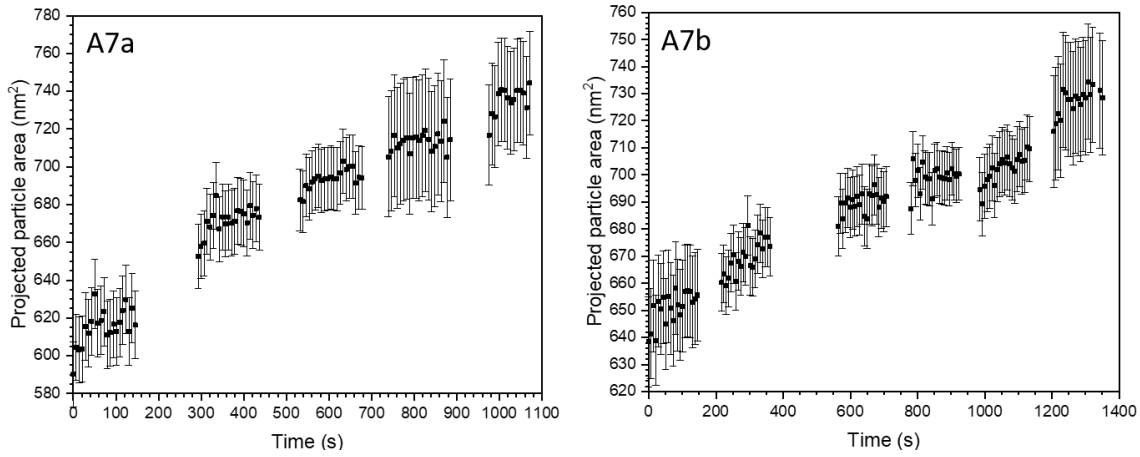

Figure 5.8: Total particle projected area versus time for A7a and A7b. These graphs show limited increase in particle size during the exposure.

As shown in Figure 5.9, measurements of the change in thickness of the outside edge of the oxide shell (ΔO_{outer}) versus the change in thickness of the inside edge of the oxide shell (ΔO_{inner}) can be used to determine in which direction the oxide front is developing.

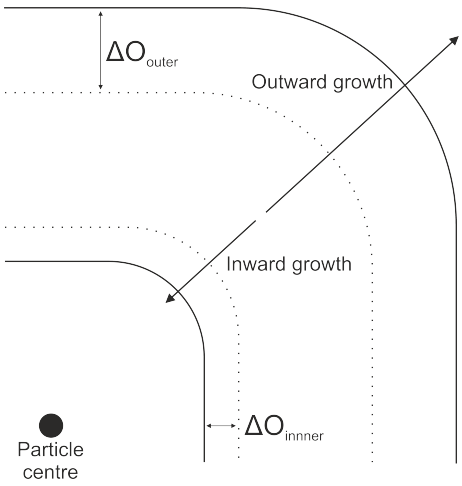

Figure 5.9: Diagram of how the mean growth rate of the oxide shell was determined by measuring the difference between the overall outward growth (ΔO_{outer}) and the overall inward growth of the oxide shell (ΔO_{inner}). Dashed lines are the initial oxide shell with the solid lines showing the final oxide shell.

The oxide shell in A7a has a mean growth of 0.60±0.04 nm compared to A8 which has a mean growth of 2.8±0.2 nm. The oxide shells of both show a total growth of 2.5±0.1 nm for A7a and 4.5±0.1 nm for A8 (shown in Figure 5.10). This starkly shows the effect of temperature as the oxide shell in A8 has grown substantially

more compared to A7a. The discrepancy between the two values (mean growth versus total growth) is due to the fact that the oxide shell is also growing inwards at a substantial rate. When the values of ΔO_{outer} and ΔO_{inner} are added then they equal the total growth shown in Figure 5.10.

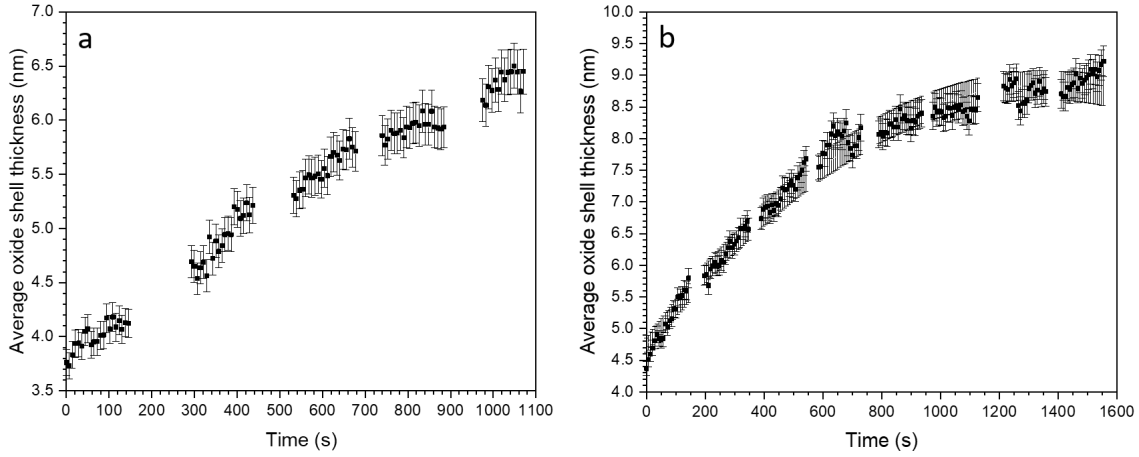

Figure 5.10: Average oxide shell thickness against time of (a) A7a and (b) A8.

The inward growth of the oxide shell in both cases can also be seen in the depletion of the core+void projected areas for A7a and A8 shown in Figure 5.11(a) and (b) respectively. The projected areas show a clear decrease as the oxidation progresses with A7a shrinking by ∼23±1% and A8 by ∼19±1%. This inward growth can be described by the fact that the oxygen anions can diffuse interstitially more easily compared to the Fe cations [140]. This means the movement is not blocked by waiting for a vacancy to appear as a nearest neighbour and so the oxygen can diffuse inwards through the oxide shell and react at the core/shell interface. As the Fe cations in A7a will have less thermal energy and therefore are moving slower, this leads to a more balanced growth between outwards and inwards which leads to the mean growth rate of 0.60±0.04 nm.

The development of voids still occurs as the Fe cations preferentially diffuse through vacancy exchange and so there is a net flux of vacancies back towards the core. This point explains why A7b has clear void formation and yet a mean oxide shell growth of -0.30±0.01 nm. This difference highlights how the final void size can be tuned due to differences in diffusion/reaction rates of the oxygen and metal ions. This was shown by Ibáñez et al. [59] where they produced different hollow Cd particles by reacting them with different reactants. For example, reacting the Cd particles with molecular

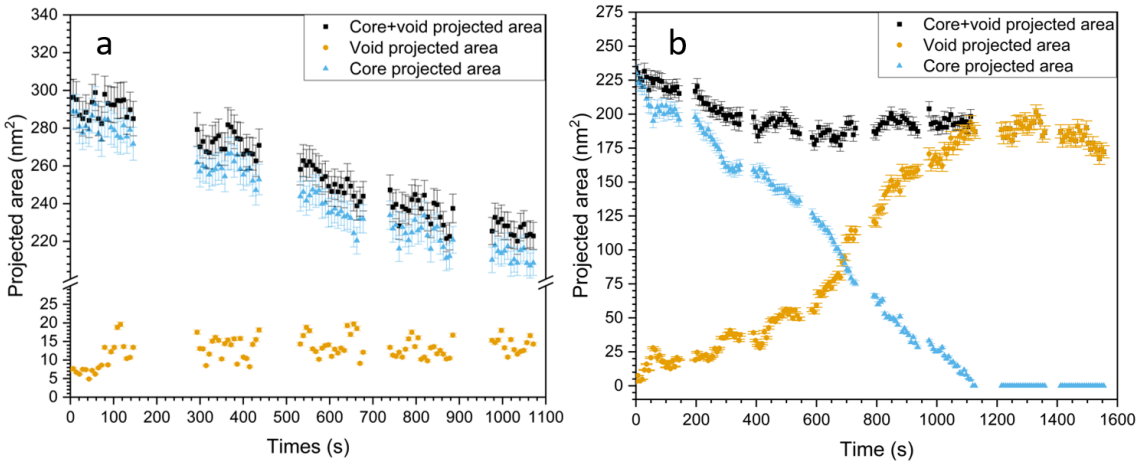

Figure 5.11: Core and void projected areas versus time for (a) A7a and (b) A8. Both figures show the decrease of the core+void projected area indicating that the oxide shell has some inward growth.

sulfur in dichlorobenzene (DCB:S) produced a very thick product shell with a small central void. However, a larger central void was synthesised through reacting the Cd with Te in TOP complexes. This can be explained by the relative self-diffusivities of each reactant which can be described more generally as the Pilling-Bedworth ratio which is a dimensionless coefficient. This ratio describes the expansion of the metal core upon reacting to form a secondary product such as oxidation or, in the case of Ibáñez et al., sulfidation. Susman et al. [141] showed through simulations how the final void structure could be tuned by varying the Pilling-Bedworth ratio. For example, as it tends towards 0 the conventional NKE occurs where the size of the void is the same as the initial core volume with the inverse being true as it tends to 1. This is due to the different reactivities and diffusivities of the different moving species in the reaction.

In the particles presented here, the moving species leading to the void structure are the Fe and O ions so it is likely that the final product of A7b would be a thicker oxide shell with a small void as compared to A8 which would have a much thinner oxide shell and larger void. As explained previously, the experimental conditions of each particle will therefore impact the relative diffusivities of the ions.

It has to be noted though, that A6 shows an all together different set of results with the total core+void projected area initially decreasing rapidly before then increasing

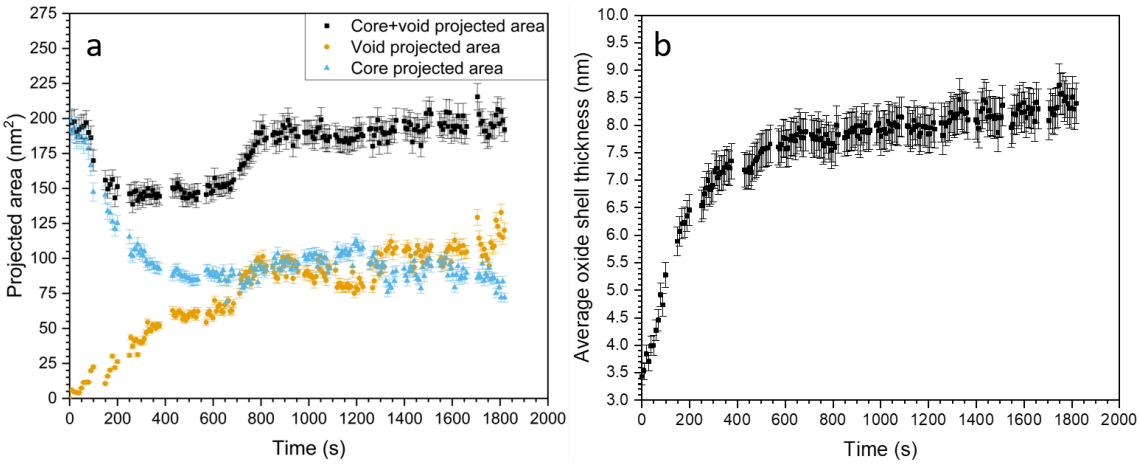

Figure 5.12: Core and void projected areas against time (a) and average oxide shell thickness against time (b) for A6.

again, shown in Figure 5.12(a). The oxide shell thickness also rapidly increases and then levels out, shown in Figure 5.12(b).

This could be due to the fact that the initial oxidation occurs through rapid inwards growth of the oxide as the inward transport of oxygen anions is dominant [140]. The outward diffusion of the Fe cations then increases as the oxide grows in thickness. The initial oxide shell thickness of A6 is $\sim 3.5\pm0.2$ nm compared to A8 that has an initial oxide shell thickness of $\sim 4.5\pm0.1$ nm. The rapid decrease of the core+void projected area shown in Figure 5.12 roughly correlates with the increase in average oxide shell thickness from 3.5 to 4.5 nm. Therefore, this behaviour could be described by the final stages of the initial oxide formation with the preferential inward diffusion of the oxygen anions followed by the Fe cation diffusion first equalling and then surpassing it as the oxygen vacancy concentration increased.

5.2.3 The Effect of Beam Dosage

While the temperature is the dominant driver in the diffusion reaction, the beam damage/dosage does have an effect on the oxidation. High energy electrons that form the electron beam and thus the image in the TEM cause what is known as beam damage by their interaction with the substrate. Different beam damage mechanisms have been proposed such as sample heating [142], ionisation of the sample/surrounding oxygen atmosphere [143], and knock-on beam damage. The work of Wang et al. [144]

showed that the most likely beam damage effect causing increased oxidation in a TEM is that of knock-on beam damage.

Knock-on beam damage occurs due to collisions of the electrons in the electron beam with atoms in the sample. The energy transfer to the atoms from this collision can be calculated via the elastic collision model [145]

$$E_{max} = (\frac{4M_iM_a}{(M_i + M_a)^2})E_0 \tag{5.3}$$

where E_{max} is the maximum energy transfer, M_i the mass of the incident ion, M_a the mass of the target atom in the material, and E_0 is the energy of the incident ion. So for a 200 keV electron, the maximum energy transfers to Fe and O atoms are 7.78 and 32.8 eV respectively. Reference values for the threshold displacement energies for Fe and O in the literature have only been found for α-Fe_2O_3 with values of 55.0 and 20.3 eV for Fe and O respectively [146]. For Fe this means that the maximum energy that an electron will transfer to an Fe atom in α-Fe_2O_3 is much less than the threshold displacement energy and therefore will not be removed from the lattice. On the other hand, the reverse is true for the O atoms in the structure which may receive enough energy to be displaced. This means that the beam is creating another source of vacancies inside the oxide shell which will help drive the diffusion process along. While these values are only applicable to α-Fe_2O_3, it is likely the values for the other Fe oxides will be similar and also for the NPs.

This extra source of vacancies at HBD clearly expedites the oxidation reaction as can be seen when comparing A8 and A6, in Figures 5.2 and 5.4. A6 is exposed to the beam for an extra 300 seconds (as compared to A8) and still does not exhibit a fully depleted core. The electron beam also causes an interesting effect in A10 where the core is fully replaced with vacancies and growth similar to A8 is observed up to this point. After the core has fully depleted the core+void projected area keeps increasing with the average oxide shell thickness then starting to decrease, as shown in Figure 5.13. This is most likely due to the continued creation of oxygen vacancies in the oxide lattice which then releases previously bonded Fe cations in the oxide shell. These Fe cations can then diffuse through the shell and react with new oxygen anions that have adsorbed to the particle surface. The vacancies created from the

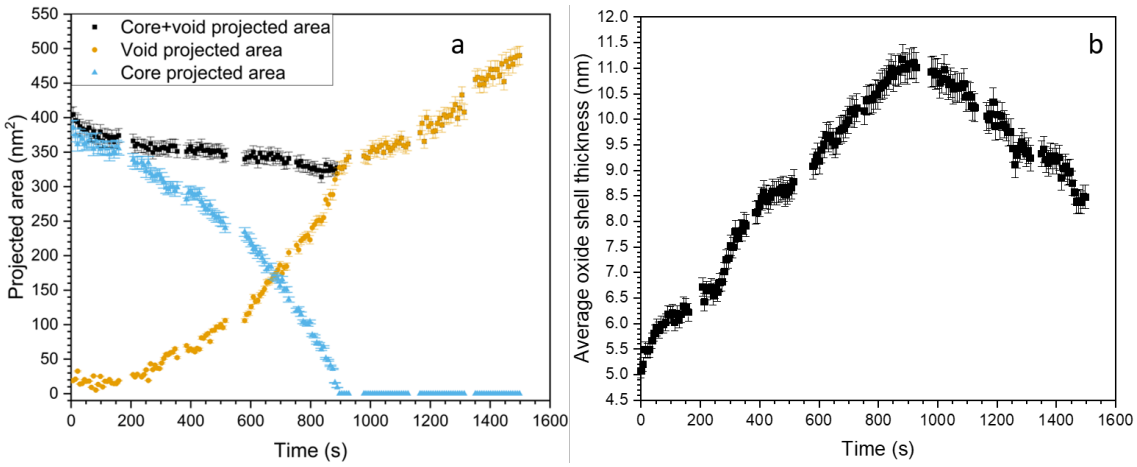

Figure 5.13: Core and void projected areas (a) and average oxide shell thickness (b) for particle A10. The oxide shell thickness starts to decrease after 950 s which is due to the continual creation of the vacancies in the oxide shell by the electron beam after the full depletion of the Fe core. This continued vacancy creation then allows the continued out diffusion of Fe cations in the oxide shell.

beam then move into the core where the central void increases in size.

While temperature has been shown to be the dominant effect in the oxidation reaction, beam damage is also important with a more nuanced interaction with the sample. This means that in future experiments the effect of the electron beam on the oxidation reaction should not be ignored.

5.2.4 Transition Points in the Oxidation Reaction

Figures 5.14 and 5.15 show transition points labelled I, II, III, and IV which coincide with the trend in the data changing gradient which points to changes in the oxidation kinetics. The red lines are fitted using the Origin graphing software with a linear fit used.

The first transition point, Point I, appears to occur in A7b where there may be a change in slope that seems to coincide with a change from inward-dominated oxidation. This can be seen in Figure 5.16 where the core and core+void projected areas both decrease without considerable void growth. The average oxide shell thickness, shown in Figure 5.17, also increases showing that the oxidation reaction is progressing. Measuring the change in the mean oxide shell thickness (such as

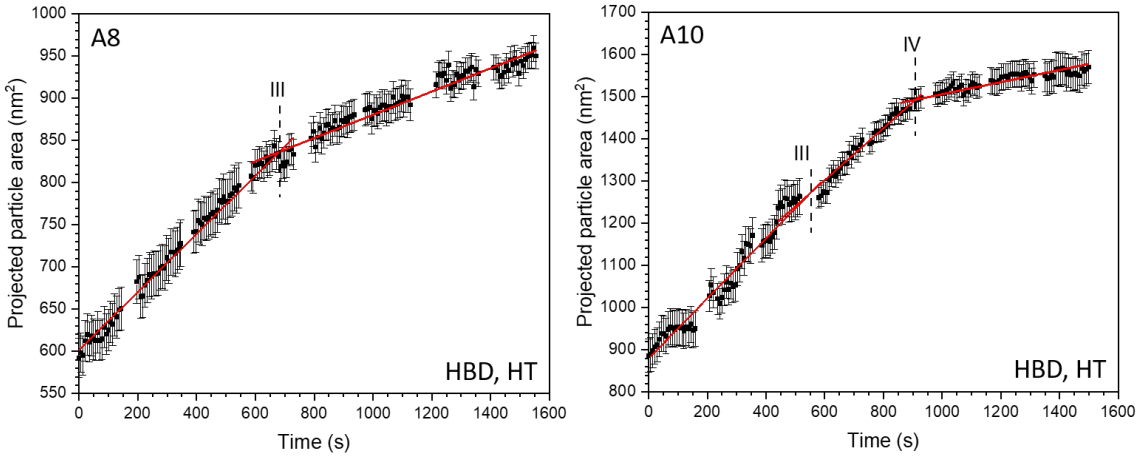

Figure 5.14: Total particle projected areas for particles A8 and A10 where the red line has been fitted in Origin to highlight the change in oxidation rate against time. Imaging conditions for each particle are also given where HT is high temperature (480 K) and HBD refers to high beam dosage (45 pA/cm^2). Labelled points are described in the text.

described in Section 5.2.2 in Figure 5.9) from t=0 s to Point I (t = 496±1 s) yields a value of -0.40±0.02 nm compared to after Point I which gives a value of +0.10±0.01 nm. This shows how initially the oxidation front is inward dominated and then after becomes more balanced. A more balanced growth is seen after Point I in the core+void projected area (Figure 5.16) as the decrease then levels out. As described in Section 2.3 and 5.2.2, the oxide shell can grow inwards due to the relative diffusivities of the Fe and O ions as well as preferential inward diffusion during the initial oxide formation.

Point II occurs in A6, A7a and b, shown in Figures 5.4, 5.5, 5.15, and 5.16, and coincides with the point at which the voids meet some critical volume and coalesce for the first time. From these figures point II occurs as the void projected areas go above $\sim$ 10 nm^2 for the first time and so this could then be the critical value that slows the oxidation reaction rate down. The voids that form in the particles preferentially grow at the corners of the core. This is because the voids grow through heterogeneous nucleation, i.e. around an initial nucleation site [147]. As with the NP discussion in Section 4.1.1, the growth rate was simulated and shown to be too slow if it was homogeneous [148]. This nucleation point can be a defect point in the lattice and as such the corner between the core and the oxide is an ideal place. This

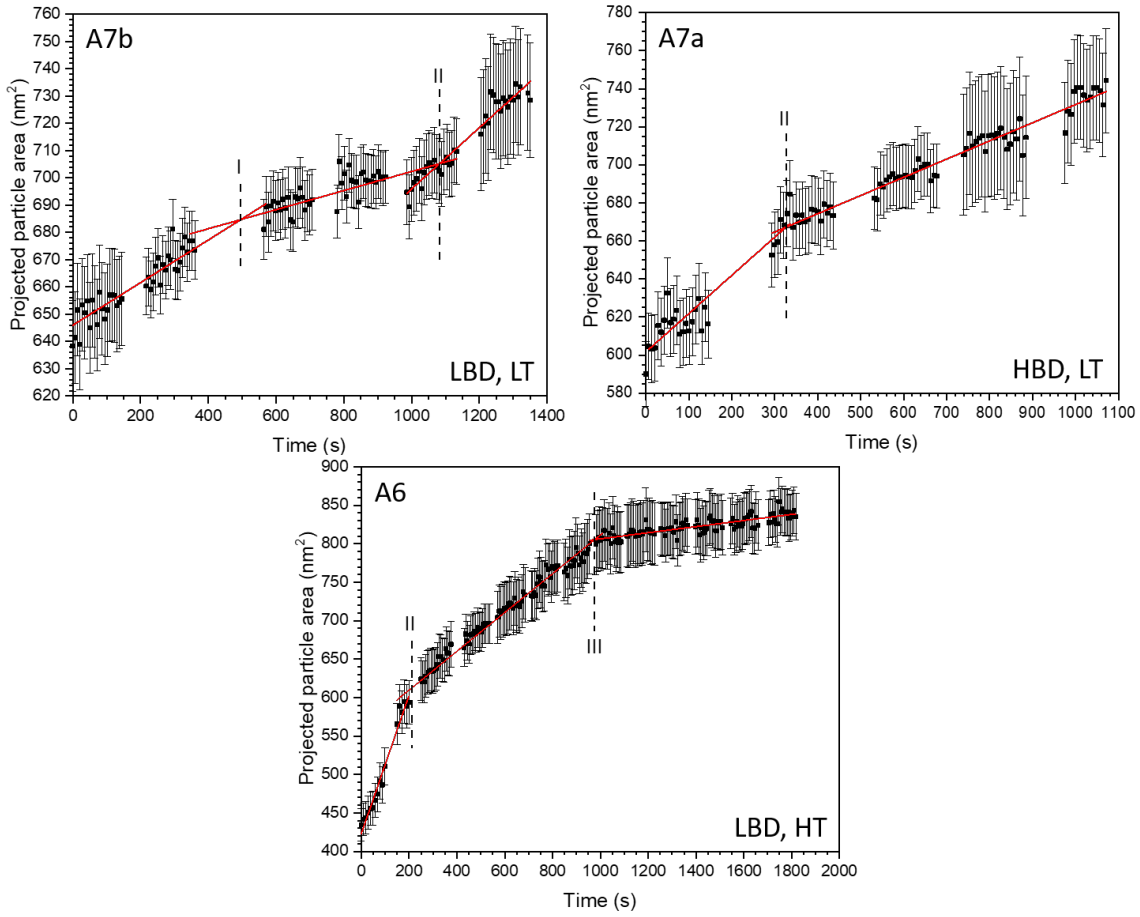

Figure 5.15: Total particle projected areas for particles A6, A7a, and A7b where the red lines have been fitted in Origin to highlight the change in oxidation rate against time. Imaging conditions for each particle are also given where LT and HT are low and high temperature respectively (382 and 480 K) and LBD and HBD refer to low and high beam dosage (23 and 45 pA/cm^2 respectively). Labelled points I, II, and III are described in the text.

is due to the highly defective grain boundary (GB) that is present at the corner of the cube in the oxide shell where two domains of the oxide meet. This GB then meets the core somewhere which will cause high levels of defects in the crystal lattice, a region that has been dubbed the triple point (TP), as shown in Figure 5.18(a).

As well as being highly defective, this site is also the location where the voids in the oxide shell will be injected into the core. This is due to the way that the Fe atoms will diffuse through the solid. As stated earlier in Chapter 2, the Fe cations will diffuse through interstitial sites (becoming point defects) or through vacancy exchange where they swap places with a vacancy in the oxide lattice. This is how

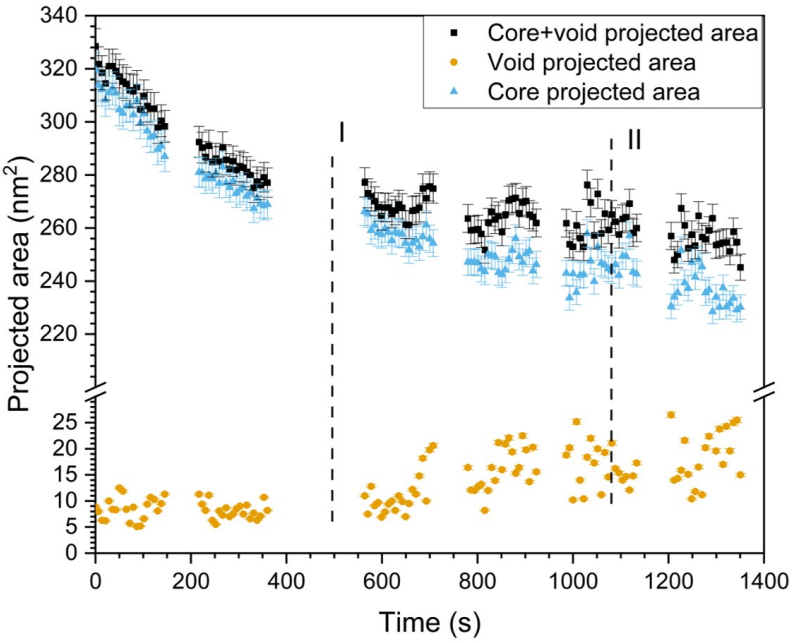

Figure 5.16: A7b core (blue triangle points) and void (yellow circle points) projected areas as well as their sum total (black square points) plotted against time. The initial period shows rapid decrease of the core+void as well as the core projected areas with little void growth which is indicative of the oxidation front progressing inwards. Once the voids have reached an area of around 20-25 nm^2 the oxidation seems to be more balanced with less shrinking of the core+void area.

the voids (and therefore the Kirkendall effect) occurs in the first place as there is a net flux of vacancies in one direction due to the faster diffusion of one of the species in the diffusion couple. GBs have been shown to be fast diffusion pathways [27] meaning the diffusion process during the NKE preferentially occurs through a GB. This means that for the oxidation reaction to occur, the Fe cation diffuses out of the core, through the GB, and then reacts with the O anion at the oxide shell/oxygen interface. This results in the vacancy exchange to occur across the GB as the Fe cation diffuses through vacancy exchange and the net flux of vacancies is along the GB towards the TP and core [54]. The Fe diffusion process via vacancy exchange is shown diagrammatically in Figure 5.18a.

The pathway that the Fe from the core or the oxygen from the atmosphere has to take to complete the oxidation reaction changes when the voids first coalesce. Looking at the diagram in Figure 5.18b, we can see that when the voids first form the core is no longer in direct contact with the oxide shell and thus must diffuse in a

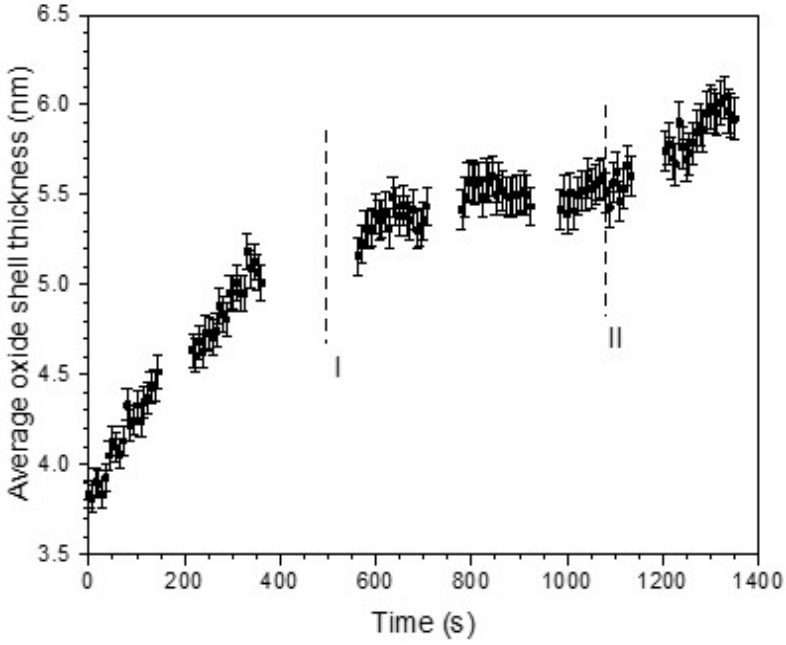

Figure 5.17: Average oxide shell thickness for A7b as a function of time showing the oxide shell continues to get larger over the period. This shows that the oxidation reaction was occurring across the whole time frame.

different way. Fe from the core must first diffuse across the surface of interface I and along the surface of II to the GB where it can then cross the oxide shell to complete the oxidation reaction. This is a longer path than before the voids coalesce where the Fe can just diffuse out of the GB explaining why the oxidation rate slows for A6 and A7a in Figure 5.15.

In fact, the oxidation rate increases after the voids coalesce at point II for A7b (as seen in Figure 5.15) contrary to what is seen in A6 and A7a. Klinger et al. [149] theorised that the voids do not nucleate instantaneously and that the oxide shell/core absorb the vacancies as stress and strain instead of forming the voids. This strain is only released when the vacancies in the lattice nucleate into voids. As described in Section 2.2.3, strain can have a large influence on the oxidation rate at the nanoscale. This could explain why the oxidation rate increases after point II in A7b as there could be oxidation-limited strain occurring due to the vacancies being absorbed by the oxide shell/core between points I and II. More evidence for this is shown in Figure 5.19 where the individual sides of the oxide shell have been measured. The black points are the average of sides 1, 3, and 4 and the yellow points are for

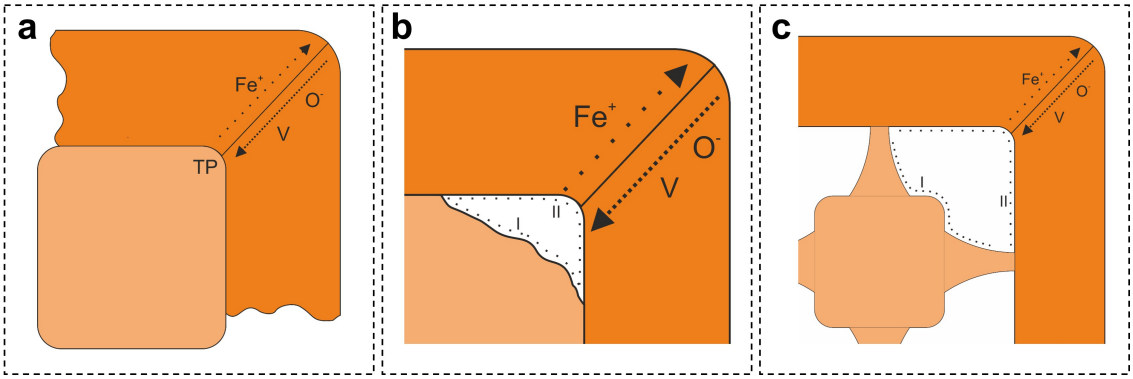

Figure 5.18: Diagrammatic view of the different oxidation pathways and processes at play during the continual NKE of NPs. (a) shows the out diffusion of the Fe cations through the GB between the two oxide domains and the net flux of vacancies against the flow of the Fe cations towards the triple point (TP) where the voids first coalesce. (b) The Fe cations then self-diffuse across the surface of the interface of I and across the interface of II towards the GB to continue the oxidation reaction and diffusion process. (c) Bridges form between the core and the oxide shell once the voids have grown to allow for the continued out-diffusion of the core material. The bridges form fast diffusion pathways through surface diffusion across interface I and then II towards the GB.

side 2 specifically with each side labelled in the inset. Side 2 has been singled out specifically because, as can be seen in the figure, at around 1100 s, at point II, there is a large shrinking of the average thickness of this side as compared to the average of the other sides. This is significant because this could point to the release of strain as the voids nucleate for the first time meaning the build up of the strain is released and then the oxidation rate increases as the vacancies can then be injected into the voids instead of being absorbed as strain.

Once the voids have nucleated they then continue to grow as the core diffuses out and the vacancies move in. For this process to continue, especially when the core has significantly diminished, a pathway has to be created for the Fe cations to diffuse across. This is shown diagrammatically in Figure 5.18c where a “bridge” between the core and the oxide shell has developed. These can be seen in Figures 5.2 and 5.4. The bridges act as fast diffusion pathways for the continual oxidation reaction and have been shown here and in the literature to preferentially form between the

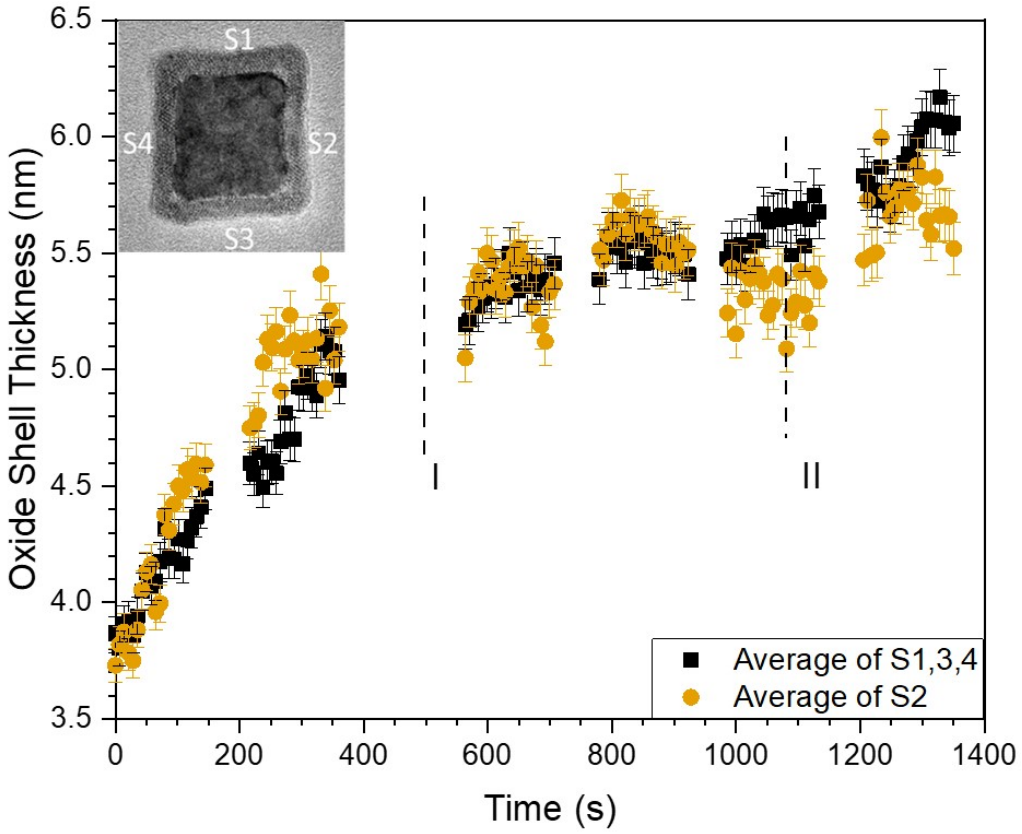

Figure 5.19: Average oxide shell thickness for each side of particle A7b. Black points are the average of sides 1, 3, and 4 and the yellow points show the average of side 2. Sides are labelled S1-4 in the insert. Points clearly show a dip in side 2 around transition point II when the voids first coalesce.

core and the middle of an oxide grain [52, 150]. Klinger et al. [58] also modelled this diffusion and showed that the core metal cations diffuse across interface I in Figure 5.18c and then move across interface II towards a GB. They showed that the oxidation reaction would proceed too quickly if the metal cation diffused through the oxide shell anywhere along interface II (i.e. lattice diffusion across the oxide shell).

Point III only occurs in A10, A8, and A6, i.e. at elevated temperatures, and coincides with the point at which the core has sufficiently depleted. The oxidation reaction rate decreases further due to the increased path length of the Fe cations moving out of the core. This is similar to Point II where the oxidation rate decreased due to an increased path length. The number of bridges that the core can support may also be reduced which will add another bottleneck to the continued oxidation. This

decrease in oxidation rate could also be due to a volume effect where the amount of Fe needed to grow the oxide shell increases as the surface area of the oxide increases with particle size. The surface area of the particle is only increasing and so therefore the size of the oxide surface is also increasing. It therefore follows that the amount of Fe needed to form a new monolayer on top of the previous layer is larger compared to the previous layer formed.

Point IV only occurs in A10 and is the point at which, as highlighted earlier in the discussion of beam damage, the core has fully depleted and the voids keep growing. The particle area shown in Figure 5.14 keeps growing alongside the increasing core+void and void area shown in Figure 5.13(a). The oxidation reaction is sustained by the continued creation of oxygen vacancies in the crystal lattice which diffuse towards the hollow core. This allows the Fe cations to continually diffuse outwards to the oxide-oxygen front where they react with adsorbed oxygen anions.

5.2.5 Determination of the Diffusion Coefficient of Fe in Fe Oxide

From the full depletion of the core in A8 and A10, and therefore what can be seen as a complete oxidation reaction, the diffusion coefficient of Fe in Fe oxide can be determined. Using the method outlined by Niu et al. [151] the values can be calculated using Fick's law and the half life of the core. The flux of Fe out of the core can be approximated using Fick's law

$$J = \frac{D(\rho - 0)}{d} \tag{5.4}$$

where J is the flux of Fe, D is the diffusion coefficient of Fe, ρ is the density of the iron oxide, and d is the average oxide shell thickness. The diffusion cross section can be approximated as the inner surface area of the shell, i.e. a cube, so $S = 6a^2$ where a is the length of a side of a cube (i.e. the inside surface of the oxide shell). The time, $t_{1/2}$, for Fe in the core to decrease to half of its initial area can then be expressed as

$$t_{1/2} = \frac{(1/2) \times a^3 \rho}{JS} = \frac{1}{2} \times \frac{da}{D} \tag{5.5}$$

which can be rearranged to

$$D = \frac{1}{2} \times \frac{da}{t_{1/2}} \tag{5.6}$$

The values of d, a, and $t_{1/2}$ can be determined from the measured values for both particles. Shown in Figure 5.20, $t_{1/2}$ is measured by determining the total change in area for the core and then finding the time it takes for half of this total change to occur. For A8, the core area decreases to 0 in a total of 1119±1 s leading to a $t_{1/2}$ value of 559±1 s. For A10, the core takes 897±1 s to decrease to 0 giving a $t_{1/2}$ value of 448±1 s. The values of d are determined by taking the average of all of the oxide shell thickness values for the period up to which the core projected area reaches 0. The average value of d is taken from the values for each particle, shown in Figures 5.10(b) and 5.13(b) for A8 and A10 respectively. This gives a value of d of 7.2±0.2 and 8.4±0.2 nm for A8 and A10 respectively.

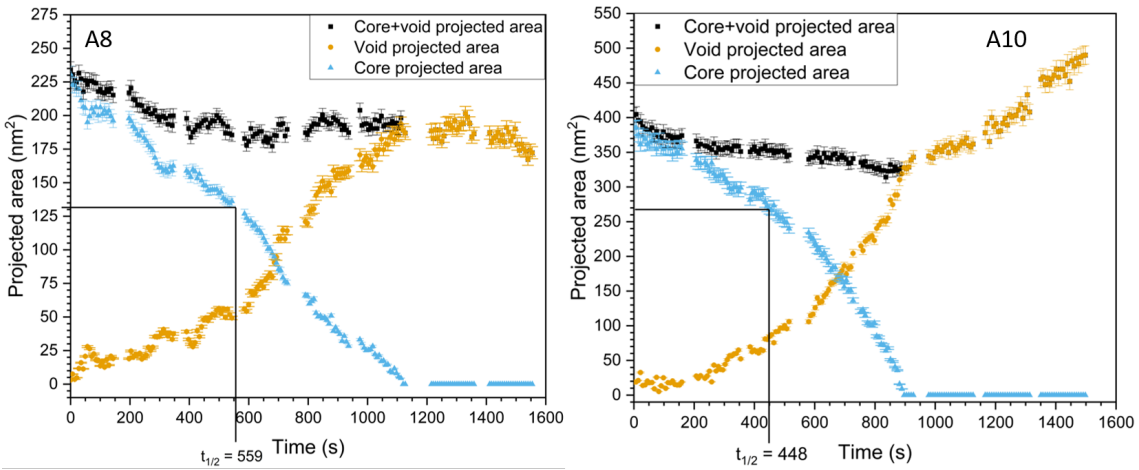

Figure 5.20: Core and void projected areas for A8 and A10 with $t_{1/2}$ labelled signifying the time taken for the cores to decrease by half of their initial area.

The determination of a is achieved by measuring the lengths of the inside of the oxide shell so that an average value could be found at $t_{1/2}$. Following this method, a was determined to be 18.8±1.0 for A10. For A8, it is slightly more difficult as $t_{1/2}$ occurs between image sets so there is not an image available to measure it from.

Therefore, an average was taken of the two images either side of the gap in the movies. This then achieves a value of 14.9±0.8 for A8.

Putting these numbers into Equation 5.6, we obtain values, believed to be the first time, for D of Fe in Fe oxide at 480 K for each particle of 9.5±0.5 $\times 10^{-16}$ and 1.8±0.1 $\times 10^{-15}$ cm^2s^{-1} for A8 and A10 respectively. The measured and calculated values are summarised in Table 5.2.

Particle	$t_{1/2}$ (s)	d (nm)	a (nm)	D (cm^2s^{-1})
A8	559±1	7.2±0.2	14.9±0.8	9.6±0.5 $\times 10^{-16}$
A10	448±1	8.4±0.2	18.8±1.0	1.8±0.1 $\times 10^{-15}$

Table 5.2: Measured values for $t_{1/2}$, d, and a leading to the calculated value of D for each particle following the methods described in the text and Equation 5.6.

The discrepancy between the two is most likely due to the size effect of the particle with the larger particle more likely to sustain a hollow core as described in Chapter 2.3. The larger oxide shell will also lead to more oxygen vacancies being created by the electron beam and so a marginally greater vacancy current for the Fe cations to exchange with during diffusion. These values are comparable to those of other transition metals such as Ti and Ni which were calculated to be 3.5 $\times$ 10^{-16} cm^2s^{-1} [147] and 7.5 $\times$ 10^{-15} cm^2s^{-1} [151] respectively. Values for the self-diffusion of Fe in α-Fe can be calculated through the empirical formulas provided by Buffington et al. [152]. Using these formulas, with the temperatures used in this experiment, yields a value of the self-diffusion of Fe in α-Fe to be 1.42 $\times 10^{-15}$ cm^2s^{-1}. This figure is of the same order of magnitude of the values calculated in this study for Fe in Fe oxide at 480 K. The value calculated for A10 is marginally quicker which is likely due to there being more defects present in the oxide structure allowing for faster diffusion. The lower value in A8, as compared to A10 and that calculated for the self-diffusion of Fe in Fe from Buffington et al., could be due to size effects such as strain which would hamper the diffusion process.

5.3 Summary

This study shows the power of e-TEM and that the real time study of these nanoscale processes is possible. The effect of beam current and temperature on the NKE process was investigated showing that the temperature is the main driving force in the reaction. The temperature allows the Fe cations to diffuse faster as they can overcome the potential barrier to their movement easier. The increased temperature will also provide an additional current of electrons to sustain the electric field in the oxide to allow the oxidation reaction to occur. The beam damage will most likely manifest in knock-on beam damage where the electron interaction with the oxygen atoms in the oxide crystal lattice will cause the oxygen atoms to be displaced. This will create an extra source of vacancies with which the Fe cations can exchange. In combination with an elevated temperature, these two effects (temperature and beam current) combine to allow for A8 to oxidise to a greater extent as compared to A7a and b. Based on the theories presented in Chapter 2, it is likely that A7a and b would form thicker oxide shells with smaller voids in the centre due to the difference in the diffusivities of the Fe and O ions.

Overall, this work highlights how at the nanoscale the oxidation behaviour can be explained by a combination of the theories presented in Chapter 2 which can then give a more complete picture. Understanding this oxidation and hollowing process is key to then applying these particles in more widespread applications. It can also be used as evidence for how the voids can be tailored depending on the conditions that the particles are oxidised in.

The diffusion coefficients of Fe in Fe oxide at 480 K were also calculated here believed to be for the first time with values of $9.5\pm0.5 \times10^{-16}$ and $1.8\pm0.1 \times10^{-15}$ cm^2s^{-1} for A8 and A10 respectively. The difference in the values is most likely due to size effects with A10 being larger. These values are similar to other transition metals that have been reported in the literature.

Chapter 6

Spectroscopic Insights on the Initial Oxidation of Fe Nanoparticles

Following the *in-situ* e-TEM experiments described in Chapter 5, a follow-up study was designed using *in-situ* spectroscopy techniques. This allowed for complementary results to be obtained in order to determine the type of Fe oxide that forms during the oxidation reaction. As previously described in Chapter 1, Fe has many different oxide states. There has been much debate in the literature regarding the initial oxide formed and its subsequent growth so it is vital to get a better understanding of this process. Using photoemission spectroscopy techniques under UHV, the Fe NPs can be deposited under vacuum onto cleaned Si crystal wafers and then exposed to oxygen gas *in-situ*. In this chapter, a description of the different Fe oxides and their properties will be given as well as a review of the current results on the initial oxide formation on Fe surfaces. The details and results of the experiment will then be presented where the formation of the initial oxide could be controlled with either $Fe_{1-x}O$ or Fe_3O_4 forming depending on the growth conditions. The oxidation of $Fe_{1-x}O$ was studied further which could also be reduced through heating. Continued exposure to oxygen transformed the $Fe_{1-x}O$ layer into Fe_3O_4.

6.1 Iron Oxides: Structures and Properties

Iron and its various oxides have been researched heavily over the years due to the variety of properties exhibited. These result from the differing crystal structure each Fe oxide takes such as cubic, spinel, and hexagonal. Fe can form four main oxides, Fe_3O_4 (magnetite), γ-Fe_2O_3 (maghemite), α-Fe_2O_3 (haematite), and $Fe_{1-x}O$ (wüstite), as well as many other intermediate phases. In general, the iron oxides are all based on a close-packed O^{2-} lattice with the Fe cations either tetrahedrally or octahedrally co-ordinated in the interstices between the oxygen anions [16]. The phase diagram for their formation is shown in Figure 6.1. It can be seen in Figure 6.1 that the expected oxide is α-Fe_2O_3 for most temperatures and oxygen pressures. Fe_3O_4 and $Fe_{1-x}O$ are only expected to form at higher temperatures. In this section, the various structural and magnetic properties of the different oxides will be discussed.

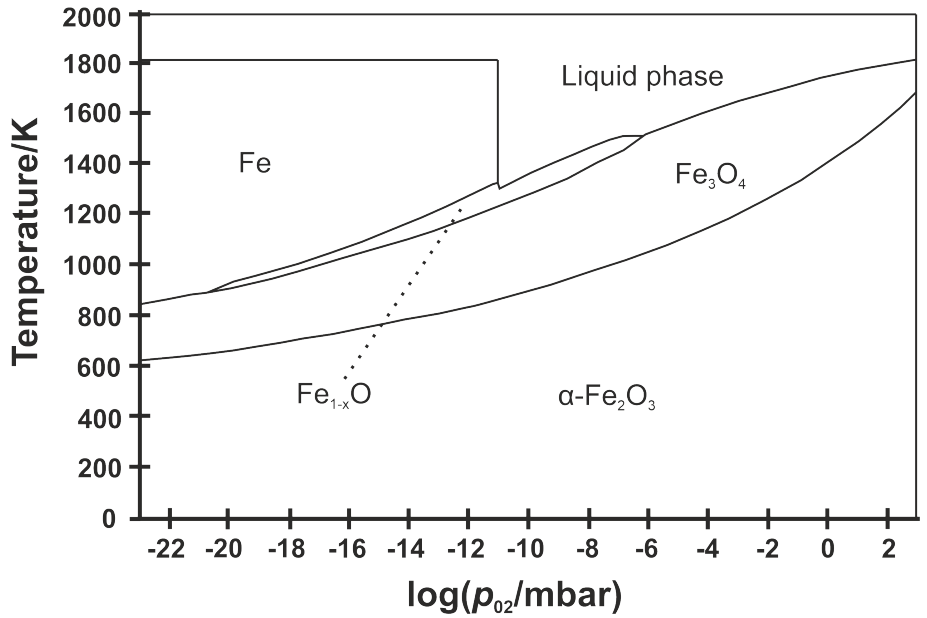

Figure 6.1: Phase diagram for the Fe-O_2 reaction reproduced with permission from Ketteler et al. [153].

6.1.1 $Fe_{1-x}O$

Wüstite, $Fe_{1-x}O$, has a cubic rocksalt structure with Fe^{2+} ions located in octahedral lattice sites. Shown in Figure 6.2, the structure is always defective with the $(1-x)$

term having values that vary from 0.83 to 0.95 meaning it is non-stoichiometric. The defects in the crystal structure are known to be Fe^{3+} cations on tetrahedral sites, also known as the Koch-Cohen defects [154]. $Fe_{1-x}O$ has a Néel temperature of 470 K so is anti-ferromagnetic at RT [16]. $Fe_{1-x}O$ can also form as an intermediary in the reduction of Fe_3O_4 and/or γ-Fe_2O_3 to Fe. As can be seen in the phase diagram, Figure 6.1, the formation of $Fe_{1-x}O$ only occurs in a small region of oxygen pressures and temperatures.

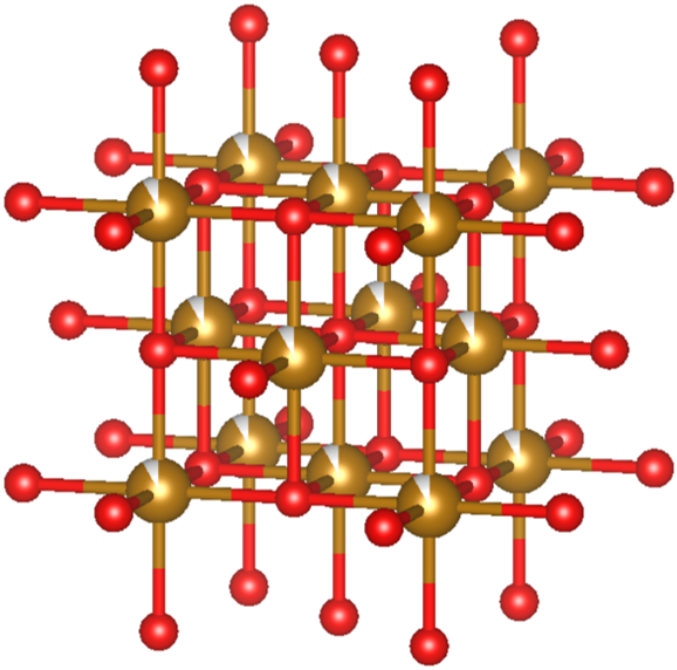

Figure 6.2: Crystal structure of $Fe_{1-x}O$ visualised in VESTA from Yamamoto [155]. Brown spheres are Fe atoms, red are O atoms, and the white colour shows the potential defect.

6.1.2 Fe_3O_4

Magnetite or Fe_3O_4, probably one of the most well studied metal oxides, has an inverse spinel structure, as shown in Figure 6.3. The spinel structure itself is where the oxide takes the form AB_2O_4 where A and B can be different elements to form an alloy or can be the same element with different oxidation states. In the case of Fe_3O_4, the structure is $Fe^{2+}Fe_2^{3+}O_4$. In the normal spinel structure the A^{2+} cations occupy the tetrahedral interstitial sites and the B^{3+} cations occupy the octahedral sites. The inverse structure occurs when the A^{2+} crystal field is large resulting in

these ions occupying half of the octahedral sites which pushes the B^{3+} cations into the tetrahedral sites. So in Fe_3O_4, the Fe^{2+} ions are octahedrally co-ordinated with the Fe^{3+} ions equally distributed over the tetrahedral and remaining octahedral sites [156].

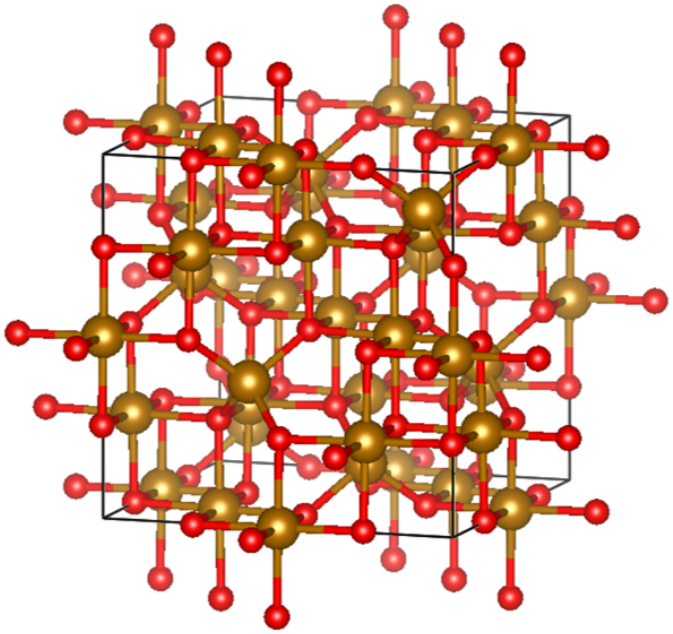

Figure 6.3: Schematic of the inverse spinel crystal structure of Fe_3O_4 in which the brown spheres are Fe and the red sphere are O atoms. Visualised in VESTA from Fleet [157].

Fe_3O_4 is magnetic at RT and is a ferrimagnet as proposed by Néel [158]. Ferrimagnetism is like a weak form of ferromagnetism where a net magnetic moment remains in the material but there is a small anti-ferromagnetic contribution. Néel proposed that in Fe_3O_4, the Fe^{3+} cations in the tetrahedral and octahedral sublattices are anti-ferromagnetically aligned and so cancel each other out. The net magnetic moment purely arises from the Fe^{2+} cations in the remaining octahedral sites leading to a magnetization equal to 4 μ_B per formula unit [16].

Fe_3O_4 has a similar conductivity to other poor metals (like Ga) but as the temperature is cooled below 125 K the conductivity plummets by a factor of 100. This is known as the Verway transition [159] which Verway theorised as being due to the electron hopping in the octahedral Fe sublattice being frozen [159]. A lot of research has been performed on the Verway transition which is beyond the scope of this thesis but is neatly summarised by Walz [160].

6.1.3 γ-Fe_2O_3

Maghemite, γ-Fe_2O_3, can form from the continued oxidation of magnetite. The Fe^{2+} cations oxidise to become Fe^{3+} and the crystal structure reverts to a normal spinel structure, shown in Figure 6.4. To achieve this structure, the crystal adds Fe vacancies in place of the Fe^{2+} cations which also helps achieve charge neutrality. The vacancies are distributed across the tetragonal lattice sites in an ordered fashion, and it was demonstrated in Ref. [161] that this configuration has the lowest energy [162].

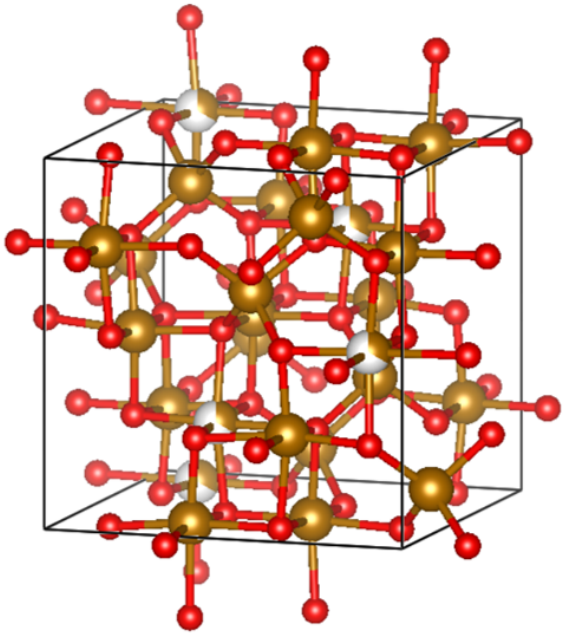

Figure 6.4: Crystal structure of γ-Fe_2O_3 visualised in VESTA from Greaves [163]. Brown spheres denote Fe and the red spheres are O atoms. The white spheres are the vacancies in the crystal lattice.

γ-Fe_2O_3 is also a ferrimagnet as the anti-ferromagnetic ordering between the octahedral and tetrahedral sublattices remains from Fe_3O_4. However, the net magnetic moment is lower at 2.5 μ_B per formula unit. γ-Fe_2O_3 has a high Curie temperature of ≈950 K which means it has been used regularly in recording media [16].

6.1.4 α-Fe_2O_3

Haemetite, α-Fe_2O_3, has the corundum crystal structure, shown in Figure 6.5, which can be seen as a dense arrangement of oxygen ions in a HCP lattice with Fe^{3+} cations

located in two thirds of the available octahedral sites [164]. This means α-Fe_2O_3 has a hexagonal unit cell with a reported highly anisotropic conductivity which can be up to four times larger in the basal plane than along the [0001] direction, for example. The conductivity of the oxide can be improved with added impurities [165].

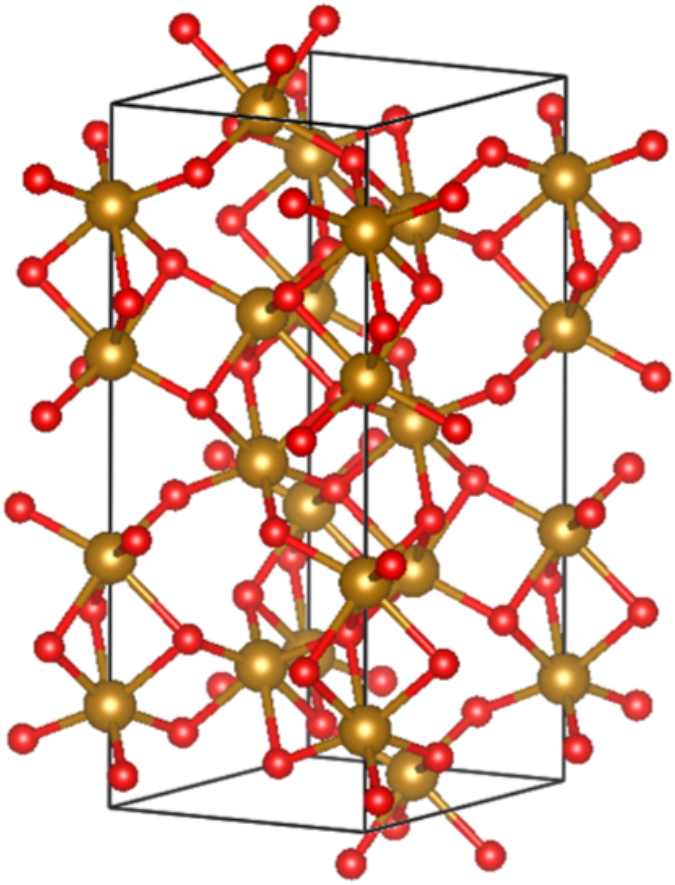

Figure 6.5: Crystal structure of α-Fe_2O_3 visualised in VESTA from Blake et al. [166]. Brown spheres represent Fe ions and the red spheres represent O ions.

α-Fe_2O_3 has a higher magnetic moment than Fe_3O_4 at 4.6 μ_B per formula unit but also a high Néel temperature of 955 K meaning that at RT α-Fe_2O_3 is an anti-ferromagnet. The transformation from γ-Fe_2O_3 to α-Fe_2O_3 is energetically expensive as the conversion from the spinel to the corundum structure requires the O^{2-} lattice to be converted from FCC to HCP. In comparison, the switching between γ-Fe_2O_3, Fe_3O_4, and $Fe_{1-x}O$ is more straightforward as it only requires a rearrangement of the Fe cations within the FCC oxygen lattice [16].

6.2 Initial Oxide Formation on Fe

The initial oxidation of Fe is something of clear importance as the properties of the system are dictated by the type of oxide that forms. There is discourse in the literature as to which oxide is formed during the initial oxidation of an Fe surface or NP. For example, Vaz et al. [167] deposited Fe NPs using a gas phase source onto passivated Si substrates so that the particles could be soft landed onto the Si surface with the removal of the SiO_2 layer. The areal density of the deposited particles was such that individual particles could be analysed using X-ray absorption spectroscopy from photoemission electron microscopy. The results showed that regardless of oxygen dosage (0-80 Langmuir exposure) and particle size, the same oxidation process and crystal structures were observed. The dosage was performed over discrete steps building from 0.5 to 80 L in steps of 1, 5, 10, and then 20 L with measurements performed at each step. The overall exposure took 7500 s at an average pressure of 1.5 $\times 10^{-8}$ mbar of oxygen. It was shown that the initial oxide surface is $Fe_{1-x}O$ up to 5 Å with the outer layer then converted into Fe_3O_4 followed by the consumption of the remaining $Fe_{1-x}O$ layer upon further oxidation to leave just an Fe_3O_4 layer.

The initial formation of $Fe_{1-x}O$ was also observed by Jeon et al. [140] who modelled the oxide growth kinetics on Fe (100), (110), and (111) surfaces using reactive molecular dynamic simulations. In these simulations, the authors showed that the initial oxidation was dominated by the inward transport of oxygen anions through interstitial sites in the crystal lattice leading to the formation of $Fe_{1-x}O$. As the oxide gets thicker, the outward Fe cation transport increases and the crystal lattice was then re-ordered as the cations sought to stabilise the crystal structure. This re-ordering leads to the formation of Fe_3O_4 and the removal of the $Fe_{1-x}O$ layer. These simulations matched the observed reaction from Vaz et al. [167] as the same process of $Fe_{1-x}O$ followed by Fe_3O_4 was also seen. Other theoretical work performed by Subbaraman et al. [51] also showed through molecular dynamic simulations that the initial oxide formed on an Fe surface was $Fe_{1-x}O$. However, the results also showed that after a layer of $Fe_{1-x}O$ had formed, the oxide then grew into a mixed crystal of $Fe_{1-x}O$ and Fe_2O_3. The authors did not discern between haemetite and maghemite

when stating the oxide is Fe_2O_3 but did show how the Fe(110) surface has the lowest activation energy and therefore the fastest oxidation rate.

These results are at odds with the observed oxide formation reported in Refs. [168–174] where the $Fe_{1-x}O$ phase is not grown. Haneda et al. [169] observed the growth of γ-Fe_2O_3 on large Fe NPs (100s of Å in diameter) using Mössbauer spectroscopy and x-ray diffraction techniques. The oxide formation was regardless of particle size and oxidation rate (i.e. slow exposure to pure oxygen versus rapid exposure to air). This result was also confirmed by Rojas et al. [170] where Fe NPs produced by a gas condensation technique formed γ-Fe_2O_3 oxide shells when exposed to O_2 and air. Kwok et al. [171] showed, using HR-TEM, that nano-islands of γ-Fe_2O_3 grew on Fe NPs. The particles were produced using gas phase methods and were around 40 nm in diameter. The islands formed an epitaxial 4-nm-thick shell surrounding the particle with compressive strain due to the mismatch between the γ-Fe_2O_3 and the Fe core. This shell then prevented further oxidation of the Fe NPs in air and in water.

Yi et al. [174] grew single domain islands of Fe_3O_4 on Fe nanowires (NWs) in a tube furnace after a chemical reduction of Fe nitrates. The authors confirmed the growth of Fe_3O_4 using HR-TEM and electron diffraction images. The Fe NWs were shown to be passivated (i.e. resistant to further oxidation) with the single domains of Fe_3O_4 forming pyramid-like structures on the wire. The growth of mixed Fe_3O_4/γ-Fe_2O_3 was also reported by Kuhn et al. [172] on Fe NPs and shown to be dependent on the oxygen exposure. A slow exposure to oxygen/air grew an epitaxial film of γ-Fe_2O_3 whereas a quick exposure grew an Fe_3O_4 shell. This result is in contradiction to the result of Haneda et al. [169] but this could be due to particle size where the Fe NPs in the study by Kuhn et al. [172] are 10-20 nm in diameter compared to the very large particles studied in Haneda et al. [169].

These results show the variance in the expected oxide grown on Fe NPs and surfaces with no consistent picture emerging from a review of the literature. The following research was undertaken to understand the initial and continued oxidation of Fe NPs by employing *in-situ* oxidation techniques coupled with the spectroscopy system. Due to the difference in the oxide structures with different amounts of Fe^{2+} or Fe^{3+},

XPS can differentiate between these as the Fe 2p core levels appear at different binding energies. The work of Grosvenor et al. [175] showed how the different oxide structures of Fe can be analysed with XPS as the oxide structures show distinct features due to the variance in the amounts of Fe^{2+} and Fe^{3+}. The authors also provided a table showing the fitting parameters for the de-convolution of the Fe $2p_{3/2}$ peak. This allows for a rigorous and repeatable method for the de-convolution of the data acquired during these experiments. A similar method was also shown by Yamashita et al. [176] where the chemical structure of the oxides can be deduced by the presence of either the Fe^{2+} or Fe^{3+} states in the Fe $2p_{3/2}$ spectra. For example, as described in Section 6.2, Fe_3O_4 contains Fe in Fe^{2+} and Fe^{3+} states whereas $Fe_{1-x}O$ only has Fe in Fe^{2+} states which can then be discerned using XPS.

6.3 Experimental Details

To perform these experiments, Merlin was connected to the electron spectroscopy system via the flange labelled in Figure 3.1. This meant that the particle beam could directly deposit under vacuum onto clean samples in the analysis chamber. A gas doser was also fitted to the analysis chamber on the spectroscopy system which allowed the controlled inlet of gas through a needle valve, as shown in Figure 6.6. The gas line was cleaned by charging the line from the gas bottle, closing the bottle off and then pumping away the line up to the needle valve, labelled in Figure 6.6(a). This process was repeated three times before finally letting O_2 into the system. During the O_2 exposure, the background pressure in the chamber was raised by a partial pressure of 5×10^{-9} mbar from a base pressure of 2×10^{-9} mbar while being careful that the total pressure did not exceed 2×10^{-8} mbar when initially letting the gas into the chamber. This would allow the Fe $2p_{3/2}$ peak to be constantly scanned during the oxygen exposure meaning that as the particles oxidised any changes in the spectra would be captured whilst also protecting the instrument.

During oxygen exposure, the Si wafer and therefore the Fe NPs were exposed to three different temperatures with the elevated temperatures provided via the pyrolitic boron nitride (PBN) heater on the manipulator in the analysis chamber. This is a radiative heater and as such the whole arm and sample plate are both heated as

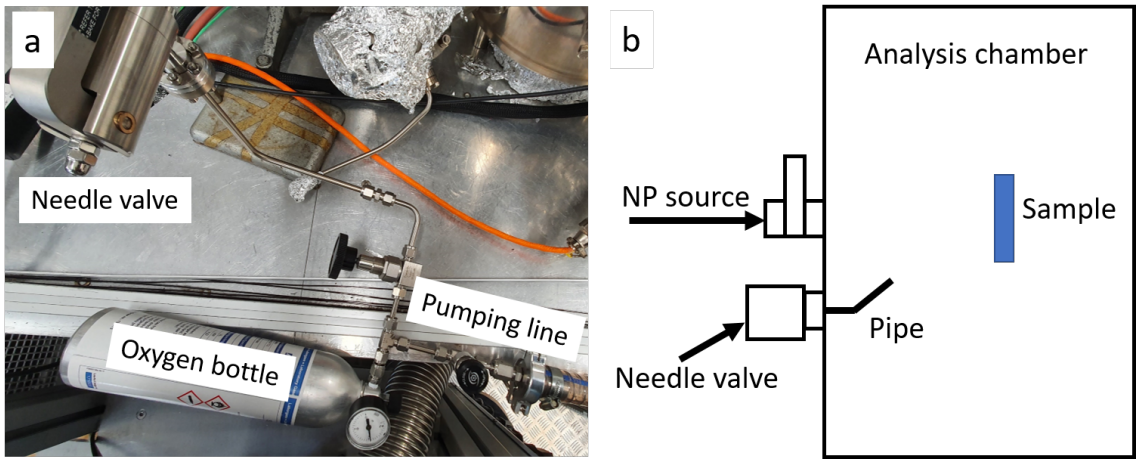

Figure 6.6: Oxygen gas doser fitted to the analysis chamber showing (a) the gas line setup allowing for the doser to be pumped and therefore purged and (b) a schematic of where the doser is located in relation to the source and the sample in the analysis chamber.

well as the sample itself. The temperatures chosen were room temperature (293 K), 648 K, and 848 K, with the maximum temperature low enough so that the NPs did not melt, as shown in Ref. [139] where heating Fe nano-cubes above 873 K caused the shape to change. Of course the temperature measured by the thermocouple for the PBN heated will not be what the true temperature is at the sample due to being in different positions. This will lead to some inaccuracies in the temperature measurement.

The exposure to the oxygen gas can be measured in Langmuirs with 1 L being equal to 1 $\times 10^{-6}$ Torr seconds. The RT and 648 K samples had a total exposure of 14 L (5.0 $\times 10^{-9}$ mbar for 60 minutes) and the 848 K sample had a total exposure of 21 L (5.0$\times 10^{-9}$ mbar for 90 minutes). The reason for the longer exposure is explained in Section 6.4.

The NPs were deposited onto Si crystal wafers which were cleaned by DC heating. Initially, the Si was out-gassed at 600 °C overnight so water vapour and other contaminants were removed before then being "flashed" at 1200 °C three times for 10 seconds each. Between flashes the sample was cooled to 900 °C and the system pressure allowed to recover. After the final flash, the sample was then slow cooled down to room temperature at ∼100 °C per minute. This allows for a clean

reconstructed surface to form as well as limiting the effect of thermal shock on the sample. The sample temperature was monitored using an infrared pyrometer with the emissivity set at 0.6 for temperatures up to 900 °C and 0.3 during the flashing stage.

The cleanliness of the Si can be checked with LEED where a clean and ordered surface will produce a diffraction pattern on the screen. The diffraction pattern produced by these Si crystal wafers is shown in Figure 6.7 where it can be seen that the Si(100) (2×1) surface reconstruction is observed. The spots are well defined meaning that the surface is well ordered and clean. While the reconstruction and ordering of the surface may play some role in the oxidation of the NPs, this was not investigated during this study. All of the Si surfaces cleaned by this method in this study produced the same surface ordering shown in Figure 6.7.

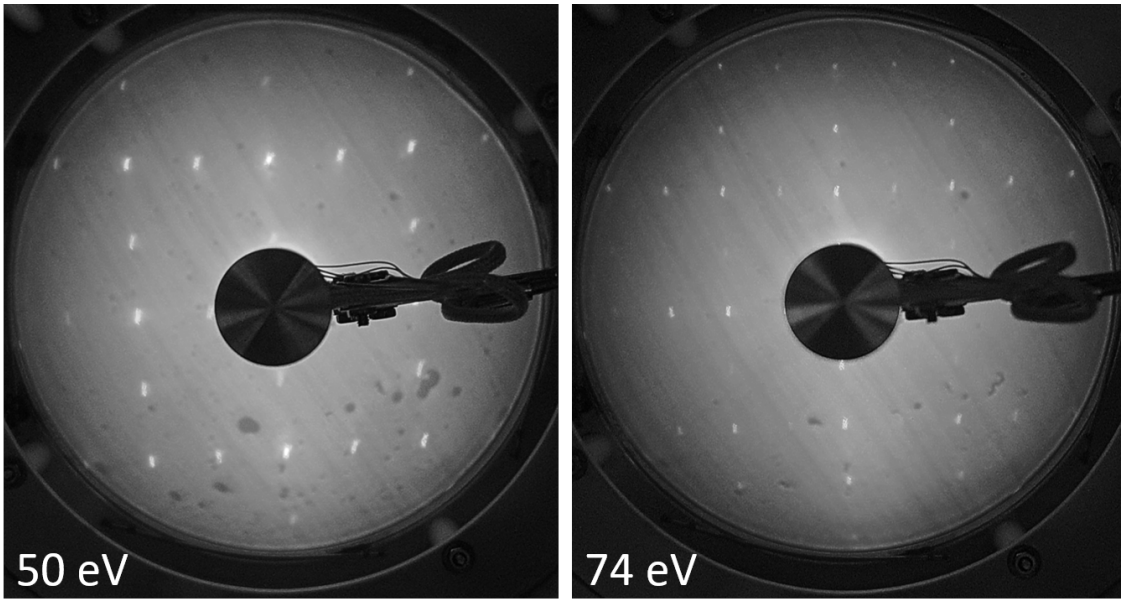

Figure 6.7: Diffraction patterns from two primary beam energies that are labelled in each image produced from clean Si samples after DC heating to form the (2×1) surface reconstruction on the Si(100) face.

Following LEED, the Si sample was then transferred to the analysis chamber where initial XPS and UPS spectra were taken pre-Fe NP deposition. The XPS spectra revealed a clean surface with no carbon present and a diminished O 1s peak, shown in Figure 6.8. Here the O 1s has been fitted with a single peak which corresponds with the sub-surface oxygen from SiO_2 [177].

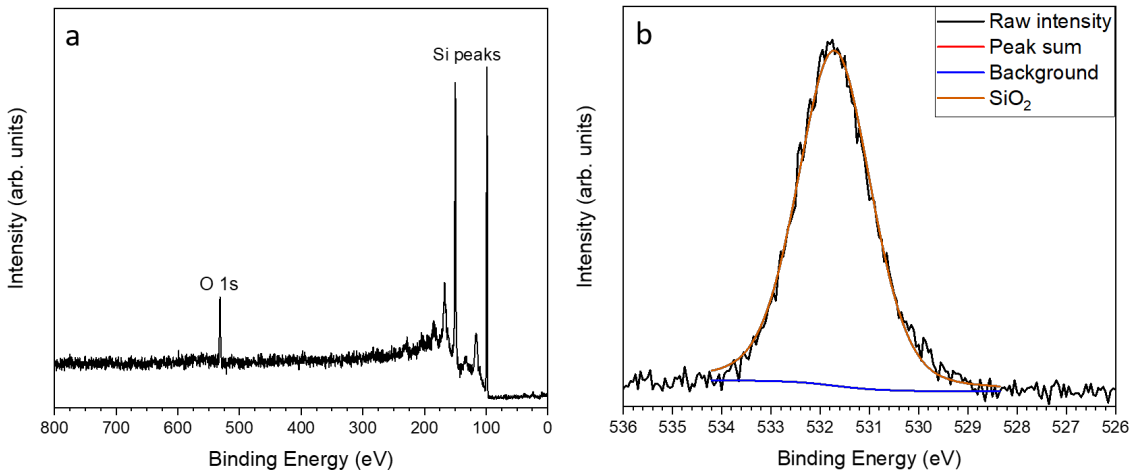

Figure 6.8: X-ray photoemission spectra obtained from a clean Si substrate. (a) shows the entire survey scan of the elements present. The lack of C 1s and a diminished O 1s peak shows that the sample surface is clean. The oxygen that is left is due to SiO_2 shown in (b).

The Si was exposed for 1 hour to the particle beam such that the coverage of particles on the surface was dense enough without forming a single monolayer. This meant that the particles would oxidise individually and the spectroscopy would then be averaging over many particles instead of a monolayer film. This can be seen in SEM images of the Si pieces after the heating and oxygen dosing experiments had been performed in Figure 6.9. The underlying Si is still visible with the coverage of the particles not exceeding 10 % areal density on the surface with the average coverage equalling 8±3 %.

The settings used on Merlin to produce each of the samples are shown in Table 6.1. These settings remained the same for each new sample and so the particle size effect should be negligible.

Plasma gas flow (sccm)	Carrier gas flow (sccm)	Plasma current (mA)	Plasma voltage (V)	Insertion length (mm)
85	95	275	217.9	140

Table 6.1: Fe NP production details for *in-situ* spectroscopy experiments.

For each new temperature the particles were exposed to, a fresh piece of Si and a new deposit of particles were used. The table below gives a summary of the conditions

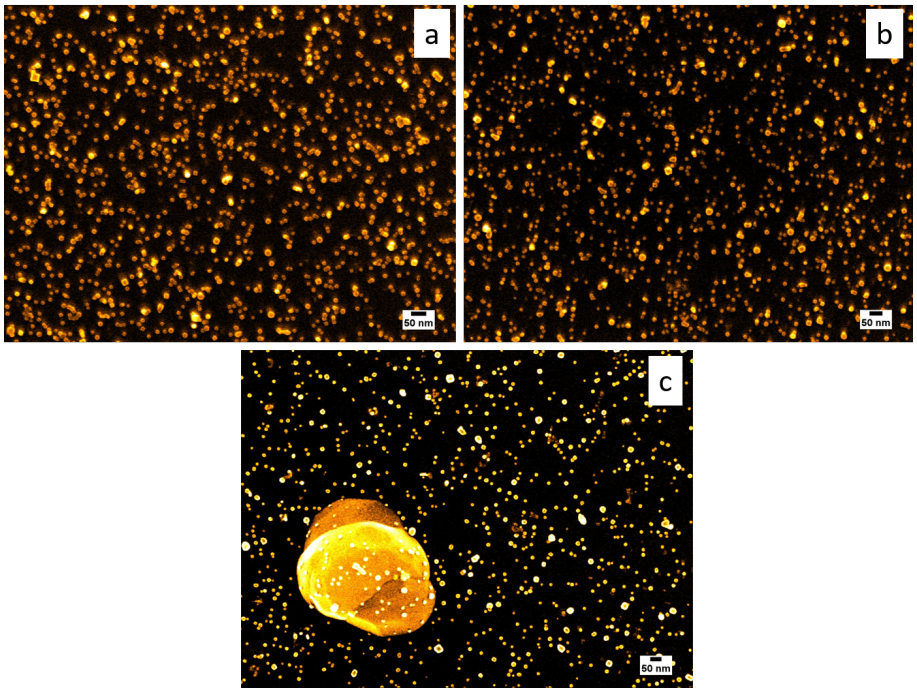

Figure 6.9: False colour SEM images of the different Si pieces for the different temperatures the particles were dosed at: (a) RT, (b) 648 K, and (c) 848 K.

that the samples were exposed to such as temperature, time, and oxygen exposure. As stated earlier, the temperature of the sample will differ from the quoted value here due to the nature of the heater and the sample, thermocouple geometry.

Sample name	Temperature (K)	Oxygen gas exposure (L)	Time (mins)
M036-1	296	2x7	60
M036-2	648	2x7	90
M035-3	848	3x7	120

Table 6.2: Summary of the samples with temperature, oxygen gas dose, and the time for the overall experiment given.

6.4 Oxidation and Development of the Oxide Shell Under Vacuum Conditions

The presence of $Fe_{1-x}O$ or Fe_3O_4 is confirmed by de-convolution of the Fe $2p_{3/2}$ peak and application of the fitting parameters from Ref. [175]. In this work, the

deconvoluted peak positions for the Fe^{2+} and Fe^{3+} states for the different oxides are given. A summary of the peak positions and FWHM are shown in Table 6.3. The multiplet structure is expected due to spin-orbit coupling in the high spin Fe^{2+} and Fe^{3+} oxide states. It can also be expected in well resolved spectra of the Fe^0 peak due to spin-orbit coupling between a photoionized Fe 2p hole and the 3d electrons present in Fe [178]. A Shirley background was also used as it is deemed the most appropriate for metal oxides [179]. This is because the background more closely mimics the electron loss process, i.e. an S-shape, compared to a linear fit. The large Fe^0 peak present in Figure 6.10 is confirmation that the oxide layer is thin and therefore has formed a Fe@$Fe_{1-x}O$ (core@shell) arrangement.

Crystal	Peak 1 (eV) [FWHM]	Peak 2 (eV) [FWHM]	Peak 3 (eV) [FWHM]	Peak 4 (eV) [FWHM]
Fe metal - Fe^0 multiplets	706.3 [1.4]	707.2 [1.4]		
$Fe_{1-x}O$ - Fe^{2+} multiplets	708.4 [1.4]	709.7 [1.6]	710.9 [1.6]	
Fe_3O_4 - Fe^{2+} multiplets	708.3 [1.2]	709.3 [1.2]	710.4 [1.4]	
Fe_3O_4 Fe^{3+} multiplets	710.2 [1.4]	711.3 [1.4]	712.4 [1.4]	713.6 [1.4]

Table 6.3: Peak positions and FWHM used for the deconvolution of the Fe $2p_{3/2}$ peak. Values reproduced here from Grosvenor et al. [175] and Biesinger et al. [178].

The initial oxide that formed could be controlled during the growth/deposition process. As described in Chapter 4, the Fe target is plasma cleaned before it is used to allow for the native Fe oxide that coats the target to be removed. A single Fe target could make multiple samples over a few days (on new pieces of Si each time) and it was found that the first Si piece to be exposed would form Fe@$Fe_{1-x}O$ initially whereas the subsequent samples were Fe@Fe_3O_4. If the Ar gas lines were purged and target plasma cleaned before each deposition then Fe@$Fe_{1-x}O$ could be grown reliably.

Two high resolution XPS spectra of the Fe $2p_{3/2}$ peak showing the difference between

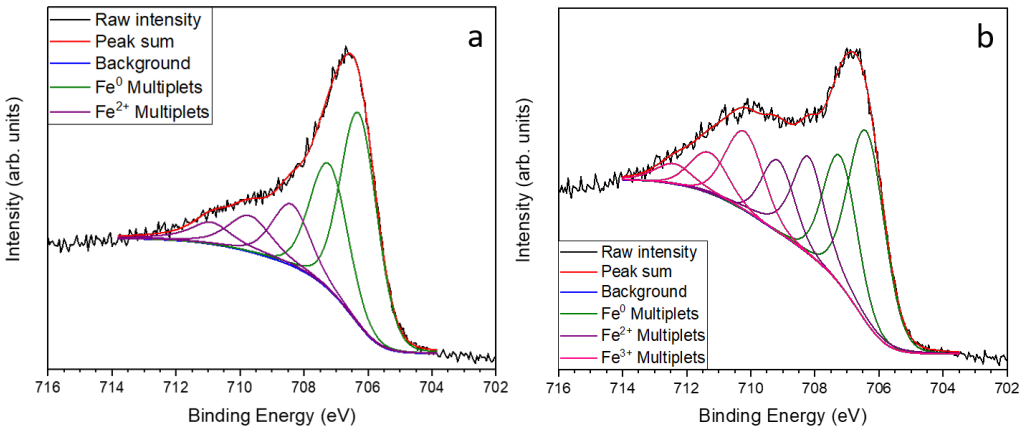

Figure 6.10: X-ray photoemission spectra of the Fe $2p_{3/2}$ region showing how the initial oxide can be either (a) $Fe_{1-x}O$ or (b) Fe_3O_4 depending on if the gas line and target have been cleaned before deposition or not.

the two growth conditions are shown in Figure 6.10. Only the continued oxidation of Fe@$Fe_{1-x}O$ was investigated as this was considered the most fundamental state where the target and gas lines were at their cleanest. It was also pertinent for the investigation as described in Section 6.2 to understand how the $Fe_{1-x}O$ layer changed. The growth of these slightly oxidised particles is most likely due to the fact the source operates in the high vacuum regime. A cleaner environment could be achieved by baking the system and running it in UHV conditions limiting the contamination of the growing particles.

The oxide features of both are comparable to that of pure Fe and Fe_3O_4 thin films. High resoultion XPS spectra of the Fe $2p_{3/2}$ peak show how these Fe multiplets occur. It can be seen in Figure 6.11(a) how the Fe^0 multiplets shift as the Fe oxidises to the regime of Fe@$Fe_{1-x}O$ in Figure 6.11(b) with the final Fe_3O_4 structure shown in Figure 6.11(c). It has to be noted that the ratio of the peak areas fitted for the Fe^0 multiplets should be the same across the samples which therefore adds an error to the fits presented here.

After 7 L of O_2 exposure, M036-1 oxidised from $Fe_{1-x}O$ to Fe_3O_4 with the zero valent peaks continuing to decrease with increased exposure up to 14 L total. This is demonstrated by the change in the Fe $2p_{3/2}$ peak as shown in Figure 6.12 where (a) is post deposition, (b) is after 7 L, and (c) is after 14 L.

It can also be seen in the high resolution scans of the O 1s peak, shown in Figure

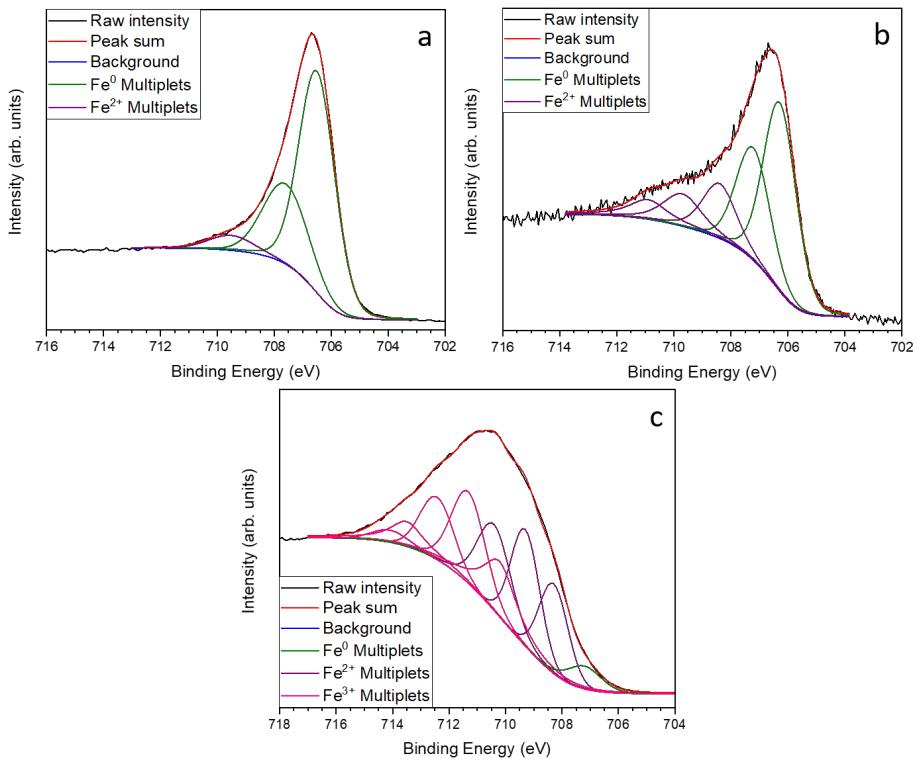

Figure 6.11: X-ray photoemission spectra of the Fe $2p_{3/2}$ region for (a) pure Fe, (b) Fe@$Fe_{1-x}O$, and (c) pure Fe_3O_4.

6.13, that the metal oxide component increases with oxygen exposure indicating a growing oxide. The metal oxide component's contribution to the overall peak grows from 28±2% to 41±3% after 7 L (Figure 6.13(a) to (b)). After 14 L, a smaller increase from 41±3 to 42±3% (Figure 6.13(c)) was observed. This indicates that the oxide growth rate is slowing down and therefore the oxide is reaching some critical value. This growth is more clearly seen in Figure 6.13(d) where the three peaks are overlayed. From Cabrera-Mott and Fromhold-Cook theory, it is expected that the oxidation rate slows and the oxide will hit a critical thickness at RT due to the decrease in electron tunnelling current as the oxide thickens. The lack of thermal energy means that thermionic emission of the electrons is also not possible.

Both M035-3 and M036-2 were brought up to temperature with no oxygen exposure and the effect of heating the particles with no oxygen dosing was explored. The samples were heated for 30 minutes with no oxygen dosing, explaining why the time given in Table 6.2 for these samples is longer compared to M036-1. High resolution XPS spectra were obtained of the Fe $2p_{3/2}$ peak after this initial heating. These are

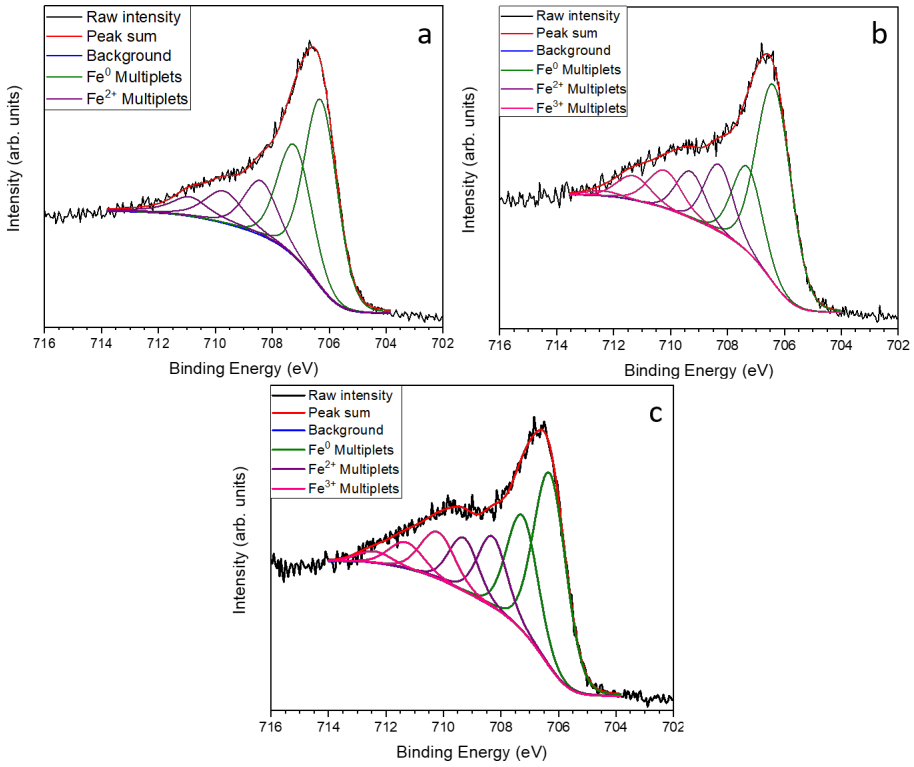

Figure 6.12: X-ray photoemission spectra of the Fe $2p_{3/2}$ peak for M036-1 with the associated deconvolution of the zero valent, Fe^{2+}, and Fe^{3+} states. (a) is for as-deposited Fe NPs on clean Si before exposure to oxygen in (b) and (c) for 7 and 14 L respectively.

shown in Figure 6.14 with (a) being M036-1 and (b) M035-3. It can be seen that the oxide component in the Fe $2p_{3/2}$ peak decreases which implies that the temperature was causing the oxide to reduce in some way.

A reduction in an Fe oxide layer was reported by Roosendaal et al. [42] where a clean thin film of Fe(100) was slowly oxidised under UHV conditions. The appearance of Fe^{3+} was determined to be the cause of the oxide growth stopping due to the cation current decreasing, as described by FC theory. They showed how upon heating the film, Fe^{3+} was reduced to Fe^{2+} which allowed the oxide film to grow thicker after further exposure to oxygen. This was repeated over many cycles of Fe^{3+} saturation, heating/reduction, and then further exposure. The authors noted however that the Fe^0 also oxidised into Fe^{2+} upon heating. However, it does appear that following the heating in this experiment the Fe^0 peak (at ~707 eV in Figure 6.14) remains a similar intensity. This suggests that the Fe^0 is not oxidising to Fe^{2+} and in fact the

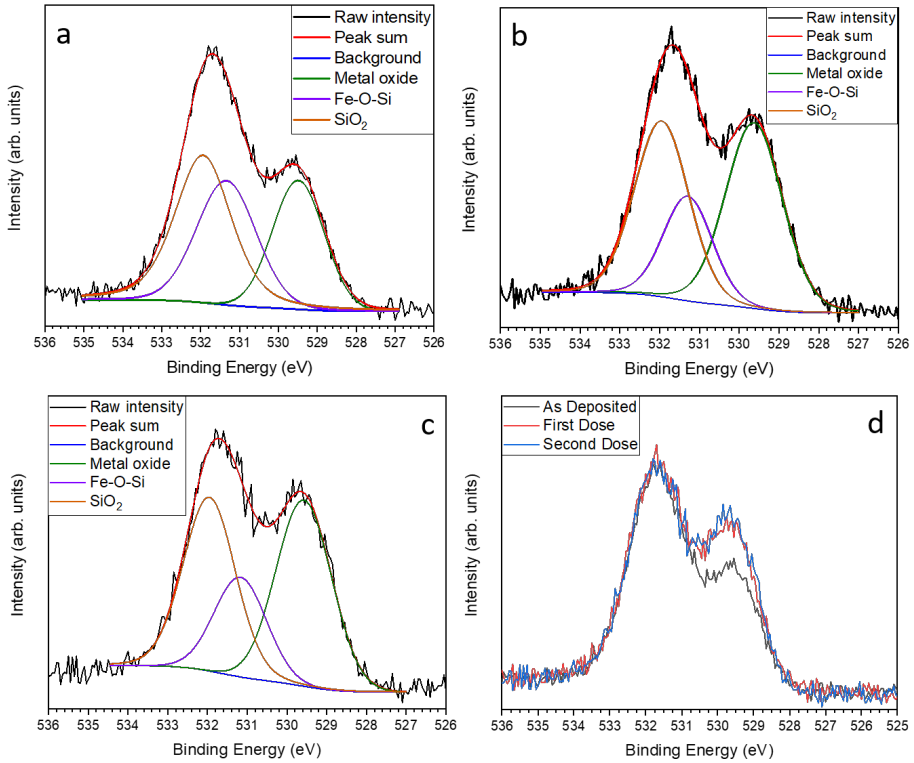

Figure 6.13: X-ray photoemission spectra of the O 1s peak for M036-1 with each peak deconvoluted to show the different oxygen contributions. (a) is for as-deposited Fe NPs with (b) and (c) the O 1s peak after being exposed to oxygen for 7 and 14 L respectively. (d) is a composite graph highlighting the overall change to the peak shape as the particles are oxidised in the vacuum system.

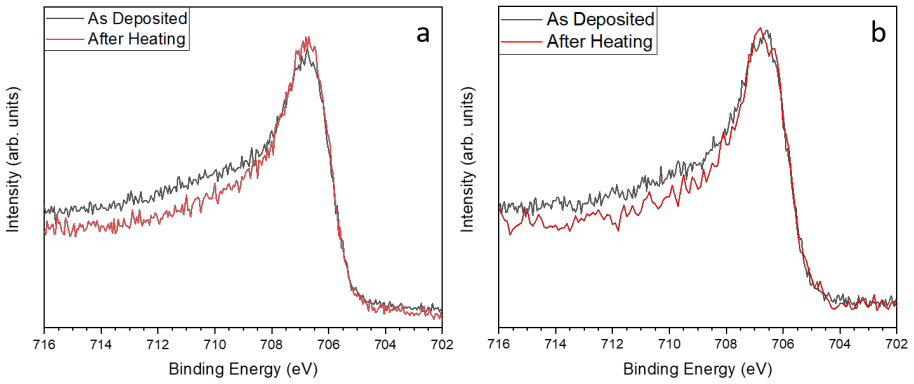

Figure 6.14: Comparison of the Fe $2p_{3/2}$ spectra after heating for M036-2 (a) and M035-3 (b) without being exposed to the oxygen gas from the doser. It appears that the oxide is reduced as the Fe^{2+} components have a lower intensity compared to the pre-heating spectra.

Fe^{2+} could be being reduced to Fe^0. Both oxides remain as $Fe_{1-x}O$ after heating with no oxygen dosing as shown in Figure 6.15.

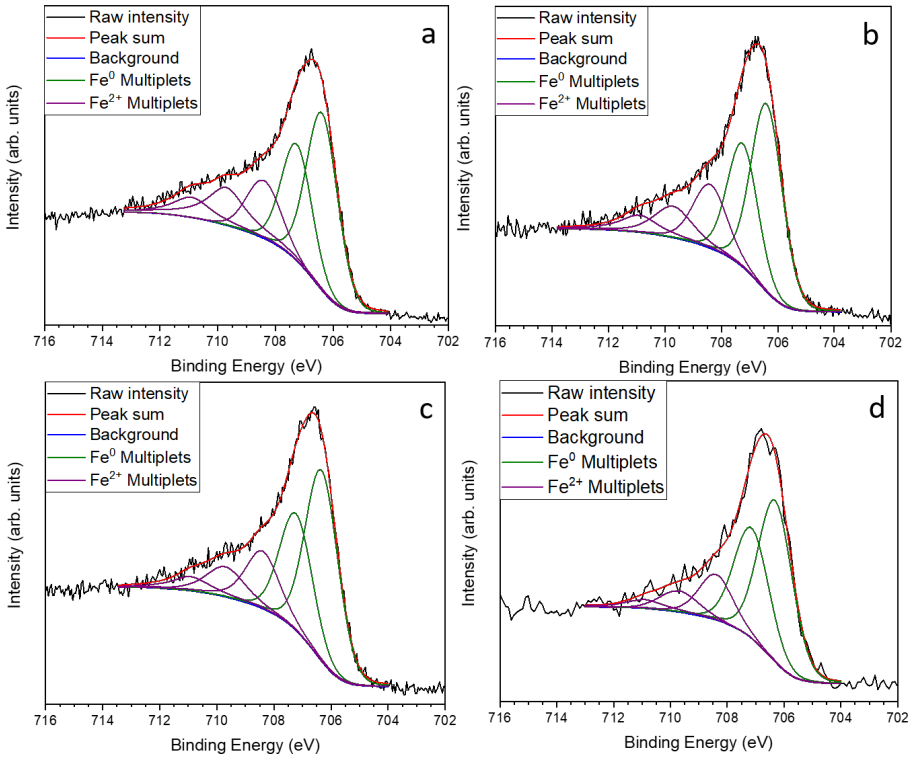

Figure 6.15: Deconvoluted X-ray photoemission spectra of the Fe $2p_{3/2}$ peaks before and after heating for M036-2 ((a) and (b)) and M035-3 ((c) and (d)). The oxide remains as $Fe_{1-x}O$ after heating at both temperatures with no exposure to oxygen gas from the doser.

The reduction of Fe oxides is of importance in steel production and catalytic reactions such as ammonia and carbon monoxide production, and Fisher-Tropsch synthesis (the production of hydrocarbons) [180]. Usually this requires the reduction of Fe in reducing atmospheres such as hydrogen and carbon monoxide at elevated temperatures [181]. The downside of this process is the large amounts of power needed to reduce the iron oxide in this way and the creation of harmful gasses such as CO_2. Carbon-free reduction of Fe oxides would counteract some of these problems as the harmful gasses would not be produced. Prabhakaran et al. [182] showed how γ-Fe_2O_3 NPs could be reduced on Ge and Si surfaces due to the bond strength to oxygen being stronger than to Fe. So under heating with no oxygen gas present, the oxygen preferentially bonds to the Si or Ge surface thus reducing Fe^{3+} to Fe^0. This is not a complete process as the authors noted that the Fe^{3+} is still present in

the XPS spectra after heating.

Interestingly, after the reduction due to heating, the Fe NPs then oxidise in different ways when exposed to oxygen at the elevated temperature. The Fe^{2+} contributions do not recover to the same level as before the sample was reduced and the zero valent component stays roughly the same. As shown in Figure 6.16, M036-2 initially reforms $Fe_{1-x}O$ after 7 L (Figure 6.16(b)) before then forming Fe_3O_4 after 14 L (Figure 6.16(c)).

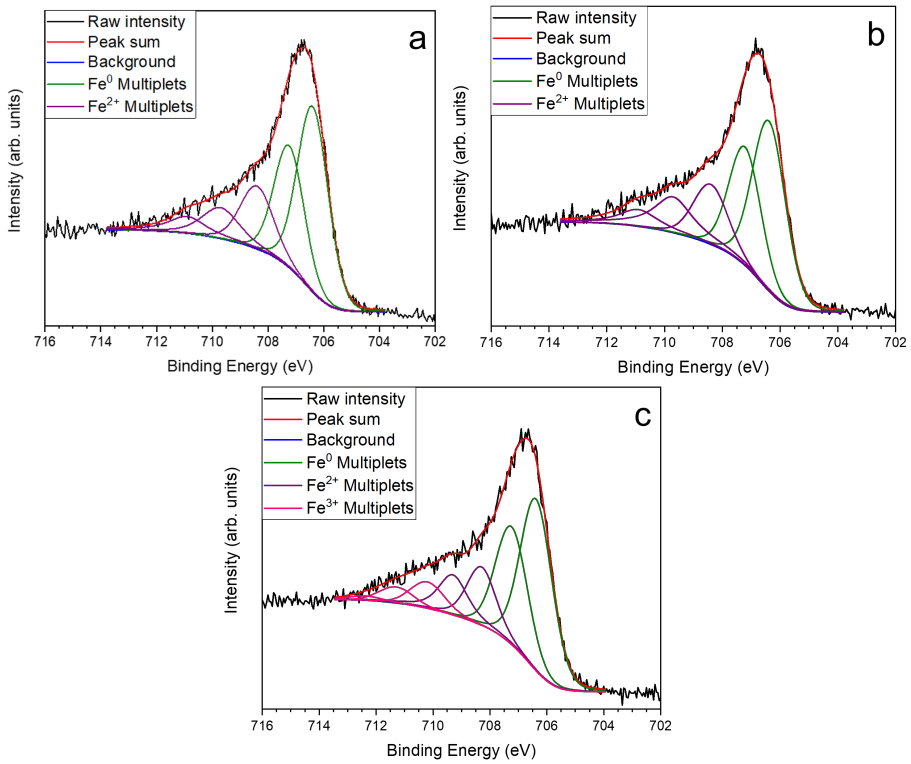

Figure 6.16: Deconvoluted Fe $2p_{3/2}$ peaks for M036-2 after oxygen exposure showing the transition from $Fe_{1-x}O$ to Fe_3O_4 after 14 L exposure to the oxygen gas at 648 K. The oxide initially re-grows as $Fe_{1-x}O$ (7 L exposure) after the reduction due to heating shown in (a) to (b) before then forming Fe_3O_4 after the 14 L exposure (c)

It can be seen in the O 1s peak for M036-2, Figure 6.17, that the SiO_2 peak grows more compared to the other two peaks with the peak contribution increasing from 41±3 to 47±3% (shown in Figure 6.17(b) and (c)) with the metal oxide peak showing no real change (29±2, 30±2, and 29±2% of the peak sums for the three peaks). This then shows how the SiO_2 peak is disproportionately growing as compared to the metal oxide peaks.

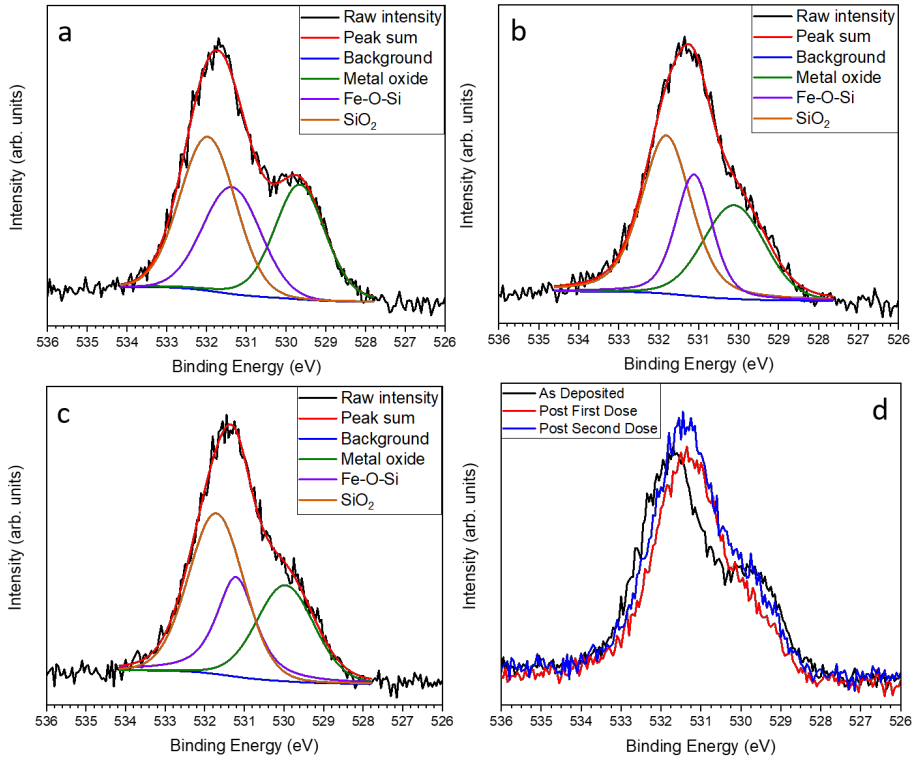

Figure 6.17: Deconvoluted O 1s peaks for M036-2 after oxygen exposure. (a) shows the as-deposited Fe NPs with (b) and (c) after oxygen exposure at 7 and 14 L respectively. These show how the SiO_2 peak grows along with the metal oxide peak due to the disproportionation between the two. The composite graph in (d) highlights the overall change of the peak.

When M035-3 was exposed to oxygen at the elevated temperature (after the heating reduction), the $Fe_{1-x}O$ layer reformed in a similar way to M036-2. However, at the higher temperature, the $Fe_{1-x}O$ layer grew over the period of 14 L instead of 7 L. It was only after another 7 L exposure (21 L total) that an Fe_3O_4 layer then formed. The Fe $2p_{3/2}$ peaks corresponding to this change are shown in Figure 6.18. The $Fe_{1-x}O$ peak fit has a reduced χ^2 value of 1.09 after 14 L (Figure 6.18(b)) and the Fe_3O_4 has a value of 1.09 (Figure 6.18(c)) after 21 L of exposure. These high values of reduced χ^2 could be due to the larger levels of noise due to the weaker Fe signal in M035-3 but could also be due to the fact that the Fe_3O_4 is not a perfect fit which hints at potential mixed oxide states. Due to the crystal structures of Fe_3O_4 and γ-Fe_2O_3 being similar, it is hard to distinguish between the two through XPS alone. A fit of the data was attempted with a mixed oxide of Fe_3O_4, γ-Fe_2O_3, and $Fe_{1-x}O$ using the parameters from Ref. [175] but the lowest reduced χ^2 value was achieved

when only Fe_3O_4 was used.

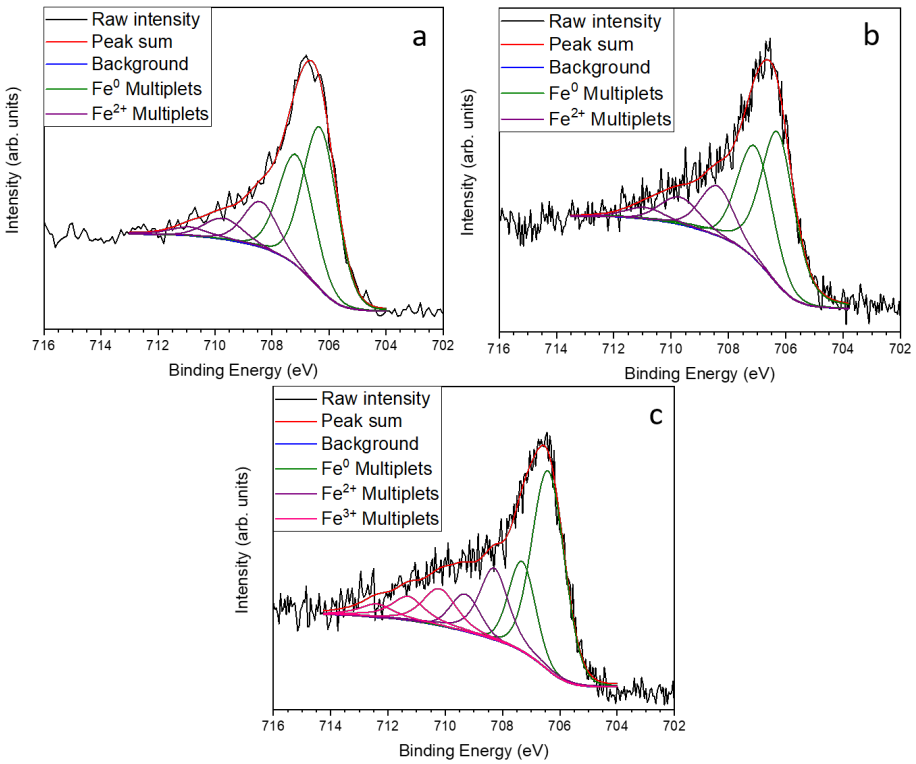

Figure 6.18: Fe $2p_{3/2}$ spectra for M035-3 where the system is Fe@$Fe_{1-x}O$ after heating (a) and also after 14 L of oxygen exposure in (b) with the sample only changing to Fe_3O_4 after 21 L of oxygen exposure in (c).

The O 1s peak for M035-3 shows a similar development to that of M036-2 with the SiO_2 growing more compared to the metal oxide peak. Figure 6.19 shows that the metal oxide feature for M035-3 decreased to 6.0±0.4% after the entire exposure from 16±1% after deposition (Figure 6.19(a) to (b)). While this could be due to the fact the entire O 1s peak area increases in size from 915±46 to 1572±79, the metal oxide contribution still shrinks in size from 146±7 to 97±5. Therefore, the reduction of the metal oxide contribution between the two peaks is due to a diminished metal oxide and not due to the overall peak just becoming larger. The peak sum in M036-2 is unchanged and so the argument remains the same. The SiO_2 peak grows from 45±3 to 51±4% of the peak area with the Fe-O-Si peak also increasing from 39±3 to 43±3%. This clearly shows the disproportionation between the oxidation of the Si and the Fe at the elevated temperature.

The changes from clean Si to deposited Fe NPs to a fully oxidised system can also

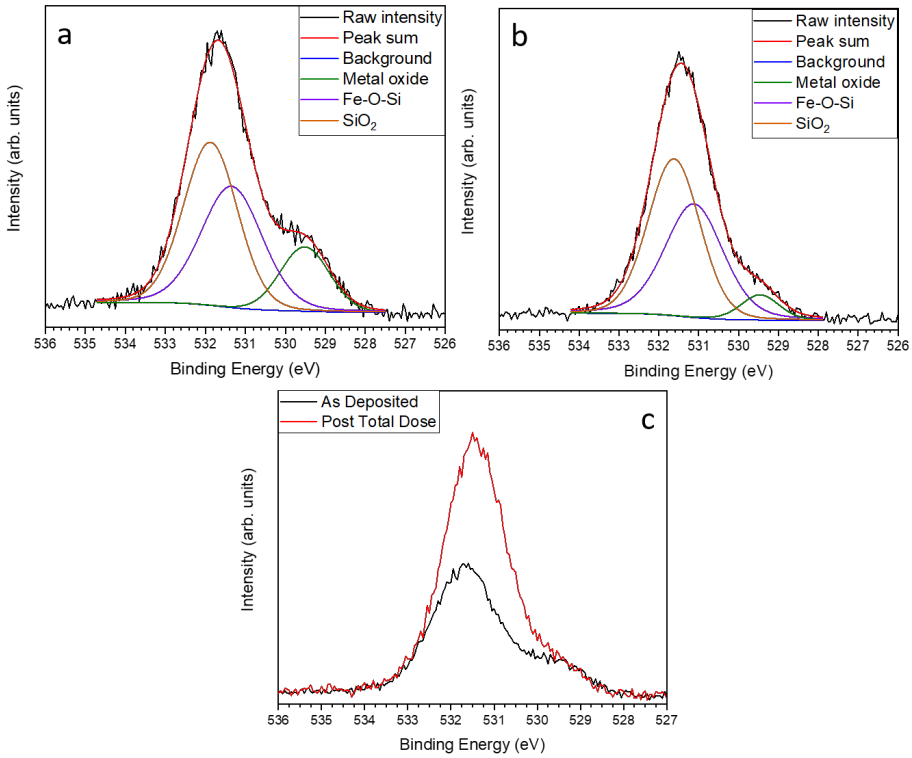

Figure 6.19: O 1s peak for M035-3 for the as-deposited Fe NPs (a) compared to after the full 21 L exposure (b). Similar to M036-2, the SiO_2 peak grows more compared to the metal oxide peak. The composite graph (c) shows how the peak has changed over the reaction.

be detected in UPS spectra. Here the changes in the features of the different spectra shed light on the changes at the surface, as shown in Figure 6.20. This figure shows how the UPS spectra changed across M036-1, from the cleaned Si, to pre-exposed particles and then to oxidised particles.

The dashed lines and numbers in Figure 6.20 show the different features in the spectra that change and develop over the exposure. Point (i) is the Fermi level, E_F defined as 0 eV. Emission in this region is due to the metal Fe NPs and is only present when they have been deposited onto the clean Si. This is to be expected due to the surface becoming more metallic due to their presence. Point (ii) at $\approx$ 2.3 eV below the Fermi level, is only present on the cleaned Si surface. This feature can be explained by emission from bulk Si states [183].

Point (iii), at $\approx$ 4.9 eV below the Fermi level, appears as the Fe NPs oxidised with the shoulder becoming more pronounced from the partially to fully oxidised states.

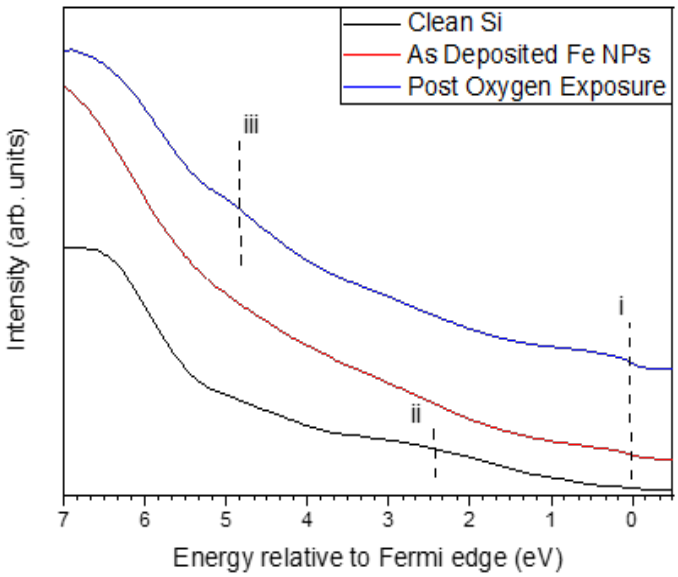

Figure 6.20: UPS spectra for M036-1 showing the development of the oxide layer at RT. The labelled features are explained in the text.

This feature is due to the d band electrons in the Fe oxide which becomes stronger as the Fe becomes fully oxidised to the Fe^{3+} state of Fe_3O_4 [184].

6.5 Summary

In this Chapter, it has been shown that the initial oxide that forms on Fe NPs through the gas condensation technique was $Fe_{1-x}O$. Fe@Fe_3O_4 (core@shell) particles could be formed if the target and gas lines had not been cleaned. On exposure to oxygen, the Fe@$Fe_{1-x}O$ layer grew to some critical thickness before transforming into an Fe_3O_4 layer. Due to the limitations of XPS, it is hard to deduce whether the final oxide product is some sort of mixed phase. The changes in the surface could also be observed using UPS with the system changing from clean Si, after the deposition of particles, and then after they had oxidised.

It was also found that the oxide could be reduced through heating the particles first, with the oxide component in the Fe $2p_{3/2}$ peak decreasing in intensity. The increase in the Fe^0 peak in the Fe $2p_{3/2}$ spectrum in M036-2 shows that Fe^{2+} is being reduced to Fe^0. This method could pave the way for carbon-free reduction of Fe oxides which is important for industrial purposes as well as important in catalytic

reactions. Interestingly, it was also observed that at the highest temperature of 848 K in M035-3 the oxidation took longer compared to the lower temperatures with a higher dose of oxygen needed to form the Fe_3O_4 layer. This could be resistive oxidation of the particles due to the disproportionation of the reaction with the SiO_2 as this appeared to preferentially form over the Fe oxide.

The fact that a single oxide crystal, and not a mixed crystal state, appears to form across the temperature ranges confirms the assumption in FC theory. The theory stated that for the oxide to grow that only one type of oxide must be involved. This is confirmed by the initial oxidation of the $Fe_{1-x}O$ layer to Fe_3O_4 followed by the growth of the Fe_3O_4 layer. The oxidation rate in M036-1 appears to slow down as the metal oxide component in the O 1s peak does not increase by as much between 7-14 L compared to 0-7 L. This confirms that firstly, the oxide layer was very thin in the as-deposited particles as well as that the oxide shell is reaching a critical thickness as confirmed in CM theory. As the sample is at RT then there is not sufficient thermal energy to produce thermionic emission of the electrons to continue the oxidation process as described in FC theory.

Chapter 7

Investigation of the Stability of Ag-Coated Metal Core-Shell Nanoparticles

Following the development of the core-shell coater, outlined in Chapter 4, silver (Ag) was loaded into the crucible so that core-shell particles could be created. Ag was chosen due to its biomedical applications [185] as well as it being non-magnetic such that exchange interactions would not occur with the magnetic Fe core. The goal of coating with Ag is to provide a sacrificial layer to the oxidation process so that Ag oxide is created and the pure metal core is preserved. This is acutely relevant for iron due to the varying properties of the Fe oxides, as discussed in Chapter 6, such as the saturation magnetisation decreasing from 217.6 emu/g for pure Fe [186] to 74 for γ-Fe_2O_3 [187]. Finding a way to control the oxidation process is extremely important so that pure Fe NPs can then be used in various applications.

In this chapter, the interaction of metallic cores (Fe and Cu) with a coating of Ag is explored. Through the use of control samples and spectroscopy, it was shown that the Ag is only present on the sample when the NP flux passes through the coater. The Fe oxidation reaction was found to be catalysed by the added Ag showing an enhanced oxidation with localised growth occurring forming a nanowire (NW). Clear voids in the Fe core were present next to the growth of the NW. The Cu NPs were found to be more stable with no NW growth present though both parts of the

particle were completely oxidised.

7.1 Core-Shell Coating

The potential uses of magnetic NPs in various industries and applications are dependent on their magnetic properties. Degradation of the metal due to oxidation can then lead to a weakened magnetic state, as explained in Chapter 6. The secondary shell material could act as a protective layer to stop the pure magnetic core from oxidising and therefore degrading. Creating a protective layer around the pure core is an important step to allow more widespread use of these particles in applications such as water treatment or the biomedical space. Coating the Fe with Ag means that exchange interactions, as described below in this section, do not occur between the magnetic core of Fe and the potential shell material of Ag. Understanding the coating mechanism and the properties of the particles produced is the first step prior to then introducing these particles to applications.

Small magnetic particles also face the problem of super-parmagnetic effects. This is the phenomenon where the magnetisation direction can change along the easy axis due to thermal fluctuations [8] with the time between each change being the Néel relaxation time. Below a certain temperature, termed the "blocking temperature" there is not enough thermal energy for the magnetisation direction to change and so the particles exhibit ferromagnetic behaviour. Above this temperature, the particles exhibit super-paramagnetic behaviour is applied as the overall magnetisation, if measured at lower frequencies than the Néel relaxation time, is shown to be zero. This has led researchers to investigate whether it is possible to stop the reversal of the magnetisation direction. One possible solution is creating core@shell particles which are magnetically coupled.

When the core@shell arrangement is a ferromagnet coupled to an anti-ferromagnet then exchange bias can occur. This is where the system is field cooled below the Néel temperature of the anti-ferromagnet which causes the spins at the interface to couple with the spins in the ferromagnet. This results in increased coercivity as well as magnetic anisotropy of the core which then produces a significant increase in the

blocking temperature [104]. This phenomenon was first observed by Meiklejohn and Bean in Co@CoO NPs [188, 189]. While this can be done by coupling a ferromagnet with an anti-ferromagnet, exchange bias can also be achieved by coupling soft and hard magnetic materials such as Fe NPs in a Pd matrix as shown by Baker et al. [190]. It can also be achieved by growing "inverted" particles where the core is anti-ferromagnetic instead of ferromagnetic [191]. Preparing the particles in this arrangement is beneficial as the controlled growth of an anti-ferromagnetic shell layer on a ferromagnetic core is difficult which can lead to poor crystallinity and therefore a weakened exchange bias [192]. These "inverted" particles have demonstrated tunable blocking temperatures by changing the size of the core and shell [192].

The atomic magnetic moment of the NPs can also be altered by changing the crystal structure through coating with a secondary material. Baker et al. [193, 194] reported how the crystallinity of Fe NPs could be changed from BCC to FCC when embedded in a sufficiently thick Cu layer which in turn led to a decrease in the atomic moments of the Fe NPs. When the particles were embedded in a Au-Cu alloy, the moments were enhanced though the Fe retained its bulk BCC structure when embedded just in Au. Ag was shown to have no effect on the crystallinity of the Fe which retained a BCC structure regardless of thickness or Fe content. The authors showed that for sufficiently low coatings of Cu or Au, the crystal structure of these coatings changed to BCC from FCC due to coupling with the Fe with strong inter-atomic forces present.

In addition to magnetic studies, research in this field has led to the creation of functionalised particles for biomedical research. Chen et al. [195] showed how Fe NPs could be better functionalised with active agents if small Au NPs were attached first. The Au NPs then acted as anchor points for the active bio agents due to their preferred interaction with the active agents compared to the Fe surface.

Cu@Ag is also relevant for electronics applications [196] where Ag is commonly used due to its high conductivity and oxidation stability. Unfortunately, Ag is expensive and rare so Cu is used instead as it has a similar electrical conductivity and is also cheaper but oxidises far more easily than Ag. If Cu NPs can be coated in Ag, then it provides a good compromise to cost, oxidation, and conductivity for potential

electrical applications.

The growth, application, and properties of core@shell NPs are of wide interest with many other applications provided in the literature in addition to those discussed in this text. Notable review articles are Refs. [197–199].

7.2 Control Samples and Calibration

Chapter 4.3.1 described the process of building the core-shell coater and calibrating the crucible temperature. During operation, the inner thermocouple used for this calibration was removed and only the outer thermocouple was present. The calibration graphs produced (see Figure 4.13) allow the current and temperature measured on the outside of the crucible to be used to determine the temperature on the inside of the crucible.

After this temperature calibration, a used high-purity Ag magnetron sputter target was cut into small chunks (around 2-5 mm in size). These were then loaded into the centre of the crucible such that when placed end-to-end they covered the 106 mm length of the crucible. The crucible and the Ag were cleaned by initially outgassing at an external crucible temperature of 200 °C with no water cooling which was followed by a second step of 600 °C with water cooling. This allowed for the crucible and Ag to be cleaned of contaminants before the particles were then exposed to the Ag vapour.

Ag has a melting point of 961.8 °C and in practice a sufficient vapour pressure is achieved at 1100 °C. The first step to producing core-shell particles was determining the point at which adequate Ag coverage was achieved without rapidly evaporating all of the Ag present in the crucible. This was determined by producing two samples of Fe on Si at different crucible temperatures and then comparing the amount of Ag present using quantitative XPS. The Si crystal wafers were exposed to the particle beam for 5 minutes each with the crucible at either 950 °C (just below the Ag melting point) and 1000 °C. The NP source settings were the same for both with the plasma current and voltage set to 373 mA, and 252.1 V respectively, the plasma gas flow at 90 sccm, the carrier gas flow at 100 sccm, and an insertion length of 140

mm (minimum insertion length).

Quantitative XPS was performed using the method described in Section 3.2.1 with charging in the spectra accounted for by referencing the C 1s peak and a normalised background used so the peaks can be compared. The XPS spectra for the Ag 3d peaks are shown in Figure 7.1 for each crucible temperature. The ratios of Fe:Ag were calculated for each crucible temperature and are shown in Table 7.1 where it can be seen that the ratios decrease with crucible temperature. This means that the amount of Ag is increasing and so the particles will be more adequately coated at the higher temperature. The associated errors in the ratio values arise from the error in the calculation of the integrated area from Origin when performing the quantitative XPS method. The error in crucible temperature is based on the error in the fit of the line given in Figure 4.13(b).

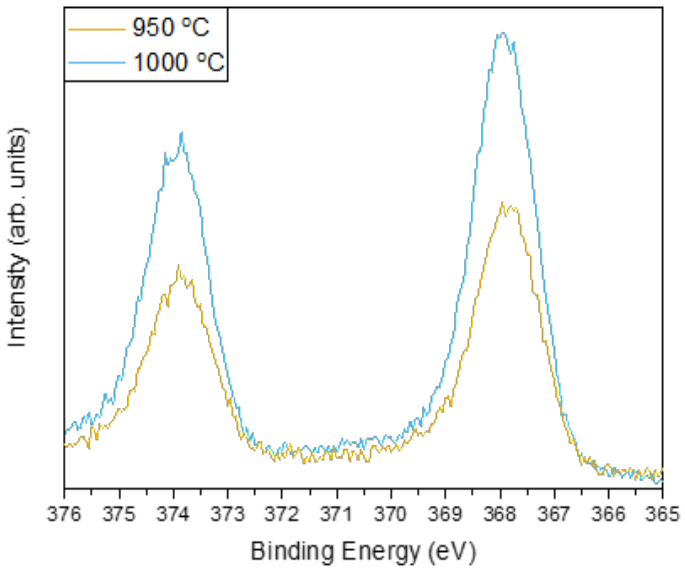

Figure 7.1: Normalised X-ray photoelectron spectra of the Ag 3d region showing the increasing amounts of Ag present in a core@shell sample as the crucible temperature is increased.

Control samples were also produced in order to clarify that the Ag being seen in the spectra was due to it being attached to Fe NPs and not in fact due to it being deposited directly onto the substrates. This was achieved by creating two Si samples, with one exposed as normal to the Fe NP beam that was passing through the crucible and the second with the sputtering plasma turned off but leaving all other conditions the same. This meant that the crucible was at 1000 °C with the same gas flow passing

Crucible Temperature (°C)	Fe:Ag ratio
950±5	10.0±0.7 : 1.0±0.1
1000±5	5.0±0.3 : 1.0±0.1

Table 7.1: Fe:Ag ratio calculated using quantitative XPS for different crucible temperatures.

through it as was used to produce the Fe NP flux. The QMF was also still on and scanning the same region as for the first Si control sample. Both were exposed for the same period of time and then removed from the system and studied using XPS. The conditions for growth were as follows: 15 minute exposure; plasma gas: 90 sccm; carrier gas: 100 sccm; core-shell coater: 5.75 A, 41.1 V. With the plasma on and sputtering the Fe target, the values on the power supply were: 373 mA, 252.1 V, 140 mm insertion length. The QMF was set to scan from 0.5 - 50 nm with a step of 0.5 nm for both samples.

The results of these control experiments are shown in the XPS spectra of Figure 7.2 which clearly demonstrate that without the Fe NP flux passing through the crucible, the Ag does not deposit on to the sample being exposed. Ag is clearly present in the first sample with the particle flux but absent in the second sample when the particle flux is removed. This is good evidence to show that the presence of Ag in the spectra is due to core-shell particles.

7.3 Core@Shell Particle Growth

Following the characterisation of the growth conditions as well as confirmation of the presence of Ag due to the core-shell arrangement, samples were grown to study the interaction of Ag as a secondary shell material. Fe@Ag and Cu@Ag particles were grown and deposited onto gold TEM grids (described in Section 4.3.3) and a Si crystal wafer to study the stability of the particles and to characterise the interaction of these metals with the shell material. The grids were imaged on the JEOL 2100+ microscope within a few hours of being removed from vacuum and then left in a desiccator at atmospheric pressure for 30 days before being imaged again.

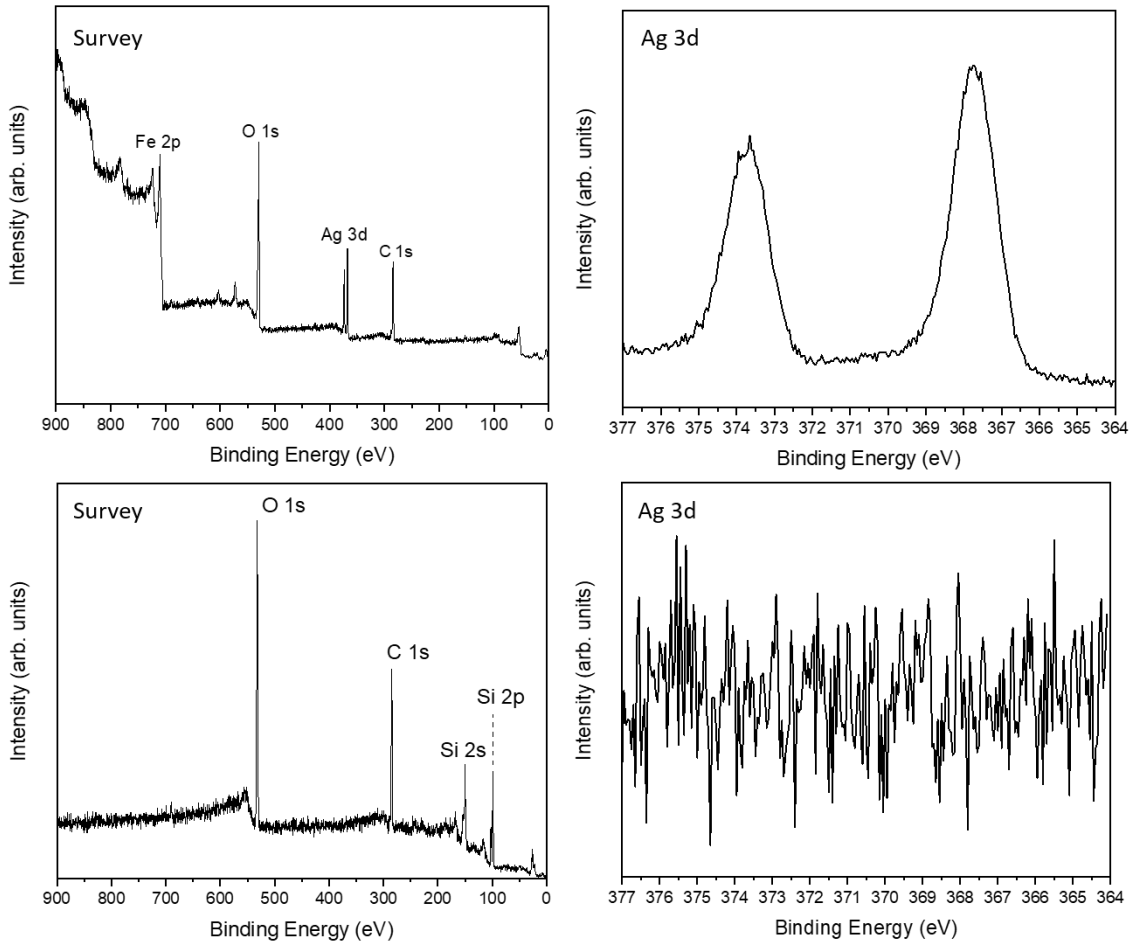

Figure 7.2: X-ray photoelectron spectra of the Fe@Ag sample (top two spectra) and the corresponding control sample (bottom two spectra) with the production details described in the text.

The Si crystal wafers were loaded into the electron spectroscopy system, described in Chapter 3, and probed using XPS within a few days of production. This was to confirm the presence of Ag in the samples and the ratio of Ag to metal as well.

The exact production details of the samples are given in Table 7.2 below. The core-shell coater was set to the same conditions for each sample using a crucible filament current of 5.75 A (41.1 V) giving a total power of 236 W. Both sets of TEM grids were exposed for 1 minute and the Si wafers were exposed for 10 minutes.

Sample	Plasma gas flow (sccm)	Carrier gas flow (sccm)	Plasma current (mA)	Plasma voltage (V)	Insertion length (mm)
Fe	85	85	273	277.6	140
Cu	35	35	164	362.7	140

Table 7.2: Settings for the cluster source used to produce both Fe@Ag and Cu@Ag core-shell NPs.

7.3.1 Characterising the Growth of Fe@Ag Particles

Following the growth of the particles, the presence of Ag in the samples was confirmed by performing XPS on the Si crystal wafer, as shown in Figure 7.3. No charging was present in the sample determined by comparing against the C 1s peak which was at 284.7 eV, as expected [200]. The Ag $3d_{5/2}$ peak was fitted with a single peak, shown in Figure 7.3 (b), with a central position of 367.8±0.1 eV which is shifted from 368.2 eV for pure Ag [201]. This shift is expected for the Ag $3d_{5/2}$ peak when Ag is oxidised to Ag_2O [202]. The ratio of Fe:Ag was calculated to be 5±1 : 1.0±0.3. A closer ratio implies a more adequate coating of Ag and with more Ag present in the sample, the interaction of the two elements can be more easily studied.

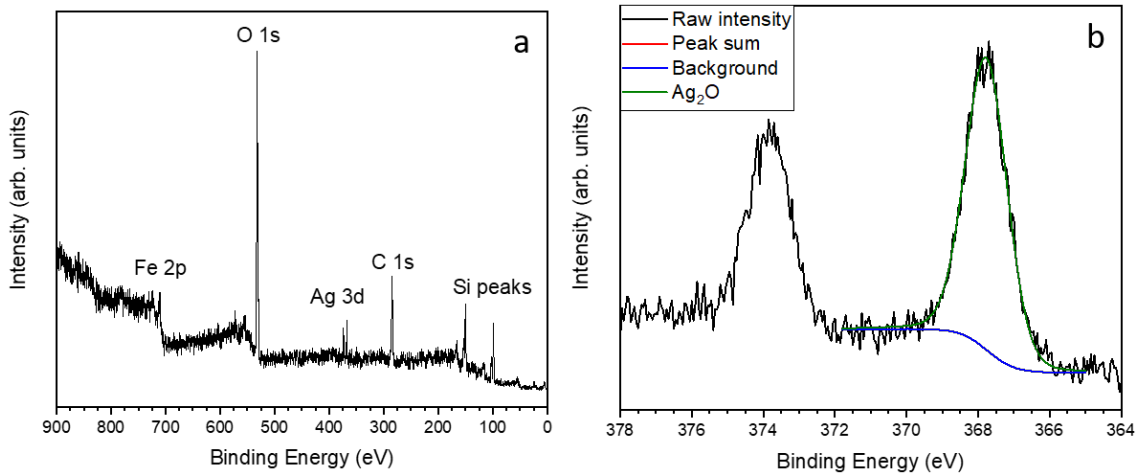

Figure 7.3: X-ray photoelectron spectra of Fe@Ag particles deposited on a Si crystal wafer. (a) shows a survey spectrum with the various chemical elements labelled and (b) shows the Ag 3d peak and a fit to the $3d_{5/2}$ peak.

The deconvolution of the Fe $2p_{3/2}$ peak is shown in Figure 7.4 which shows a relatively small amount of Fe^0 (meaning that some pure Fe is present) with a dominant oxide shell, most likely Fe_3O_4 due to the presence of the Fe^{2+} and Fe^{3+} multiplets. As in Chapter 6, the fitting procedure of the Fe oxide followed that of Grosvenor et al. [175]. As the Si was not cleaned prior to deposition, there is likely to be large contamination of the sample as the surface oxide of the Si will oxidise the Fe NPs as they deposit onto it. This would explain the large oxide contribution in the Fe $2p_{3/2}$ peak as well as the presence of carbon in the survey spectrum, Figure 7.3(a).

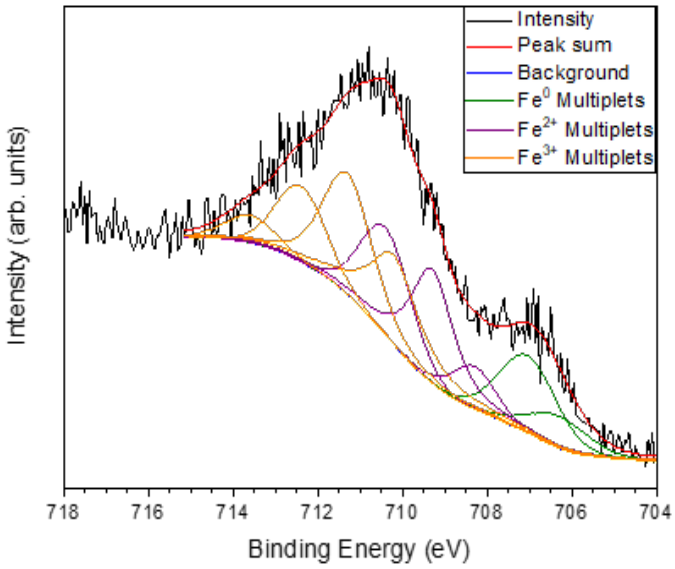

Figure 7.4: Deconvoluted X-ray photoelectron spectrum of the Fe $2p_{3/2}$ region showing the presence of Fe^0, Fe^{2+}, and Fe^{3+}. The fitting parameters of the peaks were the same as Grosvenor et al. [175] which confirms that the oxide is most likely Fe_3O_4.

The deconvoluted O 1s peak is shown in Figure 7.5. Here, a small metal oxide component is present due to Ag_2O and Fe_3O_4. The contaminants in the sample are due to silicon oxide, water vapour, and hydroxides present on the surface as the Si was not cleaned before deposition.

Bright-field TEM images of the NPs, shown in Figure 7.6, show a clear contrast between two areas of the particles which suggests that they have formed Janus-like structures. The difference in contrast is due to the difference in atomic number, Z, between Fe and Ag which causes the electron beam to scatter by increasing amounts equated to Z^4 and therefore the higher-Z, Ag, to appear darker. From the bright field images, the mean particle size was measured using ImageJ. The particles' projected

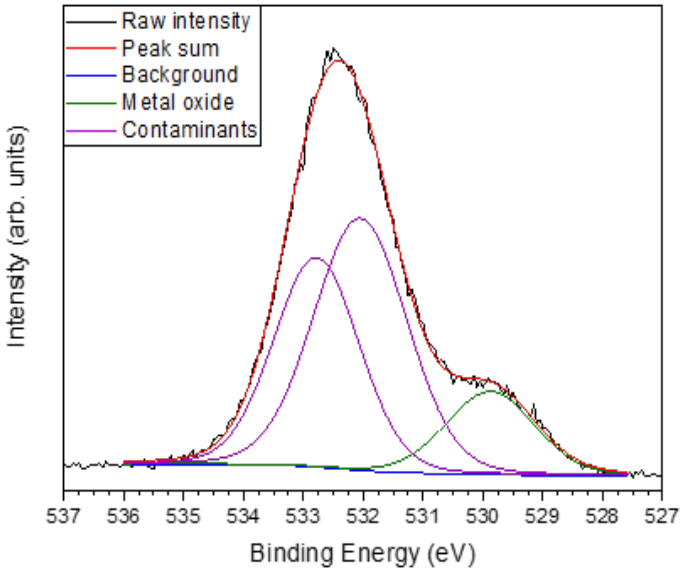

Figure 7.5: Deconvoluted X-ray photoelectron spectrum of the O 1s region showing the presence of metal oxide as well as contaminants on the surface. These contaminants will likely be silicon oxide as well as water vapour and hydroxide due to the Si not being cleaned pre-deposition.

area can be measured using the "Analyse Particles" function and then the diameter calculated assuming a spherical geometry. This only gives an estimate of the size distribution of the deposited particles as it does not account for cubic geometries, aggregated particles, or the Janus-like structure. A resulting histogram plot, shown in Figure 7.7, displays a log-normal distribution with the centre of the peak at 11.4±0.3 nm.

Magnifying certain particles under the HR-TEM reveals a clear crystal structure inside the Fe core and the Ag coating, as labelled in Figure 7.8. Here the Janus-like particle structure is more obvious with two clear distinct regions shown in the images. The Ag region shows a faceted structure which is different between the two Fe particles. This is potentially due to the fact that Figure 7.8(a) shows a more cubic Fe core whereas the NP in Figure 7.8(b) is a Wulff polyhedron, probably a truncated dodecahedron [93]. Fe and Ag are not miscible due to exhibiting no mixed phase at any atomic composition and temperature across the entire phase diagram [203]. This phenomenon is usually down to the enthalpy of mixing being a large positive number and so the two elements struggle to form alloys [204].

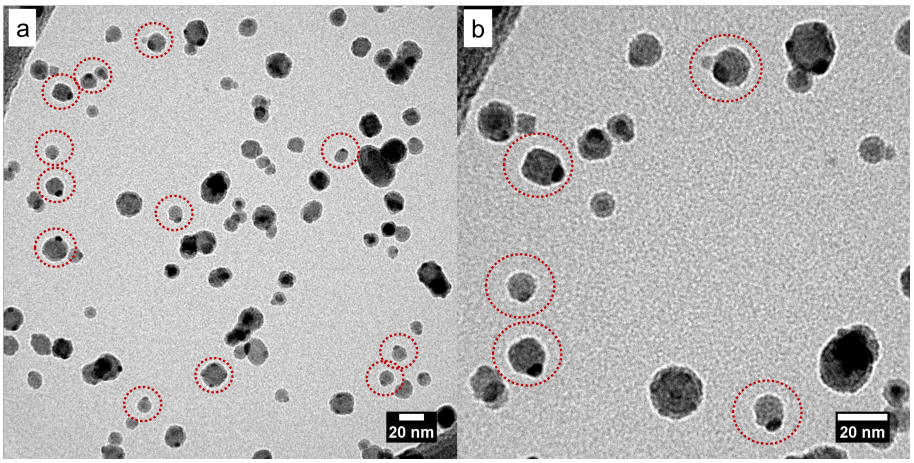

Figure 7.6: Bright-field TEM images showing the Fe@Ag particles with the red dashed outline present to highlight some of the particles that have a Janus-like structure. (b) is a magnified image of a region of (a) which shows clearly how the particles have formed Janus-like particles instead of a core-shell structure.

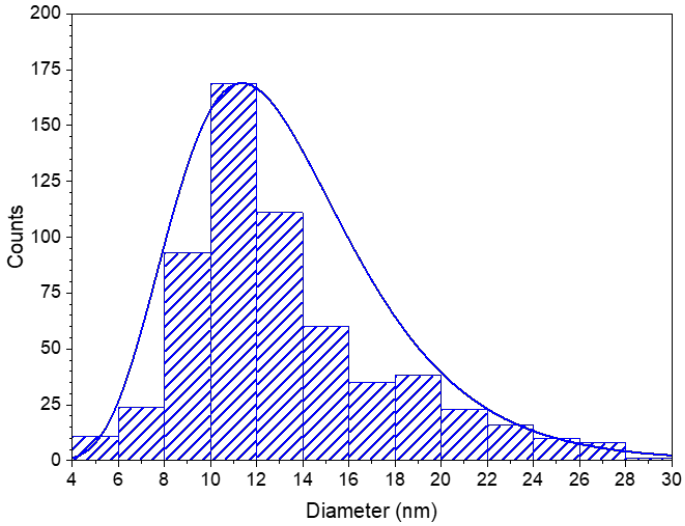

Figure 7.7: Histogram of particle sizes as measured using ImageJ from the bright field images of the Fe@Ag particles with a fitted log-normal distribution. The centre of the log-normal distribution sits at 11.4±0.3 nm.

Combettes et al. [94] modelled the growth of Fe@Au and Fe@Ag particles using density functional theory and showed how for the case of Ag on either the Wulff or cubic cores that a Janus-like structure is expected. This is due to the high interface energy and a small value for the wetting parameter for the Ag resulting in the Ag preferentially forming one main structure on deposition. By forming this structure, the NP limits the energy cost by reducing the interface area. As the amount of Ag is

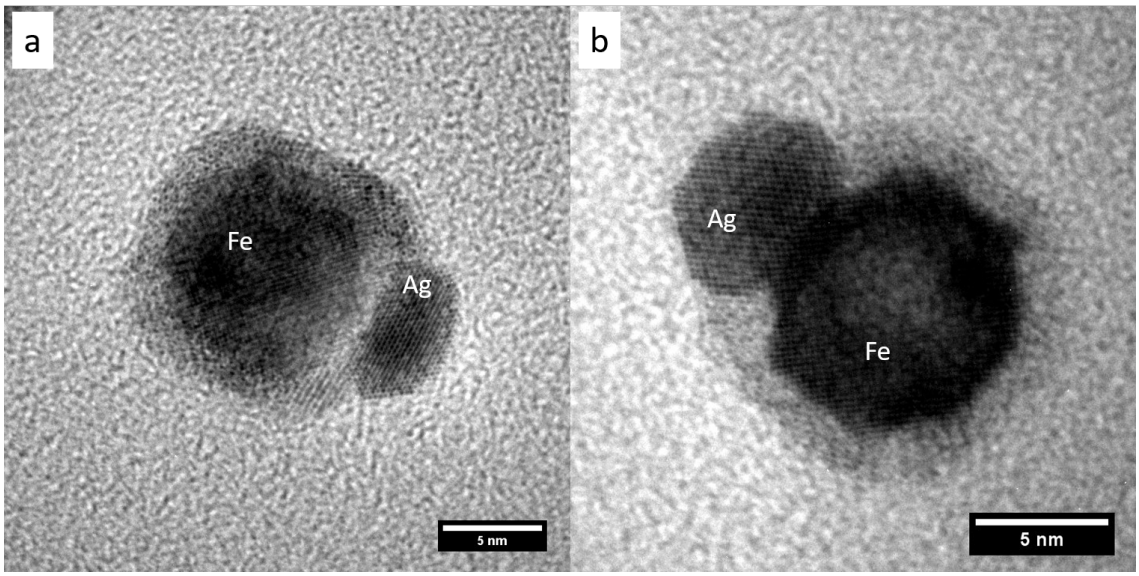

Figure 7.8: Fe@Ag (core@shell) particles with the Fe core labelled and the surrounding Fe oxide attached to the Ag particle. In (a), a cubic Fe core shows a small Ag island attached and (b) shows a Wulff Fe core with a larger Ag island attached with clear faceted structure.

increased, more of the particle is then covered with a secondary island of Ag forming when the ratio of Ag to Fe is large [94]. In contrast to Ag, a core-shell arrangement is expected for a Au coating as shown in the modelling performed in [94] which then allows the Au to fully coat the Fe core regardless of shape.

These Janus-like structures were also shown in experimental results from Ramade et al. [205, 206] where Fe@Ag particles were produced using laser vaporization of a bimetallic target. This approach leads to the formation of particles in the gas phase in a similar fashion to the magnetron sputter source used in Merlin, as described in Chapter 4. The Fe component of these particles rapidly oxidised when exposed to atmosphere to form Fe-oxide/Ag particles. Overall, it can be seen from these structures that the particles had a similar Janus-like structure which the authors described as "nano-fried eggs". The Janus-like structure was also produced by Benelmekki et al. [207] by the co-sputtering of multiple targets during the growth stage in a gas-phase aggregation cluster source. In this work, the authors co-deposited Fe and Ag alongside Si which forms a ternary multicore structure where the smaller Fe and Ag particles became trapped inside the Si. This meant that the Fe and Ag components were then separated while maintaining the desired properties of a plasmonic noble

metal coupled to a magnetic system. The authors also found that the Fe and Ag aggregated together to form a Janus-like particle inside the Si shell.

Fast fourier transforms (FFT), which show the frequency space of a selected region, are akin to a simulated diffraction pattern and can be used to perform lattice plane analysis of crystal structures. These can then be compared to known values to label zone axes as well as lattice planes in the images. A member of the NP group at York, Mr S. Alotaibi, kindly simulated the expected diffraction patterns for different zone axes of various crystal structures in the software JEMS. These can then be compared to the values obtained from the FFT analysis of the images for the Fe@Ag particles.

Figure 7.9(a) again shows the Fe@Ag NP in Figure 7.8(a) but with two regions highlighted from which the FFTs were taken. The same analysis was also performed on the NP in Figure 7.8(b) as well as other particles not shown here and the results were consistent. The respective zones are selected such that the produced FFTs are only taking into account either the Fe, Figure 7.9(b), or the Ag, Figure 7.9(c), region respectively. The values quoted in the FFTs in Figure 7.9(b) and (c) are the respective distances between the lattice planes represented by the spots. The FFT analysis was performed in ImageJ with the "Find Maxima" function used to place points on the spots at their highest intensity (based on gray value). This allowed a consistent method of measuring the lattice planes.

Figure 7.9(b), the FFT of the Fe region, shows the same FFT diffractogram structure as for Fe[001] zone axis with the labelled spots corresponding to the shape of the (110) and (200) planes shown in Figure 7.10(a). The extra specular spots between the ones circled with the yellow dashed lines in the FFT are most likely due to the oxide. The quality of the FFT makes it hard to distinguish exact spots and therefore determine the exact crystal structure in the Fe oxide, though the XPS analysis (Figure 7.4) shows a clear Fe@Fe_3O_4 relationship so it is most likely the inverse-spinel crystal structure of Fe_3O_4. Figure 7.9(c), the FFT of the Ag region, matches the Ag[110] zone axis with the labelled spots corresponding to the (111) and (020) planes shown in Figure 7.10(b).

The measured distances for the Fe core and the Ag area in Figures 7.9(b) and (c) do not match the expected distances from the JEMS simulations with each of the

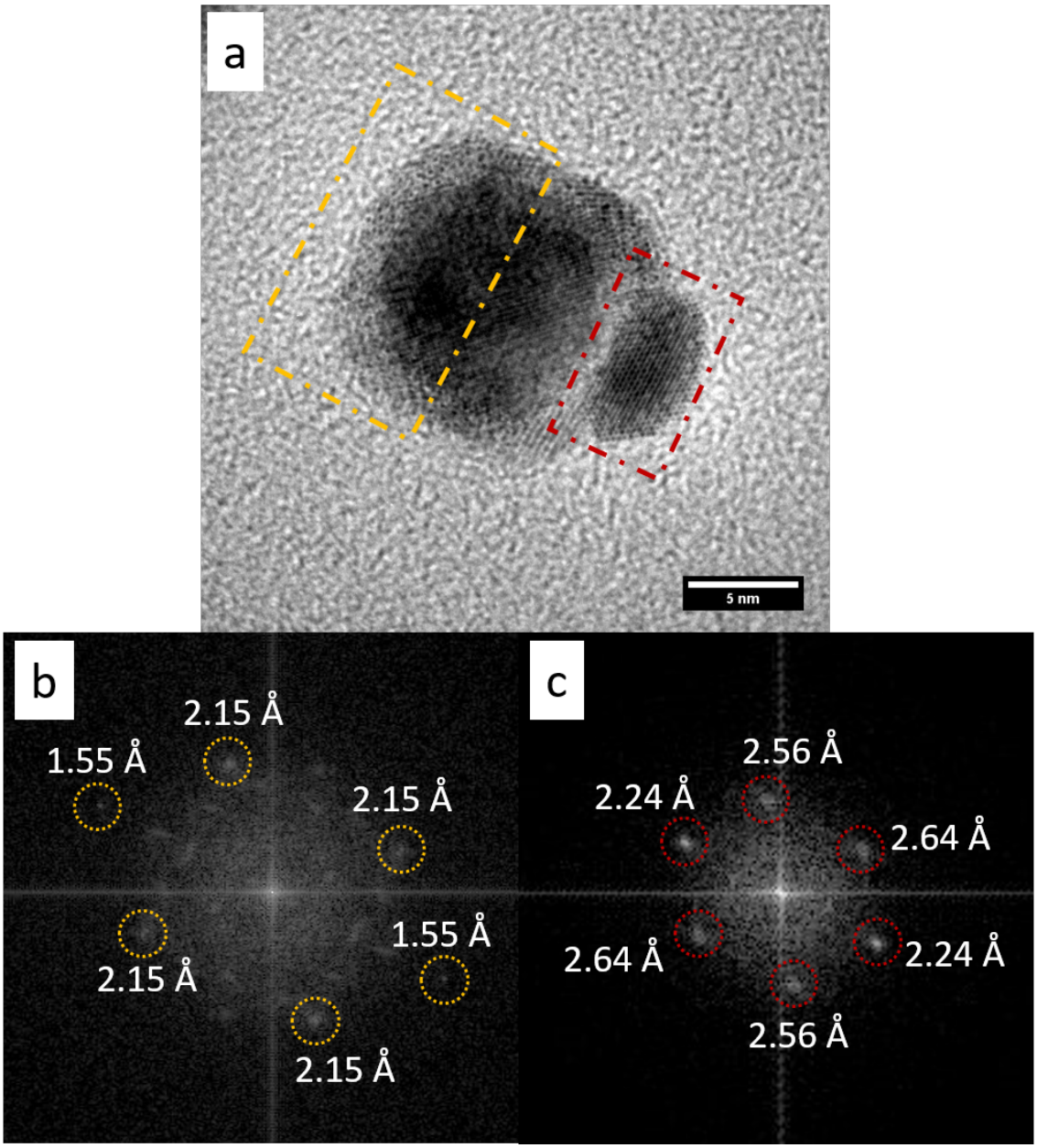

Figure 7.9: FFT analysis of a Fe@Ag particle showing distinct zones for the Fe and Ag regions. The yellow and red areas highlighted in (a) were used to produce the corresponding FFT diffractograms shown in (b) and (c). The value for the lattice plane distances is shown next to the spots.

measured planes showing an expansion of a few angstroms. The Fe shows a 0.13 Å expansion and the Ag shows an even larger expansion of 0.24-0.34 Å depending on the spots. This expansion of the lattice is the same across multiple particles that were measured and so is indicative of the sample as a whole and not just this individual particle case. Ag_2O has been discounted as the lattice planes measured

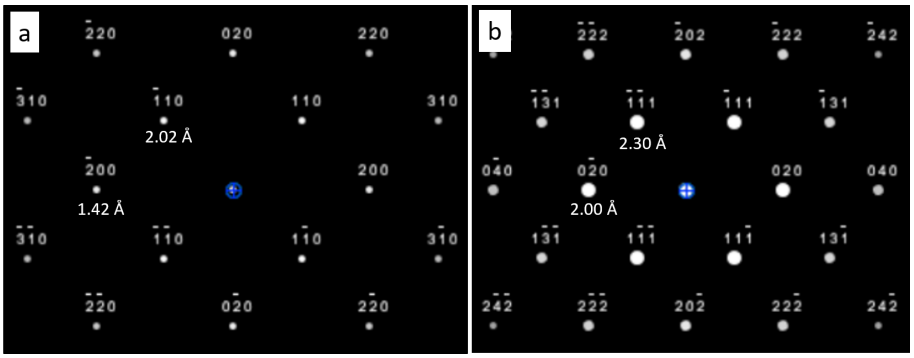

Figure 7.10: Simulated diffraction patterns from JEMS showing (a) the Fe[001] zone axis and (b) the Ag[110] zone axis. The lattice distances for the planes are shown below selected spots.

in the Ag region would have to compress by around 1 Å as well as the diffraction patterns from JEMS not matching the observed patterns here. XPS shows Ag_2O because the Si sample was left in atmosphere for a few days before being analysed compared to the TEM grid that was imaged within a few hours of leaving the vacuum. Therefore, it is likely that the Ag oxidised before it was analysed with XPS.

The reason for the observation of the lattice expansion could be due to strain. Investigating the Ag/Fe interface further in Figure 7.8(b), it can be seen that there is an angle between the two planes at the interface, shown in more detail in Figure 7.11. Here it was measured that the planes had an average angle, α, of 8.8±0.8° between them, as shown in Figure 7.11. This value was calculated by measuring the angle between a plane in the Fe and the plane in the Ag immediately next to it, shown by the yellow dotted lines in Figure 7.11 where the value of α is the angle of one such pairs of planes. An average was then taken of all the measured angles which leads to a value of 8.8±0.8° where the error is the standard deviation in the average value. This angle between the two lattice planes could be a cause or the result of the strain at the interface between the two elements.

Strain has been shown in other particle systems to cause expansion/compression of the lattice, such as alloyed FePt particles studied by Gan et al. [208] which showed an expansive strain in the Pt lattice up to 8% as compared to a compressive strain of up to 2% in normal Pt NPs. Strasser et al. [209] found that the strain in the

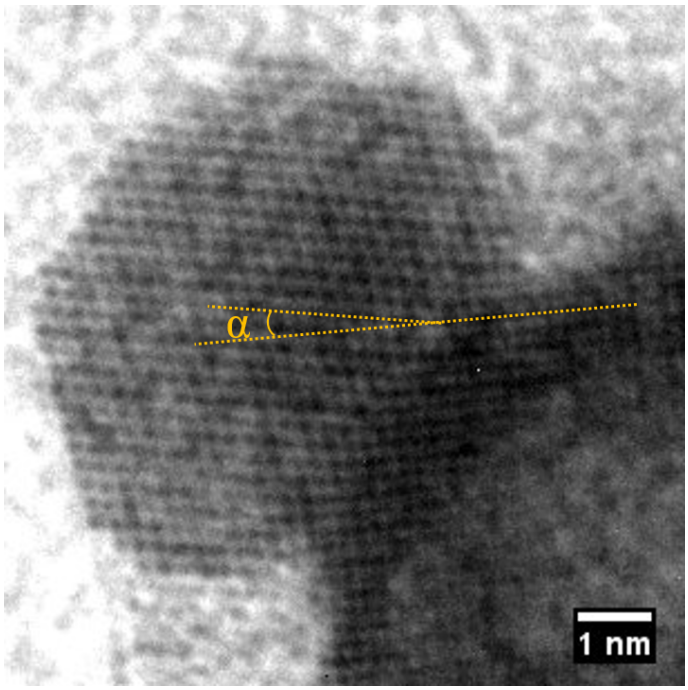

Figure 7.11: Interface of the Fe@Ag particle shown in Figure 7.8(b) with the bending at the interface shown by the yellow dotted line. The angle of the bend was calculated by measuring the value for α for each of the visible planes and taking an average.

Cu@Pt system is initially expansive up to a value of 8% and then decreases as more Pt is added to the system which was explained as being due to the lattice mismatch between Pt and Cu being ≈8%. As was discussed earlier, the work of Baker et al. [190, 193, 194] showed how the Fe crystal lattice could be stretched into an FCC arrangement due to the matrix material it was deposited in. While they showed how Ag did not change the structure of the Fe NPs, the measurements did not investigate if the Ag was altered. It is therefore possible that due to lattice mismatch and immiscibility of the Fe and Ag system, the two become strained resulting in lattice expansion.

While Fe and Ag are immiscible and do not form FeAg alloys, these elements can form what are known as Delafossite alloys [210, 211]. A Delafossite alloy takes the form of $AgFeO_2$. These crystals are formed through chemical methods, such as the reduction of nitrates of Fe and Ag in solution at high temperatures and pressures [211, 212]. To investigate the structure of $AgFeO_2$, the crystal visualisation package VESTA was used [213]. VESTA is the standard software for opening and

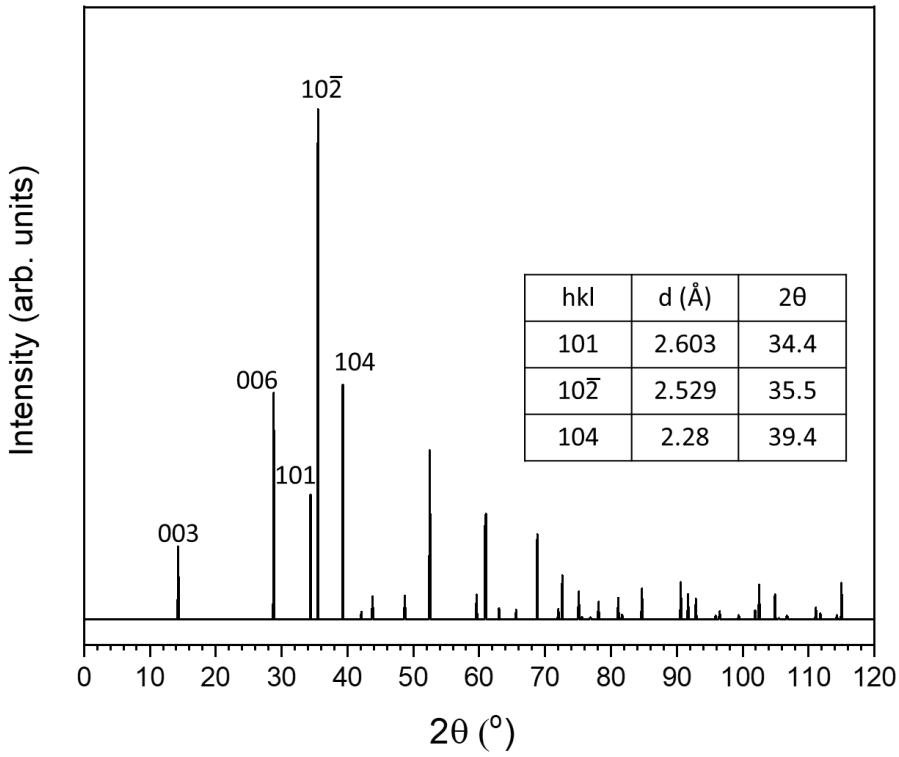

Figure 7.12: Simulated X-ray diffraction pattern in VESTA of a $AgFeO_2$ Delafossite alloy from Siedliska et al. [210] using the Cu KαI spectral line. Relevant lattice planes have been labelled with the inserted table highlighting lattice planes with lattice parameters that match the measured planes in the FFTs of the Ag region from the grown Fe@Ag particles (Fig. 7.9).

visualising ".cif" formats of crystal structures as well as allowing for the creation of custom crystal structures.

In VESTA, a powder diffraction pattern can be simulated with the Cu KαI spectral line being selected. Using the $AgFeO_2$ structure [210], the simulated pattern from VESTA was produced, as shown in Figure 7.12. The lattice planes are labelled and the inset of the table shows the expected lattice parameters of those planes. These match the lattice planes from the FFT of the Ag region in Figure 7.9 with much greater accuracy than for Ag[110] zone axis. This would imply that the region next to the Fe core is in fact this Delafossite alloy structure.

XPS spectra presented by Mishra et al. [214] of $AgFeO_2$ Delafossite crystals shows two separate states in the Ag $3d_{5/2}$ peak due to the Ag-Ag and Ag-FeO_2 bonding. If the Delafossite alloy had been synthesised due to the core-shell coating in this

experiment, then the XPS of the Ag $3d_{5/2}$ shown in Figure 7.3(b) would also show two states which is not the case. This then makes it hard to state with full accuracy what exact state the Ag is in next to the Fe core but due to the lack of a secondary feature in the XPS, it is more likely that the Ag is strained instead of being incorporated in a Delafossite alloy.

7.3.2 Stability and Reactivity of Fe@Ag NPs

Following the successful growth of Fe@Ag NPs, the stability and reactivity of the particles were then explored. As stated previously, the aim of coating with a secondary material is to prevent the oxidation of the pure core so that the desired properties are maintained. While the Fe@Ag NPs produced Janus-like particles, it is still important to understand how these particles react. Four TEM grids were initially produced and imaged with the images presented in the previous section. To study the stability and reactivity of the particles, one of the grids was placed in a ceramic tube furnace and heated in atmosphere while the other three were left in a desiccator at atmospheric pressure for 30 days.

The furnace was heated at 150 °C for 30 minutes with a 4 °C per minute ramp which equates to around 30 minutes to get to temperature. The furnace was then slowly cooled back to room temperature over the period of several hours. This experiment was performed as it was known from the *in-situ* e-TEM measurements, Chapter 5, that 150 °C would provide a good amount of oxidation but not completely deplete the core and so all the structures of the particles should still be visible. The bright-field images of the particles from the furnace are shown in Figure 7.13.

Figure 7.13 shows that substantial oxidation of the particles has occurred with a large number of them aggregating together. Clear Kirkendall voids can be seen to have formed in the particles which aligns with the results from Chapter 5. Interestingly, a number of particles also show a clear one-directional growth forming a nanowire (NW)-like feature; these have been highlighted by the dashed circles in Figure 7.13. This effect was not seen in the particles heated in Chapter 5 and implies that the Ag is acting as a catalyst for the reaction. HR-TEM images (Figure 7.14) of particles with a NW attached show limited lattice planes which makes it difficult to determine

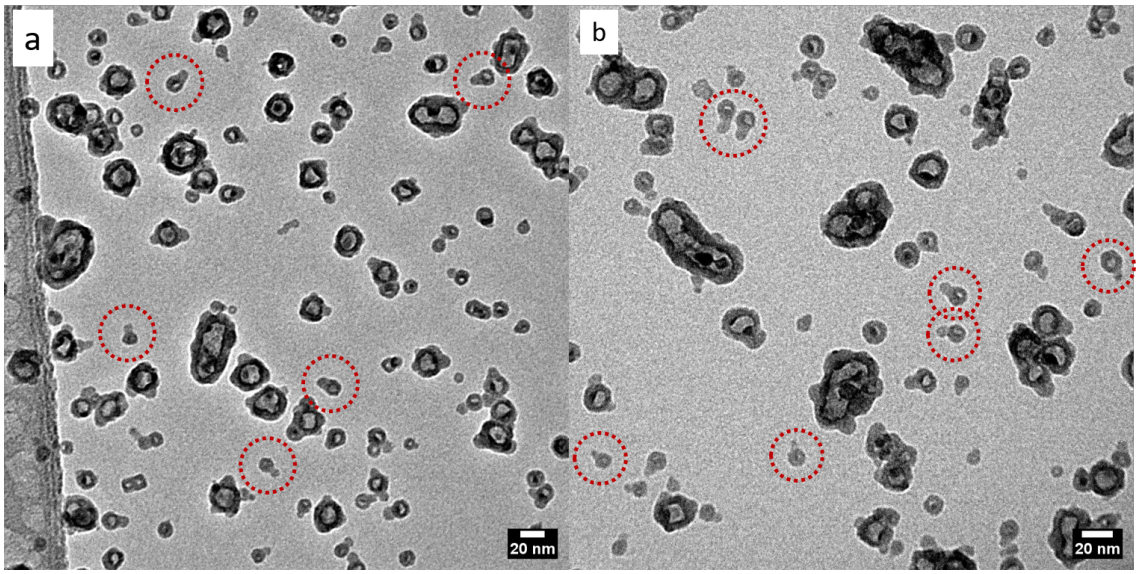

Figure 7.13: Bright-field TEM images showing NW growth on some particles (highlighted in dashed red circles) after being heated in a tube furnace for 30 minutes at 150 °C.

the crystalline structure of the NW.

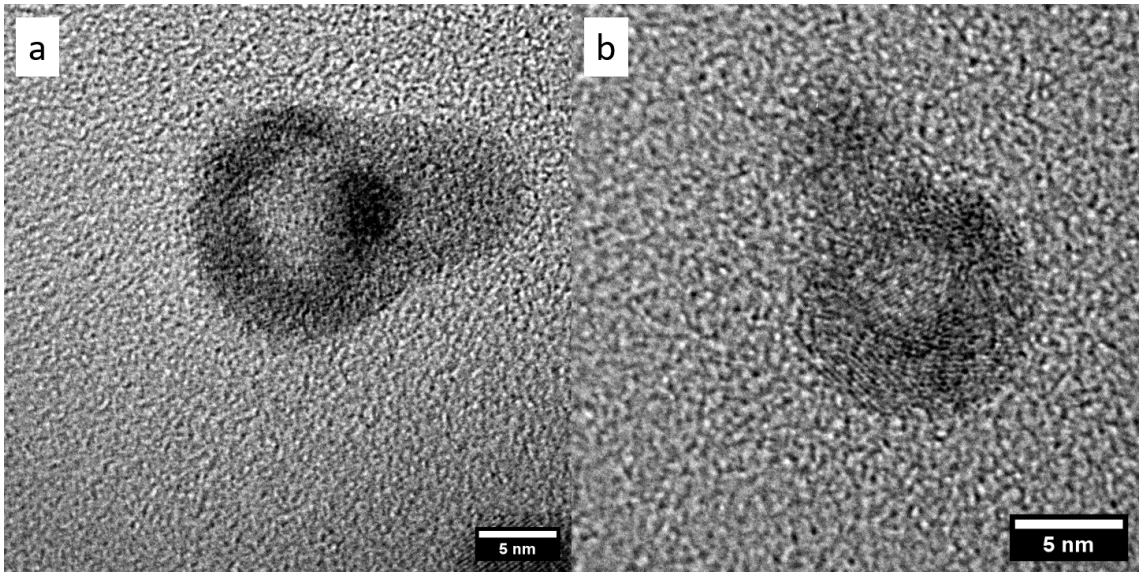

Figure 7.14: HR-TEM images of the Fe@Ag particles after being heated in the tube furnace for 30 minutes at 150 °C. Limited crystal planes are visible making it difficult to determine the crystal structure.

After 30 days, the grids that were left in the desiccator were re-imaged on the TEM to see what level of ambient oxidation had occurred and if the same NW features had grown. The bright-field images, shown in Figure 7.15, reveal that similar NW

growth has occurred with much less aggregation of the particles. The Fe core next to the NW growth has also depleted which is consistent with the process seen in the particles that were annealed in the furnace. This implies that the same NW growth process has happened in each set of particles. Though it has to be mentioned that the larger particles in Figure 7.15 still have intact cores compared to the larger particles in the furnaced sample which are depleted, shown in Figure 7.13.

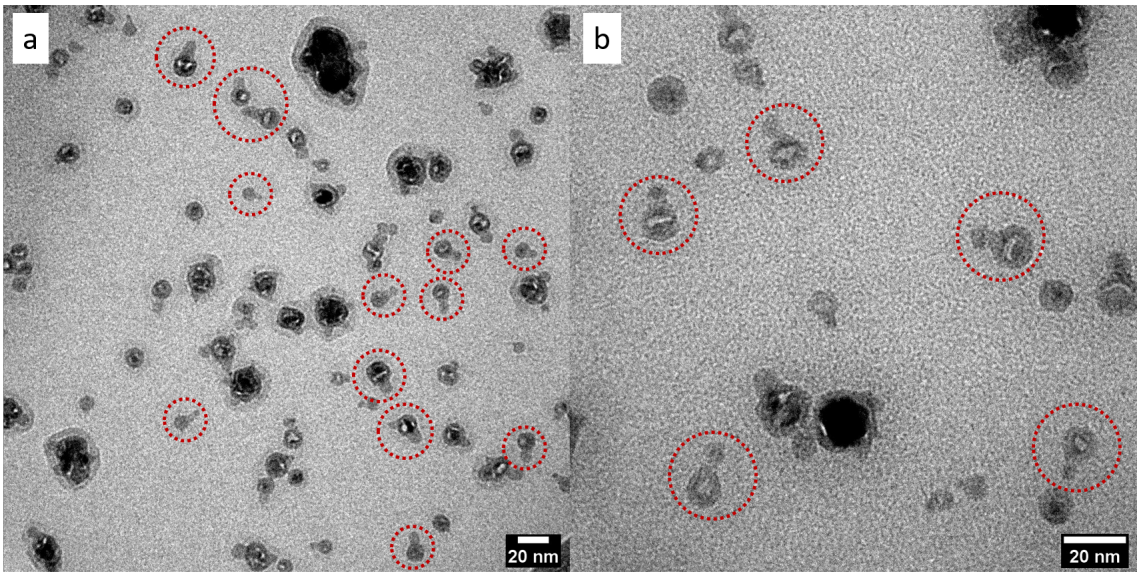

Figure 7.15: Bright-field TEM images of the particles after 30 days in a desiccator with the same NW growth highlighted by the red dashed circles.

The HR-TEM images of these particles, shown in Figure 7.16, are similar to those seen from the furnace, Figure 7.14, where both particles appear to be amorphous. Though this could be due to limitations of the microscope that could be resolved with a higher resolution microscope. This makes it difficult to determine the detailed structure of the NWs in Figures 7.14 and 7.16. The Ag has also seemingly been consumed in the growth of the NWs as it is not visible in the images. If the Ag was catalysing the reaction, then it would likely not be consumed in the oxidation reaction and would be present in the images. The fact that it is not visible in either the furnace or 30-day sample implies that the Ag has behaved in the same way in both cases. Obtaining crystallography data of the NW would elucidate the structure as well as give an understanding of where the Ag has gone. Though, once again due to the limitations of the microscope it cannot be said if the Ag has been consumed or not.

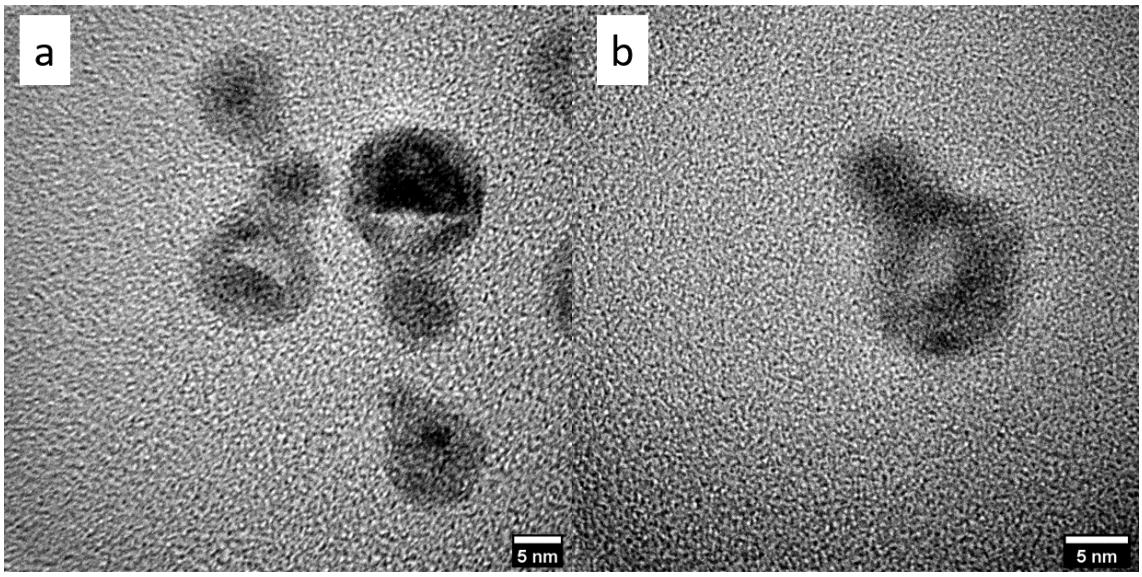

Figure 7.16: HR-TEM images of amorphous NW growth on the particles after being stored in the desiccator for 30 days.

The lengths and diameters of the NWs can be determined for both cases and are shown in Figures 7.17 and 7.18. These were measured in ImageJ and plotted against the particle diameter with the associated errors calculated from the resolution of the images from the microscope. In the furnace sample, it can be seen that the average NW length (Figure 7.17(a)) and NW diameter (Figure 7.17(b)) increases with the average particle diameter. The increasing NW diameter with increasing particle size can be explained by the fact that the original size of the Ag is limited to the size of the particle. This means that the growing NW diameter is therefore constrained to the particle size it originates from as it can not be wider than the particle it is attached to. The change in length (Figure 7.17(a)) is interesting as it implies a difference in growth rate depending on size with the larger particles growing longer NWs. The larger particles will effectively be a larger source of Fe cations for the NW to grow meaning that the growth is not rate limited by the supply of the ions. Though from the bright-field images in Figure 7.13, aggregation of particles can be seen and so small NPs could have aggregated and attached to larger particles therefore appearing as NWs.

In the 30 day sample, it can be seen in Figure 7.18(a) that the NW length versus particle diameter has no real clear trend with particle size. This is at odds with the furnace sample in Figure 7.17(a) where there was a clear trend with particle size.

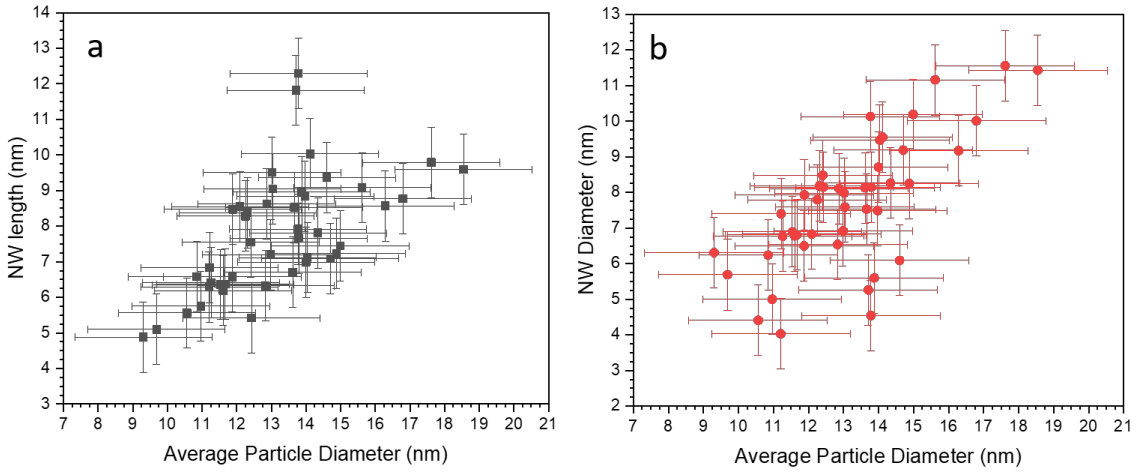

Figure 7.17: Measured NW length (a) and diameter (b) versus particle diameter for the particles that had been placed in the tube furnace. Associated errors are due to the resolution of the images from the microscope.

As was noted before, the larger particles in the furnaced sample have completely depleted cores compared to the intact cores in the 30-day samples. This means that there is enhanced diffusion in the furnaced sample. This would then mean that the length could increase with particle size as there are more Fe cations to diffuse into the growing NW. In Figure 7.18(b) it can be seen that the NW diameter also shows a clear trend with particle size and decreases as the overall particle diameter decreases. This confirms that the effect seen in the furnace sample that the diameter of the NWs is constrained by the size of the initial particle.

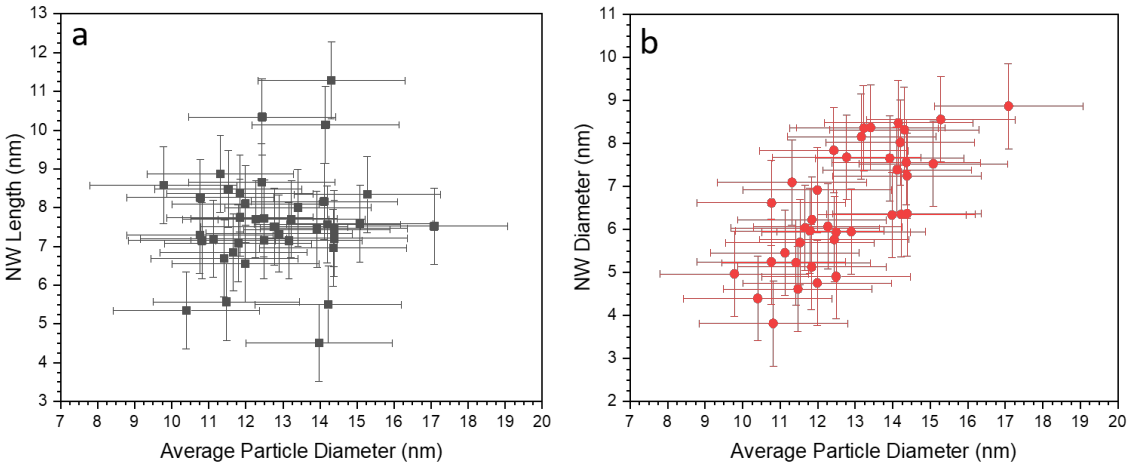

Figure 7.18: Measured NW length (a) and diameter (b) versus particle diameter for the particles that were left in the desiccator for 30 days. Associated errors are due to the resolution of the images from the microscope.

From Figures 7.17 and 7.18, the average NW lengths and diameters can be calculated along with the corresponding growth rates, assuming that the observed NW lengths for the furnace sample are due to true NW growth and not aggregated particles. The time periods were also assumed to be 6 hours and 30 days exactly for each sample respectively. These assumptions are thought to be valid as it can be seen in Figure 7.16 and 7.18 that some of the cores are still intact for the NPs meaning that the NW is still growing. This means that the time assumed for the dessicator sample can be viewed as a valid assumption. The reverse is true for the furnaced sample where in Figures 7.14 and 7.17 the core is completely depleted and there is a dependence between NP diameter and NW length. Therefore, this implies that the NW has fully grown and the time can be assumed for this growth. The average values for NW length and diameter were calculated by taking an average of the measured values shown in Figures 7.17 and 7.18. These values and associated growth rate are shown in Table 7.3.

Grids	NW Length (nm)	NW Diameter (nm)	NW Growth Rate (nms^{-1})
Furnace	7.8±1.6	7.7±1.8	3.6±0.8 $\times 10^{-4}$
30 day	7.6±1.3	6.6±1.3	2.9±0.5 $\times 10^{-6}$

Table 7.3: Measured NW lengths and diameters for each sample with the associated growth rates assuming exactly 6 hours and 30 days for each sample respectively.

Using Fick's law, as in Chapter 5, a diffusion coefficient can be determined assuming that all the growth occurs inside the NW and that it is only the Fe that is causing the outward growth. This leads to

$$J = \frac{D(x-0)}{d} \tag{7.1}$$

where J is the growth rate, D is the diffusion coefficient, x is the average length of the NWs, and d is the average diameter of the NWs. Rearranging Equation (7.1), the diffusion coefficient can then be determined for the NW growth in both cases. The calculated values for each case are shown in Table 7.4.

The calculated values in Table 7.4 ($3.6\pm1.4\times10^{-11}$ and $2.5\pm0.8\times10^{-13}$ cm^2s^{-1}) show an enhanced diffusion rate as compared to the values calculated in Chapter 5 of

Grid	Diffusion Coefficient (cm^2s^{-1})
Furnace	$3.6\pm1.4 \times10^{-11}$
30 day	$2.5\pm0.8 \times10^{-13}$

Table 7.4: Calculated diffusion coefficients for the growth of the NWs using the values from Table 7.3 and Equation 7.1.

$9.6\pm0.5\times10^{-16}$ and $1.8\pm0.1\times10^{-15}$ cm^2s^{-1}. The experimental conditions for these values are different so a direct comparison is difficult but it is worth noting that the *in-situ* e-TEM experiments that produced the values in Chapter 5 were performed at a higher temperature than the Fe@Ag samples in this Chapter. This suggests that the Ag is most likely acting as a catalyst causing the NWs to grow.

In materials science, the growth of NWs from a surface is well known with many studies performed on various metal surfaces [215–219]. When exposed to elevated temperatures and a low oxygen gas flow, pre-oxidised metal surfaces then show NW growth. For the oxide to keep growing, the metal cations must cross the oxide interface, and in these studies the oxide scales are generally rather thick such that the parabolic rate law is observed regardless of temperature. The NWs grow due to the imbalance of diffusion rates between the lattice and GB with the NWs growing out of the boundaries between oxide domains. In this case, the metal surface is essentially an infinite reservoir so void growth is limited and NWs then form out of the GBs as the metal cations are appearing there faster than through the lattice. As the NW keeps growing, the metal cations then diffuse across the NW surface to continue the oxidation reaction. This process is similar to that of vapour-solid-solid or vapour-liquid-solid growth of nanowires [220, 221].

Most of these studies have shown that NWs can grow out of a metal/metal oxide surface due to elevated temperature. Tai et al. [222] showed that this process could be activated by using Cu NPs as a catalyst to the reaction, in a process the authors termed catalysed oxidation for nanowire growth (CONG). Here the authors believe that the Cu NP catalyses the oxidation reaction as the Cu is a noble metal whereas the other metal surfaces used were not. The authors show that the Cu NPs act as a catalyst as the NWs that grow in their studies are capped with a Cu NP so it is

not being used up in the catalysis process. For this to occur, the oxygen is adsorbed to the Cu surface which then donates the oxygen to the growing NW as the Gibbs free energy of formation for the metal oxide NW is more negative compared to the Cu oxide that would otherwise form. It was also shown by Rackauskas et al. [218] that the growth of NWs out of a surface can be due to the relaxation of strain at the surface, though the authors believe this to be unlikely and due to temperature-related effects.

Ag is also a noble metal and so using the analysis from Tai et al. [222], it would also catalyse the growth of NWs if the Gibbs formation energy of Ag_2O is less negative compared to Fe oxide. Reference values show that this is indeed true with Ag_2O having a value of -11.25 kJ/mol compared to the lowest value for an Fe oxide (FeO) of -251.4 kJ/mol [223]. However, the Ag would have to still be visible on the end of the NW for this exact mechanism to apply as Tai et al. [222] showed that the use of Cu NPs resulted in Cu-capped NWs. The Ag is not visible in the NWs grown here (Figures 7.14 and 7.16) and so suggests that a different mechanism is taking place. Though, again, this is hard to confirm due to the limitations of the microscope. The Ag could be catalysing the oxygen reduction reaction to create the O^{2-} ions for the oxidation reaction to take place [224]. This would then create an extra source of ions for the Fe ions to react with.

It has also been argued that strain can have an influence on the NW growth on metal surfaces as the system looks to relieve the strain by forming the NWs [215]. As stated previously, it is likely that the Janus-like particle was under large amounts of expansive strain and so this could also be an explanation to the growth of the NWs. As stated in Section 2.2.3, expansive strain is known to cause enhanced oxidation at the nanoscale as the potential barrier for atomic movement is lower. The Ag particle could have acted as one large short circuit path to the oxidation reaction due to the expansive strain it was experiencing. This coupled with the fact it would most likely catalyse the oxidation reaction in the first place means that the NW growth can be explained by these two factors.

Firstly, the expansive strain across the Ag particle allows for the enhanced Fe cation diffusion out of the core as it acts as a short circuit diffusion path, as described in

Section 2.1.2. Once the NW growth has started, the Ag actively catalyses the oxidation reaction due to being a more noble metal compared to Fe. This could proceed by the adsorbed oxygen on the surface of the Ag being donated to the growing Fe oxide NW. The NW growth then continues out of the core with a Kirkendall void forming below the NW, shown in Figures 7.15 and 7.16.

In conclusion, coating the Fe in Ag was proven to be difficult due to the low wetting parameter and poor miscibility of the two elements [94, 203]. The two elements formed a Janus-like particle which then showed enhanced oxidation resulting in NW growth. The enhanced oxidation is believed to occur through two mechanisms: firstly, the initial Ag component is highly strained and so acts as a short-circuit diffusion path for the oxidation of the Fe core. Secondly, the Ag is a more noble metal as compared to the Fe and therefore will donate the oxygen ions to the growing oxide NW as well as catalysing the reduction of the oxygen molecules into ions. The enhanced oxidation was proven by comparing the diffusion coefficient for the growth of the NWs as compared to the *in-situ* e-TEM particles from Chapter 5 with the NW growth rate shown to be quicker. This enhanced oxidation means that the use of Ag as a protective coating for the pure metal Fe core is not viable where the Fe core needs to remain in tact to retain its magnetic properties.

7.3.3 Characterising the Growth of Cu@Ag Particles

Following the results of the Fe@Ag particles it was investigated whether Ag would cause the growth of NWs on Cu. Comparing the Gibbs free energies again, CuO and Cu_2O both have more negative values compared to Ag_2O of -129.7 and -146 kJ/mol respectively [223]. These values would imply that the Ag should indeed catalyse the growth of copper oxide NWs. The Cu@Ag core-shell system is important for printable electronics as discussed previously but the two metals also do not alloy very well. The phase diagram of Cu-Ag follows a eutectic relationship as the metals either form a Cu- or Ag- rich solid crystal meaning that Janus-like particles are also expected as for the Fe@Ag case.

The successful coating of Cu NPs with Ag was proven once again by performing XPS on coated NPs deposited on a Si crystal wafer. The presence of a strong satellite

after the Cu $2p_{3/2}$ peak in the XPS spectrum shown in Figure 7.19(b) is an indication of CuO [225]. The Cu 2p peak also shows a zero-valent Cu peak though the peak position is the same for Cu_2O so it is hard to make the distinction between the two. The presence of two copper oxide peaks gives an indication of strong oxidation. The Ag $3d_{5/2}$ in Figure 7.19(d) is also shifted to 367.8 eV which, as stated in the Fe@Ag case, is indicative of the Ag being oxidised in some capacity [202]. The ratio of Cu:Ag was calculated to be $14\pm8 : 1\pm1$ through the same analysis technique as before using Wagner's empirical technique for relative amounts in XPS [66].

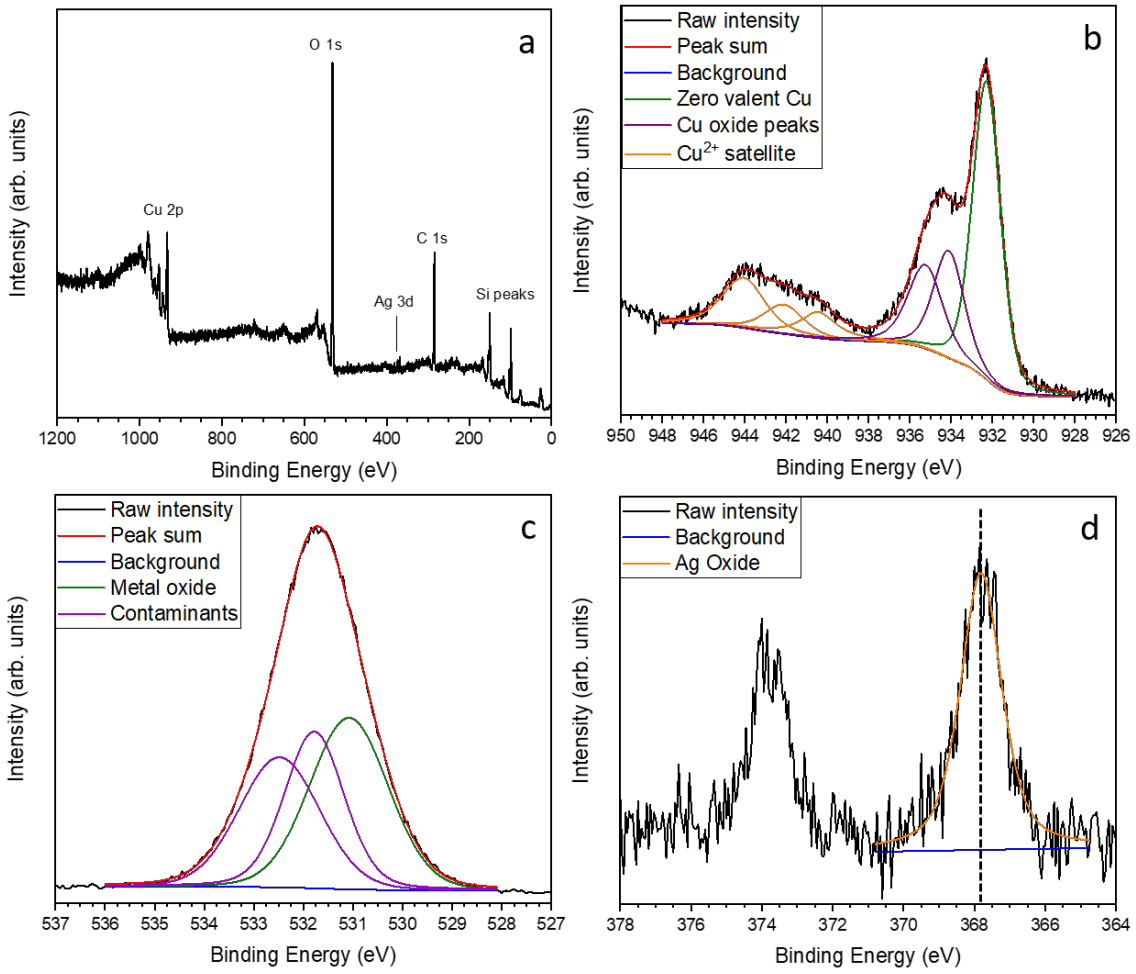

Figure 7.19: XPS spectra of the Cu@Ag particles showing (a) the overall survey of the elements. (b) The deconvoluted Cu $2p_{3/2}$ spectra with a strong Cu^{2+} satellite present in the spectrum which is an indication of oxidation as this feature is only present in CuO. (c) The deconvoluted O 1s spectrum, and (d) the Ag 3d with a single peak fitted with the dotted line showing the peak position of 367.8 eV.

Bright-field TEM images of the Cu@Ag NPs are shown in Figure 7.20. Clear contrast

between two zones in most of the particles can be seen throughout the bright-field images suggesting Janus-like particles. While the produced histogram of particle sizes (Figure 7.21) shows a central peak position of 8.2±0.5 nm, lots of very large particles (25 nm plus) can be seen showing the clear distinction between two zones of the particles.

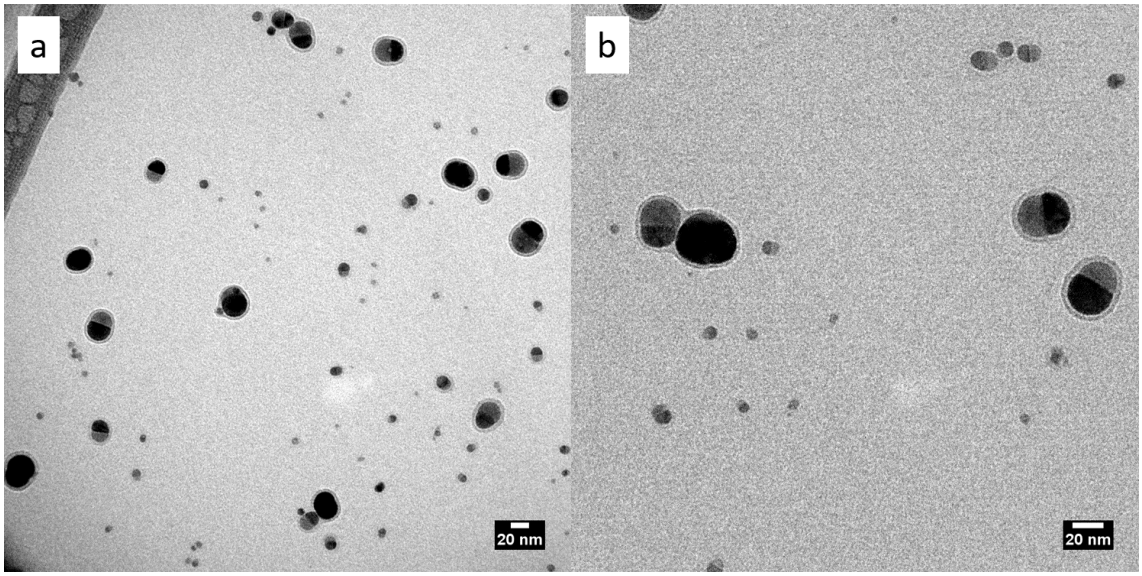

Figure 7.20: Initial bright-field TEM images of the Cu@Ag particles where (a) and (b) show different regions of the grid. Distinct zones, shown by changes in contrast, in the particles are present throughout the images suggesting a Janus-like structure.

HR-TEM images were taken of individual particles, shown in Figure 7.22. These particles have again formed Janus-like particles where there are two distinct zones. Interestingly, in comparison to the Fe@Ag NPs, the particles are much larger with an interface that runs the entire length of the particle diameter. Overall, the metal core/oxide shell system with a Ag particle attached as seen for Fe@Ag is not replicated here. Instead, both parts of the particle seem to be fully oxidised as the crystal structure inside the lighter contrast area is hard to image. Also, a core-shell arrangement of metal-oxide is expected where a lighter contrast oxide surrounds the metal core, as shown in previous Figures such as Figure 7.8. A lighter contrast points to an oxide as the microscope does not image the oxygen columns in the crystal due to the lack of sufficient interaction with the electron beam.

Crystallinity can be seen inside the dark regions in many of the particles and performing FFT analysis on these areas once again allows for the crystal structure to

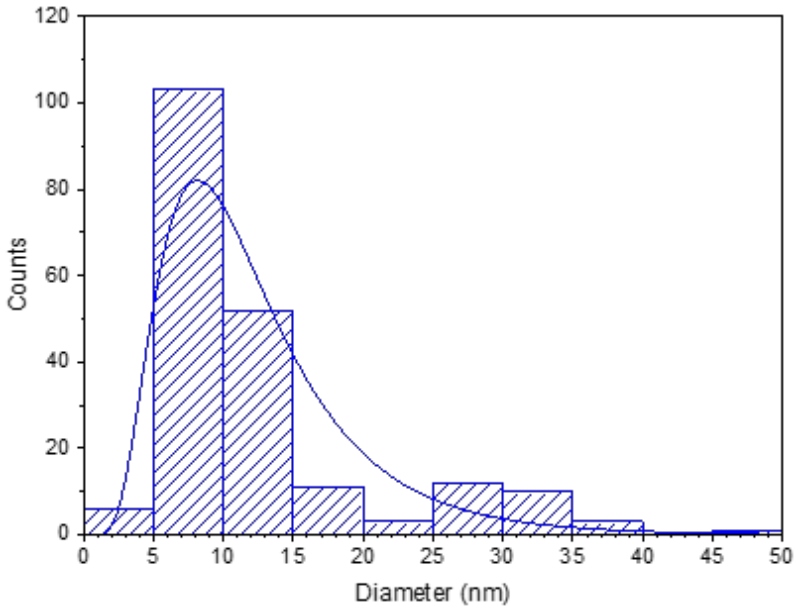

Figure 7.21: Histogram of particle sizes calculated by ImageJ from the bright-field images of the Cu@Ag particles with a fitted log-normal peak. The centre point of the fitted peak is 8.2±0.5 nm.

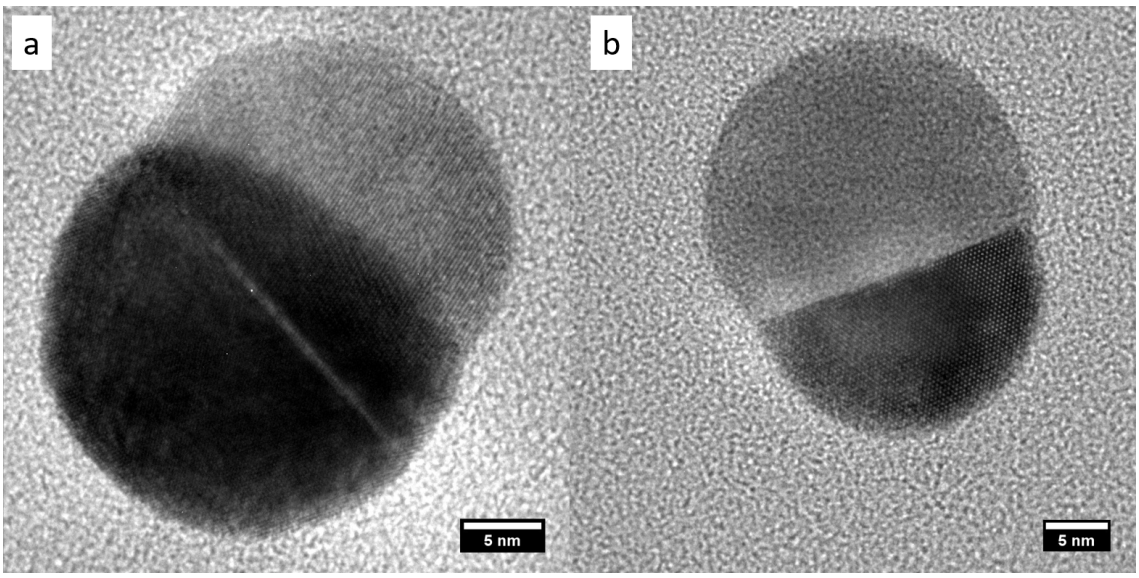

Figure 7.22: HR-TEM images of the Cu@Ag particles showing limited crystallinity in the lighter area with the opposite being true in the darker region, most clearly demonstrated in (b).

be deduced. This analysis is shown in Figure 7.23 with the region the FFT was taken from highlighted by the red dashed rectangle in Figure 7.23(b). The produced FFT is shown in Figure 7.23(c). The pattern produced by the FFT shows

the same pattern for $Ag_2O[111]$ with this simulated in JEMS and shown in Figure 7.23(d). Ag[111] is discounted as the measured lattice parameters are too large. The red, yellow, and blue dashed circles correspond to the (110), (022), and (112) planes respectively for $Ag_2O[111]$ with the lattice parameters labelled next to them.

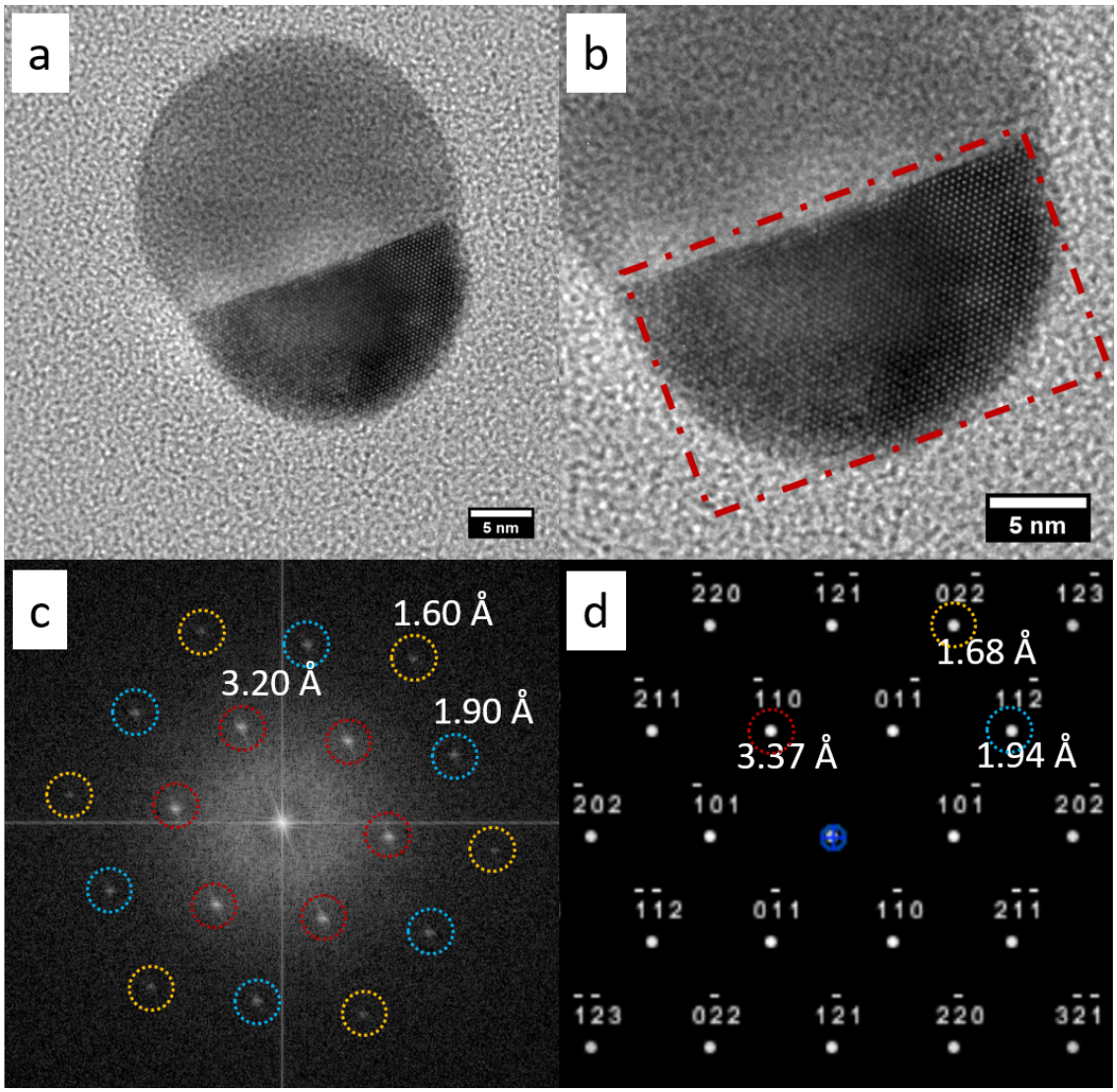

Figure 7.23: FFT analysis of the lattice planes visible in the HR-TEM image (a) with the zone where the FFT was taken marked by the red dashed square in (b). The produced FFT and measured lattice planes are is shown in (c). Each colour circle representing a family of planes with the same lattice parameter. The simulated diffraction pattern from JEMS for Ag_2O is shown in (d) along with the calculated distances and the corresponding coloured circles to the FFT to allow for the planes to be matched.

The measured lattice planes do not match exactly the expected values from JEMS

with some amount of compression occurring due to strain in the particle, as for the Fe@Ag particles. The lattice mismatch between Cu and Ag is 1.1% though the lattice mismatch between Ag_2O and CuO and Cu_2O is 10-13%. This means that if the two elements had oxidised each other after production then the amount of strain might have increased due to the increase in the lattice mismatch between the pure and oxidised forms of the elements.

It is also possible that some alloying has occurred between the two elements to form $Ag_2Cu_2O_3$ [226]. The simulated powder diffraction pattern for this structure, calculated using VESTA [213], is shown in Figure 7.24. The crystal structure for this simulation was taken from [226]. Lots of lattice planes that appear in the simulated diffraction pattern are not visible in the FFT in Figure 7.23, such as the (202) in Figure 7.24 which is clearly a dominant plane. It therefore seems unlikely that this region is due to the alloy structure and is more likely due to strain from the lattice mismatch. Much like the Fe-Ag case, Cu-Ag does not alloy very well and forms either a Cu- or Ag-rich crystal structure [227]. This then results in this Janus-like crystal structure as the two elements separate out.

It is interesting to note that the two elements seem to be completely oxidised with the Cu region in the XPS showing clear signs of CuO development due to the satellite peak shown in Figure 7.19. The Ag region is then close to the expected lattice planes of Ag_2O suggesting that the two elements have formed a completely oxidised particle system. This could be due to the growth conditions as the temperature inside the crucible is near the bulk value for the melting point of copper ($\sim$1050 °C). It is known that the melting point of elements decreases as particle size decreases [228, 229]. This is due to the surface-to-volume ratio increasing with decreasing particle size, for example the melting point of Sn NPs was shown to decrease from 220 to 150 °C as the particle size was decreased from 100 to 10 nm in diameter [230].

Therefore, the Cu NPs will likely partially melt inside the hot crucible as the bulk melting point is $\sim$1050 °C and so the two elements (Cu and Ag) will be in some sort of liquid state. It is known from the studies performed in Chapter 6 that some degree of oxidation occurs inside the source as the samples in that study produced Fe@$Fe_{1-x}O$ particles under vacuum conditions. Therefore, it is likely that the Cu

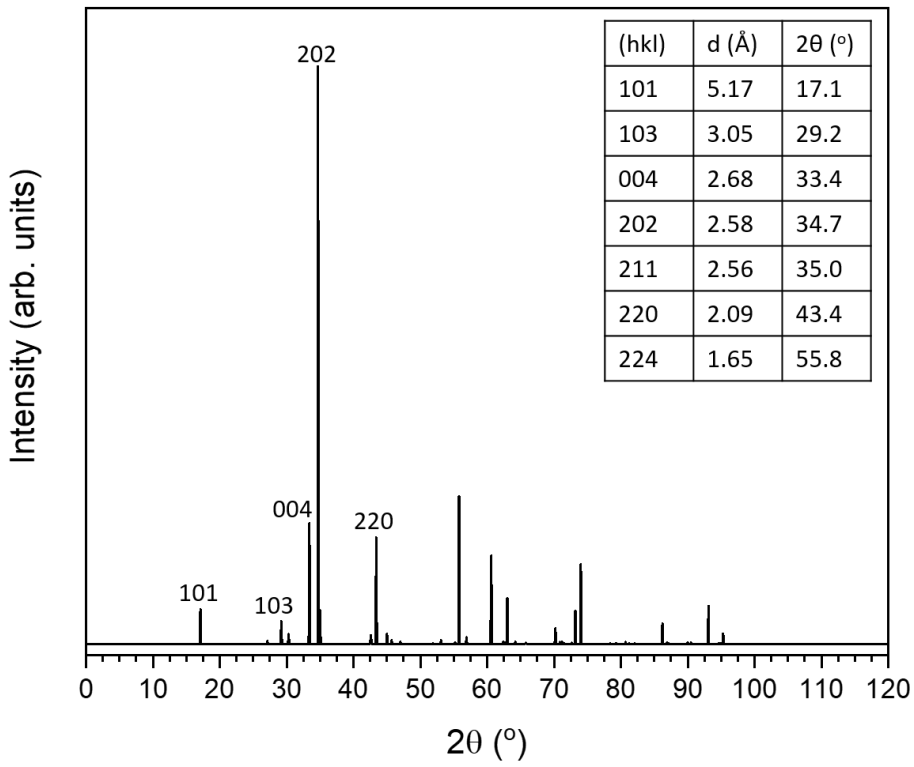

Figure 7.24: Simulated powder diffraction pattern from VESTA [213] of $Ag_2Cu_2O_3$ using the crystal structure from Adelsberger et al. [226]. The inserted table shows the dominant lattice planes and their lattice parameter and 2θ value.

NPs also have a core-shell arrangement of pure and oxidised components before they enter the crucible. If this is the case then this will explain the production of completely oxidised particles as the copper will melt, oxidise, and re-crystallise while the Ag is also being oxidised as the two liquid components mix. The melting point of Fe is much higher than Cu, at ∼1500 °C, explaining why the pure core-oxide shell arrangement remained in tact.

Once again, after a 30 day period had elapsed, the particles were then imaged again on the JEOL 2100+ microscope. It can be seen in the bright field and HR-TEM images, Figure 7.25, that very little change has occurred.

As there is no pure metal to oxidise as in the Fe@Ag case then it is unsurprising that no further oxidation took place as both parts of the particle were completely oxidised to begin with. Copper and silver oxides are undesirable for applications such as printable electronics [196, 231] due to their lower conductivity when compared to their pure metal counterparts. This work shows that the growth of Cu@Ag particles

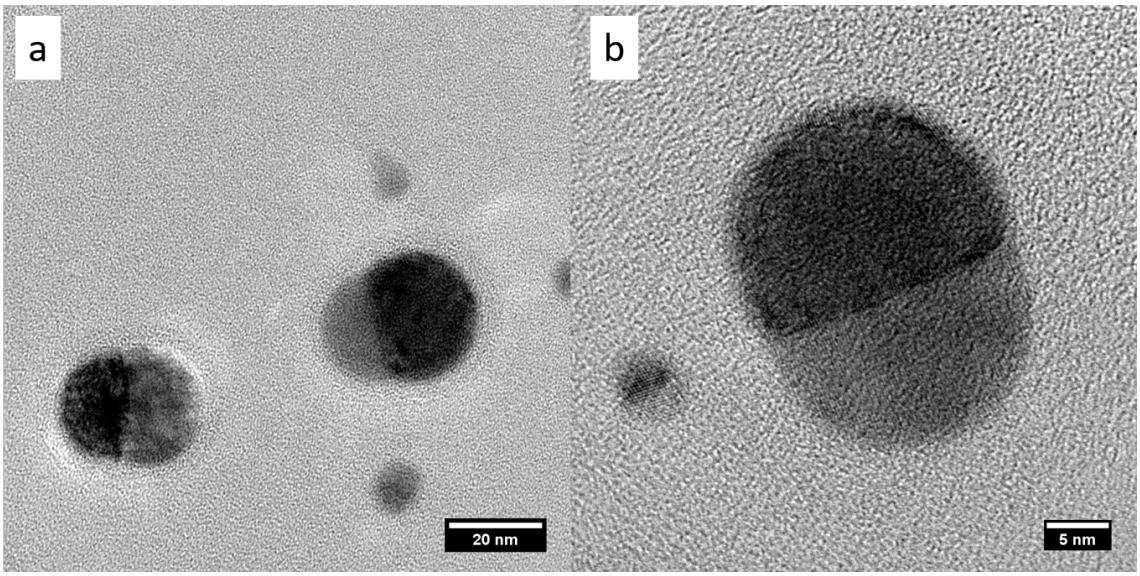

Figure 7.25: TEM images showing the Cu@Ag particles after 30 days in the desiccator, showing little change to the images in Figures 7.20 and 7.22.

through a gas-phase technique could be possible but the problem of whether they oxidise rapidly due to catalysis needs to be addressed. The method demonstrated here is believed to be the first attempt at growing Cu@Ag particles through a gas phase synthesis method.

7.4 Summary

The interaction of Ag as a coating material on two core metal NPs has been investigated and discussed. Through careful control experiments, it was shown that the Ag was only present in the samples if a NP flux was passing through the crucible. The presence of Ag was confirmed using XPS and TEM. It was shown that Ag deposition on both Cu and Fe leads to the formation of Janus-like particles but the systems are very different. When the Ag was attached to the Fe core the Ag formed a large island with the structure depending on if it was attached to a cubic or Wulff polyhedra type core. The Fe remained pure during the growth and then formed Fe-Fe oxide-Ag particles with the oxide terminating at the Ag. The Ag region was shown to be highly strained due to the lattice mismatch with the Fe core causing an expansive strain inside the Ag.

Attaching Ag to Cu resulted in much larger particles with the interface between the two elements running the entire diameter of the particle. The elements were shown to be oxidised completely after growth which is believed to be because of the two elements being in a liquid state as they come into contact in the crucible. The formation of these Janus-like structures is due to the low miscibility of Ag with Cu and Fe as well as a low wetting parameter between Ag vapour onto surfaces of Cu and Fe [94, 227].

In the Fe@Ag particles, clear NW growth was observed which is believed to be due to the Ag catalysing the oxidation reaction. This catalysis could occur via two interactions where, firstly, the Gibbs free formation energy of the growing Fe oxide is more negative compared to Ag oxide which therefore means the Ag donates the adsorbed oxygen to the growing oxide layer. This could then act as a short-circuit path to the diffusion of Fe out of the core which caused the NW growth. The Cu@Ag particles were shown to be completely oxidised after growth and stable over the 30 day investigation period. This has implications for printable electronics where the growth of Cu@Ag is necessary to couple conductance with cost [231]. The growth of these Cu@Ag core@shell particles using the gas condensation method is believed to be reported here for the first time.

Chapter 8

Conclusions and Further Work

8.1 Conclusions

The work demonstrated in this thesis shows the development and characterisation of a gas aggregation cluster source to produce NPs. Fe NPs were produced to investigate oxidation at the nanoscale first using e-TEM to image the development of the nanoscale Kirkendall effect (NKE) *in-situ*. The Fe NPs were then deposited under UHV conditions onto a clean Si surface and oxidised *in-situ* with the oxidation investigated using spectroscopic techniques. The Fe NPs were then coated with Ag to try and prevent the oxidation process with a sacrificial layer.

Following an Introduction, Chapter 2 outlined how solid-state diffusion occurs and gave an overview of the theory of oxidation. Chapter 3 described in detail the experimental techniques that were employed in this work to investigate the oxidation process of the NPs. Chapter 4 focused on the gas aggregation cluster source that was newly acquired in York and further developed during this work. The chapter explains the theory of particle beam formation and manipulation followed by a description of the development of the cluster source. The steps taken to make improvements are also explained in the context of the theory of the gas aggregation cluster source.

Chapter 5 detailed the *in-situ* e-TEM experiments where individual particles were imaged under different conditions. This allowed the NKE process to be investigated and the differences between the oxidation processes due to the different imaging

conditions was reported. It was found that temperature was the main driver in the oxidation process as the particles exposed to the oxygen gas at higher temperature had a much more complete oxidation. This is due to the Fe cations having greater energy and therefore diffusing at a faster rate, in addition to the thermionic current of electrons being more easily established which allows the oxidation reaction to occur. Beam damage was found to be most likely causing oxygen vacancies through knock-on beam effects and so the higher beam dosage leads to more vacancies for the Fe cations to exchange with. This additional vacancy flux explains why at the higher temperature and higher beam dosage conditions, the particles formed completely hollow cores whereas under the other conditions these did not occur. The results suggest that the final hollow structure could be tuned by the imaging conditions where the lower temperature and lower beam dosage particles would form thicker oxide shells with a smaller central void. Following the complete depletion of the cores of two of the particles, the diffusion coefficient of Fe in Fe oxide at 480 K was calculated. These values were $9.5\pm0.5 \times 10^{-16}$ and $1.8\pm0.1 \times 10^{-15}$ cm^2s^{-1}, with the discrepancy due to size effects, which are similar to diffusion coefficients for other transition metals quoted in the literature.

Chapter 6 explained the *in-situ* spectroscopy investigation of Fe NPs. The electron spectroscopy system, described in Chapter 3, is an UHV system to which the cluster source was attached. This allowed the particles to be deposited onto a clean Si surface under vacuum conditions. The initial oxide formation on the Fe surfaces is one that is hotly debated in the literature and so the work undertaken in this chapter was aimed at providing clarity on this subject. The particles were exposed to low doses (7-14 L) of oxygen at different temperatures to understand which type of Fe oxide formed. It was found that the initial particles were Fe@$Fe_{1-x}O$ with the $Fe_{1-x}O$ layer then oxidising further into Fe_3O_4 on exposure to the oxygen dosing. At higher temperatures, the oxide was found to reduce due to the greater bond strength of Si-O compared to Fe-O. This oxide layer then formed more slowly as compared to room temperature when then exposed to oxygen at the higher temperatures due to the disproportionation of the silicon oxide formation to the Fe oxide.

Chapter 7 explored core-shell coating where coating the particles in a secondary material can enhance the properties of the particles. Ag was used in this study due its

biomedical properties as well as being non-magnetic so exchange bias effects would not occur. The Ag is intended to act as a protective coating so that during oxidation the Ag would oxidise instead of the pure Fe core. This would mean that pure Fe NPs could then be produced and used in a variety of applications which is desirable due to the superior magnetic qualities of pure Fe metal compared to its oxides. Instead of coating the core, the immiscibility of the two elements produced Janus-like particles where large islands of Ag were present on the Fe core. The Ag catalysed the oxidation reaction causing NWs to grow out of the core. This growth was seen in particles that had been heated in a tube furnace under atmospheric conditions as well as left in a desiccator for 30 days. This growth allowed the calculation of the diffusion coefficient which had values of $3.6\pm1.4 \times10^{-11}$ and $2.5\pm0.8 \times10^{-13}$ cm^2s^{-1}. In comparison to the values calculated in Chapter 5, these show an enhanced diffusion coefficient which is explained by the Ag catalysing the reaction. Cu@Ag particles were also created to investigate whether the same NW growth would be seen in a different system which was not the case. The Cu seemingly had fully oxidised on growth which is believed to be due to the growth conditions in the crucible during the coating procedure.

This thesis explores the reactivity of metal NPs produced by a vacuum cluster source. Critical theory was presented on the operation and development of the gas aggregation cluster source with the hope for further development examined below. The use of magnetic metal NPs in a variety of applications is becoming more widespread and so understanding how they degrade due to oxidation is key. The oxidation of the particles during this work was shown to follow the theories presented in Chapter 2 with the added understanding from the work of others to adapt them to the nanoscale. The work presented in Chapter 5, shows for the first time the use of the e-TEM technique to image the NKE effect in Fe NPs. A hollow particle, such as those seen in this experiment, will have a reduced magnetic moment due to the depletion of the pure Fe core region. Critical insight into this process was shown during this work which will help further understand how metal NPs oxidise in a variety of conditions. The effect of coating with a secondary material, as outlined in Chapter 7, shows how the NPs can be tailored during growth to expand their properties. The work presented here shows that the miscibility of the two elements

must be taken into account for the desired coating to be seen. The two elements can not just be chosen due to their individual desired properties as was shown that the Fe and Ag then led to a separate interesting reaction, one that has not been reported in the literature for this system.

8.2 Further Work

The results from Chapter 5 highlight how e-TEM measurements can gain critical insight into the oxidation process at the nanoscale. It would therefore be interesting to investigate the theory that the lower temperatures and lower beam dosages would form smaller central voids and thicker oxide shells. This would then open the way to understanding how these hollow structures can be tailor made. Another interesting experiment would be to perform spatially resolved electron energy loss spectroscopy (EELS) across the central void. As shown by Schierholz et al. [232], they could detect trapped He inside the pores in the amorphous porous Si film grown in an He environment. It would therefore be interesting to investigate what the central void contained and therefore whether the central void could then be "back-filled" with a separate substance. An investigation of higher temperatures would also be interesting as an Arrhenius plot could then be produced which would allow for a separate calculation of the diffusion coefficients as it would be akin to the reaction rate that the plot would obtain.

The *in-situ* spectroscopy measurements showed an interesting premise where the oxide was reduced upon heating on the Si surface. A thorough investigation of whether a more oxidised particle could be reduced would be interesting due to the need for more carbon free reduction of Fe oxide. Different surfaces could also be of interest to see what effect either different materials or different reconstructions of Si have on the reduction process. It would also be pertinent to investigate whether the particles could be oxidised and then reduced in cycles and at what point this process would stop.

Coating with Ag showed how allowing for the miscibility of the two elements is key. Therefore, coating with Au would be of interest as this is predicted to more

easily coat the core [94]. Spatially resolved EELS would also allow for the structure to be easily identified. It would also show whether the Fe and Ag form alloys or whether the differences in the FFT are due to expansive strain arising from the lattice mismatch. Atomically resolved STEM imaging would also allow for strain mapping analysis to be performed which so far has not been reported for Fe@Ag core@shell particles. An investigation of coating with magnetic materials would also be of interest due to the exchange bias effect and therefore the effect on the superparamagnetic limit.

Finally, further developments to the cluster source could be made. As stated in Chapter 4, the aerodynamic lensing has a large effect on the particles which can dictate size through the Stokes particle and lens numbers. The effect of particle size due to the aperture arrangement needs to be fully investigated as this could lead the way to a completely new design of these particle sources. If the particle size was seen to vary with the different aperture arrangements, then an adaptive system could be developed which would allow for large real time changes to the produced particle distribution. This in turn would generate a more versatile cluster source where the particle size could be more easily controlled.

Acronyms

BF bright field.

CAE constant analyser energy.

CM Cabrera-Mott.

CRR constant retard ratio.

DF dark field.

e-TEM environmental transmission electron microscope.

FC Fromhold-Cook.

FEL fast entry lock.

FFT fast fourier transform.

FWHM full width half maximum.

GACS gas aggregation cluster source.

GB grain boundary.

HAADF high-angle annular dark field.

HBD high beam dosage.

HR-TEM high-resolution transmission electron microscopy.

LBD low beam dosage.

LEED low energy electron diffraction.

MFCs mass flow controllers.

NKE nano-Kirkendall effect.

NP nanoparticle.

NPs nanoparticles.

NW nanowire.

NWs nanowires.

QCM quartz crystal microbalance.

QMF quadrupole mass filter.

RT room temperature.

sccm standard cubic centimeter per minute.

SEM scanning electron microscope.

SLUMPS Small Leicester University Mesoscopic Particle System.

STEM scanning transmission electron microscopy.

TEM transmission electron microscopy.

TMP turbo molecular pump.

TP triple point.

UHV ultra-high vacuum.

UPS ultraviolet photoemission spectroscopy.

XPS X-ray photoemission spectroscopy.

Bibliography

[1] M. Arruebo, R. Fernández-Pacheco, M. R. Ibarra, and J. Santamaría. Magnetic nanoparticles for drug delivery. *Nano Today*, 2(3):22–32, 2007.

[2] S. Pinel, N. Thomas, C. Boura, and M. Barberi-Heyob. Approaches to physical stimulation of metallic nanoparticles for glioblastoma treatment. *Adv. Drug Deliv. Rev.*, 138:344 – 357, 2019.

[3] S. A. Corr, S. J. Byrne, R. Tekoriute, C. J. Meledandri, D. F. Brougham, M. Lynch, C. Kerskens, L. O'Dwyer, and Y. K. Gun'ko. Linear assemblies of magnetic nanoparticles as MRI contrast agents. *J. Am. Chem. Soc.*, 130(13):4214–4215, 2008.

[4] B. Jiang, L. Lian, Y. Xing, N. Zhang, Y. Chen, P. Lu, and D. Zhang. Advances of magnetic nanoparticles in environmental application: environmental remediation and (bio)sensors as case studies. *Environ. Sci. Pollut. Res.*, 25(31):30863–30879, 2018.

[5] D. Astruc. Introduction: Nanoparticles in catalysis. *Chem.*, 120(2):461–463, 2020.

[6] L. Zhou and M. R. Zachariah. Size resolved particle work function measurement of free nanoparticles: Aggregates vs. spheres. *Chem. Phys. Lett.*, 525-526:77–81, 2012.

[7] M. Blanco-Mantecón and K. O'Grady. Interaction and size effects in magnetic nanoparticles. *J. Magn. Magn. Mater.*, 296(2):124–133, 2006.

[8] B. D. Cullity and C. D. Graham. *Introduction to Magnetic Materials*. Wiley, 2nd edition, 2008.

[9] T. Hyeon. Chemical synthesis of magnetic nanoparticles. *Chem. Commun.*, pages 927–934, 2003.

[10] P. Singh, Y.-J. Kim, D. Zhang, and D.-C. Yang. Biological synthesis of nanoparticles from plants and microorganisms. *Trends Biotechnol.*, 34(7):588–599, 2016.

[11] A. Aires, S. M. Ocampo, D. Cabrera, L. de la Cueva, G. Salas, F. J. Teran, and A. L. Cortajarena. BSA-coated magnetic nanoparticles for improved therapeutic properties. *J. Mater. Chem. B*, 3:6239–6247, 2015.

[12] Lasting impact of lipid nanoparticles. *Nat. Rev. Mater.*, 6:1071–1071, 2021.

[13] E. A. Périgo, G. Hemery, O. Sandre, D. Ortega, E. Garaio, F. Plazaola, and F. J. Teran. Fundamentals and advances in magnetic hyperthermia. *Appl. Phys. Rev.*, 2(4):041302, 2015.

[14] S. Shukla, R. Khan, and A. Daverey. Synthesis and characterization of magnetic nanoparticles, and their applications in wastewater treatment: A review. *Environ. Technol. Innov.*, 24:101924, 2021.

[15] Y.-P. Sun, X.-q. Li, J. Cao, W.-x. Zhang, and H. P. Wang. Characterization of zero-valent iron nanoparticles. *Adv. Colloid Interface Sci.*, 120(1):47–56, 2006.

[16] G. S. Parkinson. Iron oxide surfaces. *Surf. Sci. Rep*, 71(1):272–365, 2016.

[17] N. Cabrera and N. F. Mott. Theory of the oxidation of metals. *Rep. Prog. Phys.*, 12:163–184, 1949.

[18] C. Wagner. Beitrag zur theorie des anlafvorgangs. *Z. Phys. Chem. (N F)*, 21:25–41, 1933.

[19] A. Pratt, L. Lari, O. Hovorka, A. Shah, C. Woffinden, S.P. Tear, and Kröger R. Enhanced oxidation of nanoparticles through strain-mediated ionic transport. *Nat. Mater.*, 13:26–30, 2014.

[20] A. T. Fromhold and E. L. Cook. Kinetics of oxide film growth on metal crystals: Electronic and ionic diffusion in large surface-charge and space-charge fields. *Phys. Rev. Lett.*, 175:877–897, 1968.

[21] A. D. Smigelskas and E. O. Kirkendall. Zinc diffusion in alpha brass. *Trans. AIME.*, 171:130–142, 1947.

[22] Z. Xu, K. M. Rosso, and S. Bruemmer. Metal oxidation kinetics and the transition from thin to thick films. *Phys. Chem. Chem. Phys.*, 14:14534–14539, 2012.

[23] J. Crangle, G. M. Goodman, and W. Sucksmith. The magnetization of pure iron and nickel. *Proc. Math. Phys. Eng. Sci.*, 321(1547):477–491, 1971.

[24] D. Zhang, W. Choi, Y. Oshima, U. Wiedwald, S.-H. Cho, H.-P. Lin, Y. K. Li, Y. Ito, and K. Sugioka. Magnetic Fe@FeOx, Fe@C and α-Fe_2O_3 single-crystal nanoblends synthesized by femtosecond laser ablation of Fe in acetone. *Nanomaterials*, 8(8), 2018.

[25] W. S. Gorski. Theorie der elastischen nachwirkung in ungeordneten mischkristallen zweiter. *Phys.Z. Sowj.*, pages 457–471, 1935.

[26] J. Philibert. *Atom movements - diffusion and mass transport in solids.* Editions de Physique, 1991.

[27] R. W. Balluffi and R. F. Mehl. Grain boundary diffusion mechanisms in metals. *Metall. Trans. A*, 13(12):2069–2095, 1982.

[28] A. G. Naumovets and Y. S. Vedula. Surface diffusion of adsorbates. *Surf. Sci. Rep.*, 4(7):365–434, 1985.

[29] K. W. Ingle and A. G. Crocker. Migration of vacancies near twin boundaries in body-centred-cubic metals. *Phil. Mag. A.*, 37(2):297–303, 1978.

[30] L. Bataillou, C. Desgranges, L. Martinelli, and D. Monceau. Modelling of the effect of grain boundary diffusion on the oxidation of Ni-Cr alloys at high temperature. *Corros. Sci.*, 136:148–160, 2018.

[31] E. W. Hart. On the role of dislocations in bulk diffusion. *Act. Metal.*, 5(10):597, 1957.

[32] J. D. Baran, H. Grönbeck, and A. Hellman. Mechanism for limiting thickness of thin oxide films on aluminum. *Phys. Rev. Lett.*, 112:146103, 2014.

[33] A. Atkinson. Transport processes during the growth of oxide films at elevated temperature. *Rev. Mod. Phys.*, 57:437–470, 1985.

[34] A. Ermoline and E. L. Dreizin. Equations for the cabrera–mott kinetics of oxidation for spherical nanoparticles. *Chem. Phys. Lett.*, 505(1):47–50, 2011.

[35] V. P. Zhdanov and B. Kasemo. Cabrera–mott kinetics of oxidation of nm-sized metal particles. *Chem. Phys. Lett.*, 452(4):285–288, 2008.

[36] A. T. Fromhold and E. L. Cook. Kinetics of oxide film growth on metal crystals: Electron tunneling and ionic diffusion. *Phys. Rev.*, 158:600–612, 1967.

[37] A. T. Fromhold and E. L. Cook. Kinetics of oxide film growth on metal crystals: Thermal electron emission and ionic diffusion. *Phys. Rev.*, 163:650–664, 1967.

[38] A. T. Fromhold. Kinetics of oxide film growth on metal crystals—I.: Formulation and numerical solutions. *J. Phys. Chem. Solids.*, 24(9):1081–1092, 1963.

[39] A. T. Fromhold. Kinetics of oxide film growth on metal crystals—II: Homogeneous field approximations. *J. Phys. Chem. Solids.*, 24(11):1309–1323, 1963.

[40] A. T Fromhold. Kinetics of oxide film growth on metal crystals—III. perturbation treatment of space charge fields. *J. Phys. Chem. Solids.*, 25(10):1129–1137, 1964.

[41] G. W. R. Leibbrandt, G. Hoogers, and F. H. P. M. Habraken. Thin oxide film growth on Fe(100). *Phys. Rev. Lett.*, 68:1947–1950, 1992.

[42] S. J. Roosendaal, A. M. Vredenberg, and F. H. P. M. Habraken. Oxidation of iron: The relation between oxidation kinetics and oxide electronic structure. *Phys. Rev. Lett.*, 84:3366–3369, 2000.

[43] P. C. J. Graat, M. A. J. Somers, A. M. Vredenberg, and E. J. Mittemeijer. On the initial oxidation of iron: Quantification of growth kinetics by the coupled-currents approach. *J. Appl. Phys.*, 82(3):1416–1422, 1997.

[44] S. Mrowec and A. Stokłosa. Oxidation of copper at high temperatures. *Oxid. Met.*, 3(3):291 – 311, 1971.

[45] R. Y. Chen and W. Y. D. Yeun. Review of the high-temperature oxidation of iron and carbon steels in air or oxygen. *Oxid. Met.*, 59(5):433–468, 2003.

[46] D. Monceau and B. Pieraggi. Determination of parabolic rate constants from a local analysis of mass-gain curves. *Oxid. Met.*, 50(5):477 – 493, 1998.

[47] E. Sutter, F. Ivars-Barcelo, and P. Sutter. Size-dependent room temperature oxidation of tin particles. *Part. Part. Syst. Charact*, 31(8):879–885, 2014.

[48] A. T. Fromhold. Easy insight into space-charge effects on steady-state transport in oxide films. *Oxid. Met.*, 13(5):475–479, 1979.

[49] C.-H. Chen, T. Yamaguchi, K.-I. Sugawara, and K. Koga. Role of stress in the self-limiting oxidation of copper nanoparticles. *J. Phys. Chem. B*, 109(44):20669–20672, 2005.

[50] B. Jeon, S. K. R. S. Sankaranarayanan, A. C. T. van Duin, and S. Ramanathan. Influence of surface orientation and defects on early-stage oxidation and ultrathin oxide growth on pure copper. *Philos. Mag.*, 91(32):4073–4088, 2011.

[51] R. Subbaraman, S. A. Deshmukh, and S. K. R. S. Sankaranarayanan. Atomistic insights into early stage oxidation and nanoscale oxide growth on Fe(100), Fe(111) and Fe(110) surfaces. *J. Phys. Chem. C.*, 117(10):5195–5207, 2013.

[52] W. Wang, M. Dahl, and Y. Yin. Hollow nanocrystals through the nanoscale kirkendall effect. *Chem. Mater.*, 25(8):1179–1189, 2013.

[53] H. J. Fan, U. Gösele, and M. Zacharias. Formation of nanotubes and hollow nanoparticles based on kirkendall and diffusion processes: A review. *Small*, 3(10):1660–1671, 2007.

[54] Y. Yin, R. M. Rioux, C. K. Erdonmez, S. Hughes, G. A. Somorjal, and A. P. Alivisatos. Formation of hollow nanocrystals through the nanoscale kirkendall effect. *Science*, 304(5671):711–714, 2004.

[55] Y. Yin, C. K. Erdonmez, A. Cabot, S. Hughes, and A. P. Alivisatos. Colloidal synthesis of hollow cobalt sulfide nanocrystals. *Adv. Funct. Mater.*, 16(11):1389–1399, 2006.

[56] K. N. Tu and U. Gösele. Hollow nanostructures based on the kirkendall effect: Design and stability considerations. *Appl. Phys. Lett.*, 86(9):093111, 2005.

[57] A. M. Gusak, T. V. Zaporozhets, K. N. Tu, and U. Gösele. Kinetic analysis of the instability of hollow nanoparticles. *Philos. Mag.*, 85(36):4445–4464, 2005.

[58] L. Klinger, O. Kraft, and E. Rabkin. A model of kirkendall hollowing of core–shell nanowires and nanoparticles controlled by short-circuit diffusion. *Acta Mater.*, 83:180–186, 2015.

[59] M. Ibáñez, J. Fan, W. Li, D. Cadavid, R. Nafria, A. Carrete, and A. Cabot. Means and limits of control of the shell parameters in hollow nanoparticles obtained by the kirkendall effect. *Chem. Mater.*, 23(12):3095–3104, 2011.

[60] M. Ohring. *Materials Science of Thin Films*, chapter Chapter 2 - Vacuum Science and Technology, pages 57–93. Academic Press, 2nd edition, 2002.

[61] K. M. G. Siegbahn, R. Mason, C. N. R. Rao, N. Sheppard, and M. W. Roberts. Photoelectron spectroscopy: retrospects and prospects. *Philos. Trans. Royal Soc. A*, 318(1541):3–36, 1986.

[62] G. Sauerbrey. The use of quartz oscillators for weighing thin layers and for microweighing. *Z. Phys.*, 155(2):206–222, 1959.

[63] M. Prutton. *Introduction to Surface Physics*. Oxford University Press, 1994.

[64] A. Einstein. On a heuristic point of view concerning the production and transformation of light. *Ann. Phys. (Berl.)*, 17(132):132–148, 1905.

[65] D Briggs and M. P. Seah. *Practical surface analysis by Auger and X-ray photoelectron spectroscopy*, volume 1. John Wiley and Sons Ltd., 1990.

[66] C. D. Wagner. Sensitivity factors for xps analysis of surface atoms. *J Electron Spectros Relat Phenomena*, 32(2):99–102, 1983.

[67] G. Attard and C. Barnes. *Surfaces*. Oxford University Press, 1998.

[68] C. Kittel. *Introduction to Solid State Physics*. John Wiley and Sons., 1976.

[69] G. Ertl. Low energy electrons and surface chemistry, second, completely revised edition. *Ber. Bunsenges. Phys. Chem.*, 91(2), 1987.

[70] L. Reimer and H. Kohl. *Transmission Electron Microscopy*. Springer, 2007.

[71] D. B. Williams and C. B. Carter. *Transmission Electron Microscopy, Parts 1 - 4*. Springer, 2009.

[72] E. D. Boyes and P. L. Gai. Environmental high resolution electron microscopy and applications to chemical science. *Ultramicroscopy*, 67(1):219–232, 1997.

[73] E. D. Boyes, M. R. Ward, L. Lari, and P. L. Gai. ESTEM imaging of single atoms under controlled temperature and gas environment conditions in catalyst reaction studies. *Ann. Phys.*, 525(6):423–429, 2013.

[74] P. L. Gai and E. D. Boyes. Advances in atomic resolution in situ environmental transmission electron microscopy and 1Å aberration corrected in situ electron microscopy. *Microsc. Res. Tech.*, 72(3):153–164, 2009.

[75] P. Grammatikopoulos, S. Steinhauer, J. Vernieres, V. Singh, and M. Sowwan. Nanoparticle design by gas-phase synthesis. *Adv. Phys.-X*, 1(1):81–100, 2016.

[76] C. Binns, K. N. Trohidou, J. Bansmann, S. H. Baker, J. A. Blackman, J-P Bucher, D. Kechrakos, A. Kleibert, S. Louch, K-H Meiwes-Broer, G. M. Pastor, A. Perez, and Y. Xie. The behaviour of nanostructured magnetic materials produced by depositing gas-phase nanoparticles. *J. Phys. D.*, 38(22):R357–R379, 2005.

[77] H. Haberland, M. Karrais, and M. Mall. A new type of cluster and cluster ion source. *Z. Phys. D.*, 20(1):413–415, 1991.

[78] T. Hihara and K. Sumiyama. Formation and size control of a Ni cluster by plasma gas condensation. *J. Appl. Phys.*, 84(9):5270–5276, 1998.

[79] S. Swann. Magnetron sputtering. *Phys. Technol*, 19(2):67–75, 1988.

[80] G. Coquerel. Crystallization of molecular systems from solution: phase diagrams, supersaturation and other basic concepts. *Chem. Soc. Rev.*, 43:2286–2300, 2014.

[81] E. Quesnel, E. Pauliac-Vaujour, and V. Muffato. Modeling metallic nanoparticle synthesis in a magnetron-based nanocluster source by gas condensation of a sputtered vapor. *J. Appl. Phys.*, 107(5):054309, 2010.

[82] P. Grammatikopoulos. Atomistic modeling of the nucleation and growth of pure and hybrid nanoparticles by cluster beam deposition. *Curr. Opin. Chem. Eng.*, 23:164–173, 2019.

[83] M.J. Shaw. Penning ionization. *Contemp Phys.*, 15(5):445–464, 1974.

[84] S. Sharma, N. Sirse, M. M. Turner, and A. R. Ellingboe. Influence of excitation frequency on the metastable atoms and electron energy distribution function in a capacitively coupled argon discharge. *Phys. Plasmas*, 25(6):063501, 2018.

[85] P. M. Winkler, G. Steiner, A. Vrtala, H. Vehkamäki, M. Noppel, K. E. J. Lehtinen, G. P. Reischl, P. E. Wagner, and M. Kulmala. Heterogeneous nucleation experiments bridging the scale from molecular ion clusters to nanoparticles. *Science*, 319(5868):1374–1377, 2008.

[86] W. Knauer. Formation of large metal clusters by surface nucleation. *J. Appl. Phys.*, 62(3):841–851, 1987.

[87] K. Wegner, P. Piseri, H. Vahedi Tafreshi, and P. Milani. Cluster beam deposition: a tool for nanoscale science and technology. *J. Phys. D*, 39(22):R439–R459, 2006.

[88] M. Khojasteh and V. V. Kresin. Influence of source parameters on the growth of metal nanoparticles by sputter gas-aggregation. *Appl. Nanosci.*, 7(8):875–883, 2017.

[89] M. Gracia-Pinilla, E. Martínez, G. S. Vidaurri, and E. Pérez-Tijerina. Deposition of size-selected Cu nanoparticles by inert gas condensation. *Nanoscale Res. Lett.*, 5:180, 2009.

[90] C. Liu, L. Zhang, S. Zhang, F. Liu, G. Wang, and M. Han. Influence of discharge power on the size of the Pd cluster generated with a magnetron plasma gas aggregation cluster source. *Vacuum*, 179:109486, 2020.

[91] J. Vernieres, S. Steinhauer, J. Zhao, A. Chapelle, P. Menini, N. Dufour, R. Diaz, K. Nordlund, F. Djurabekova, P. Grammatikopoulos, and M. Sowwan. Gas phase synthesis of multifunctional Fe-based nanocubes. *Adv. Funct. Mater.*, 27(11):1605328, 2017.

[92] J. Zhao, E. Baibuz, J. Vernieres, P. Grammatikopoulos, V. Jansson, M. Nagel, S. Steinhauer, M. Sowwan, A. Kuronen, K. Nordlund, and F. Djurabekova. Formation mechanism of Fe nanocubes by magnetron sputtering inert gas condensation. *ACS Nano*, 10(4):4684–4694, 2016.

[93] B. Zhu, J. Meng, and Y. Gao. Equilibrium shape of metal nanoparticles under reactive gas conditions. *J. Phys. Chem. C*, 121(10):5629–5634, 2017.

[94] S. Combettes, J. Lam, P. Benzo, A. Ponchet, M.-J. Casanove, F. Calvo, and M. Benoit. How interface properties control the equilibrium shape of core–shell Fe–Au and Fe–Ag nanoparticles. *Nanoscale*, 12:18079–18090, 2020.

[95] S. J. Liu, H. Huang, and C. H. Woo. Schwoebel-Ehrlich barrier: from two to three dimensions. *Appl.Phys. Lett.*, 80(18):3295–3297, 2002.

[96] P. Liu, P. J. Ziemann, D. B. Kittelson, and P. H. McMurry. Generating particle beams of controlled dimensions and divergence: I. theory of particle motion in aerodynamic lenses and nozzle expansions. *Aerosol Sci Technol.*, 22(3):293–313, 1995.

[97] X. Zhang, K. A. Smith, D. R. Worsnop, J. Jimenez, J.T. Jayne, and C. E. Kolb. A numerical characterization of particle beam collimation by an aerodynamic lens-nozzle system: Part I. an individual lens or nozzle. *Aerosol Sci Technol.*, 36(5):617–631, 2002.

[98] F. Di Fonzo, A. Gidwani, M. H. Fan, D. Neumann, D. I. Iordanoglou, J. V. R. Heberlein, P. H. McMurry, S. L. Girshick, N. Tymiak, W. W. Gerberich, and N. P. Rao. Focused nanoparticle-beam deposition of patterned microstructures. *Appl. Phys. Lett.*, 77(6):910–912, 2000.

[99] P. Liu, P.J. Ziemann, D.B. Kittelson, and P.H. McMurry. Generating particle beams of controlled dimensions and divergence: II. experimental evaluation of particle motion in aerodynamic lenses and nozzle expansions. *Aerosol Sci. Technol.*, 22(3):314–324, 1995.

[100] G. J. Pert. *Introductory Fluid Mechanics for Physicists and Mathermaticians*. Wiley, 2013.

[101] X. Wang, A. Gidwani, S. L. Girshick, and P.H. McMurry. Aerodynamic focusing of nanoparticles: II. numerical simulation of particle motion through aerodynamic lenses. *Aerosol Sci Technol.*, 39(7):624–636, 2005.

[102] X. Zhang, K.A. Smith, D.R. Worsnop, J.L. Jimenez, J.T. Jayne, C.E. Kolb, J. Morris, and P. Davidovits. Numerical characterization of particle beam collimation: Part II integrated aerodynamic-lens–nozzle system. *Aerosol Sci Technol.*, 38(6):619–638, 2004.

[103] I. Kim, Y. Kim, K. Woo, E.-H. Ryu, K.-Y. Yon, G. Cao, and J. Moon. Synthesis of oxidation-resistant core–shell copper nanoparticles. *RSC Adv.*, 3:15169–15177, 2013.

[104] C. Binns, M. T. Qureshi, D. Peddis, S. H. Baker, P. B. Howes, A. Boatwright, S. A. Cavill, S. S. Dhesi, L. Lari, R. Kröger, and S. Langridge. Exchange bias in Fe@Cr core–shell nanoparticles. *Nano Lett.*, 13(7):3334–3339, 2013.

[105] S. H. Baker, C. Binns, K. W. Edmonds, M. J. Maher, S. C. Thornton, S. Louch, and S. S. Dhesi. Enhancements in magnetic moments of exposed and Co-

coated Fe nanoclusters as a function of cluster size. *J. Magn. Magn. Mater.*, 247(1):19–25, 2002.

[106] T. Kretková, J. Hanuš, O. Kylián, P. Solař, M. Dopita, M. Cieslar, I. Khalakhan, A. Choukourov, and H. Biederman. In-flight modification of Ni nanoparticles by tubular magnetron sputtering. *J. Phys. D: Appl. Phys.*, 52(20):205302, 2019.

[107] J. Hanuš, M. Vaidulych, O. Kylián, A. Choukourov, J. Kousal, I. Khalakhan, M. Cieslar, P. Solař, and H. Biederman. Fabrication of Ni@Ti core-shell nanoparticles by modified gas aggregation source. *J. Phys. D: Appl. Phys.*, 50(47):475307, 2017.

[108] P. E. Miller and M. B. Denton. The quadrupole mass filter: Basic operating concepts. *J. Chem. Educ.*, 63(7):617, 1986.

[109] J. E. Campana. Elementary theory of the quadrupole mass filter. *Int. j. mass spectrom. ion phys.*, 33(2):101–117, 1980.

[110] C. Binns, P. Prieto, S. Baker, P. Howes, R. Dondi, G. Burley, L. Lari, R. Kröger, A. Pratt, S. Aktas, and J. K. Mellon. Preparation of hydrosol suspensions of elemental and core–shell nanoparticles by co-deposition with water vapour from the gas-phase in ultra-high vacuum conditions. *J. Nanopart Res.*, 14(9):1136, 2012.

[111] S. H. Baker, M. Roy, S. Louch, and C. Binns. Atomic structure in magnetic cluster assembled Fe/Co films as determined from extended absorption fine structure. *J. Phys. Condens. Matter*, 18(8):2385–2399, 2006.

[112] S. Atkas, S. C. Thornton, C. Binns, and P. Denby. Gas phase synthesis of core-shell Fe@FeOx magnetic nanoparticles into fluids. *J. Nanopart Res.*, 18(12):365, 2016.

[113] J. Trygg, B. Johansson, O. Eriksson, and J. M. Wills. Total energy calculation of the magnetocrystalline anisotropy energy in the ferromagnetic $3d$ metals. *Phys. Rev. Lett.*, 75:2871–2874, 1995.

[114] V. Skumryev, S. Stoyanov, Y. Zhang, G. Hadjipanayis, D. Givord, and J. Nogués. Beating the superparamagnetic limit with exchange bias. *Nature*, 423:850–853, 2003.

[115] J.-M. Qiu, Y.-H. Xu, J. H. Judy, and J.-P. Wang. Nanocluster deposition for high density magnetic recording tape media. *J. Appl. Phys.*, 97(10):10P704, 2005.

[116] K.S. Suslick, S-B. Choe, A.A Cichowlas, and M.W. Grinstaff. Sonochemical synthesis of amorphous iron. *Nature*, 353:414–416, 1991.

[117] K-C. Huang and S.H. Ehrman. Synthesis of iron nanoparticles via chemical reduction with palladium ion seeds. *Langmuir*, 23:1419–1426, 2007.

[118] D.L. Huber. Synthesis, properties, and applications of iron nanoparticles. *Small*, 1(5):482–501, 2005.

[119] Sigma-Aldrich. Iron (0) pentacarbonyl data sheet. Technical Report CAS-No. 13463-40-6, Sigma-Aldrich, Merck Life Science UK Limited New Road The Old Brickyard Gillingham Dorset SP8 4XT United Kingdom, 2020.

[120] C. T. Seip and C. J. O'Connor. The fabrication and organization of self-assembled metallic nanoparticles formed in reverse micelles. *Nanostruc. Mat.*, 12(1):183–186, 1999.

[121] N. Xiaomin, S. Xiaobo, Z. Huagui, Z. Dongen, Y. Dandan, and Z. Qingbiao. Studies on the one-step preparation of iron nanoparticles in solution. *J. Cryst. Growth*, 275(3):548–553, 2005.

[122] C. Yang, J. Xing, Y. Guan, J. Liu, and Liu. H. Synthesis and characterization of superparamagnetic iron nanocomposites by hydrazine reduction. *J. Alloys Compd.*, 385(1):283–287, 2004.

[123] N. G. Bastús, J. Comenge, and V. Puntes. Kinetically controlled seeded growth synthesis of citrate-stabilized gold nanoparticles of up to 200 nm: Size focusing versus ostwald ripening. *Langmuir*, 27(17):11098–11105, 2011.

[124] C. T. Yavuz, J. T. Mayo, W. W. Yu, A. Prakash, J. C. Falkner, S. Yean, L. Cong, H. J. Shipley, A. Kan, M. Tomson, D. Natelson, and V. L. Colvin. Low-field magnetic separation of monodisperse Fe_3O_4 nanocrystals. *Science*, 314(5801):964–967, 2006.

[125] Siswoyo, L. W. Lim, and T. Takeuchi. Separation of gold nanoparticles with a monolithic silica capillary column in liquid chromatography. *Anal Sci.*, 28(2):107–107, 2012.

[126] O. Akbulut, C. R. Mace, R. V. Martinez, A. A. Kumar, Z. Nie, M. R. Patton, and G. M. Whitesides. Separation of nanoparticles in aqueous multiphase systems through centrifugation. *Nano Lett.*, 12(8):4060–4064, 2012.

[127] N. Surugau and P. L. Urban. Electrophoretic methods for separation of nanoparticles. *J. Sep. Sci.*, 32(11):1889–1906, 2009.

[128] G. D. Moeser, K. A. Roach, W. H. Green, T. Alan Hatton, and P. E. Laibinis. High-gradient magnetic separation of coated magnetic nanoparticles. *AICHE J.*, 50(11):2835–2848, 2004.

[129] H. Duan, D. Wang, and Y. Li. Green chemistry for nanoparticle synthesis. *Chem. Soc. Rev.*, 44:5778–5792, 2015.

[130] M.P. Seah. Pure element sputtering yields using 500–1000 ev argon ions. *Thin Solid Films*, 81(3):279–287, 1981.

[131] J. Kousal, A. Shelemin, M. Schwartzkopf, O. Polonskyi, J. Hanuš, P. Solař, M. Vaidulych, D. Nikitin, P. Pleskunov, Z. Krtouš, T. Strunskus, F. Faupel, S. Roth, H. Biederman, and A. Choukourov. Magnetron-sputtered copper nanoparticles: lost in gas aggregation and found by in situ x-ray scattering. *Nanoscale*, 10(38):18275–18281, 2018.

[132] COMSOL. *CFD Module: User's Guide v5.6.*

[133] K. R. Bray, C. Q. Jiao, and J. N. DeCerbo. Influence of carrier gas on the nucleation and growth of Nb nanoclusters formed through plasma gas condensation. *J. Vac. Sci. Technol.*, 32(3):031805, 2014.

[134] J. Passig, K-H. Meiwes-Broer, and J. Tiggesbäumker. Collimation of metal nanoparticle beams using aerodynamic lenses. *Rev. Sci. Instrum.*, 77(9):093304, 2006.

[135] Sitki Aktas. *Gas phase preparation of magnetic nanoparticle hydrosols.* PhD thesis, Leicester, UK, Oct 2014.

[136] Q. Zhang, W. Wang, J. Goebl, and Y. Yin. Self-templated synthesis of hollow nanostructures. *Nano Today*, 4(6):494–507, 2009.

[137] X. W. Lou, L. A. Archer, and Z. Yang. Hollow micro-/nanostructures: Synthesis and applications. *Adv. Mater.*, 20(21):3987–4019, 2008.

[138] M. Ibáñez, J. Fan, W. Li, D. Cadavid, R. Nafria, A. Carrete, and A. Cabot. Means and limits of control of the shell parameters in hollow nanoparticles obtained by the kirkendall effect. *Chem. Mater.*, 23(12):3095–3104, 2011.

[139] C. W. Woffinden. *The Surface Electronic and Magnetic Properties of Rare Earth Silicides and Iron Nanoclusters Using Metastable De-Excitation Spectroscopy.* PhD thesis, York, UK, 2010.

[140] B. Jeon, Q. Van Overmeere, A. C. T. van Duin, and S. Ramanathan. Nanoscale oxidation and complex oxide growth on single crystal iron surfaces and external electric field effects. *Phys. Chem. Chem. Phys.*, 15:1821–1830, 2013.

[141] M. D. Susman, A. Vaskevich, and I. Rubinstein. A general kinetic-optical model for solid-state reactions involving the nano kirkendall effect. the case of copper nanoparticle oxidation. *J. Phys. Chem. C.*, 120(29):16140–16152, 2016.

[142] K. K. Fung, B. Qin, and X. X. Zhang. Passivation of α-Fe nanoparticle by epitaxial γ-Fe_2O_3 shell. *Mater. Sci. Eng. C*, 286(1):135–138, 2000.

[143] D. E. Fowler and J. M. Blakely. An auger electron spectroscopy (AES) study of the initial stages of oxidation of the single crystal Be (0001) surface. *J. Vac. Sci. Technol. A*, 20(4):930–933, 1982.

[144] C. M Wang, D. R. Baer, J. E. Amonette, M. H. Engelhard, J. J. Antony, and Y. Qiang. Electron beam-induced thickening of the protective oxide layer around Fe nanoparticles. *Ultramicroscopy*, 108(1):43–51, 2007.

[145] W. K. Chu, J. W. Mayer, and M. A. Nicolet. *Backscattering Spectrometry*. Academic Press Inc., 1982.

[146] C. R. A. Catlow, J. Corish, J. Hennessy, and W. C. Mackrodt. Atomistic simulation of defect structures and ion transport in α-Fe_2O_3 and α-Cr_2O_3. *J. Am. Ceram. Soc.*, 71(1):42–49, 1988.

[147] H. J. Fan, M. Knez, R. Scholz, D. Hesse, K. Nielsch, M. Zacharias, and U. Gösele. Influence of surface diffusion on the formation of hollow nanostructures induced by the kirkendall effect: The basic concept. *Nano Lett.*, 7(4):993–997, 2007.

[148] A. M. Gusak, F. Hodaj, and T. V. Zaporozhets. Thermodynamics of void nucleation in nanoparticles. *Philos. Mag. Lett.*, 91(12):741–750, 2011.

[149] L. Klinger and E. Rabkin. On the nucleation of pores during the nanoscale kirkendall effect. *Mater. Lett.*, 161:508–510, 2015.

[150] S. Peng and S. Sun. Synthesis and characterization of monodisperse hollow Fe_3O_4 nanoparticles. *Angew. Chem. Int. Ed*, 46(22):4155–4158, 2007.

[151] K.-Y. Niu, J. Park, H. Zheng, and A. P. Alivisatos. Revealing bismuth oxide hollow nanoparticle formation by the kirkendall effect. *Nano Lett.*, 13(11):5715–5719, 2013.

[152] F. S. Buffington, K. Hirano, and M. Cohen. Self diffusion in iron. *Acta Mater.*, 9(5):434–439, 1961.

[153] G. Ketteler, W. Weiss, W. Ranke, and R. Schlögl. Bulk and surface phases of iron oxides in an oxygen and water atmosphere at low pressure. *Phys. Chem. Chem. Phys.*, 3:1114–1122, 2001.

[154] F. Koch and J. B. Cohen. The defect structure of $Fe_{1-x}O$. *Acta Crystallogr. B*, 25(2):275–287, 1969.

[155] A. Yamamoto. Modulated structure of wüstite ($Fe_{1-x}O$) (three-dimensional modulation). *Acta Cryst. B*, 38(5):1451–1456, 1982.

[156] W. H. Bragg. The structure of magnetite and the spinels. *Nature*, 95:561–561, 1915.

[157] M. E. Fleet. The structure of magnetite. *Acta Cryst. B*, 37(4):917–920, 1981.

[158] L. Néel. Propriétés magnétiques des ferrites; ferrimagnétisme et antiferromagnétisme. *Ann. Phys.*, 12(3):137–198, 1948.

[159] E. J. W. Verway. Electronic conduction of magnetite (Fe_3O_4) and its transition point at low temperatures. *Nature*, pages 327–328, 1939.

[160] Walz. F. The verwey transition - a topical review. *J. Phys. Condens. Matter*, 14(12):R285–R340, 2002.

[161] D. Santos-Carballal, A. Roldan, R. Grau-Crespo, and N. H. de Leeuw. A DFT study of the structures, stabilities and redox behaviour of the major surfaces of magnetite Fe_3O_4. *Phys. Chem. Chem. Phys.*, 16(39):21082–21097, 2014.

[162] R. Grau-Crespo, A. Y. Al-Baitai, I. Saadoune, and N. H. De Leeuw. Vacancy ordering and electronic structure of γ-Fe_2O_3 (maghemite): theoretical investigation. *J. Phys. Condens. Matter.*, 22(25):255401, 2010.

[163] C. Greaves. A powder neutron diffraction investigation of vacancy ordering and covalence in γ-Fe_2O_3. *J. Solid State Chem.*, 49(3):325–333, 1983.

[164] G. Rollmann, A. Rohrbach, P. Entel, and J. Hafner. First-principles calculation of the structure and magnetic phases of hematite. *Phys. Rev. B*, 69:165107, 2004.

[165] B. M. Warnes, F. F. Aplan, and G. Simkovich. Electrical conductivity and seebeck voltage of Fe_2O_3, pure and doped, as a function of temperature and oxygen pressure. *Solid State Ion.*, 12:271–276, 1984.

[166] R. L. Blake, R. E. Hessevick, T. Zoltai, and L. W. Finger. Refinement of the hematite structure. *Am. Mineral.*, 51(1-2):123–129, 1966.

[167] C. A. F. Vaz, A. Balan, F. Nolting, and A. Kleibert. In situ magnetic and electronic investigation of the early stage oxidation of fe nanoparticles using x-ray photo-emission electron microscopy. *Phys. Chem. Chem. Phys.*, 16:26624–26630, 2014.

[168] A. Cabot, V. F. Puntes, E. Shevchenko, Y. Yin, L. Balcells, M. A. Marcus, S. M. Hughes, and A. P. Alivisatos. Vacancy coalescence during oxidation of iron nanoparticles. *J. Am. Chem. Soc.*, 129:10358–10360, 2007.

[169] K. Haneda and A. H. Morrish. Oxidation of aerosoled ultrafine iron particles. *Nature*, 282:186–188, 1979.

[170] T. C. Rojas, J. C. Sánchez-López, J. M. Greneche, A. Conde, and A. Fernández. Characterization of oxygen passivated iron nanoparticles and thermal evolution to γ-Fe_2O_3. *J. Mat. Sci.*, 39:4877–4885, 2004.

[171] Y. S. Kwok, X. X. Zhang, B. Qin, and K. K. Fung. High-resolution transmission electron microscopy study of epitaxial oxide shell on nanoparticles of iron. *Appl. Phys. Lett.*, 77(24):3971–3973, 2000.

[172] L. T. Kuhn, A. Bojesen, L. Timmermann, M. M. Nielsen, and S. Mørup. Structural and magnetic properties of core shell iron iron oxide nanoparticles. *J. Phys. Condens. Matter.*, 14(49):13551–13567, 2002.

[173] L. Signorini, L. Pasquini, L. Savini, R. Carboni, F. Boscherini, E. Bonetti, A. Giglia, M. Pedio, N. Mahne, and S. Nannarone. Size-dependent oxidation in iron/iron oxide core-shell nanoparticles. *Phys. Rev. B*, 68:195423, 2003.

[174] W. Yi, W. MoberlyChan, V. Narayanamurti, Y. F. Hu, Q. Li, I. Kaya, M. Burns, and D. M. Chen. Characterization of spinel iron-oxide nanocrystals grown on fe whiskers. *J. Appl. Phys.*, 95(11):7136–7138, 2004.

[175] A. P. Grosvenor, B. A. Kobe, M. C. Biesinger, and N. S. McIntyre. Investigation of multiplet splitting of Fe 2p XPS spectra and bonding in iron compounds. *Surf. Interface Anal.*, 36(12):1564–1574, 2004.

[176] T. Yamashita and P. Hayes. Analysis of xps spectra of Fe^{2+} and Fe^{3+} ions in oxide materials. *Appl. Surf. Sci.*, 254(8):2441–2449, 2008.

[177] J. Finster. SiO_2 in 6:3 (stishovite) and 4:2 Co-ordination—Characterization by core level spectroscopy (XPS/XAES). *Surf. Interface Anal.*, 12(5):309–314, 1988.

[178] M. C. Biesinger, B. P. Payne, A. P. Grosvenor, Lau. L. W. M., A. R. Gerson, and R. St. C. Smart. Resolving surface chemical states in XPS analysis of first row transition metals, oxides and hydroxides: Cr, Mn, Fe, Co and Ni. *Appl. Surf. Sci.*, 257(7):2717–2730, 2011.

[179] M. P. Seah. *Quantification of AES and XPS in Practical Surface Analysis by Auger and X-ray Photoelectron Spectroscopy.* John Wiley & Sons, 1983.

[180] U. Colombo, Gazzarrini. F., and G. Lanzavecchia. Mechanisms of iron oxides reduction at temperatures below 400°C. *Mater. Sci. Eng. C.*, 2(3):125–135, 1967.

[181] W. K. Jozwiak, E. Kaczmarek, T. P. Maniecki, W. Ignaczak, and W. Maniukiewicz. Reduction behavior of iron oxides in hydrogen and carbon monoxide atmospheres. *Appl. Catal. A-Gen.*, 326(1):17–27, 2007.

[182] K. Prabhakaran, K. V. P. M Shafi, A. Ulman, P. M. Ajayan, Y. Homma, and T. Ogino. Low-temperature, carbon-free reduction of iron oxide. *Surf. Sci.*, 506(1):L250–L254, 2002.

[183] W. Radlik and H. Neddermeyer. UV photoemission study of the system Cu on Si(100)2×1. *Surf. Sci.*, 195(1):195–206, 1988.

[184] S. G. Bishop and P. C. Kemeny. Photoemission study of the electronic structure of magnetite. *Solid State Commun.*, 15(11):1877–1880, 1974.

[185] A.-C. Burdușel, O. Gherasim, A. M. Grumezescu, L. Mogoantă, A. Ficai, and E. Andronescu. Biomedical applications of silver nanoparticles: An up-to-date overview. *Nanomaterials*, 8(9), 2018.

[186] J. Crangle and G. M. Goodman. The magnetization of pure iron and nickel. *Proc. Roy. Soc. Lond. A.*, 321:477–491, 1971.

[187] D. Cao, H. Li, L. Pan, J. Li, X. Wang, P. Jing, X. Cheng, W. Wang, J. Wang, and Q. Liu. High saturation magnetization of γ-Fe_2O_3 nano-particles by a facile one-step synthesis approach. *Sci. Rep.*, 6:32360, 2016.

[188] W. H. Meiklejohn and C. P. Bean. New magnetic anisotropy. *Phys. Rev.*, 102(5):1413, 1956.

[189] W. H. Meiklejohn and C. P. Bean. New magnetic anisotropy. *Phys. Rev.*, 105(3):904, 1957.

[190] S. H. Baker, M. Lees, M. Roy, and C. Binns. Structure and magnetism in Fe/Fe_xPd_{1-x} core/shell nanoparticles formed by alloying in Pd-embedded Fe nanoparticles. *J. Phys.: Condens. Matter*, 25(38):386004, 2013.

[191] G. Salazar-Alvarez, J. Sort, S. Suriñach, M. D. Baró, and J. Nogués. Synthesis and size-dependent exchange bias in inverted core-shell MnO-Mn_3O_4 nanoparticles. *J. Am. Chem. Soc.*, 129(29):9102–9108, 2007.

[192] M. Vasilakaki, K. N. Trohidou, and J. Nogués. Enhanced magnetic properties in antiferromagnetic-core/ferrimagnetic-shell nanoparticles. *Sci. Rep.*, 5(1):9609, 2015.

[193] S. H. Baker, M. Roy, S. J. Gurman, S. Louch, A. Bleloch, and C. Binns. Atomic structure of embedded Fe nanoclusters as a function of host matrix material: a synchrotron radiation study. *J. Phys.: Condens. Matter*, 16:7813–7821, 2004.

[194] S. H. Baker, M. Roy, S. C. Thornton, M. Qureshi, and C. Binns. Probing atomic structure in magnetic core/shell nanoparticles using synchrotron radiation. *J. Phys.: Condens. Matter*, 22(38):385301, 2010.

[195] H. Chen, H. Hu, C. Tao, R. M. Clauson, I. Moncion, X. Luan, S. Hwang, A. Sough, K. Sansanaphongpricha, J. Liao, H. J. Paholak, N. O. Stevers, G. Wang, B. Liu, and D. Sun. Self-assembled Au@Fe core/satellite magnetic nanoparticles for versatile biomolecule functionalization. *ACS Appl. Mater. Inter.*, 11(27):23858–23869, 2019.

[196] C. Lee, N. R. Kim, J. Koo, Y. J. Lee, and H. M. Lee. Cu-Ag core-shell nanoparticles with enhanced oxidation stability for printed electronics. *Nanotechnology*, 26(45), 2015.

[197] R. G. Chaudhuri and S. Paria. Core/Shell nanoparticles: Classes, properties, synthesis mechanisms, characterization, and applications. *Chem. Rev.*, 112(4):2373–2433, 2012.

[198] K. Chatterjee, S. Sarkar, K. Jagajjanani Rao, and S. Paria. Core/shell nanoparticles in biomedical applications. *Adv. Colloid Interface Sci.*, 209:8–39, 2014.

[199] W. Sch artl. Current directions in core–shell nanoparticle design. *Nanoscale*, 2:829–843, 2010.

[200] W. M. Tong, D. A. A. Ohlberg, H. K. You, R. S. Williams, S. J. Anz, M. M. Alvarez, R. L. Whetten, Y. Rubin, and F. N. Diederich. X-ray diffraction and electron spectroscopy of epitaxial molecular buckminsterfullerene films. *J. Phys. Chem.*, 95(12):4709–4712, 1991.

[201] G. Johansson, J. Hedman, A. Berndtsson, M. Klasson, and R. l. Nilsson. Calibration of electron spectra. *J. Electron Spectrosc. Relat. Phenom.*, 2(3):295–317, 1973.

[202] S. W. Gaarenstroom and N. J. T. J. Winograd. Initial and final state effects in the esca spectra of cadmium and silver oxides. *J. Phys. Chem.*, 67(8):3500–3506, 1977.

[203] L. J. Swartzendruber. The Ag-Fe (Silver-Iron) system. *Bull. alloy phase diagr.*, 5:560–564, 1984.

[204] T. Nagase, T. Terai, T. Kakeshita, and K. Morita. Solidification microstructure and magnetic properties of Ag-Rich Ag–Cu–La–Fe immiscible alloys. *Mat. Trans.*, 61(2):311–317, 2020.

[205] J. Ramade, E. Cottancin, M.-A. Lebeault, C. Langlois, L. Piccolo, M. Broyer, M. Hillenkamp, J. Lermé, F. Calvo, and M. Pellarin. Environmental plasmonic

spectroscopy of silver–iron nanoparticles: Chemical ordering under oxidizing and reducing conditions. *J. Phys. Chem. C.*, 123(25):15693–15706, 2019.

[206] J. Ramade, N. Troc, O. Boisron, M. Pellarin, M.-A. Lebault, E. Cottancin, V. T. A. Oiko, R. C. Gomes, V. Rodrigues, and M. Hillenkamp. Nano-fried-eggs: Structural, optical, and magnetic characterization of physically prepared iron-silver nanoparticles. *Nano Res.*, 11:6074–6085, 2018.

[207] M. Benelmekki, M. Bohra, J.-H. Kim, R. E. Diaz, J. Vernieres, P. Grammatikopoulos, and M. Sowwan. A facile single-step synthesis of ternary multicore magneto-plasmonic nanoparticles. *Nanoscale*, 6:3532–3535, 2014.

[208] L. Gan, R. Yu, J. Luo, Z. Cheng, and J. Zhu. Lattice strain distributions in individual dealloyed Pt–Fe catalyst nanoparticles. *J. Phys. Chem. Lett.*, 3(7):934–938, 2012.

[209] P. Strasser, S. Koh, T. Anniyev, J. Greeley, K. More, C. Yu, Z. Liu, S. Kaya, D. Nordlund, H. Ogasawara, M. F. Toney, and A. Nilsson. Lattice-strain control of the activity in dealloyed core-shell cell catalysts. *Nat. Chem.*, 2:454–460, 2010.

[210] K. Siedliska, T. Pikula, Z. Surowiec, D. Chocyk, and E. Jartych. X-ray diffraction and 57Fe mössbauer spectroscopy studies of delafossite $AgFeO_2$ prepared by co-precipitation method. *J. Alloys Compd.*, 690:182–188, 2017.

[211] J. Ahmed, N. Alhokbany, A. Husain, A. Husain, T. Ahmad, M. A. M. Khan, and S. M. Alshehri. Synthesis, characterization, and significant photochemical performances of delafossite $AgFeO_2$ nanoparticles. *J. Solgel. Sci. Technol.*, 94:493–503, 2020.

[212] K. Siedliska, T. Pikula, Z. Surowiec, D. Chocyk, and E. Jartych. X-ray diffraction and 57fe mössbauer spectroscopy studies of delafossite agfeo2 prepared by co-precipitation method. *J. Alloys Compd.*, 690:182–188, 2017.

[213] K. Momma and F. Izumi. Vesta 3 for three-dimensional visualization of crystal, volumetric and morphology data. *J. Appl. Crystallogr.*, 44:1272–1276, 2011.

[214] S. Mishra, P. Kumar, and S. K. Samanta. Atomic sheets of silver ferrite with universal microwave catalytic behavior. *Sci. Total. Environ.*, 818:151735, 2022.

[215] M. Chen, Y. Yue, and Y. Ju. Growth of metal and metal oxide nanowires driven by the stress-induced migration. *J. Appl. Phys.*, 111(10):104305, 2012.

[216] A. M. B. Gonçalves, L. C. Campos, A. S. Ferlauto, and R. G. Lacerda. On the growth and electrical characterization of CuO nanowires by thermal oxidation. *J. Appl. Phys.*, 106(3):034303, 2009.

[217] P. Hiralal, H. E. Unalan, K. G. U. Wijayantha, A. Kursumovic, D. Jefferson, J. L. MacManus-Driscoll, and G. A. J. Amaratunga. Growth and process conditions of aligned and patternable films of iron(III) oxide nanowires by thermal oxidation of iron. *Nanotechnology*, 19(45):455608, 2008.

[218] S. Rackauskas, A. G. Nasibulin, H. Jiang, Y. Tian, V. I. Kleshch, J. Sainio, E. D. Obraztsova, S. N. Bokova, A. N. Obraztsov, and E. I. Kauppinen. A novel method for metal oxide nanowire synthesis. *Nanotechnology*, 20(16):165603, 2009.

[219] X. Wen, S. Wang, Y. Ding, Z. L. Wang, and S. Yang. Controlled growth of large-area, uniform, vertically aligned arrays of α-Fe_2O_3 nanobelts and nanowires. *J. Phys. Chem. B.*, 109(1):215–220, 2005.

[220] C.-Y. Wen, M. C. Reuter, J. Tersoff, E. A. Stach, and F. M. Ross. Structure, growth kinetics, and ledge flow during vapour-solid-solid growth of copper-catalyzed silicon nanowires. *Nano Lett.*, 10(2):514–519, 2010.

[221] S. Kodambaka, J. Tersoff, M. C. Reuter, and F. M. Ross. Diameter-independent kinetics in the vapour-liquid-solid growth of Si nanowires. *Phys. Rev. Lett.*, 96:096105, 2006.

[222] K. Tai, K. Sun, B. Huang, and S. J. Dillon. Catalyzed oxidation for nanowire growth. *Nanotechnology*, 25(14):145603, 2014.

[223] P. J. Linstrom and W. G. Mallard. NIST chemistry webbook, NIST standard reference database number 69. https://doi.org/10.18434/T4D303, may 2022.

[224] W.-X. Li, C. Stampfl, and M. Scheffler. Why is a noble metal catalytically active? the role of the O-Ag interaction in the function of silver as an oxidation catalyst. *Phys. Rev. Lett.*, 90:256102, 2003.

[225] M. C. Biesinger. Advanced analysis of copper x-ray photoelectron spectra. *Surf. Interface Anal.*, 49(13):1325–1334, 2017.

[226] K. Adelsberger, J. Curda, S. Vensky, and M. Jansen. High-pressure synthesis and electrochemical investigation of $Ag_2Cu_2O_3$. *J. Solid State Chem.*, 158(1):82–86, 2001.

[227] P. R. Subramanian and J. H. Perepezko. The Ag-Cu (silver-copper) system. *J. Phase. Equilib.*, 14:62–75, 1993.

[228] T. Ohashi, K. Kuroda, and H. Saka. In situ electron microscopy of melting and solidification of in particles embedded in an Fe matrix. *Philos. Mag. B.*, 65(5):1041–1052, 1992.

[229] W. H. Qi and M. P. Wang. Size and shape dependent melting temperature of metallic nanoparticles. *Mater. Chem. Phys.*, 88(2):280–284, 2004.

[230] S. L. Lai, J. Y. Guo, V. Petrova, G. Ramanath, and L. H. Allen. Size-dependent melting properties of small tin particles: Nanocalorimetric measurements. *Phys. Rev. Lett.*, 77:99–102, 1996.

[231] S. Magdassi, M. Grouchko, and A. Kamyshny. Copper nanoparticles for printed electronics: Routes towards achieving oxidation stability. *Materials*, 3:4626–4638, 2010.

[232] R. Schierholz, B. Lacroix, V. Godinho, J. Caballero-Hernández, M. Duchamp, and A. Fernández. STEM–EELS analysis reveals stable high-density He in nanopores of amorphous silicon coatings deposited by magnetron sputtering. *Nanotechnology*, 26(7):075703, 2015.